# Inhomogeneous potential vorticity homogenization and equilibration in simple models of baroclinic instability with implications for the extratropical circulation

by

Pablo Zurita-Gotor

Submitted to the Department of Earth, Atmospheric and Planetary Sciences
in partial fulfillment of the requirements for the degree of

Doctor of Philosophy

at the

MASSACHUSETTS INSTITUTE OF TECHNOLOGY

February 2003



Author .....
Department of Earth, Atmospheric and Planetary Sciences
October 28, 2002

Certified by .....
Richard S. Lindzen
Alfred P. Sloan Professor of Meteorology
Thesis Supervisor

Certified by .....
Edmund K.M. Chang
Associate Professor, SUNY Stony Brook
Thesis Supervisor

Accepted by .....
Ronald G. Prinn
Head, Department of Earth, Atmospheric and Planetary Sciences

# Inhomogeneous potential vorticity homogenization and equilibration in simple models of baroclinic instability with implications for the extratropical circulation

by

Pablo Zurita-Gotor

Submitted to the Department of Earth, Atmospheric and Planetary Sciences
on October 28, 2002, in partial fulfillment of the
requirements for the degree of
Doctor of Philosophy

## Abstract

Baroclinic eddies are an important component of the General Circulation which regulate the extratropical climate by transporting heat and momentum. An idealization of this feedback is provided by baroclinic adjustment theories (Stone, 1978), which envision a linearly neutralized mean state. Based on the Charney-Stern condition, most baroclinic adjustment formulations propose basic states with homogenized potential vorticity.

In this thesis we investigate the degree of potential vorticity homogenization in the extratropical troposphere. We show that homogenization is only observed across a shallow region around 700 mb, and propose an adjusted state with homogenized PV at the steering level alone. We demonstrate that this state can be neutral under certain conditions, and investigate its relevance for the equilibration of an idealized model.

Because of the role of the PV flux as an eddy forcing of momentum, it is illuminating to describe the equilibration in terms of the redistribution of momentum. This affects both the PV gradient and the steering level of the waves, but the condition of homogenization at the steering level is very robust. In the 2D problem, a local balance can be written between the dynamical and frictional forcing of momentum. However, in the 3D problem there is an additional redistribution by a remotely forced meridional circulation.

To circumvent this difficulty, we have developed a momentum-based formulation that exploits the interchangeability of momentum and temperature for quasi-balanced stratified rotating flow. By rewritting the thermodynamic equation as a momentum equation, we eliminate the forcing by the mean meridional circulation and formulate a local balance between the eddy PV flux and the non-conservative forcing of momentum. This introduces a new variable, which we call potential momentum. The circulation can then be described in terms of the conversion between potential and physical momentum.

A major simplification of this formulation is that temperature and momentum can be directly compared. For instance, the surface temperature gradient appears as a momentum source, which helps ellucidate the role of the momentum fluxes and the so-called "barotropic governor" (James, 1987) for the baroclinic equilibration. Our results suggest that mechanical friction might prevent thermal homogenization at the surface.

Thesis Supervisor: Richard S. Lindzen
Title: Alfred P. Sloan Professor of Meteorology

Thesis Supervisor: Edmund K.M. Chang
Title: Associate Professor, SUNY Stony Brook

# Acknowledgments

Looking back, I must say I had a good time. Six years is a long period and spans many moments, some happy, others not so happy. The pursuit of a PhD is never an easy task and MIT can be tough at times. Like everyone else, I also had to go through some bad moments in the last few years. However, looking in retrospect, I think the balance is still positive... I am for sure going to miss the people I met, the city of Boston and I'd say that even MIT! Here are my thanks to everybody who helped me make it to the finish line.

First, I'd like to thank my advisor Dick Lindzen. His insight and encouragement helped me stay on the right track, and this thesis wouldn't have been the same without his advice. He gave me his trust and camaraderie, which has made me a much more confident person than I was six years ago. I am also really appreciative of Dick and Nadine's hospitality, and thankful for those huge photographic portraits.

Edmund Chang was another important piece in the puzzle. He is smart and well-read, and I learned a lot from him. He also helped me to deal with the stress of being a foreign student at a place like MIT, by always being understanding and flexible.

The rest of my committee was also very helpful. I was fortunate to have there Alan Plumb, Glenn Flierl and Reggie Newell. They were always willing to listen to me despite their busy schedule, and gave me great suggestions and useful pointers to the literature.

The staff at MIT was really helpful, warm and friendly, and I owe a lot to Linda Meinke, Mary Elliff and Joel Sloman. In the evenings, I also enjoyed the occasional chat with Tony Pallota, who has many interesting life stories and knows the North End better than anyone.

For many outside people, MIT has the reputation of a cold, unfriendly and competitive place. However, I must say that despite the pressure, my fellow students have always been most friendly and collaborative. I have met some really nice people here. From my classmates, I became especially good friends with Yu Han Chen, Juan Botella, Galen McKinley, Jelena Popovic, Caixia Wang, Tieh Yong Koh and Don Lucas.

I had the 'party' office, and many great officemates like Bill Ramstrom, Rob Korty, Shangao Nong, Patty Bradshaw, and others. But I should make a special mention to Greg Lawson and Juli Atherton, who have also become two of my best friends. Greg is always willing to catch a movie or a beer and we have had many good times together. He has also given me a lot of sensible advice, and helped me get acquainted with the American culture.

It wasn't easy to understand Juli's English at first, but she likes to talk and gave me plenty of chances to get used to it. A few years ago, I had a bad depressive episode and Juli spent a lot of time trying to help me, even though she was also struggling with her own work. Eventually, I did get better, but Juli's work resented and she was told to leave with a Masters after 4 years and having successfully gone through both her General Exam and thesis proposal. I can't help but think that she wasn't treated fairly.

There are so many other people I should mention. It was long ago that he left, but Vince Larson helped me a lot during my first few years, and we still sort of keep in touch. I also had many interesting discussions with Nili Harnik, who shares similar research interests, and with Constantine Giannitsis, who is sorely missed by all of us.

I enjoyed many chess challenges with Peter Huybers, and fierce battles on the island of Catan with Olivier Pauluis. Outside the department, I also had many good times running with Kathryn Butler, catching movies with Elke Duchardt and Annette Rohr, and watching soccer and sipping tea (or drinking beer!) with Adrian Vetta.

I leave for the end perhaps the most important person, my brother Blas. For a long time, he was also my roommate, and gave me his love and support when I most needed it. I am happy however that he moved out, since it was because he met an exceptional person, his now-wife Elena Gavrikova. Blas and Elena were also kind to host me during the last couple of months, when my lease was over but my thesis was not. And though he doesn't know much Meteorology, Blas did help me bounce some ideas as I was writing this thesis.

I was also fortunate to have in the area another of my brothers, Mauricio (and his wife Raquel). He doesn't live in Boston, so I didn't get to hang out with him as often as with Blas or as much as I'd have liked. But it still made a difference for me to know him close.

Having Blas and Mauricio around was great, but not enough. My other siblings: Carlos, Maricarmen, Macu, Pilu and Espe are still in Spain, as well as my parents Blas Zurita and Carmen Gotor, to whom I dedicate this thesis. The toughest part of being here was to only get to see you once a year: I've missed you dearly, as I know that you have also missed me. I hope that it was for a good cause and that I made you proud. Without the education and values that you gave me, I'd have never made it where I am. Thank you.

Finally, I acknowledge the financial support by Program PG-94 of the Secretaria de Estado de Universidades e Investigacion of Spain, and thank my Spanish advisor Joaquin Tintore and Professor Antonio Barrero for helping me prepare the application to MIT.

# Contents


**1 Introduction** **21**

1.1 Outline . . . . . 23

**2 Baroclinic adjustment and PV mixing in the extratropical troposphere** **25**

2.1 Introduction . . . . . 25

2.2 The concept of baroclinic adjustment . . . . . 26

2.2.1 Adjustment in continuous models: boundary vs interior PV mixing . 27

2.3 Is the interior PV really homogenized? . . . . . 31

2.3.1 The curvature PV gradient. . . . . 37

2.4 The mixing depth constraint . . . . . 40

**3 Short Charney waves: the stability of partially homogenized states** **45**

3.1 Formulation . . . . . 46

3.2 Vertical scales in the Charney problem . . . . . 48

3.2.1 Scaling for the barotropic point jet . . . . . 51

3.3 Implications . . . . . 52

3.4 Dispersion relation . . . . . 54

3.5 Neutral states . . . . . 58

3.5.1 Analytical model . . . . . 58

3.5.2 Numerical results . . . . . 62

3.5.3 Wave geometry interpretation . . . . . 67

3.6 Summary . . . . . 69

**4 The equilibration of short Charney waves** **71**

4.1 The barotropic point jet . . . . . 72

4.1.1 PV homogenization and steering level . . . 74
4.1.2 The mixing length constraint . . . 84
4.1.3 Forced-dissipative problem . . . 87
4.2 3D equilibration of the baroclinic problem . . . 92
4.2.1 PV homogenization and steering level . . . 92
4.2.2 The role of surface friction . . . 95
4.2.3 Mean circulation and fluxes . . . 98
4.2.4 The mixing depth constraint . . . 103
4.2.5 Eddy enstrophy dissipation and the frictional forcing of momentum 106
4.3 Summary . . . 109

**5 A momentum-based formulation of the 3D extratropical circulation 125**
5.1 Motivation: local vs non-local forcing of momentum . . . 125
5.2 The concept of potential momentum . . . 127
5.2.1 Physical interpretation . . . 130
5.3 Potential momentum balance . . . 133
5.4 Implications . . . 136
5.4.1 The 3D mixing depth constraint . . . 137
5.4.2 Local momentum balance in a forced-dissipative system . . . 139
5.5 Potential momentum diagnostics of the idealized runs . . . 142

**6 Kinematic aspects 151**
6.1 Motivation and literature review . . . 152
6.2 PV homogenization in the barotropic problem . . . 157
6.2.1 Statistical diagnostics . . . 161
6.2.2 Discussion . . . 165
6.3 Dynamical evolution . . . 166
6.3.1 Evolution of the weakly growing wave ($L/l = 1.25$) . . . 168
6.3.2 Evolution of the most unstable mode ($L/l = 3.9$) . . . 169
6.4 Cross-stream flow, chaotic advection and mixing . . . 176

**7 Conclusion 183**
7.1 Summary of the main results . . . 183

7.1.1 Conclusions . . . . . 190
7.2 Limitations of this work and possible extensions . . . . . 191

**A Vertical scales** **193**

**B Model description** **195**
B.1 Contour advection model . . . . . 199

# List of Figures


2-1 Comparison of adjusted and observed profiles of $h$ at a number of latitudes. The adjusted profile is the solid line with dots. Taken from Stone and Nemet (1996). . 31

2-2 Comparison of the thermal structure predicted by a model of full PV homogenization (top), and a model with an interior PV gradient of $\beta$ (bottom) against observations (middle). Taken from Sun and Lindzen (1994). . . . . 33

2-3 Zonal mean PV gradient (normalized by $\beta$) for the months indicated. Taken from Kirk-Davidoff and Lindzen (2000). . . . . 36

2-4 Zonal wind (left) and horizontal curvature PV gradient (right), mass-weighted and normalized by $\beta$. Three types of values are shown: (top panels) Zonal and time mean, January 2001, (second panels) Zonal mean, January 15th 2001, (third panels) Meandering mean for the same day, (bottom) Vertical mean values. Data taken from the NCEP/NCAR reanalysis project. . . . . 39

2-5 Sketch illustrating how a wave with mixing depth $H_0$ equilibrates the mean flow $U(z)$ in the Charney-Boussinesq problem. See text for details. . . . . 40

2-6 Diagram illustrating the regions with different sign of the integrated PV gradient over the mixing depth $H_0$, as a function of $H_0/H_S$ and $h_0/H_S$. Also shown are Held's (1978) scaling for the mixing depth of the most unstable mode in the limits $h_0 << H_S$ and $h_0 >> H_S$. . . . . 42

3-1 Sketch showing the three regions, in terms of wave propagation characteristics, in the Charney problem. Regions I and III are evanescent, while region II allows wave propagation. . . . . 50

3-2 Diagram illustrating the definition of a short Charney wave as a wave with $H/h <$ 3.9, or shorter than the most unstable mode. . . . . 51

3-3 Vertical structure (magnitude only) for a short Charney wave (H/h=0.45) and the most unstable Charney mode (H/h=3.9): streamfunction perturbation (dashed), PV perturbation (thin solid) and PV flux (thick solid). The steering level is the dash-dotted line and only interior values are shown. Vertical scales are nondimensionalized with $H$. . . . . 55

3-4 Dispersion relation for the Charney-Boussinesq problem as a function of $H/h$: (top) real phase speed, (bottom) imaginary phase speed. The phase speed is nondimensionalized with $\Lambda H$, where $H$ is the half Rossby depth, and $\frac{c_i}{\Lambda H}$ is proportional to the growth rate (see text). The dashed line in both panels show the shortwave asymptotic expansion of Branscome (1983), and the dash-dotted line labeled $g_2$ in the bottom panel is the growth rate of the second harmonic, based on the value of $H/h$ for the primary wave. Note that the diagram emphasizes the shortwave part of the spectrum; the multiple zeros of the Charney problem occur for larger values of $H/h$. . . . . 57

3-5 Solutions of the problem defined by equation 3.17 for $\tilde{k} = \pi$, $R = 3$ (nondimensionalizing with $D = H$). See text for details. . . . . 61

3-6 Real phase speed for the neutral solutions of the analytical model discussed in the text: R=0.5 (solid), R=1 (solid), R=5 (dashed) and R=10 (dot-dashed). The lines are interrupted where the phase speed becomes imaginary or convergence was not reached in 100 iterations. . . . . 63

3-7 Vertical structure of the two eigenmodes for the modified Green problem for $R = 3$ and $k = 2.8$ (solid) and 5 (dashed). The horizontal marks show the position of the steering level for each mode. . . . . 64

3-8 Vertical structure of the unstable Green wave at the Eady shortwave cutoff when $\beta = 1.6 * 10^{-11} m^{-1} s^{-1}$. This mode has $H/h = 0.38$ and is also short in a Charney sense. The mode becomes neutral when the PV gradient is brought to zero across the shaded region alone. . . . . 65

3-9 Vertical structure and steering level for Charney modes with $H/h = 1.6$. Left panel: mode with uniform interior PV gradient. Right panel: mode when the PV gradient is brought to zero across a broad region surrounding the original steering level. Note that the PV flux vanishes in the region of zero PV gradient, which includes the modified steering level, and yet the mode is still unstable. However, when the PV gradient is brought to zero across the region shaded in the left panel the mode becomes neutral. See text for details. . . . . 66

3-10 Growth rate (upper panel) and phase speed (lower panel), nondimensionalized with $\Lambda H$, as a function of the thickness of the region of homogenized PV gradient surrounding the steering level. The different curves correspond to different values of $H/h$ in the unhomogenized profile. . . . . 68

4-1 Time series of the zonal mean potential vorticity and zonal wind for the run with $\beta = 5 \times 10^{-12} m^{-1} s^{-1}$ (L/l=1.25). (top left) $|\overline{q}_y|/\beta$, contour unit $0.2\beta$, values smaller than the contour unit are non-shaded. (top right) zonal mean $|\overline{q}_y|/\beta$ (initial dashed; equilibration, solid). (bottom left) $|U - c|$, contour unit 2 $m/s$, values smaller than 1 $m/s$ are non-shaded. (bottom right) zonal mean $|U - c|$ (initial dashed; equilibration, solid). The horizontal marks show the position of the steering level. 75

4-2 Time series of the net negative vorticity jump, normalized by $\Lambda$, for the runs with L/l=1.25 (solid), 2.5 (dash-dotted) and 3.9 (dashed). . . . . 76

4-3 As figure 4-1, but for the case of the most unstable mode ($\beta = 1.6 \times 10^{-11} m^{-1} s^{-1}$, L/l=3.9). . . . . 77

4-4 Time series of phase speed (solid) and minimum zonal mean wind (dashed) for the $L/l = 1.25$ (top) and $L/l = 3.9$ (bottom) runs. . . . . 79

4-5 A) Time-mean correction to the zonal flow for $L/l = 1.25$ (solid), 2.5 (dashed), 3.25 (dash-dotted) and 3.9 (dotted). B) As A but for the time-integrated eddy momentum flux in $m^2/s^2 \times day$. C, D, E, F) Time series of the eddy momentum flux for the cases indicated. . . . . 81

4-6 Mean flow correction $\overline{U} - \overline{U_0}$ (thick solid), and $\overline{U} - c$ (dash-dotted) for the cases indicated. Points A, B, C, and D show the position of the original steering level, whereas points A', B' and C' show its final position. . . . . 82

4-7 Zonal mean PV distribution, initial (dashed) and at equilibration (solid) for the cases indicated. The vertical marks indicate the position of the steering level. . . . 83

4-8 Zonal mean relative vorticity for the runs with L/l=1.25 (solid), 2.5 (dash-dotted) and 3.9 (dashed). Also shown is the $\beta$ slope for the same cases. . . . . 85

4-9 Sketch illustrating the smoothing effect on the zonal mean (right) resulting from the wavy distortion of a contour (left). . . . . 86

4-10 Zonal mean relative vorticity (left) and absolute vorticity (right) for the runs with $\beta = 2.1 \times 10^{-11}\ m^{-1}s^{-1}$. The solid and dashed lines correspond to runs initialized with perturbations of zonal wavenumbers 1 and 2, respectively. . . . . 86

4-11 Net negative vorticity jump (normalized by $\Lambda$) at equilibration as a function of the forcing time scale $\tau$ for the values of $L/l$ indicated. . . . . 88

4-12 (Top) Mean PV gradient (normalized by $\beta$) at equilibration for the runs with $L/l = 5$ and forcing time $\tau = 250$ *days* (solid), $\tau = 30$ *days* (dash-dotted) and $\tau = \infty$ (dashed). (Bottom left) Eddy enstrophy balance for the run with $L/l = 5$ and $\tau = 250$ *days*: wave-mean flow interaction (thin solid), eddy advection (dashed), dissipation (dash-dotted) and residue (thick solid). (Bottom right) Same but for $\tau = 30$ *days*. . . . . 91

4-13 Time-mean equilibrium state for the run with $\beta = 1.0 \times 10^{-11}\ m^{-1}s^{-1}$ ($H/h = 0.54$). (Upper panel). Left: absolute value of the zonal mean potential vorticity gradient, normalized by $\beta$ (contour unit $0.15\beta$). Right: profile at the center of the channel at equilibration (solid) and radiative equilibrium (dashed). (Lower panel). Left: absolute value of $\overline{U} - c$ (contour unit 2 $m/s$). Right: zonal velocity $\overline{U}$ at the center of the channel at equilibration (solid) and radiative equilibrium (dashed). The horizontal line highlights the steering level. Regions with values of $|\bar{q}_y|$ and $|U - c|$ smaller than the corresponding contour unit are non-shaded in the contour plots. Vertical distances are nondimensionalized with the half Rossby depth $H$ and the lowest level PV gradient includes the delta function at the ground smoothed at model resolution. . . . . 113

4-14 As in figure 4-13 but for a snapshot at time $t = 135$, when the wave is just starting to modify the basic state. . . . . 114

4-15 Time series at the center of the channel for the run with $\beta = 1.0 \times 10^{-11}\ m^{-1}s^{-1}$ ($H/h = 0.54$). Upper panel: $|\bar{q}_y|$ (contour unit $0.15\beta$). Medium panel: $|U - c|$ (contour unit 2 $m/s$). Lower panel: surface wind (lower curve) and phase speed of the wave (upper curve). The thickness of the shaded region is related to the height of the steering level. . . . . 115

4-16 As in figures 4-13, 4-15 but for the run with $\beta = 1.3 \times 10^{-11}\ m^{-1}s^{-1}$ ($H/h = 0.7$). 116

4-17 As in figures 4-13, 4-15 but for the run with $\beta = 1.6 \times 10^{-11}\ m^{-1}s^{-1}$ ($H/h = 0.86$). 117

4-18 As in figure 4-13 but for the run with $\beta = 1.0 \times 10^{-11}\ m^{-1}s^{-1}$ ($H/h = 0.54$) and surface damping time scale 5 days. . . . . 118

4-19 As in figure 4-15 but for the run with $\beta = 1.0 \times 10^{-11}\ m^{-1}s^{-1}$ ($H/h = 0.54$) and surface damping time scale 5 days. . . . . 119

4-20 As in figures 4-13, 4-15 but for the run with $\beta = 3.0 \times 10^{-11}\ m^{-1}s^{-1}$ ($H/h = 1.6$) and surface damping time scale 1 day. . . . . 120

4-21 Maintenance of the equilibrated state for the simulation with $\beta = 3.0 \times 10^{-11}\ m^{-1}s^{-1}$ ($H/h = 1.6$) and 1 day surface damping. (A) Potential temperature (dashed) and zonal mean wind (solid) in radiative equilibrium. (B) Same but for the equilibrated flow. Contour unit: 4 K for temperature and 4 m/s for zonal wind, the zero wind line is dash-dotted. (C) Eddy heat flux in $Kms^{-1}$. (D) Eddy momentum flux in $m^2s^{-2}$. (E) Mean meridional circulation (solid is counterclockwise). (F) Eliassen-Palm fluxes (vectors) and convergence in $s^{-2}$ (dashed line) . . . . . 121

4-22 (Left) Contributions to the zonal mean PV gradient resulting from: (top) vertical curvature, (mid) horizontal curvature, and (bot) total PV gradient, normalized by $\beta$ for the run with $\beta = 1.6 \times 10^{-11}\ m^{-1}s^{-1}$ ($H/h = 0.86$), and surface damping time scale 3 days. (Right) Same but for the vertical profiles at the center of the channel, with radiative equilibrium distributions shown dashed. . . . . 122

4-23 As figure 4-23 but with surface damping 10 days. . . . . 123

4-24 Comparison of the zonal mean flow for the initial profile (dashed), and the equilibrated states for the runs with $H/h = 0.86$ and the surface damping time scales indicated. . . . . 124

5-1 Sketch illustrating the potential momentum distribution associated to an isentropic layer whose thickness: (left) increases with latitude, (right) decreases with latitude. 131

5-2 Sketch illustrating how low latitude heating and high latitude cooling results in a downward transfer of easterly potential momentum. . . . . 134

5-3 Potential momentum diagnostics for the run with $\beta = 3.0 \times 10^{-11}\ m^{-1}s^{-1}$ ($H/h = 1.6$) and friction time scale 1 day. (A) Interior potential momentum (in m/s). (B) Zonal mean flow. (C) Total momentum. (D) Isentropic thickness, normalized by the reference thickness. (E) Potential momentum contribution to the zonal mean PV gradient, normalized by $\beta$. (F) Zonal mean PV gradient, normalized by $\beta$. . . 147

5-3 (continued) (G) Vertical profile of the Held scale $h$ at selected latitudes. (H) Vertically integrated potential momentum at the surface (solid), in the interior (dashed), and at the surface in radiative equilibrium (dash-dotted). For the surface profiles, two alternative distributions corresponding to different choices of $y_0$, $y_L$ are shown (see text for details). (I) Diabatic forcing of potential momentum in the interior, in $m/s^2$. (J) Interior eddy drag $\overline{v'q'}$ in $m/s^2$. (K) Time series of the different contributions to the interior forcing of total momentum, vertically integrated at the center of the channel: diabatic (red), eddy drag (blue) and frictional (magenta). (L) As K, but for a run with weaker surface friction, of time scale 5 days. . . . . 148

5-4 For the runs with $\beta = 1.6 \times 10^{-11}\ m^{-1}s^{-1}$ ($H/h = 0.86$) and the frictional time scales indicated: (Left) Integrated potential momentum in the interior (dashed), at the surface (solid), and in radiative equilibrium (dash-dotted). (Right) Vertical profiles of zonal mean flow (dashed) and (easterly) potential momentum (solid) at the center of the channel. . . . . 149

6-1 Snapshots of the long-time potential vorticity field for the runs indicated (contour unit $0.1\beta L$). Also shown on the right panels are the zonal-mean profiles of $\overline{q}/\beta L$ for the equilibrated state (solid) and radiative equilibrium (dashed). . . . . 158

6-2 Comparison of the zonal mean PV gradient (top) and eddy enstrophy (bottom) profiles for the cases indicated. We also provide for reference the domain-integrated eddy enstrophy. . . . . 160

6-3 For the run with $L/l = 3.9$: A) Streamlines in the corrotating frame at $t = 45\ days$, B) Potential vorticity field at the same time. C) and D) As A and B but for $t = 191\ days$. E) Scatter plot of $q$ (normalized by $\beta L$) vs $\Psi$ at $t = 45\ days$. F) As E but at $t = 191\ days$. G) and H) As E and F but for the run with $L/l = 1.25$. . . 162

6-4 Snapshots of the PV field (repeated 4 times) for the standard channel length with $L/l = 3.9$ (left), and for a channel 4 times longer (right). . . . . 163

6-5 Time series of the potential vorticity cumulative distribution for the runs indicated; a 5% of the total distribution lies between any two adjacent contours. Also shown on the right are the initial (dashed) and final (solid) cumulative distributions. . . . 164

6-6 For the run with $\beta = 5 \times 10^{-12}\ m^{-1}s^{-1}$ ($L/l = 1.25$) and $t$ = 26, 42, 53, 57, 68 and 98 *days*. Left: streamlines in the corrotating frame (dashed when closed), and material contour initially at the jet vertex (thick, solid line); areas with $U-c < 1\ m/s$ are also shaded. Right: PV fields for the same times. . . . . 170

6-6 (continued) . . . . . 171

6-7 As figure 6-6 but for the run with $\beta = 1.6 \times 10^{-11}\ m^{-1}s^{-1}$ ($L/l = 3.9$) and the times indicated. . . . . 174

6-7 (continued) . . . . . 175

6-8 (Top) Time series of phase speed for the short wave run (dashed) and the most unstable mode (solid), with the long-time mean subtracted. (Bottom) Same but for the instantaneous growth rate. In both panels, the vertical axis line shows the time at which the perturbed material contour described in the text first reaches the steering level. . . . . 176

6-9 Distribution of the cross-stream velocity on the mean streamline at selected times. 178

6-10 For the $L/l = 3.9$ run: A) Time-integrated flux of PV across the $\Psi = 0$ streamline. B) Time series of the RMS of the cross-stream velocity on that contour. C) Spatial distribution of the time-mean RMS cross-stream velocity (days 100-150), and contours of mean potential vorticity. . . . . 179

6-11 Distribution of PV on the layer defined by the streamlines $\Psi = 1-2\times10^6\ m^2s^{-1}$ for the $L/l = 3.9$ run. A-C) Snapshots of the distribution at selected times. D) Range of positions occupied by the mean streamline. E) Time-series of the mean PV on the layer. F) Time-series of the PV variance on the layer. G) Time-series of the full PDF. . . . . 180

6-12 As figure 6-11 but for the $L/l = 1.25$ run. . . . . 181

A-1 Sketch illustrating the meaning of the different vertical scales for a short Charney mode. The maximum depth of the PV fluxes scales as $H$, but they are usually shallower, $O(H/h)$. Neutrality requires homogenization over a depth $H^*$ of that order. 194

B-1 Model basic state. (A) Zonal velocity for the barotropic model. (B) Contours of zonal velocity (solid) and potential temperature (dashed) for the qg model. Contour unit: 4 $m/s$ and $4K$. . . . . 197

B-2 Snapshots of the potential vorticity field for 3 different runs. (A) Non-diffusive with standard basic state. (B) Non-diffusive with a modified basic state in which the primary wave is stationary. (C) Diffusive in the stationary basic state. . . . . 198

B-3 Computer time required to perform 5000 direct and inverse Fast Fourier Transforms, with varying $NX$ and fixed $NY = 64$. This is compared to $O(M^2)$ (upper curve) and $O(M \log(M))$ (lower curve). Dimensions that are power of 2 are emphasized in red. . . . . 199

# Chapter 1

# Introduction

An important unresolved question in the study of the General Circulation of the atmosphere is what determines the mean surface temperature gradient in the midlatitudes. In these latitudes the temperature gradient reaches a local maximum, which is however much weaker than in a hypothetical state of radiative-convective equilibrium. This is due to the dynamical transport of heat by the baroclinic eddies (Peixoto and Oort, 1992). The observed midlatitude temperature gradient appears to be very robust for both hemispheres and all seasons, despite large seasonal differences in the forcing and Equator-to-Pole temperature difference (Stone, 1978). However, there is not a simple balance that explains why the temperature gradient adopts this particular value.

An idealization that can be useful for understanding the thermal structure is baroclinic adjustment (Stone, 1978). The basic idea is that the observed equilibrium should be nearly neutral because the diabatic processes are slow. However, this does not constrain the basic state as much as it would seem at first. The baroclinic problem is very complex, and no stability condition is known that is both necessary and sufficient. Moreover, most stability conditions for this problem, like the Charney-Stern condition, are nonlocal in nature. Hence, interpreting the adjustment in terms of some local constraint would be an oversimplification and the whole system with its internal transports should rather be considered.

Another difficulty is the fact that the basic state can be adjusted in many different ways. The eddies transport both momentum and heat, and both horizontally and vertically. When quasigeostrophic theory is used, we can encapsulate the problem in terms of the PV fluxes alone, but even then the situation is far from trivial. As we lack a necessary and

sufficient stability condition, it is not clear what neutral state best represents the observed atmospheric state.

As discussed in chapter 2, the Charney-Stern condition is usually invoked in this regard, and baroclinic adjustment models assume that either the surface temperature gradient, or the interior PV gradient, or both are well mixed. However, because the Charney-Stern condition is only a necessary condition for instability, its violation is by no means a requirement for neutrality. In fact, if we look at the mean tropospheric state, it appears that neither of them is really well mixed, except for a narrow region around 700 mb. This is roughly the level where the synoptic eddies have their steering level. In the inviscid case, the elimination of the PV gradients at the steering level is a necessary condition for stability (Bretherton, 1966). One of the issues that we investigate in this thesis is whether this condition can also be sufficient in some cases.

Because the tropospheric eddies are thought to originate through baroclinic instability, most models of baroclinic adjustment emphasize the vertical structure of the basic state. As a result, these models tend to concentrate on the role of the eddy heat flux and diabatic time scales, while ignoring the eddy momentum flux. In principle, this could seem a reasonable simplification because the Eliassen-Palm fluxes (and their convergence) are dominated by the vertical component. However, it is not clear that this is justified: the fact that any given term dominates the observed equilibrium does not imply that the equilibrium state is most sensitive to changes in that term. It will be argued in this thesis, based on the results from an idealized model, that the momentum fluxes play a major role in the observed equilibrium. Indeed, in our model friction appears to be the limiting factor to the reduction of the surface temperature gradient.

The important role of the momentum fluxes is of course not new. James (1987) was the first author to point out that in the absence of friction, the flow equilibrates by developing a strong barotropic component. At the same time, the surface temperature gradient is reduced. However, it is not obvious from his analysis how these two effects are related dynamically. This will be elucidated in the present thesis by comparing the eddy redistribution of momentum in the 3D Charney problem and its 2D analog, the point jet.

It is well known that zonally symmetric 2D flow can be described in terms of momentum alone, while vorticity adds unnecessary complication. Likewise, we shall develop in this thesis a momentum-based formulation for the zonally symmetric 3D problem. In this for-

mulation, the symmetric 3D problem is encapsulated in terms of a generalized momentum, which also includes a 'potential momentum' contribution related to the stretching term. This is analogous to, but provides a simpler description than, a more traditional description in terms of potential vorticity. In this momentum-based formulation, temperature and momentum can be directly compared, which allows us to get a better appreciation on the role of the momentum fluxes and the constraint exerted by friction.

## 1.1 Outline

In this thesis we address some of the issues described above by studying the three-dimensional baroclinic equilibration in a highly idealized framework. The thesis is structured as follows.

Chapter 2 reviews the concept of baroclinic adjustment, emphasizing the distinction between boundary and interior PV mixing. We also discuss in this chapter the extent to which the interior PV gradient is better homogenized than surface temperature. Finally, we provide a simple geometrical argument, called the mixing depth constraint, on why the eddies might be unable to eliminate the surface temperature gradient when the interior PV gradient is small. This provides the motivation for subsequent chapters.

Chapter 3 defines the concept of a short Charney wave, and considers the implications of this concept for linear stability. It will be shown in this chapter that short Charney waves can be neutralized by potential vorticity homogenization at the steering level alone. This might explain the observed lack of potential vorticity homogenization (except for a shallow region) in the mean tropospheric state, as described in chapter 2.

In chapter 4 we look at the equilibration of short Charney waves. This is done both for the 3D Charney problem and for the 2D barotropic point jet, which are homomorphic in the linear regime. The contrast between both models allows us to get some insight into how three-dimensionality affects the baroclinic problem. In particular, it will be shown in this chapter that the eddy momentum flux convergence plays a very important role in the baroclinic equilibration. While this result is not really new (James, 1987), our analysis clarifies the underlying dynamical mechanism by interpreting the baroclinic equilibration in terms of the redistribution of momentum.

The relation between momentum and temperature is made most transparent in chapter 5. In this chapter we derive a momentum-based formulation of the extratropical circulation,

in which temperature and momentum can be directly compared. For instance, the surface temperature gradient appears in this framework as a momentum source, a result that is in fact implicit in the Eliassen-Palm formulation of the extratropical circulation (Edmon et al., 1980). Moreover, in the new formalism the momentum redistribution by the mean meridional circulation disappears, and the only dynamical forcing of momentum is the eddy PV flux. This allows us to infer some interesting results by exploiting the local character of this flux, which can be related under certain conditions to the local diabatic dissipation of eddy enstrophy.

While chapters 3-4 concentrate on the dynamical implications of partial PV homogenization for equilibration, in chapter 6 we examine the same problem from a kinematic perspective. It is not clear a priori whether idealized kinematic models, like chaotic advection, can be applied to this problem because the phase space evolves as the wave equilibrates.

Finally, in chapter 7 we provide a rather exhaustive summary of the results presented in this thesis, and briefly discuss some of the limitations of our study.

# Chapter 2

# Baroclinic adjustment and PV mixing in the extratropical troposphere

## 2.1 Introduction

In this chapter we discuss the degree of PV homogenization observed in the extratropical troposphere, as well as the dynamical implications for the stability of baroclinic waves. The concept of PV homogenization is ubiquitous in the geophysical literature and has been used as a dynamical model for such various phenomena as the stratospheric surf zone (McIntyre and Palmer, 1984) or mid-oceanic gyres (Pedlosky, 1996). In the case of the extratropical troposphere the main argument for PV homogenization comes from baroclinic adjustment theories, which rely on the violation of the Charney and Stern (1962) condition for instability and the elimination of the interior and/or boundary PV gradients.

One of the basic questions in the General Circulation of the atmosphere is what determines the degree of homogenization of surface temperature by the eddies. This issue is discussed in section 2.2, where we give a brief literature review about baroclinic adjustment, with a focus on the distinction between interior and boundary PV mixing. After that, we discuss in section 2.3 in more detail the degree to which the interior PV gradient is mixed in the extratropical troposphere, specifically whether it is better mixed than the surface temperature gradient. Finally, we give in section 2.4 a simple geometrical argument why

the baroclinic eddies might not be able to eliminate the surface temperature gradient. This provides the basic motivation for the work presented in this thesis.

## 2.2 The concept of baroclinic adjustment

Despite its basic nature and important climatic implications, the question of what determines the Equator-to-Pole temperature gradient remains an unsolved problem in the General Circulation of the atmosphere. Current numerical models do reasonably well at reproducing the present climate. However, models of this complexity can only provide a limited understanding and a simple answer to this basic question has yet to be established.

A useful approach to this problem is provided by the concept of baroclinic adjustment (Stone, 1978). This author noted that the observed temperature gradient in the midlatitude troposphere is very robust in both hemispheres for all seasons, despite large seasonal differences in the radiative forcing and in the Equator-to-Pole temperature difference. Stone (1978) argued that this robustness is due to the strong feedback by the baroclinic eddies, which act as a regulating thermostat of the extratropical climate. The basic idea is that because the eddies act on much faster time scales than the destabilizing diabatic processes, the time-mean tropospheric state should be close to neutral. In other words, in this framework, the observed temperature gradient just reflects the neutrality of the time-mean state. This is akin to convective adjustment, where the strong feedback by the vertical buoyancy fluxes prevents unstable lapse rates. The existence of a similar feedback between eddy heat transports and mean temperature structure has been demonstrated by a number of observational studies (see Stone (1982) for a review).

Stone (1978) also showed that the observed lower troposphere vertical shear is close to the critical shear of the two-layer model, which he proposed as the prototypical neutral state. Hence, this critical shear can be interpreted as the baroclinic counterpart to the adiabatic lapse rate. Note that because the critical shear of the two-layer model is proportional to the static stability, this can also be regarded as a constraint on the isentropic slope.

However, there are some difficulties with this idea. For instance, it is open to debate whether a clear scale separation between the forcing and dynamical time scales exists (Barry et al., 2000). Moreover, baroclinic adjustment is a linear concept, and does not account for the possibility that the waves may saturate nonlinearly in a supercritical environment.

In fact, the actual two-layer model itself appears to equilibrate supercritically (Salmon, 1980), which led Stone and Branscome (1992) to propose a modified version of baroclinic adjustment, in which the isentropic slope is simply proportional to the critical slope of the two-layer model. This supercriticality has been explained by Cehelsky and Tung (1991) (and more recently by Welch and Tung (1998)) using a nonlinear extension of baroclinic adjustment. These authors have argued that there is a limit to how much heat a baroclinic wave can transport, which depends on its scale. As a result, the shorter waves saturate nonlinearly in the presence of a large enough driving, and the bulk of the heat is transported by longer, less unstable waves. Welch and Tung (1998) claim that this produces an equilibrium state which is supercritical for the former and neutral for the latter.

Even accepting that the time-mean tropospheric state is linearly neutral, it is not clear what makes it so. The critical shear of the two-layer model is an artifact of its coarse vertical discretization, and a continuous atmosphere does not have such a critical shear. At a more basic level, the difficulty is that no general stability condition is known which is both necessary and sufficient, unlike in the convective case. Moreover, because the baroclinic eddies transport heat and momentum, meridionally and vertically, the situation is much more complex since the basic state can be adjusted in many different ways. For instance, the vertical heat fluxes (Gutowski, 1985) or the momentum fluxes (Ioannou and Lindzen (1986), James (1987)) can also play a role in the adjustment.

The situation is a bit simpler in the qg limit. Then, there is no need to distinguish between the heat and momentum fluxes and the adjustment can be understood in terms of PV fluxes and PV adjustment alone. However, even in this case no obvious adjustment scenario exists, as discussed in detail in the next section.

### 2.2.1 Adjustment in continuous models: boundary vs interior PV mixing

Unlike the two-layer model, continuous models do not have in general a critical shear. The simplest example is the Charney problem (Charney, 1947): with westerly shear, this model is unstable for all wavenumbers (except at a discrete number of points). This led Lindzen et al. (1980) to propose that the continuous baroclinic instability problem should equilibrate by eliminating the vertical shear at the ground, or the surface temperature gradient.

From a potential vorticity viewpoint, the Charney problem is characterized by a negative delta-function PV gradient at the surface, and a constant positive PV gradient in the

interior. The same is true for the barotropic point jet, which consists of a triangular easterly jet in the presence of constant $\beta$. At the jet vertex, the discontinuity in shear produces a negative delta-function PV gradient. This problem has been shown to have the same stability properties as the Charney-Boussinesq problem (Lindzen et al., 1983).

Schoeberl and Lindzen (1984) and Nielsen and Schoeberl (1984) studied numerically the equilibration of the barotropic point jet, and found that in the inviscid case, this problem equilibrates in the manner mentioned above, by eliminating the negative PV gradient at the vertex. However, they also found that in the presence of forcing/dissipation, the point jet smooths its curvature but does not fully eliminate the negative PV gradient.

On the other hand, the homogenization of the negative PV gradient is not so efficient in the 3D problem. Numerical simulations of inviscid adiabatic baroclinic life-cycles suggest that baroclinic waves eliminate *locally* the surface temperature gradient as they equilibrate (Simmons and Hoskins, 1978). In the actual atmosphere, this condition is sometimes observed locally following the development of a synoptic system; however, in the time-mean, there is a well-defined surface temperature gradient for all seasons. One possibility why this might be so is that dissipative processes are important over those time scales. For instance, Simmons and Hoskins (1978) note that in the presence of friction, the eddies are not so efficient in reducing the surface temperature gradient. Gutowski et al. (1989) looked in more detail at the effect of surface fluxes on the adjustment of the mean flow, using a primitive equation model. They found that in the fully inviscid case, the equilibration involves two stabilizing effects: the low level vertical shear is reduced or eliminated and the low level static stability is enhanced. They also found that the inclusion of surface friction inhibits the former stabilizing effect, while the inclusion of surface heat fluxes inhibits the latter.

An alternative explanation to the non-zero surface temperature gradient was provided by Lindzen (1993). This author noted that the Eady problem (Eady, 1949) is neutral in the shortwave region, even in the inviscid case and in the presence of a non-zero surface temperature gradient. Lindzen (1993) proposed that the mean tropospheric state could also fall into this regime: if the tropopause is high enough, the eddies can equilibrate by mixing the interior PV gradient alone. Lindzen (1993) further argued that, due to the strong sensitivity of the PV gradient to the values of vertical shear and static stability, observations do not really allow us to distinguish interior PV gradients $O(\beta)$ from zero.

Lindzen's geometric equilibration scenario requires that the scale of the waves be con-

strained externally, so that only waves shorter than the Eady cutoff are allowed. For a jet profile, the meridional scale of the jet can be regarded as an effective meridional wavenumber (Ioannou and Lindzen, 1986), which in the Earth's atmosphere dominates the zonal wavenumber for waves of planetary scale. Using this meridional scale and characteristic parameters, Lindzen (1993) argued that the height of the tropopause is comparable to the Eady cutoff, and proposed that the baroclinic waves could equilibrate by raising the tropopause. However, the GCM simulations of Thuburn and Craig (1997) suggest that the tropopause height does not exhibit the sensitivity predicted by Lindzen (1993). Alternatively, the eddies could equilibrate by narrowing the jet, as suggested by the convergent character of the eddy momentum flux both in linear modes (Ioannou and Lindzen, 1986), observations (Peixoto and Oort, 1992) and nonlinear simulations (Thorncroft et al., 1993).

The idea that the PV gradient is better mixed in the interior than at the surface has been tested by Sun and Lindzen (1994). Using the assumption that PV is well-mixed along the isentropes, they obtained characteristic curves for the isentropic slope. This allowed them to reconstruct the full isentropic structure in terms of the observed values of potential temperature and static stability at the surface. Sun and Lindzen (1994) argue that this procedure gives a good agreement with observations.

Kirk-Davidoff and Lindzen (2000) went a step further and used the concept of PV homogenization to construct a 2D climate model in which the baroclinic eddies are parameterized in this manner. Essentially, their model only needs to predict the temperature and static stability at the surface; the rest of the thermal structure can then be calculated assuming PV homogenization. This thermal structure in turn constrains the radiative balance and, together with other processes, the surface temperature, which they evolve using a simple energy balance model. Kirk-Davidoff and Lindzen (2000) argue that this simple representation of the baroclinic eddies produces a realistic climate.

A similar approach to Sun and Lindzen (1994) was taken by Stone and Nemet (1996). These authors also compared the observed thermal structure to idealized states based on PV homogenization, but they used a qg model instead. Neglecting the contribution by the horizontal curvature of the zonal wind, they express the interior PV gradient as:

$$\overline{q}_y = \beta \left[ 1 - e^{z/H_S} \frac{\partial}{\partial z} \left( h e^{-z/H_S} \right) \right] \qquad \text{with } h = \frac{\Lambda \epsilon}{\beta} = \frac{f_0^2}{N^2} \frac{1}{\beta} \frac{\partial \overline{U}}{\partial z}, \tag{2.1}$$

where $\Lambda = \frac{\partial \overline{U}}{\partial z}$ is the vertical shear, $\epsilon = \frac{f_0^2}{N^2}$ is the inertial ratio, and $H_S$ is the density height scale. It can be easily shown using the thermal wind relation that $h$ is proportional to the isentropic slope. Note that this expression also applies to the surface PV gradient, which is modeled as a jump in $h$ from zero to its interior value $h_0$ (Bretherton, 1966). This gives an integrated PV gradient at the surface: $\int_0^{0^+} \overline{q}_y dz = -\beta h_0 = -\epsilon \left. \frac{\partial U}{\partial z} \right)_{z=0^+}$.

The Charney and Stern (1962) condition for instability states that a necessary condition for instability is that the PV gradient $\overline{q}_y$ changes sign, including the surface temperature gradient. The violation of this condition thus requires that the baroclinic eddies smooth down the positive PV gradient in the interior, or the temperature gradient at the surface, or both. As Sun and Lindzen (1994), Stone and Nemet (1996) assumed that the PV gradient is zero in the interior below some tropopause height. This allowed them to integrate equation 2.1 and obtain an adjusted profile $h_{adj}$, which they compared to observations. The integration also requires the specification of a value for $h_0$ at the surface. Instead of taking the observed value of $h_0$ as Sun and Lindzen (1994), they assumed the Charney-Stern condition to be also violated at the surface, and took $h_0 = 0$. Stone and Nemet (1996) claim that this gives a better agreement with observations than had they taken the observed $h_0$.

We reproduce their results in figure 2-1. This figure compares the adjusted profile of $h$, calculated assuming full PV homogenization, to the observed vertical profiles at a number of latitudes. Stone and Nemet (1996) distinguish three regimes in the midlatitudes. There is an adjusted region between about 2 and 8 km where the agreement is reasonably good and baroclinic adjustment holds. Below this region, the profiles diverge, which Stone and Nemet (1996) attribute to dissipative processes over the boundary layer. This is the same argument used by Swanson and Pierrehumbert (1997) to justify the apparent higher efficiency of the baroclinic eddies in homogenizing the interior PV gradients; they claim that thermal anomalies are damped over the boundary layer in very short time scales, of the order of a day. Finally, above 8 km the profiles of figure 2-1 diverge again. Stone and Nemet (1996) argue that this is due to the limited mixing depth of the eddies, which extend primarily over the troposphere. Note that this is again consistent with the conception of the tropopause as a boundary to eddy mixing in the midlatitudes (Held (1982), Lindzen (1993)). For instance, Held's simplified model assumes that the tropopause is in radiative equilibrium.

In summary, baroclinic waves mix down the interior and surface PV gradients as they

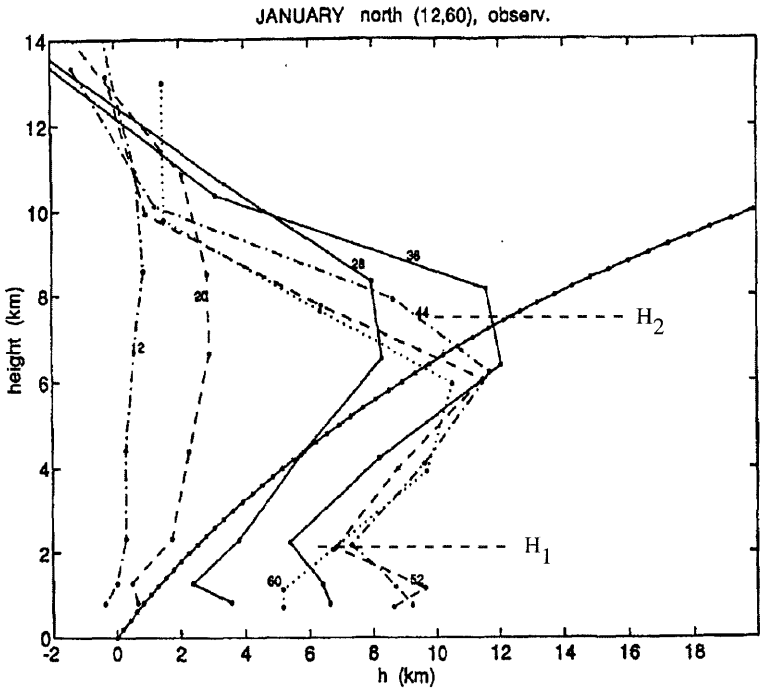


Figure 2-1: Comparison of adjusted and observed profiles of $h$ at a number of latitudes. The adjusted profile is the solid line with dots. Taken from Stone and Nemet (1996).

equilibrate. If the restoring diabatic processes are slow, these gradients should be small. However, the observed surface temperature gradient is not small. It has been argued by a number of authors that the eddies are more efficient in eliminating the interior than the surface PV gradient, perhaps because dissipative processes are most important at the surface. We analyze in next section whether the interior PV gradient is indeed well homogenized.

## 2.3 Is the interior PV really homogenized?

As discussed above, it is often argued in the literature (e.g., Lindzen (1993), Stone and Nemet (1996), Swanson and Pierrehumbert (1997)) that the baroclinic eddies homogenize more efficiently the interior than the surface PV gradients.

Lindzen (1993) argues that observations do not have enough accuracy to discard $\overline{q}_y = 0$, due to the high sensitivity of the PV gradient to the vertical shear and static stability. However, because the PV gradient is essentially a derivative of the isentropic slope (equation 2.1), the vertically integrated PV gradient is somewhat better behaved. When this is taken into account, there seems to be little doubt that the interior PV gradient is positive definite.

One way to look at the vertically integrated PV gradient is to consider the mean isen-

tropic slope, or the latitude at which any given isentrope reaches the tropopause. This can be examined in figure 2-2, taken from Sun and Lindzen (1994). The upper panel shows the thermal structure predicted by a model of full PV homogenization, based on the observed values of temperature and static stability at the surface. On the other hand, the medium panel shows the climatology for the same period (northern winter). The agreement is reasonable, and Sun and Lindzen (1994) use this agreement in support of the theory of PV homogenization. However, the agreement is even better when a mean interior PV gradient of $\beta$ is considered (lower panel, also taken from that paper). This suggests that the interior PV gradient is closer to $O(\beta)$ than homogenized.

The same has been noticed by Kirk-Davidoff (1998). This author estimated the best fit to the interior PV gradient (assumed constant) by minimizing the RMS difference between the observed potential temperature and the reconstructed potential temperature based on a given degree of homogenization. He found the best agreement for a mean interior PV gradient of $O(1.1\beta)$, very robustly for all seasons. In fact, the so-called climate model of PV homogenization of Kirk-Davidoff and Lindzen (2000) uses an interior PV gradient of $\beta$.

It may be argued that an interior PV gradient of $\beta$ is still small, at least compared to the stratospheric PV gradient or the surface delta-function. However, in the context of baroclinic adjustment the relevant question is whether the interior PV gradient is better homogenized than temperature at the surface. One way to answer this is by noting that the observed tropospheric shear is of the order of the two-layer model critical shear (Stone, 1978). This scaling implies that $\beta$ integrated over half troposphere is already of the order of the integrated delta-function PV gradient at the ground (Lindzen, 1990). From that point of view, an interior troposphere of order $\beta$ is not small but reflects a comparable degree of homogenization as surface temperature.

Stone and Nemet (1996) also argue that the PV gradient is better mixed in the interior than at the surface because the observed $h$ is closest to the adjusted profile in that region (figure 2-1). However, from equation 2.1, it is the derivative of $h$, rather than $h$ itself, that enters the PV gradient. Hence, what matters is not so much how close the observed $h$ is to the adjusted profile, but how 'parallel' both profiles are. In a way, $h$ can be regarded as a measure of the *integrated* PV gradient, to which it can be related as follows:

$$h = \left[ h_0 + H_S \left( 1 - e^{-z/H_S} \right) - \frac{1}{\beta} \int_{0^+}^{z} \overline{q}_y e^{-z/H_S} dz \right] e^{z/H_S} \tag{2.2}$$

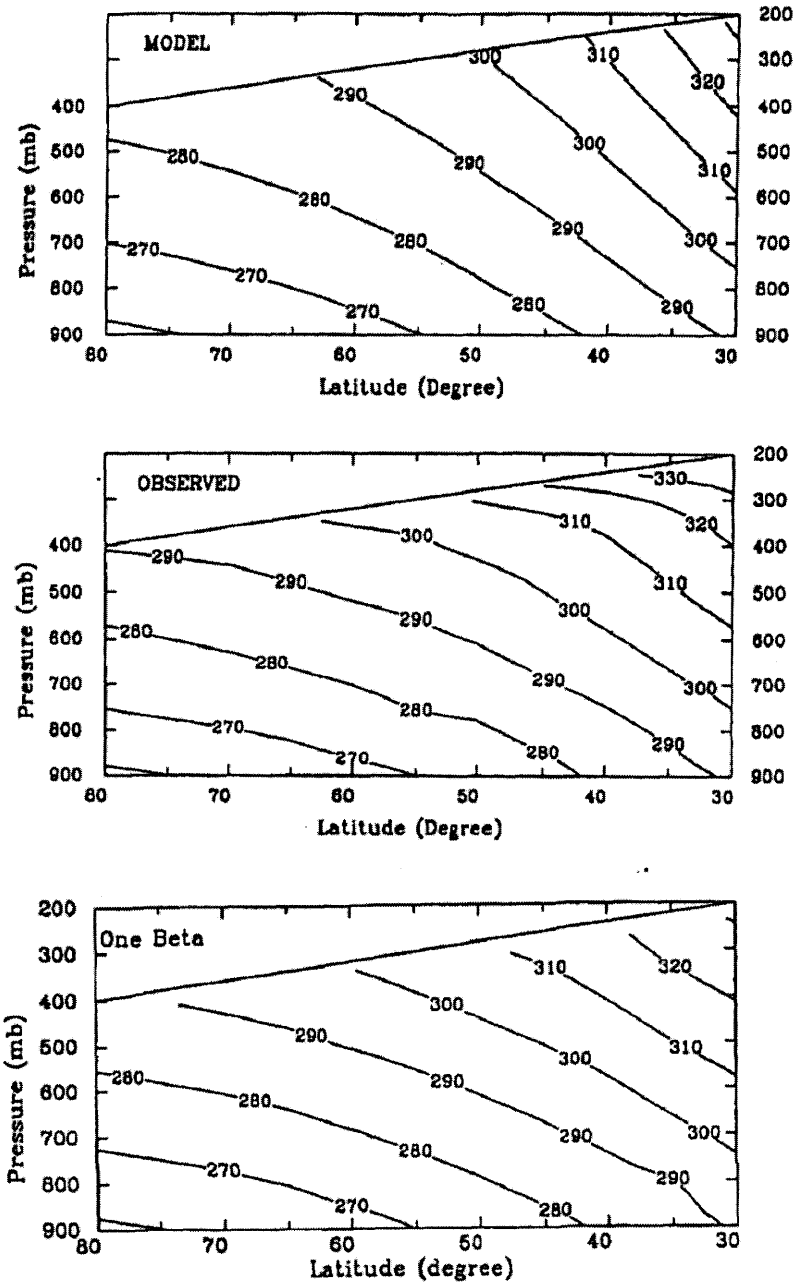


Figure 2-2: Comparison of the thermal structure predicted by a model of full PV homogenization (top), and a model with an interior PV gradient of $\beta$ (bottom) against observations (middle). Taken from Sun and Lindzen (1994).

Note that the integral in the right hand side only includes the interior PV gradient because we already included the surface PV gradient in the term $h_0$ (alternatively, we could take $h_0 = 0$ and include the surface delta-function in the integral). As mentioned above, Stone and Nemet (1996) neglect the surface temperature gradient and take $h_0 = 0$ for the adjusted profile, claiming that this produces a better fit to observations than when the observed $h_0$ is included. This is inconsistent, and obscures the fact that the interior PV gradient is not negligible either, but has a vertical integral of the same order.

A cursory inspection of figure 2-1 suggests that the observed profiles of $h$ are quasi-parallel to the adjusted profile in the interior. However, they are not perfectly parallel, as the observed profiles somewhat appear to converge toward the adjusted profile as we move up. To be precise, $\frac{\partial h}{\partial z}$ is smaller in the observed than in the adjusted profile, which can be taken as the signature of an interior positive PV gradient. We can use figure 2-1 to estimate the ratio between the mass-weighted interior and boundary PV gradients. Neglecting again the PV gradient contribution from the jet curvature, we rewrite equation 2.1 as follows:

$$\bar{q}_y(z) = -\beta e^{z/H_S} \frac{d}{dz}\left[(H_S + h)e^{-z/H_S}\right] \tag{2.3}$$

The ratio between the net interior and boundary PV gradients is then given by:

$$-\frac{\int_{0+}^{H} e^{-z/H_S}\bar{q}_y\, dz}{\int_{0}^{0+} \bar{q}_y\, dz} = \frac{-\left[(H_S + h)e^{-z/H_S}\right]_{0+}^{H}}{h_0} = \frac{\gamma\,(H_S + h(H)) - \Delta h}{h_0}, \tag{2.4}$$

where $\Delta h = h(H) - h_0$, $H$ is some tropospheric mixing depth, and we define the factor $\gamma = 1 - e^{-H/H_S}$. In terms of the isentropic slope in scaled coordinates ($S = h/H_S$):

$$-\frac{\int_{0+}^{H} e^{-z/H_S}\bar{q}_y\, dz}{\int_{0}^{0+} \bar{q}_y\, dz} = \frac{\gamma\,(1 + S(H)) - (S(H) - S(0))}{S(0)} \tag{2.5}$$

We can estimate these values from figure 2-1. We will choose $H$ to be the distance from the top of the boundary layer (defined for our purposes by the minimum $h$) to the height at which $h$ is maximized. Those heights are denoted $H_1$ and $H_2$ in figure 2-1, respectively. If $\bar{q}_y$ were zero in the interior, as in the study of Sun and Lindzen (1994), $h$ would describe a line roughly parallel to the adjustment curve, but with $h_0 > 0$. This is approximately observed up to the $h$ maximum; thereafter $\bar{q}_y$ increases significantly. We can interpret this as a boundary to the vertical penetration of the waves since above that height the EP fluxes

tend to be dominated by their horizontal component, as discussed by Edmon et al. (1980). The value of $H$ thus obtained can be regarded as an empirical measure of the penetration of the eddy fluxes. Specifically, we take:

$$h_0 \approx 7\ km \quad h(H) \approx 12\ km \quad H_S \approx 7.5\ km \quad H \approx 6\ km, \tag{2.6}$$

yielding a ratio of interior to boundary PV gradient of 0.82. This number should not be taken too seriously because our estimates of $H$, $h$ are, to an important extent, ambiguous. Nevertheless, this suggests that the positive interior PV gradient above the boundary layer is comparable to the negative PV gradient at the ground. This net interior PV gradient arises because the rate of change of the isentropic slopes $O(\Delta h/H_S)$, which is the only negative contribution, is not large enough to compensate the beta effect $O(\gamma)$ and non-Boussinesq corrections $O(\gamma h(H)/H_S)$. Note that these three terms are roughly of the same order, as is the integrated delta function at the ground, $O(h_0/H_S)$. Hence, when properly interpreted, the results of Stone and Nemet (1996) also suggest that the PV gradient is not homogenized any better in the interior than at the surface.

Finally, figure 2-3 (taken from Kirk-Davidoff and Lindzen (2000)) shows the vertical structure of the observed zonal-mean PV gradient for different seasons. Though there is a region with small PV gradients around 700 $mb$, this well-homogenized region is very shallow and over most of the troposphere the interior PV gradient is actually of order $\beta$. Note that the interior PV gradient has a very well defined vertical structure, with large positive values at the tropopause and over the boundary layer. These large boundary layer gradients could be due to the strong vertical mixing of heat at the surface, which tends to produce nearly vertical isentropes in that region (Solomon and Stone, 2001). It is noteworthy that the vertical structure of the zonal mean PV gradient is very robust for both hemispheres and all seasons, as is the surface temperature gradient itself (Stone, 1978). Idealized numerical models also produce a similar structure (c.f., figure 2 of Solomon and Stone (2001)).

The failure of the eddies to homogenize the interior PV gradient comes as no surprise when one realizes that the positive/negative PV gradients are related via the appropriate diffusivities to the equatorward/poleward eddy PV fluxes, and hence to the poleward/equatorward mass fluxes (Held and Schneider, 1999), which should balance in steady state. As Held and Schneider (1999) have shown using isentropic coordinates, the areas

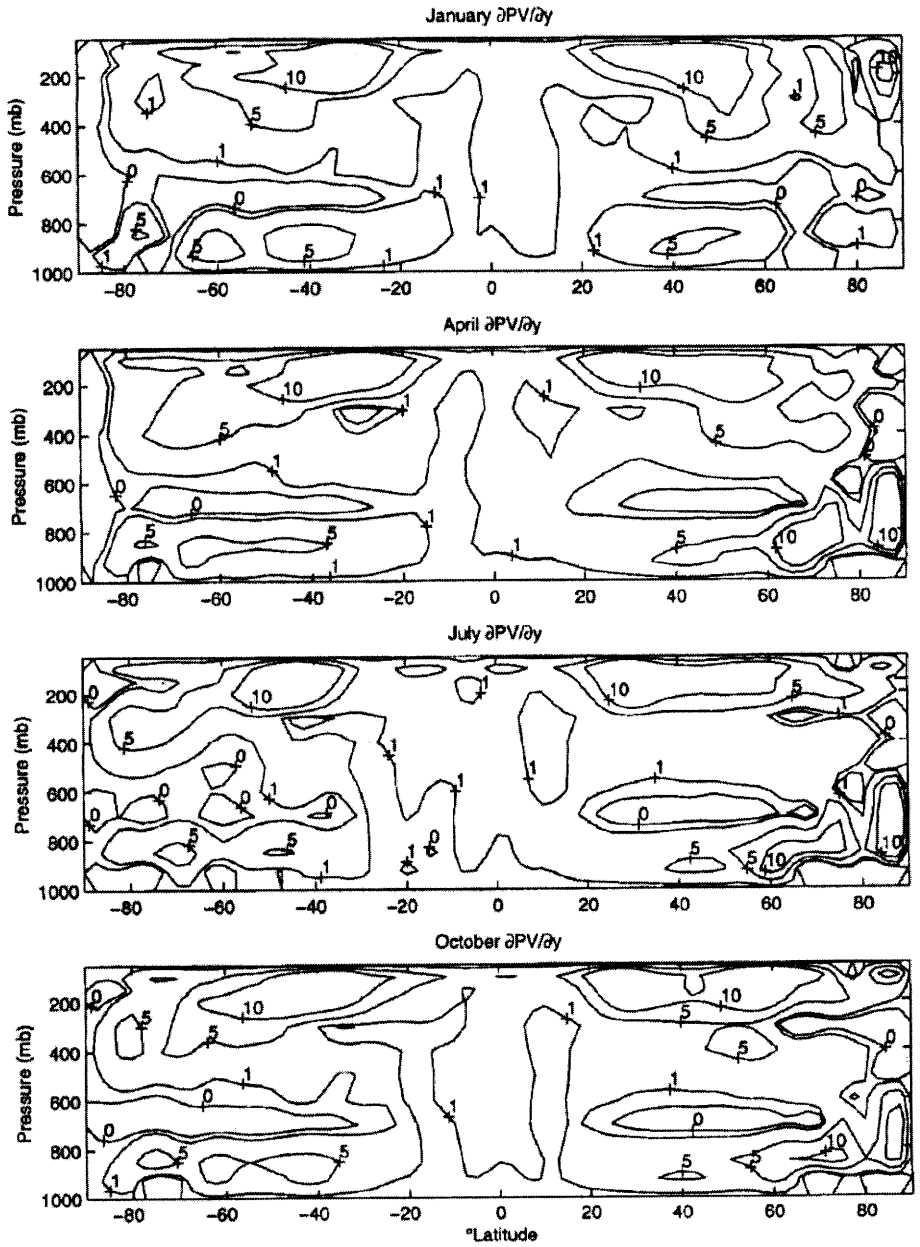


Figure 2-3: Zonal mean PV gradient (normalized by $\beta$) for the months indicated. Taken from Kirk-Davidoff and Lindzen (2000).

of poleward and equatorward mass flux are comparable and the apparent largeness of the negative PV gradients/equatorward eddy fluxes should be regarded as an artifact of quasi-geostrophy, which concentrates the return flux on the lower boundary.

Thus, the fact that the interior PV homogenization is incomplete should not be regarded per se as an additional argument against baroclinic adjustment but as a manifestation of this balance. In a steady state, the ratio between the PV gradients should just equal the inverse ratio between the respective average diffusivities (Held, 1999), which in the observed atmosphere appears to be of order 1. Hence, to the extent that dissipative effects prevent the eddies from eliminating the surface temperature gradients they prevent as well the homogenization of the interior PV gradient. Similarly, assuming the observed PV diffusivities to be robust, if some other mechanism prevented interior PV homogenization we would expect this mechanism to also set up a limit to the reduction of the surface temperature gradient.

### 2.3.1 The curvature PV gradient.

In the previous analysis we neglected the horizontal curvature PV gradient, following Stone and Nemet (1996). However, we argue below that this term is not really negligible.

To see this, assume a linear wind profile with maximum wind speed $\Lambda H$, and neglect density corrections. We can then estimate the vertically-integrated curvature contribution to the zonal-mean PV gradient as $\frac{1}{2}\frac{\Lambda H^2}{L^2}$, where $L$ is some characteristic jet width. If the jet width is linked to the meridional scale of the eddies, then we expect $L$ to scale as the Rossby deformation radius, i.e. $H \sim \epsilon^{1/2} L$. This implies that the integrated curvature contribution to the zonal mean PV gradient is of order $O(\frac{1}{2}\Lambda\epsilon) = O(\frac{1}{2}h_0)$. This simple scaling thus suggests that the curvature contribution is not negligible either, but has an interior integral of the order of the integrated delta-function at the surface.

This result is at odds with previous studies in the literature (e.g., Fullmer (1982)), which typically neglect this term. However, it is possible that the local curvature of the jet is larger than indicated by the time and/or zonal mean estimates because of the smoothing involved in averaging across a meandering jet (Morgan, 1994). In the tropospheric case, this smoothing is quite severe because the meridional excursions of the jet are of the order of the jet width itself. This might be one reason why previous estimates of the jet curvature produce smaller values than it would be expected based on dynamical grounds alone.

To investigate this issue, we have estimated the horizontal curvature contribution to the PV gradient from observations. We use data from the NCEP/NCAR reanalysis project (Kalnay et al., 1996), and choose for the purpose of discussion the observed winds during January 15th 2001, as well as the monthly mean for the same month. The results are shown in figure 2-4. The left panels display the observed zonal wind, and the right panels the associated curvature PV gradient. Note that the latter is mass-weighted (with a correction $P/P_S$), and normalized by the latitude-dependent value of $\beta$ (i.e., $2\Omega cos\theta/a$, where $\theta$ is latitude and $a$ the radius of Earth)[1]. We show three different types of results: the time and zonal mean on the top panels, the instantaneous zonal mean on the second panels, and the instantaneous 'meandering mean' on the third ones. The latter is calculated as the longitudinal average following the local maximum of $\overline{U}$. Finally, we compare on the bottom panels the vertically-averaged values for the three cases.

For the time and zonal mean, the curvature PV gradient is somewhat smaller than $\beta$, but not completely negligible. Note that because of the mass-weighting, this term has a comparable impact throughout the troposphere. Comparing with the third panel, we can see that as anticipated above, the process of zonally-averaging does smooth down significantly the contribution of this term to the total PV gradient. At upper levels, the curvature PV gradients are 3 times larger for the meandering mean than for the time and zonal mean, while they are on average 2 times larger over the whole troposphere. The reason is that because the meridional excursions of the jet are so large, the jet appears to have a much broader scale in the zonal mean than is locally observed. This is the main effect; the zonal-mean velocity is not smoothed down as much. Note that the fact that the jet width is overestimated may also have important implications for Lindzen's 1993 equilibration scenario, which predicts too large tropopause heights when the zonal-mean jet is considered.

In summary, the actual data seems to confirm the dynamical expectation that the horizontal curvature of the jet is not negligible. In fact, when the local curvature is considered, this term is order $\beta$ on average, and thus gives an additional contribution to the interior PV gradient of the order of the integrated delta-function at the surface.

[1]This normalization factor does not incorporate any density correction.

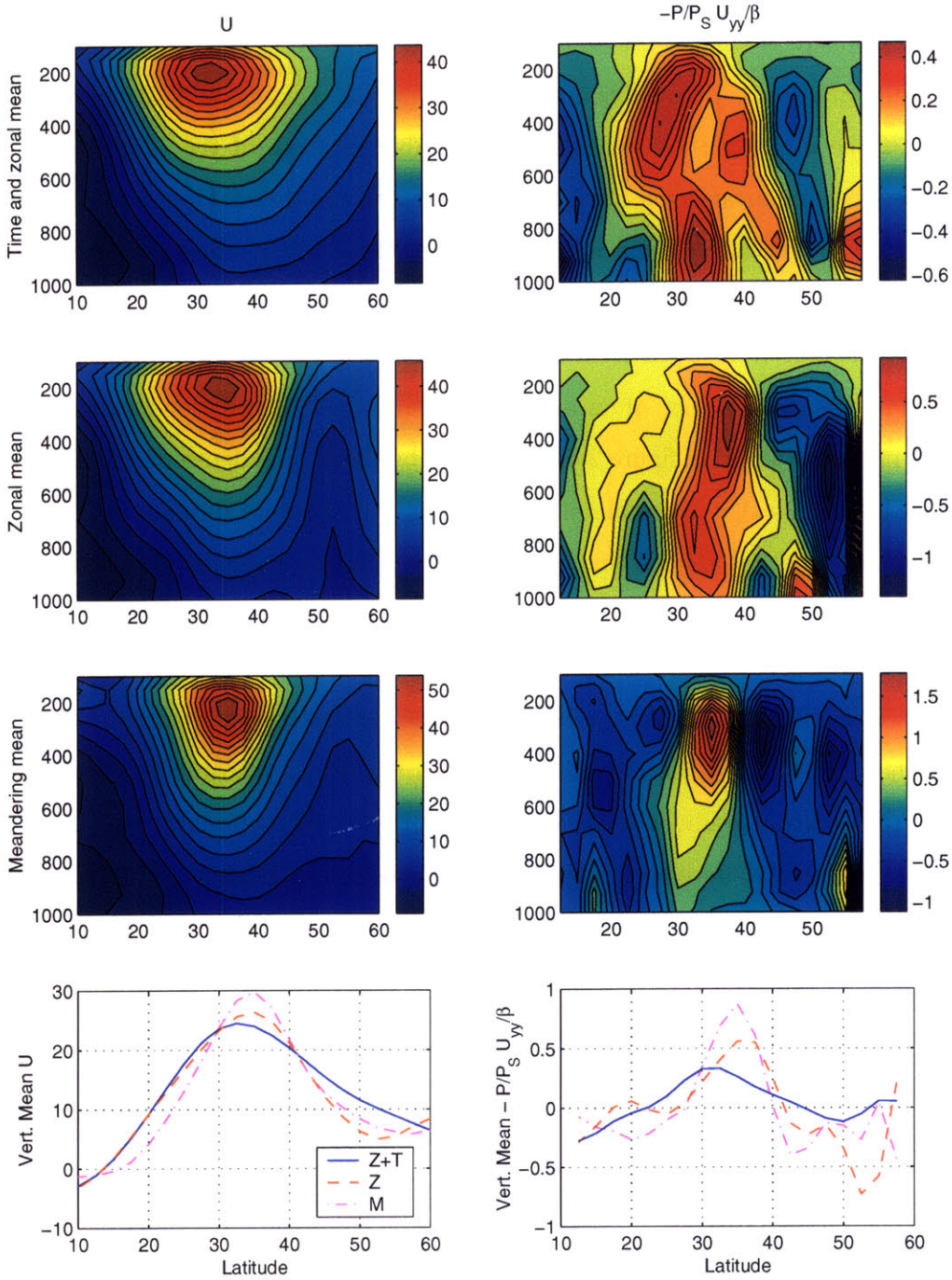


Figure 2-4: Zonal wind (left) and horizontal curvature PV gradient (right), mass-weighted and normalized by $\beta$. Three types of values are shown: (top panels) Zonal and time mean, January 2001, (second panels) Zonal mean, January 15th 2001, (third panels) Meandering mean for the same day, (bottom) Vertical mean values. Data taken from the NCEP/NCAR reanalysis project.

## 2.4 The mixing depth constraint

As discussed in section 2.2, one of the outstanding questions in the General Circulation of the atmosphere is what prevents the baroclinic eddies from smoothing out the surface temperature gradient. A plausible answer is dissipation. For instance, Barry et al. (2000) argue that the diabatic time scales are comparable to those of the eddies. Dissipation should be most important over the boundary layer, where thermal anomalies are damped in very short time scales (Swanson and Pierrehumbert, 1997). However, this is not the only possibility: we discuss in this section an additional constraint that may prevent full homogenization, even in the inviscid case.

Consider the equilibration of an unstable mode in the Charney-Boussinesq problem, as sketched in the left panel of figure 2-5, and let $H_0$ be the mixing depth of that mode. What we mean by that is that the scale of the mode is such that its fluxes only extend up to the height $H_0$. We thus assume that the basic state remains unmodified at and above that height throughout the equilibration. As the wave equilibrates, it reduces the interior PV gradient and the zonal wind develops some curvature, as illustrated in the sketch shown in the right panel of figure 2-5. At the same time, the surface shear is reduced.

For the profile shown the reduction in the surface shear is insufficient and there is a remnant temperature gradient at the surface. In order to fully eliminate the surface shear, the flow would need to develop a larger vertical curvature, as indicated by the dash-dotted line on the far right. However, there is a limit to how much curvature the flow can develop, a limit that depends on $\beta$. The reason is that when the curvature is too large compared to

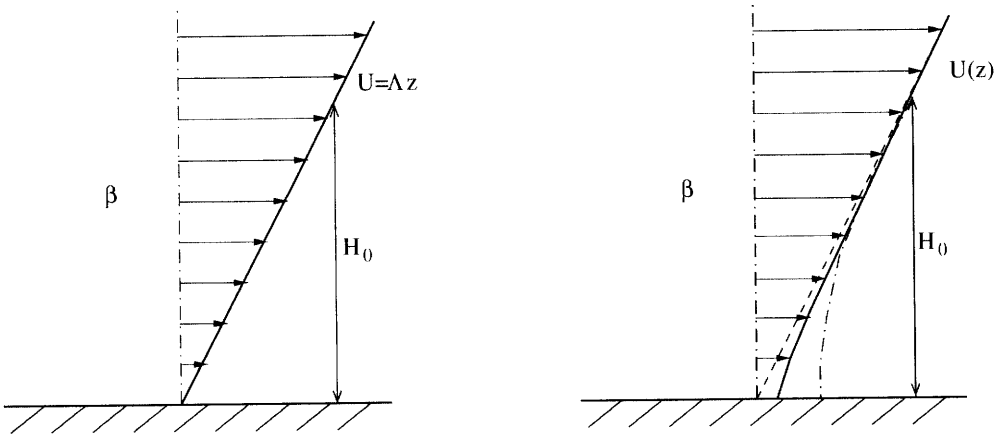


Figure 2-5: Sketch illustrating how a wave with mixing depth $H_0$ equilibrates the mean flow $U(z)$ in the Charney-Boussinesq problem. See text for details.

$\beta$, the interior PV gradient is negative, which would be unstable. Hence, the interior PV gradient and mixing depth set up a limit to the maximum reduction in the surface shear.

Another way to see this is to consider the vertically integrated PV gradient between the surface and the height $H_0$. For the simple 1D Charney-Boussinesq problem:

$$\int_0^{H_0} \overline{q}_y \, dz = \int_0^{H_0} \left(\beta - \beta \frac{\partial h}{\partial z}\right) dz = \beta H_0 - \beta h(H_0) = \beta(H_0 - h_0), \tag{2.7}$$

where the vertically integrated PV gradient also includes the delta-function at the surface, this being the reason why we took $h(0) = 0$. Note that we also took into account above that, by definition, $h$ must remain unchanged at the mixing depth $H_0$. Hence, $h(H_0) = h_0 = \frac{\Lambda\epsilon}{\beta}$ where $\Lambda$ is the constant vertical shear of the initial profile.

Note that the final result in equation 2.7 only depends on the initial configuration of the flow. In other words, all the eddies can do is to redistribute vertically the interior PV gradient, but its integrated value over the mixing depth remains unchanged. In particular, when $H_0 < h_0$ the integrated PV gradient must be negative. Short waves are thus unable to eliminate the negative delta-function PV gradient at the surface, even in the inviscid limit.

The previous argument easily generalizes to the non-Boussinesq limit. Integrating equation 2.3, we get the following mass-weighted, vertically-integrated PV gradient:

$$\int_0^{H_0} e^{-z/H_S} \, \overline{q}_y dz = \beta \left[H_S - (H_S + h_0)e^{-H_0/H_S}\right] \tag{2.8}$$

As before, the sign of equation 2.8 is a function of $H_0$. For small mixing depths the integrated PV gradient between 0 and $H_0$ is always negative, whereas it is positive for large $H_0$. Hence, the scale of the waves essentially constrains the sign of this integrated PV gradient. Consequently, full homogenization of both the surface and interior PV gradients, as assumed by theories of baroclinic adjustment, is only possible for the appropriate value of $H_0$. Note that a similar result to 2.8 has been derived by Harnik (2000). She studied the stability properties of basic states with small tropospheric PV gradients, and noted that the shear at the top of the model sets up a constraint on the net mass-weighted PV gradient of the basic state in a one-dimensional model.

This is illustrated in figure 2-6, which shows the regions in which the integrated PV gradient is positive or negative as a function of $h_0/H_S$ and $H_0/H_S$. For reference, we also show in that figure the parameter regime in which the most unstable mode lies. As discussed

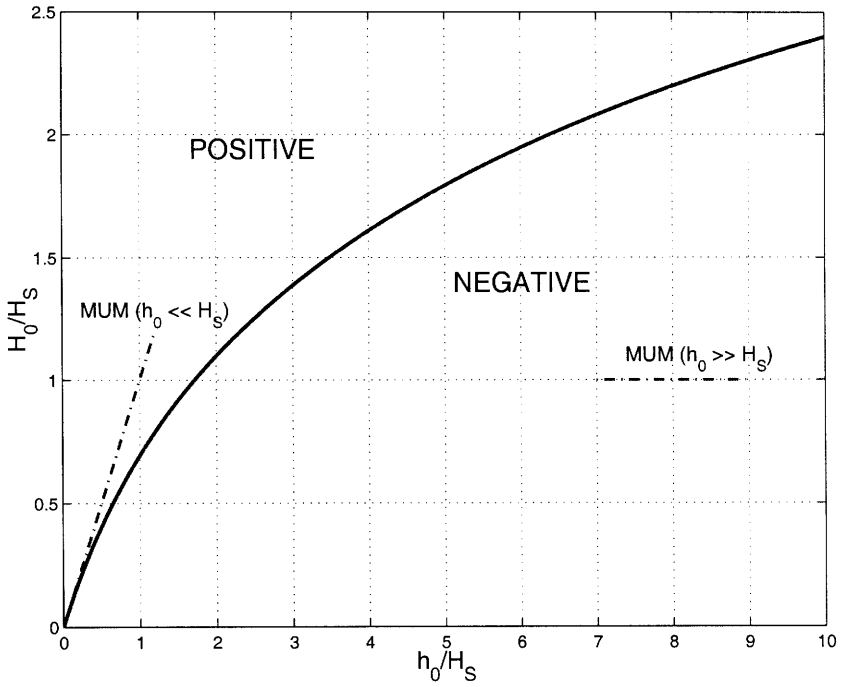


Figure 2-6: Diagram illustrating the regions with different sign of the integrated PV gradient over the mixing depth $H_0$, as a function of $H_0/H_S$ and $h_0/H_S$. Also shown are Held's (1978) scaling for the mixing depth of the most unstable mode in the limits $h_0 << H_S$ and $h_0 >> H_S$.

by Held (1978), when $h_0 << H_S$ the mixing depth of the most unstable mode scales as $H_0 \sim h_0$. In that case, the scale of the most unstable would be just adequate to produce full homogenization, as shown in the figure. However, when $h_0 >> H_S$ the most unstable mode scales as $H_0 \sim H_S << h_0$ instead, and lacks enough depth to eliminate the negative PV gradient. The same would be true if some other mechanism, such as the meridional confinement by the shear of the jet (Lindzen, 1993), constrained the baroclinic spectrum to waves shorter than the most unstable mode.

It is not clear how applicable the mixing depth constraint is for the real troposphere. For instance, the simple argument provided above is one-dimensional and neglects the contribution from the curvature PV gradient. Yet this contribution is probably not negligible, as discussed above. Another obvious problem is that the geometrical argument relies on the fact that there is an unperturbed shear $\Lambda$ above the mixing depth. On the other hand, the situation is very different in the real atmosphere, in which the zonal wind eventually stops growing. In fact, figure 2-1 shows that $h$ falls quite abruptly to zero above the tropopause, which is of course consistent with the fact that the isentropes are quasi-horizontal in the stratosphere. Hence, when the tropopause is also included, the baroclinic term integrates to

zero (i.e., $h$ drops as much as it grows) and the integrated PV gradient is of necessity positive. However, it is not obvious whether the large positive PV gradients at the tropopause should be included in the integral, at least to the extent that the tropopause can be conceptually regarded as a boundary to eddy mixing. For instance, Held (1982) hypothesized that the tropopause is close to radiative equilibrium, an assumption that has also been recently addressed by Thuburn and Craig (2000). In that case, the upper-troposphere isentropic slope is diabatically determined and should have no bearing to the dynamics. On the other hand, if the PV gradient concentration at the tropopause is a result of the redistribution of the interior PV gradient by the eddies (Lindzen, 1993), it would seem inconsistent not to include this term.

In this thesis we will study the equilibration of the Charney-Boussinesq problem, which is the simplest continuous model of baroclinic instability with non-zero interior PV gradients. This simple model provides us with an idealized framework in which to examine some of the issues introduced in this chapter, such as the relative role of boundary and interior PV homogenization for equilibration, or whether the interior PV mixing is sufficient to produce a tropopause in the absence of diabatic forcing. Based on the mixing depth ideas discussed above, we expect that an important parameter in this regard should be the ratio between the interior and boundary PV gradients of the basic state. In chapter 3, we use this idea to define more properly the concept of a short Charney mode, and discuss plausible equilibration scenarios for such modes.

# Chapter 3

# Short Charney waves: the stability of partially homogenized states

We argued in chapter 2 that the observed PV gradients in the interior troposphere are not small: in an integral sense, they are in fact comparable to the surface PV gradients. As discussed, the vertical structure of the PV gradients shows a well homogenized region around 700 mb, with positive values elsewhere. This raises the questions: What determines the homogenized region? Could a partially homogenized state be neutral? From Bretherton's (1966) theorem, a necessary condition for neutrality is that the PV gradient vanishes at the critical level. This is also consistent with the kinematic expectation that mixing is most efficient at the steering level, where the streamlines in a reference system moving with the wave are closed. In this chapter, we will discuss under what conditions a basic state with zero PV gradient at the steering level is neutral.

To study these issues, we look at the simplest instability problem with non-zero interior PV gradients: the Charney problem. We discuss the vertical scaling of the normal modes in this problem and define the concept of a short Charney wave. Essentially, we makes rigorous the discussion of section 2.4 by providing an estimate of the mixing depth. The original analysis of the scaling in this problem was done by Held (1978), who showed that the vertical depth scale of the most unstable mode scales as the smaller of two vertical length scales existing for this problem. We extend his analysis by formally including an additional vertical scale: the depth of the mode, which need not be the most unstable one. Because the atmosphere is not an unbounded fluid, it is plausible that geometric constraints, such as

the meridional shear of the jet (Lindzen, 1993), might limit the penetration of the modes to heights smaller than those proposed by Held (1978). In that case, the arguments of section 2.4 suggest that the modes would lack enough depth to eliminate the negative PV gradient at the surface.

The structure of this chapter is as follows. We formulate the problem in section 3.1 and introduce the concept of a short Charney wave in section 3.2. In section 3.3, we discuss the implications of this scaling for the mixing of interior and boundary PV. Section 3.4 discusses the dispersion relation for this problem, while section 3.5 is concerned with examining the neutrality of partially homogenized basic states. Finally, we summarize the main results of this chapter in section 3.6.

## 3.1 Formulation

The conservation of quasi-geostrophic potential vorticity for a Boussinesq fluid, linearized around a zonal basic state with velocity $U = \Lambda z$ and stratification $N^2$ can be written as:

$$\frac{\partial q'}{\partial t} + U\frac{\partial q'}{\partial x} + v'\bar{q}_y = 0\,, \tag{3.1}$$

being $q' = \frac{\partial^2\psi'}{\partial x^2} + \frac{\partial^2\psi'}{\partial y^2} + \epsilon\frac{\partial^2\psi'}{\partial z^2}$ the perturbation potential vorticity, $\psi'$ the geostrophic streamfunction, $v' = \frac{\partial\psi'}{\partial x}$ the meridional velocity, $\epsilon = \frac{f_0^2}{N^2}$ and $\bar{q}_y$ the interior gradient of potential vorticity in the basic state, defined as:

$$\bar{q}_y = \beta - f_0^2\frac{\partial}{\partial z}\left(\frac{1}{N^2}\frac{\partial U}{\partial z}\right) \tag{3.2}$$

As usual, we denote perturbation variables with primes. Basic state variables are written either capitalized or with an overbar.

Assuming plane wave solutions $\psi'(x,y,z,t) = \phi'(z)e^{i(k_x x + k_y y - k_x ct)}$:

$$\phi'_{zz} + \frac{1}{\epsilon}\left[\frac{\bar{q}_y}{\Lambda z - c} - k^2\right]\phi' = 0 \tag{3.3}$$

with $k^2 = k_x^2 + k_y^2$. The boundary conditions are a rigid lower surface, and either a rigid lid at the top (Green problem) or the radiation condition at infinity (Charney problem). In the former case:

$$\phi'_z - \frac{\Lambda}{\Lambda z - c}\phi' = 0 \qquad at\ z = 0,\ D \tag{3.4}$$

This yields an eigenvalue problem for the phase speed $c$. The associated eigenvector is $\phi'(z)$, the vertical structure of the modes. When the phase speed $c$ has a positive/negative imaginary part $c_i$, which also requires a complex $\phi'$ (e.g., a phase tilt with height) the modes are growing/decaying.

Bretherton (1966) showed that the domain integral of the perturbation PV flux vanishes. Neglecting the contribution of the momentum fluxes, this translates into the one-dimensional constraint:

$$\int_0^\infty \overline{v'q'}\, dz = 0 \tag{3.5}$$

This expression is true provided that the heat flux at the boundaries is generalized as a delta-function PV flux. Bretherton further showed that this PV flux is always downgradient for a growing mode:

$$\overline{v'q'} = -\frac{k_x c_i}{2}|\eta'|^2 \bar{q}_y\ , \tag{3.6}$$

which allows us to interpret $|\eta'|^2$ as a height-dependent PV diffusivity for the linear case. Here $\eta'$ is the meridional displacement of the basic state PV contours, defined as:

$$\eta' = -\frac{q'}{\bar{q}_y} = \frac{\phi'}{\Lambda(z - z_c) - ic_i} \tag{3.7}$$

At $z = z_c$ the meridional displacement $|\eta'| \to \infty$ for neutral modes ($c_i \to 0$), and residue calculus shows that this implies a non-zero PV flux at the steering level if $\bar{q}_y(z_c) \neq 0$. However, equation 3.6 shows that for a neutral mode, the PV flux must be zero away from the singularity at the steering level. Because the domain integrated PV flux must be zero, Bretherton (1966) concluded that neutral modes are not possible whenever there is a PV gradient at the steering level.

From Bretherton's argument the neutrality of a mode requires that it either has no steering level or is collocated with a region of zero PV gradient. An example of the latter is a short wave in the Eady problem. An example of the former occurs when the PV gradient of the basic state is one-signed, positive for instance. In that case, the Rossby propagation correction to the zonal mean flow is westward at all levels, which implies that the phase

speed (if a mode exists at all) must be slower than the zonal flow velocity at all levels.

Bretherton's argument is consistent with the fact that all wavenumbers are unstable in the Charney problem, except at a discrete number of neutral points[1]. Note that the existence of these neutral modes is not inconsistent with Bretherton's argument because they all have their steering level at the surface, which is a singular case. Because the PV gradient is a negative delta function at $z = 0^-$ and positive in the interior at $z = 0^+$, it can be thought to change sign at $z = 0$.

## 3.2 Vertical scales in the Charney problem

Consider a temperature perturbation with wavelength $\lambda = \frac{2\pi}{k}$ at the lower boundary of the Charney problem. Away from the steering level, the PV flux decays with a vertical scale $H = \frac{1}{2}H_R = \frac{1}{2}\lambda\sqrt{\epsilon}$, where the Rossby penetration depth $H_R$ gives the height of influence of the lower perturbation. The 1/2 factor arises from the fact that $\overline{v'q'}$ is a quadratic quantity in $\phi'$, and it is assumed that the structure of the mode is equivalent barotropic (i.e., does not tilt) away from the range of influence of the lower level perturbation. Note that this definition of $H$ simply provides an estimate for the mixing depth $H_0$ used in section 2.4.

We also introduce the Held Scale $h$ (Held, 1978):

$$h = \frac{-\int_0^{0^+} \bar{q}_y dz}{\beta} = \frac{\Lambda\epsilon}{\beta}\,, \tag{3.8}$$

where $\beta$ is the mean value of the interior PV gradient. As discussed by Held (1978), the Rossby depth of the most unstable mode in the Boussinesq-Charney problem scales as $h$.

It is important to realize that, unlike $H$, the Held scale is a property of the basic state. $h$ can be interpreted as the height over which the vertically integrated PV gradient in the interior balances the negative contribution by the delta function at the ground. In other words, for waves with $H < h$ the vertically integrated potential vorticity gradient in the interior is smaller than the delta function at the ground, while the reverse is true for $H > h$. Moreover, for a fluid of depth $H_R$ the two-layer shortwave cutoff is $H = h$ (Lindzen, 1990). For reference, we provide in appendix A a list with all the scales used in this thesis.

We emphasize at this point that our approach is different from that of Held (1978), and

[1]Properly speaking, there is still growth at those points, albeit not exponential (Burger, 1962).

the reader should be careful to avoid confusion. The point of that paper was to estimate the vertical scale of the *most unstable mode* depending on the ratio between the scale height ($H$ in his notation) and $h$. In our case, however, $H$ is the vertical scale of a mode, which may be set up externally (for instance through the meridional scale), and may not correspond to the most unstable one. In fact, modes with $H << h$ will always be weakly unstable.

The fact that the half Rossby depth $H$ gives a good estimate of the region of interior PV fluxes needs additional clarification because there are regions of wave propagation in the Charney problem. This is illustrated in figure 3-1, which describes the vertical structure of the Charney problem in terms of the sign of the refraction index $Q = \frac{1}{\epsilon}\left[\frac{\bar{q}_y}{\Lambda z - c} - k^2\right]$, neglecting the imaginary part of $c$. There is an evanescent region below the steering level, with depth $H_1$, followed by a propagation region with depth $H_2$ up to the turning point. Finally, there is an additional evanescent region, with depth $H_3$. The delta function at the surface can also be interpreted as an infinitesimal region of wave propagation, as required by the wave geometry (Lindzen et al., 1980). We can estimate the depths of these three regions as follows:

*Region I*: The steering level is highest for $\beta = 0$ (edge wave):

$$H_1 \leq \frac{\epsilon^{1/2}}{k} = \frac{H}{\pi}$$

*Region II*: Neglecting $c_i$, $Q$ vanishes at a height from the steering level:

$$H_2 = \frac{\beta}{\Lambda k^2} = \frac{\epsilon}{hk^2}$$

*Region III*: Again, a conservative estimate is given for the case $\beta = 0$:

$$H_3 \leq \frac{\epsilon^{1/2}}{k} = \frac{H}{\pi}$$

Hence, while regions I and III are at most as deep as the Rossby depth, the propagating region can be much deeper when $\epsilon^{1/2}/k >> h$. However, for the cases of interest in this thesis $\epsilon^{1/2}/k \leq O(h)$, so that the Rossby depth provides a good estimate of the depth of the modes[2]. We define short Charney waves as waves with depths $H$ smaller than, or of

[2]In fact, even for deeper modes, the depth of the mode can overestimate the region of interior PV fluxes. Lindzen et al. (1980) show that the PV fluxes extend over a region of depth $c_i/\Lambda$ around the steering level.

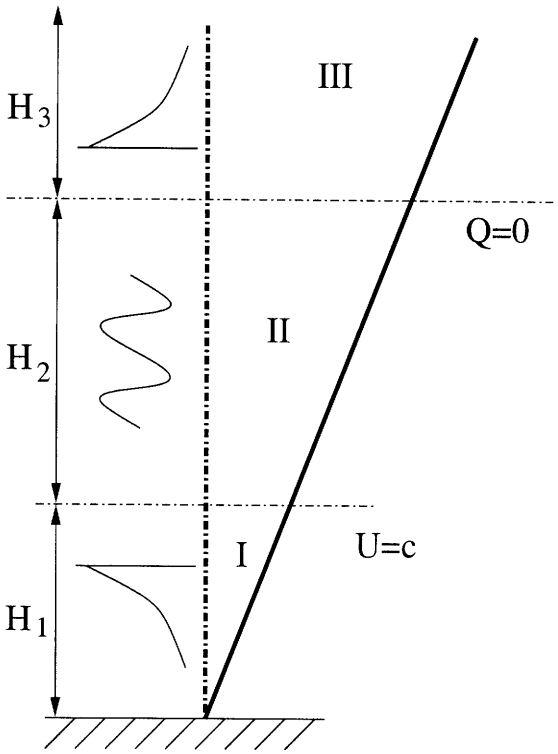


Figure 3-1: Sketch showing the three regions, in terms of wave propagation characteristics, in the Charney problem. Regions I and III are evanescent, while region II allows wave propagation.

the order of, $h$. This will be taken to include modes with wavelengths shorter than the most unstable mode, which has $H/h = 3.9$ based on our definition of parameters. This is illustrated in figure 3-2, which shows the dispersion relation for this problem as a function of the dimensionless parameter $H/h$. We highlight in that figure the region of the spectrum occupied by short Charney waves.

For typical midlatitude values, such as an interior PV gradient $\beta = 1.65 * 10^{-11}\ m^{-1}s^{-1}$, a jet with linear shear and maximum wind speed $U = 30\ m/s$ at a height of 10 $km$, and an inertial ratio $\epsilon = 10^{-4}$, equation 3.8 gives a Held scale $h = 18\ km$ (which is slightly higher than the estimates of Stone and Nemet (1996), see figure 2-1). The Eady shortwave cutoff has $H/h = 0.63$ for this choice of parameters and therefore a wave short enough to equilibrate according to Lindzen's (1993) mechanism would also be a short Charney wave.

Moreover, for this parameter setting, the most unstable Charney mode has $H = 3.9h = 70\ km$, or $L = 14 \times 10^3\ km$. This scale is much larger than allowed when the meridional confinement by the jet is also taken into account (Lindzen, 1993). For instance, if we consider a typical meridional wavenumber $l = \pi/4000\ km$, we get an $H/h$ ratio of 1.1, which is comparable to our estimate of section 2.3 based on the results of Stone and Nemet

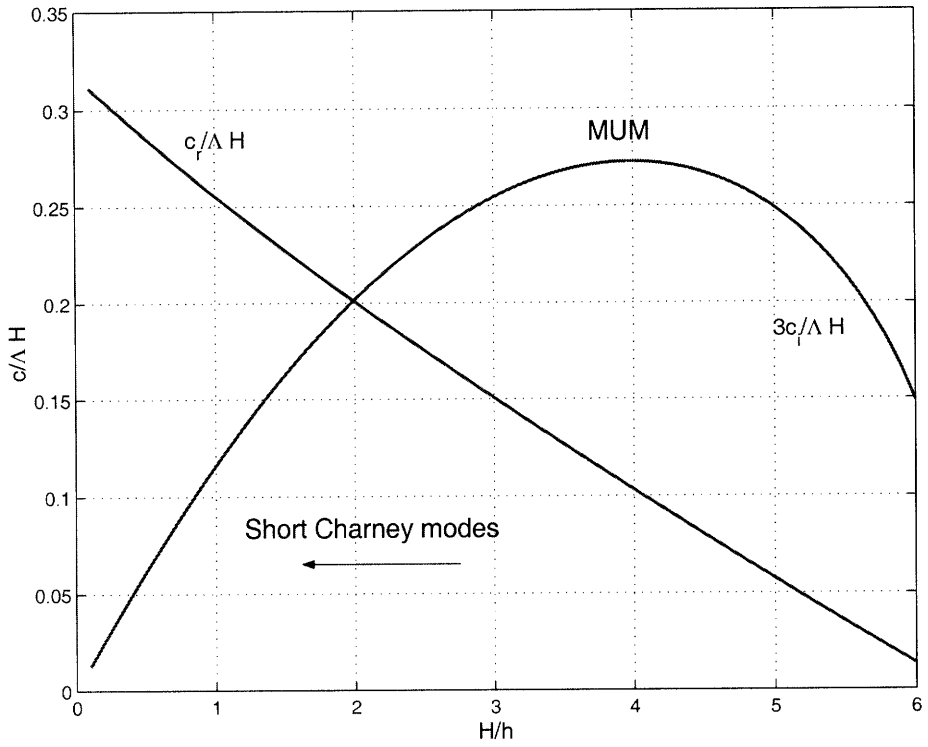


Figure 3-2: Diagram illustrating the definition of a short Charney wave as a wave with $H/h < 3.9$, or shorter than the most unstable mode.

(1996). This suggests that, when the meridional confinement by the jet is taken into account, there is no room for the most unstable mode, and modes of tropospheric extent are short Charney modes. In the next section, we discuss the implications of this fact.

### 3.2.1 Scaling for the barotropic point jet

The scaling derived above extends naturally to the barotropic point jet, for which we can define the following meridional length scales (see also Solomon and Lindzen (2000)):

$$L = \frac{\lambda}{2} = \frac{\pi}{k} \qquad l = \frac{\Lambda}{\beta}\,, \tag{3.9}$$

where $\lambda$ is the wavelength of the perturbation, and $\Lambda$ the (constant) meridional shear. As before, $l$ can be interpreted as the depth over which the integrated positive PV gradient in the interior balances the integrated negative delta function at the vertex. $L$ and $l$ have identical roles as $H$ and $h$ in the Charney problem, so that the results of the Charney-Boussinesq problem for a given $H/h$ agree with those of the barotropic point jet for the same value of $L/l$.

## 3.3 Implications

We showed in section 2.4 that there is a constraint on the vertically-integrated PV gradient over the mixing depth (including the surface delta-function), which cannot be changed during the adjustment. Moreover, when the mixing depth is externally constrained the integrated PV gradient should be negative, which implies that the eddies are unable to eliminate the surface temperature gradient when only short Charney waves are allowed, even in the inviscid case.

In the presence of a surface temperature gradient, the violation of the Charney-Stern condition for instability would demand full interior PV homogenization. It might then be expected that short Charney modes equilibrate in the inviscid problem by eliminating the interior PV gradient, as suggested by Lindzen (1993). However, because the Charney-Stern is not a necessary condition for stability, there could also exist alternative neutral states in which the PV gradient does change sign. We argue below that short Charney modes could equilibrate by eliminating the PV gradient at the steering level alone, rather than all over the troposphere. This would explain the shallow region of homogenized PV seen in observations (refer to figure 2-3).

When $H << h$ the interior PV gradient seen by the wave is smaller than the integrated delta function at the ground. Because the net PV flux has to integrate to zero, this requires a larger diffusivity in the interior than at the surface. To see this, we can combine equations 3.5, 3.6 and the definition of $h$ to derive:

$$hc_i|\eta'(0)|^2 = c_i \int_{0^+}^{H} |\eta'(z)|^2 dz \tag{3.10}$$

For waves with $H << h$ equation 3.10 can only be satisfied if the diffusivity $|\eta'|^2$ is larger in the interior than at the surface. On the other hand, equation 3.7 shows that the PV diffusivity is maximized at the steering level $z_c$, where it can get arbitrarily large as $c_i \to 0$, but is bounded away from that level (recall that $\phi'$ is a well-behaved function). Hence, modes with $H << h$ can only satisfy 3.10 by developing a very large diffusivity at the steering level: $|\eta'(z_c)| >> |\eta'(0)|$. This implies that the vertical structure of the modal PV flux also peaks very strongly at that level and suggests that, if such a mode were to equilibrate quasi-linearly according to such a highly structured profile, it would tend to reduce the PV gradient of the basic state primarily in the vicinity of the steering level, but

not so much elsewhere. This narrow mixing might be sufficient by itself to stabilize the wave. The reason is that when $H << h$, equation 3.10 can never be satisfied once that the PV gradient is eliminated at the steering level and contributions to the integral in the right hand side can only come from interior regions distant enough from the steering level that their diffusivity is bounded $\frac{\eta'(z)}{\eta'(0)} \sim O(1)$.

This is illustrated in figure 3-3. The left panel shows a short Charney wave with $H/h = 0.45$ and the right panel the most unstable mode, which has $H/h = 3.9$. The dimensional wavenumber and Rossby depth are the same in both cases; only the interior PV gradient, and hence the Held scale $h$, change. Note that the vertical coordinate in this figure has been nondimensionalized with the half Rossby depth $H$. As can be seen, this gives a reasonable estimate of the *maximum* penetration of the modes. The interior PV flux peaks in both cases at the steering level (shown with dash-dotted line in the figure). For the case of the most unstable mode, this PV flux has a very broad structure and extends over most of the depth $H$ of the mode. However, for the short Charney mode, the PV flux is very shallow and only extends over a small fraction of the half Rossby depth $H$. This is consistent with the results of Lindzen et al. (1980), who showed that the region with nonzero PV fluxes scales as $c_i$. As shown by Branscome (1983) and reviewed in the next section, the imaginary phase speed scales as $H/h$ for short waves.

The structure described by figure 3-3 is consistent with equation 3.10. Essentially, shortwave instability requires a large diffusivity at the steering level, and hence a shallow PV flux at that height. Figure 3-3 also suggests that when $H << h$, the elimination of the PV gradients across a neighborhood of the steering level alone might be sufficient for neutrality. On the other hand, when the modes are not so short (i.e., $H = O(h)$), there is a significant contribution to the interior PV flux away from the steering level. For these cases, equation 3.10 would suggest that neutrality requires PV homogenization over a finite region $H^*$. We can get a simple estimate of the required homogenization depth around the steering level $H^*$ by making the *unhomogenized* depth $H - H^*$ smaller than $h$. This yields:

$$\frac{H*}{H} > 1 - \frac{1}{H/h} \tag{3.11}$$

In section 3.5 we will calculate the required homogenization depth for waves of different scales, using a numerical model. It will be shown in that section that the simple expression

provided above overestimates the homogenization depth. The main reason is that this estimate does not account for the weighting of the interior PV gradient by the modal structure. Figure 3-3 shows that, even in the case of the most unstable mode, the PV flux has a lot of structure around the steering level. Indeed, this is why the most unstable mode must have $H/h > 1$: the weighting by the height-dependent diffusivity effectively reduces the available positive PV gradient in the interior.

## 3.4 Dispersion relation

In this section we present the dispersion relation of the Charney problem. Because the solution of the Charney problem has been discussed in many occasions in the literature (e.g., Branscome (1983)), we only emphasize here a few points that will be relevant for the discussion in subsequent chapters.

The dispersion relation for the Charney-Boussinesq problem is shown in figure 3-4. In the Boussinesq limit, the dispersion relation can be written in the form $\frac{c}{\Lambda H} = f(H/h)$. Note that $\frac{c_r}{\Lambda H}$ gives the height of the steering level, measured as a fraction of $H$, while $\frac{c_i}{\Lambda H}$ is proportional to the growth rate nondimensionalized by $\Lambda$ (i.e., $\frac{c_i}{\Lambda H} = \frac{1}{\pi\sqrt{\epsilon}}\frac{q}{\Lambda}$). Hence, the dimensionless phase speed and growth rate can be written as a function of the parameter $H/h$ alone. In fact, figure 3-4 was constructed from a series of runs in which the dimensional wavelength was kept constant, and only the interior PV gradient $\beta$ was changed. This changes the Held scale and hence the dimensionless wavelength of the mode.

The first thing to notice is that for all Charney modes the steering level decreases (relative to the Rossby depth) monotonically with increasing $H/h$. It is highest for $H/h = 0$ (or $\beta = 0$), for which case we recover the phase speed of the edge wave. For the most unstable mode on the other hand, the steering level is very low, at a height of just $0.1H$.

The fact that the phase speed decreases with increasing $H/h$ is not surprising because, based on the simple dispersion relation for a barotropic Rossby wave, we expect enhanced westward propagation and lower steering levels as we increase $\beta$ (i.e., as we reduce $h$). Of course, the situation is more complicated than for the barotropic Rossby wave because the mode has vertical structure, and possibly a phase tilt with height. Nevertheless, there still exists a simple integral relation which is reminiscent of the barotropic dispersion relation. The derivation of the semi-circle theorem (Pedlosky (1987), pp. 514) yields for the phase

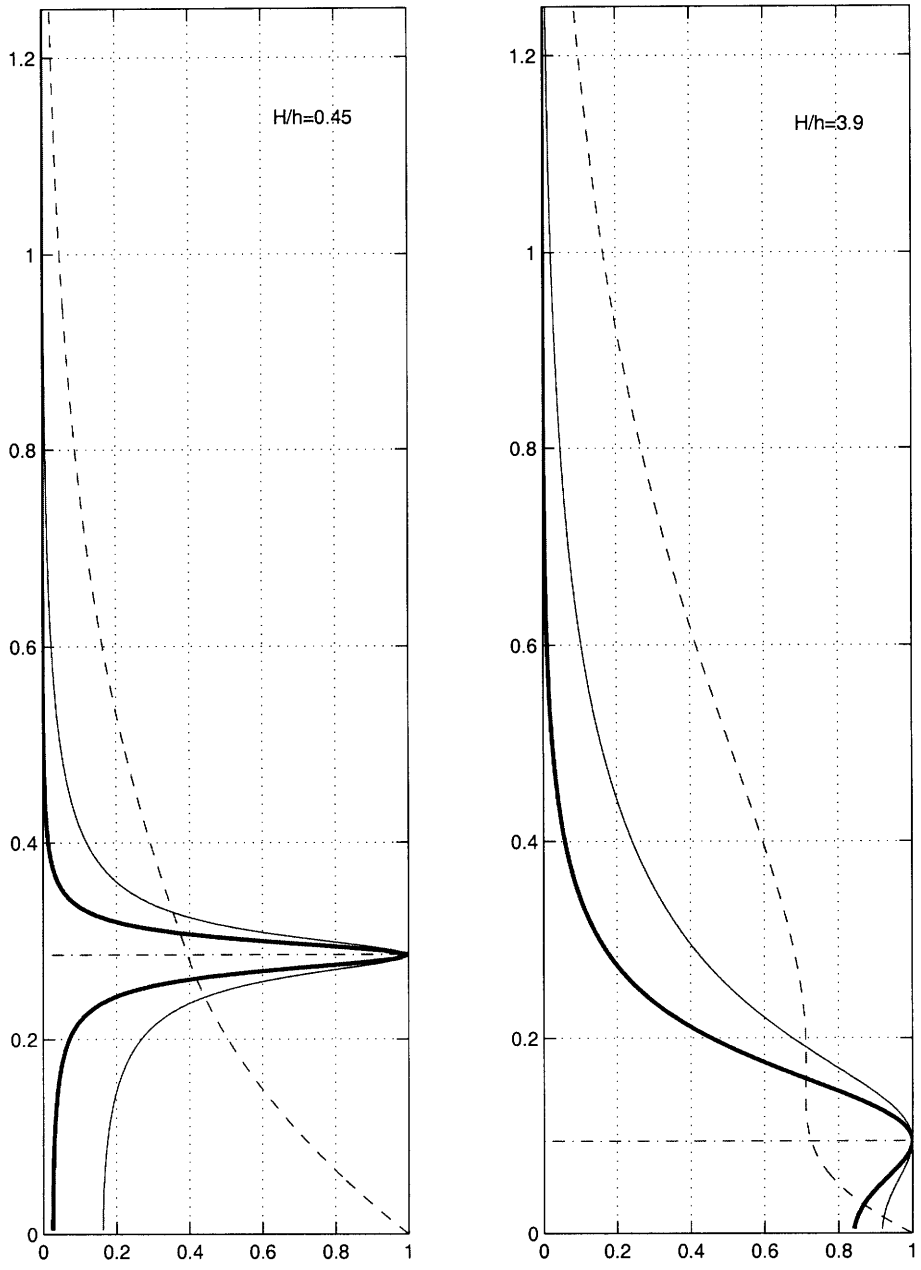


Figure 3-3: Vertical structure (magnitude only) for a short Charney wave (H/h=0.45) and the most unstable Charney mode (H/h=3.9): streamfunction perturbation (dashed), PV perturbation (thin solid) and PV flux (thick solid). The steering level is the dash-dotted line and only interior values are shown. Vertical scales are nondimensionalized with $H$.

speed of an *unstable* wave:

$$c_r = \frac{\int\int U\,|\nabla\eta'|^2 dydz}{\int\int |\nabla\eta'|^2 dydz} - \frac{1}{2}\frac{\int\int \beta\,|\eta'|^2 dydz}{\int\int |\nabla\eta'|^2 dydz}\,, \tag{3.12}$$

where $|\nabla\eta'|^2 = \epsilon\left|\frac{\partial\eta'}{\partial z}\right|^2 + \left|\frac{\partial\eta'}{\partial y}\right|^2 + {k_x}^2|\eta'|^2$.

As in the barotropic Rossby wave dispersion relation, there is a component proportional to the zonal flow $U$ and a component proportional to $\beta$, the latter always being westward. The only difference is that now both components are weighted with a function of the eigenmode structure: i.e., the phase speed is sensitive to some weighted mean of the zonal mean flow over the depth of the wave, instead of just at one level. Because equation 3.12 involves the eigenmode spatial structure $\eta'(y,z)$, which is of course part of the solution, there is no simple explicit expression $c_r(U,\beta)$ as in the barotropic case. Nevertheless, equation 3.12 will be quite useful for discussing the results of chapter 4.

A simpler form of the dispersion relation can be found in the asymptotic shortwave limit, by means of an expansion in terms of the small parameter $H/h$. In the Boussinesq case, these expressions are (Branscome, 1983):

$$\frac{c_r}{\Lambda H} = \frac{1}{\pi}\left(1 - \frac{1.34}{2\pi}\frac{H}{h}\right) \tag{3.13}$$

$$\frac{c_i}{\Lambda H} = \frac{1}{\pi e^2}\left[\frac{H}{h} - \frac{0.26}{\pi}\left(\frac{H}{h}\right)^2\right] \tag{3.14}$$

The zeroth order term in 3.13 is the phase speed of the edge wave, while the first order term is a westward correction proportional to $\beta$. On the other hand, the shortwave growth rate is small, and order $H/h$. The dashed lines in figure 3-4 show that this asymptotic expansion works well when $H/h$ is small, but not so well for $H/h > 1$ or in the vicinity of the most unstable mode.

Finally, we also plot in figure 3-4 the (dimensionless) growth rate of the second harmonic $g_2$, as a function of the value of $H/h$, where $H$ is the half Rossby depth of the *primary* wave. As can be seen, $g_2$ is always smaller than $g$ for $H/h < 5.1$. Hence, for $H/h < 5.1$ the most unstable mode in a channel is always the longest wave fitting the channel.

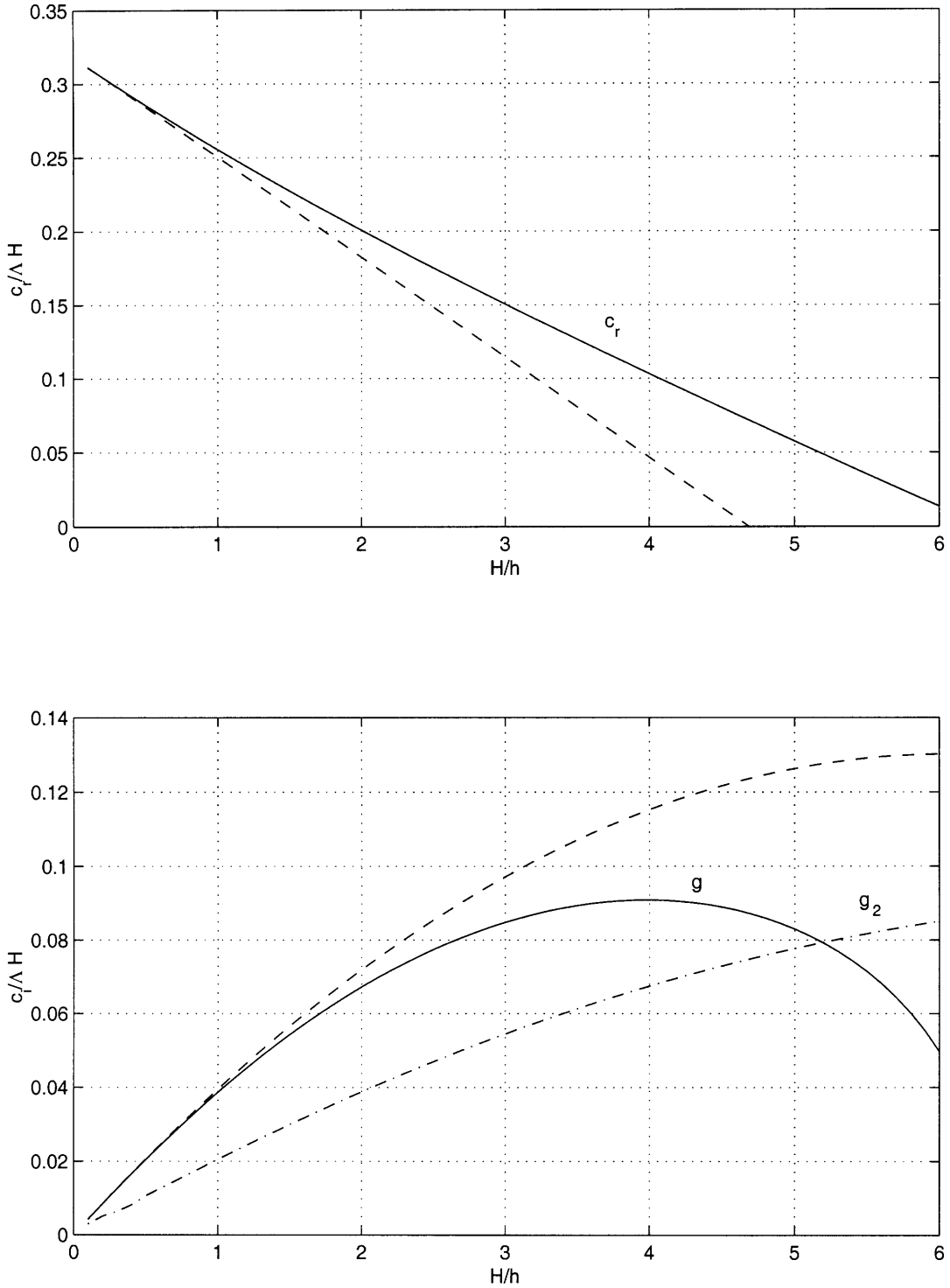


Figure 3-4: Dispersion relation for the Charney-Boussinesq problem as a function of $H/h$: (top) real phase speed, (bottom) imaginary phase speed. The phase speed is nondimensionalized with $\Lambda H$, where $H$ is the half Rossby depth, and $\frac{c_i}{\Lambda H}$ is proportional to the growth rate (see text). The dashed line in both panels show the shortwave asymptotic expansion of Branscome (1983), and the dash-dotted line labeled $g_2$ in the bottom panel is the growth rate of the second harmonic, based on the value of $H/h$ for the primary wave. Note that the diagram emphasizes the shortwave part of the spectrum; the multiple zeros of the Charney problem occur for larger values of $H/h$.

## 3.5 Neutral states

In this section we prove that short Charney waves become neutral when the PV gradient of the basic state vanishes in a neighborhood of the steering level, as suggested by the scaling argument of the previous sections. This is shown analytically for a simple idealized distribution of the interior PV gradient and numerically for more general cases.

### 3.5.1 Analytical model

The Charney and Green models are known to be unstable for all wavenumbers and shears. This is consistent with the discussion of Bretherton (1966) because in both cases there is a non-zero PV gradient at the steering level. We will consider here a variation of these problems in which the interior PV gradient is not constant but has a vertical structure with a single zero at the steering level. We will show that in the presence of small interior PV gradients elsewhere this is sufficient to stabilize the waves.

Specifically, we assume that the basic state interior PV gradient has the form:

$$\bar{q}_y(z) = \alpha(\Lambda z - c)^2 \,, \tag{3.15}$$

where $c$ is the phase speed of the waves (the eigenvalue of the problem). This idealized distribution can be regarded as the first term in a Taylor expansion satisfying the basic requirements that the PV gradient is positive definite and vanishes only at the steering level. In principle, this definition is meaningful only when $c$ is real. However, this is not a limitation for the present analysis because the purpose of this section is to prove the existence of neutral solutions. Note that this ad hoc PV gradient is inconsistent with the basic state $\Lambda$, $N^2$, assumed constant. However, Lindzen (1993) showed that tiny variations in $U$ and $N^2$ can produce changes in the PV gradient of order $\beta$. In that sense, our analysis should be regarded as the leading order term of a perturbation expansion about some slowly varying functions $U(z)$, $N^2(z)$ in balance with $\bar{q}_y(z)$.

We will nondimensionalize equation 3.3 as follows: $z = D\tilde{z}$, $k = \frac{\sqrt{\epsilon}\tilde{k}}{D}$, and $c = (\Lambda D)\tilde{c}$, with the tilde variables being dimensionless. $D$ is a vertical fluid depth, as of yet unspecified.

We will further define the dimensionless parameter:

$$R = \frac{\alpha\Lambda D^3}{\epsilon} = O\left(\frac{D}{h}\right) \,, \tag{3.16}$$

which gives a measure of how important is the integrated PV gradient over the depth $D$ $O(\alpha\Lambda^2 D^3)$ compared to the delta function at the lower boundary (*viz.* 3.8).

After nondimensionalizing and applying the change of variable $\xi = R^{1/3}(\tilde{z}_t - \tilde{z})$, where $\tilde{z}_t = \tilde{c} + \frac{\tilde{k}^2}{R}$ is the turning point of the vertical structure equation, this equation becomes:

$$\phi'_{\xi\xi} - \xi\phi' = 0\,, \tag{3.17}$$

whose solution can be formally written in terms of the Airy functions of the first and second kind $A_i$ and $B_i$ (Abramowitz and Stegun, 1965):

$$\phi' = C_1 A_i(\xi) + C_2 B_i(\xi) \tag{3.18}$$

For real $\xi$ both $A_i$ and $B_i$ are real, implying that both solutions are vertically trapped.

We concentrate first on the modified Charney problem, and let the upper boundary go to infinity. In this case, it is convenient to choose $D = H = \pi\frac{\sqrt{\epsilon}}{k}$ as the height scale (this is equivalent to fixing $\tilde{k} = \pi$). Figure 3-5 shows the vertical structure in physical space[3] of the two solutions of the homogeneous equation for $R = 3$. As can be seen, one of the solutions $(B_i)$ is trapped at the lower boundary, while the other one $(A_i)$ peaks at a height of order $\xi = -1$, $\tilde{z} = \tilde{z}_t + R^{-1/3}$, and decays very slowly aloft. The structure of the solutions for other values of $R$ is very similar. As we change $R$, $A_i$ is shifted and rescaled, while $B_i$ remains essentially unmodified.

Note that both solutions go to zero as $\tilde{z} \to \infty$, $\xi \to -\infty$, so that they both satisfy the upper boundary condition independently. Hence, each solution is by itself an admissible solutions to the modified Charney problem when $c$ is chosen so that the lower boundary condition is satisfied. As a result, each of them (as well as any of their real combinations) gives a different branch of the dispersion relation $\tilde{c}$ $(\tilde{k})$. In particular, for any choice of $C_1/C_2$ a solution $\tilde{c}$ $(\tilde{k};\ C_1/C_2)$ can be found imposing a rigid surface boundary condition at $\tilde{z} = 0$. Reversely, we can find a pair $C_1/C_2$ matching a given value of $\tilde{c}$. For reasonable values of $R$, it is possible to show that the eigenvalue $\tilde{c}$ is real and the solution neutral as long as the vertical structure consists of just one solution $A_i$ or $B_i$. However, this is not

[3]The conversion from $\xi$ to $z$ coordinates requires to input a value for $c$. For the solutions shown in figure 3-5, $c$ was calculated by forcing each of them to satisfy the lower boundary condition in isolation. For more details, see the discussion below.

always true when a combination of both modes is used, in which case imaginary values of $\tilde{c}$ can be obtained. Note that equation 3.15 is no longer physical when that happens.

Now we turn our attention to the modified Green problem (Green, 1960). As is well known, the original Green problem with constant $\beta$ shares more similarities with the Charney than with the Eady problem: it has no top-trapped modal solution or shortwave cutoff.

A significant difference from the modified Charney model discussed above is the presence of an upper rigid lid at some vertical height $D$ (note that we thus choose the depth of the fluid as the height scale in this case). Since this supports a second delta function PV gradient at that level, deep modes are expected to be unstable regardless of how small the interior PV gradient is; indeed, they are also unstable for $\beta = 0$ (the Eady problem). For this reason, we will concentrate on modes shorter than the Eady shortwave cutoff, for which the boundary perturbations can only see the interior PV gradient.

The eigenvalue problem is formulated by imposing rigid boundary conditions (c.f. equation 3.4) at $z = 0,\ D$. In dimensionless form:

$$\begin{aligned} &\phi'_\xi - R^{-1/3}\tfrac{\phi'}{\tilde{c}} = 0 \quad &&at\ \xi = \xi_0 = R^{1/3}\tilde{z}_t \\ &\phi'_\xi + R^{-1/3}\tfrac{\phi'}{1-\tilde{c}} = 0 \quad &&at\ \xi = \xi_D = R^{1/3}(\tilde{z}_t - 1) \end{aligned} \tag{3.19}$$

After some algebra, this leads to the dispersion relation[4]:

$$A\tilde{c}^2 + B\tilde{c} + C = 0 \tag{3.20}$$

where $A$, $B$, and $C$ are given by:

$$\begin{aligned} A &= B_i'(\xi_0)A_i'(\xi_D) - A_i'(\xi_0)B_i'(\xi_D) \\ C &= -R^{-1/3}A_i(\xi_0)\left[B_i'(\xi_D) + R^{-1/3}B_i(\xi_D)\right] + R^{-1/3}B_i(\xi_0)\left[A_i'(\xi_D) + R^{-1/3}A_i(\xi_D)\right] \\ B &= -A - C + R^{-1/3}\left[A_i'(\xi_0)B_i(\xi_D) - B_i'(\xi_0)A_i(\xi_D)\right] - R^{-2/3}\left[A_i(\xi_0)B_i(\xi_D) - B_i(\xi_0)A_i(\xi_D)\right] \end{aligned} \tag{3.21}$$

Note that although equation 3.20 looks like a quadratic equation there is some additional dependence on the eigenvalue through the coefficients. As a result, the dispersion relation must be solved iteratively starting with some initial guess $\tilde{c}_0$. For small $R$ this dependence is weak and the iterative procedure converges rapidly. Note that, while this

[4]Strictly speaking, the solution should not be called a dispersion relation because the basic state is different for each $\tilde{k}$.

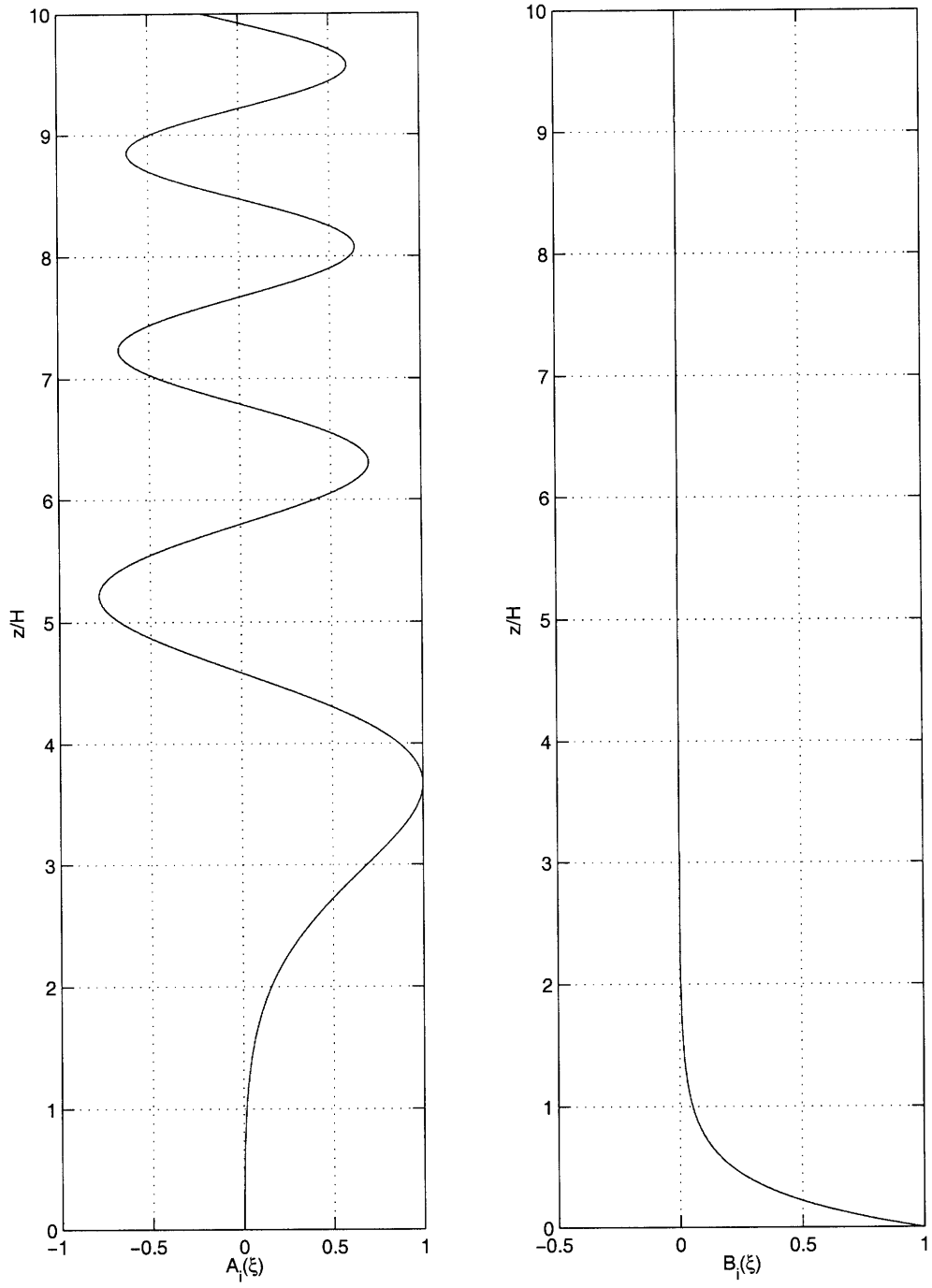


Figure 3-5: Solutions of the problem defined by equation 3.17 for $\tilde{k} = \pi$, $R = 3$ (nondimensionalizing with $D = H$). See text for details.

iterative procedure usually yields *one* solution, we cannot be sure that this is the only one because the dependence of the coefficients on $\tilde{c}$ makes equation 3.20 transcendental.

Figure 3-6 shows the real phase speed of the *neutral* solutions to 3.20 for different values of $R$. The curves are interrupted where no convergence is found or when the converged value is imaginary. Note that this typically occurs for those wavenumbers for which the Eady problem itself is unstable, though the shortwave cutoff does show some sensitivity to the magnitude of the interior PV gradient. For small $R$ the solutions agree very well with the Eady dispersion relation, yielding a shortwave cutoff $\tilde{k} \approx 2.4$. As $R$ is increased, the shortwave cutoff moves to larger values of $k$ and the steering level drops, particularly for the upper branch of the dispersion relation. This is of course consistent with the enhanced positive PV gradient in the interior (see equation 3.12).

Finally note that, as in the Eady problem, the dispersion relation consists of two branches. Not surprisingly, this upper branch is associated to a top trapped mode, as speculated by Rivest et al. (1992). This is illustrated in figure 3-7, which shows the structure of the modes for $R = 3$ and two values of $k$. Note the slight asymmetry between the top and bottom modes for the longer wave ($k = 2.8$, close to the shortwave cutoff): the interior PV gradient appears to favor the upper level disturbance. Our results suggest that the zero PV gradient at the steering level removes the singularity of the Green problem and yields a solution closer to Eady's when the interior PV gradient is sufficiently small.

In conclusion, at least for this idealized distribution of $\bar{q}_y$, neutral solutions can be found in the presence of positive interior PV gradients as long as Bretherton's (1966) condition is violated and the PV gradient at the steering level is zero.

### 3.5.2 Numerical results

For moderate values of the parameter $R$, a vertical structure as in 3.15 gives very small values of the PV gradient across a broad neighborhood of the steering level, even though $\bar{q}_y$ only vanishes exactly at that point. Hence, it would be desirable to examine if neutral solutions can still exist when the region with small PV gradients is narrower. Furthermore, the existence of neutral solutions for a given position of the steering level does not rule out additional unstable solutions with the same steering level; for those solutions equation 3.15 would just not be valid.

We have looked at these issues using a linear, time-dependent, 1D model, in which

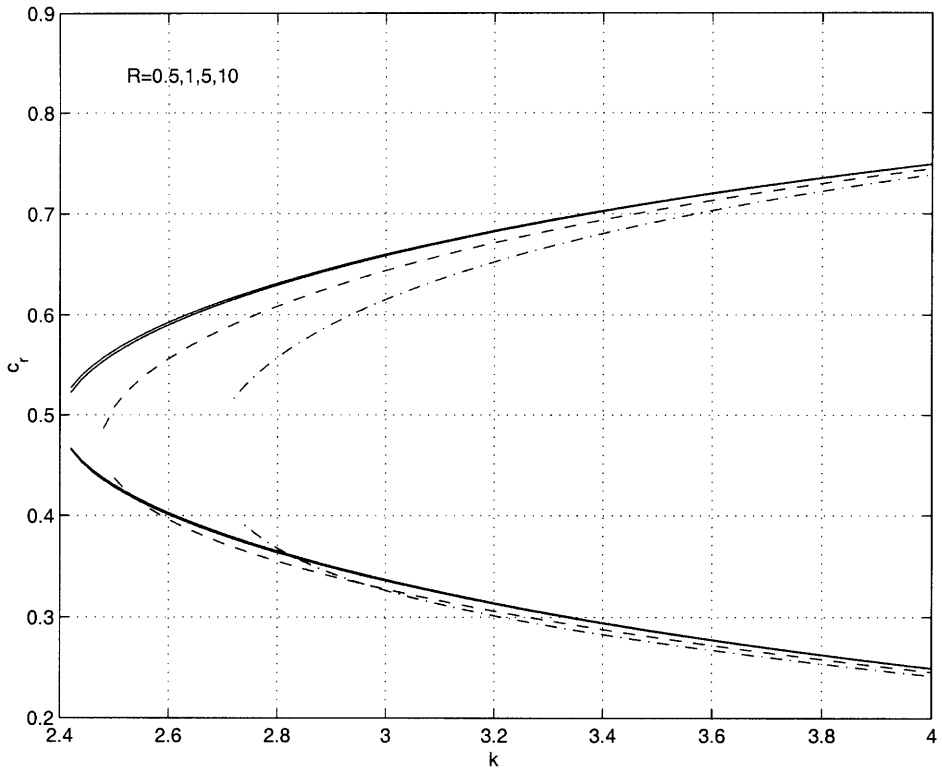


Figure 3-6: Real phase speed for the neutral solutions of the analytical model discussed in the text: R=0.5 (solid), R=1 (solid), R=5 (dashed) and R=10 (dot-dashed). The lines are interrupted where the phase speed becomes imaginary or convergence was not reached in 100 iterations.

the most unstable solutions, when they exist, are found integrating forward in time. For simplicity, a rigid lid is used as the model top boundary condition, though we restrict the analysis to waves shorter than the Eady shortwave cutoff. We validated the model by comparing some of the results with those obtained through direct eigenvalue calculation.

The methodology is the following. We first run the model with constant interior $\bar{q}_y$ and let the most unstable mode emerge. Then, we solve a new linear problem with modified interior PV gradient; the PV gradient is typically brought to zero across a finite neighborhood of the steering level and left unmodified elsewhere. The depth of the region with zero PV gradients is changed until neutrality is achieved.

To illustrate this, figure 3-8 shows a mode right at the Eady shortwave cutoff, which is made unstable by the addition of interior $\beta$. Nevertheless, note that because of the smallness of the interior $\beta$ the inversion is still dominated by the boundary perturbations as in the Eady problem (including the upper boundary perturbation). This mode has $H/h = 0.38$ and is therefore also short in a Charney sense. As shown in figure 3-8 this implies a small

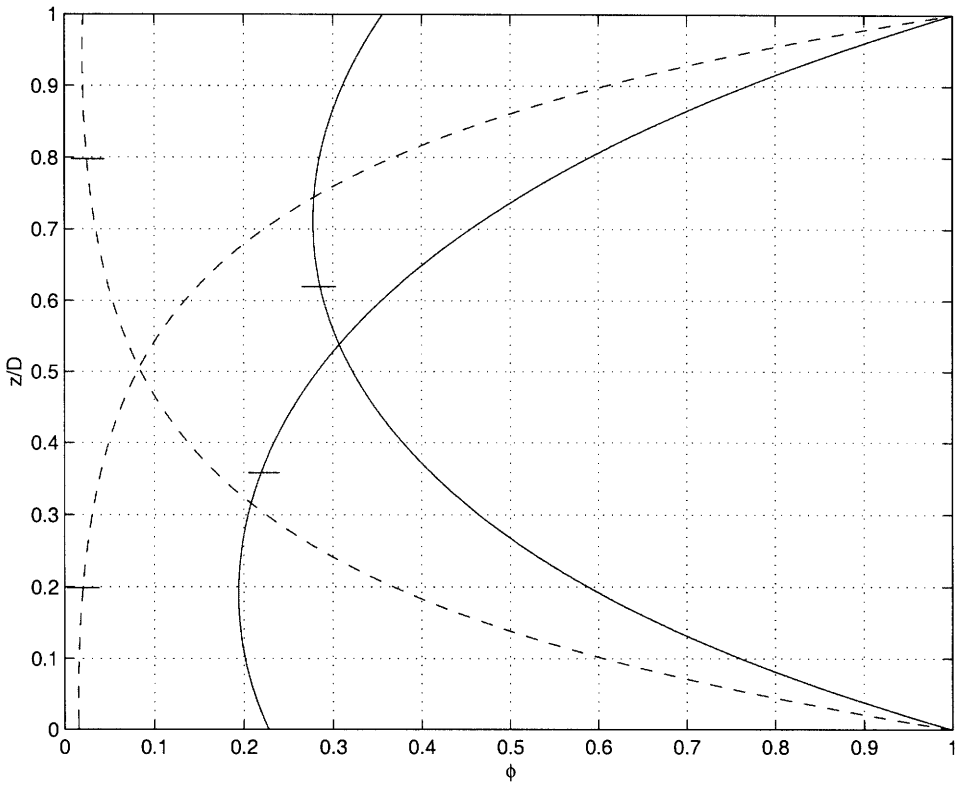


Figure 3-7: Vertical structure of the two eigenmodes for the modified Green problem for $R = 3$ and $k = 2.8$ (solid) and 5 (dashed). The horizontal marks show the position of the steering level for each mode.

growth rate and consequently a PV flux peaking strongly at the steering level (Lindzen et al., 1980). When the PV gradient is brought to zero in the shaded region the wave becomes neutral. The structure of the mode and steering level change very little in the modified state. Hence, it seems a reasonable assumption that such a mode could stabilize quasi-linearly by mixing the basic state PV at the steering level, rather than by eliminating the shear at the ground or homogenizing the full interior PV.

However, this is no longer the case when the value of $H/h$ is not so small. This is illustrated in figure 3-9 for a mode with $H/h = 1.6$. The left panel, corresponding to the run with uniform $\bar{q}_y$, shows that the PV flux has much broader structure than in the previous case and extends to the ground. When the PV gradient is smoothed out across a region of order $0.25H$ surrounding the steering level the mode is still unstable, and has the structure shown in the right panel (note that the PV perturbation and PV flux are zero across the region of zero PV gradient). This is partly due to the fact that the steering level rises significantly when the positive interior PV gradient is reduced, which qualitatively has

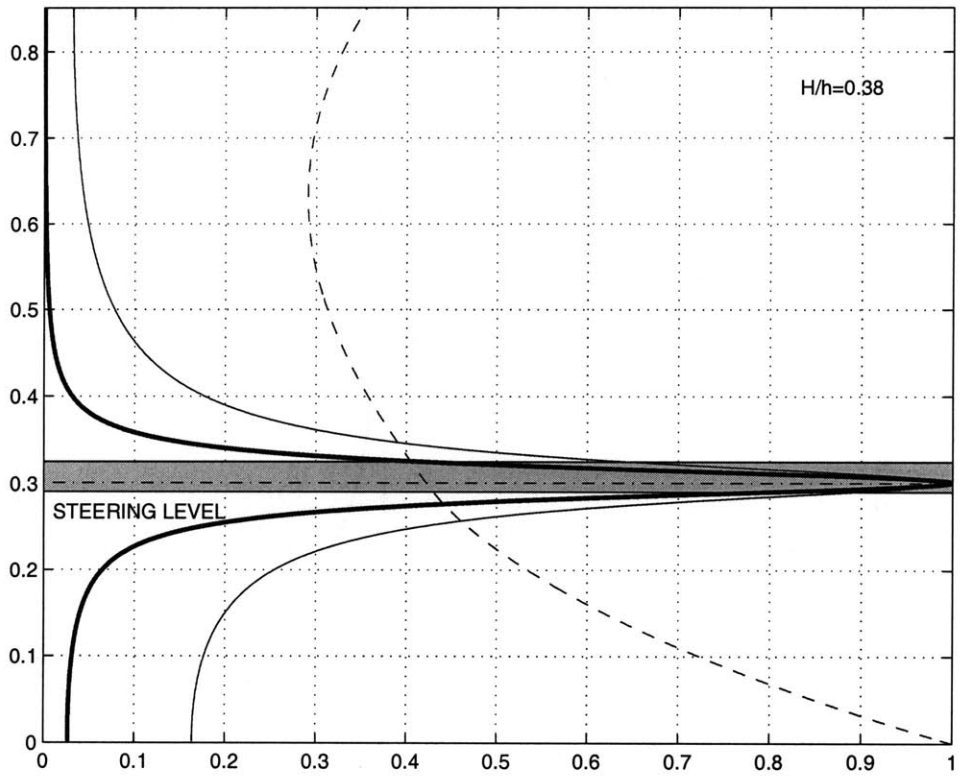


Figure 3-8: Vertical structure of the unstable Green wave at the Eady shortwave cutoff when $\beta = 1.6 * 10^{-11} m^{-1} s^{-1}$. This mode has $H/h = 0.38$ and is also short in a Charney sense. The mode becomes neutral when the PV gradient is brought to zero across the shaded region alone.

the effect of weakening westward propagation relative to the case with full PV gradient (recall equation 3.12). Indeed, note that when the basic state PV gradient is brought to zero across the narrower region shown shaded in the left panel, centered on the new steering level rather than the original one, the mode becomes neutral.

The differentiation between these modes raises an interesting point: in a continuous atmosphere with fine vertical structure different waves may play different roles in the equilibration. For instance, short waves might equilibrate by smoothing out the PV gradient at the steering level while longer waves could also concentrate the barotropic shear of the jet. This scenario of a quasilinear equilibration in which the different modes modify in different ways the mean state raises the interesting question of how sensitive each mode is to the modifications of the basic state induced by the others.

The results of our calculations are summarized in figure 3-10. This figure shows how the growth rate and phase speed of the waves vary with the width $H^*$ of the homogenized region around the (modified) steering level. The different curves correspond to different values of

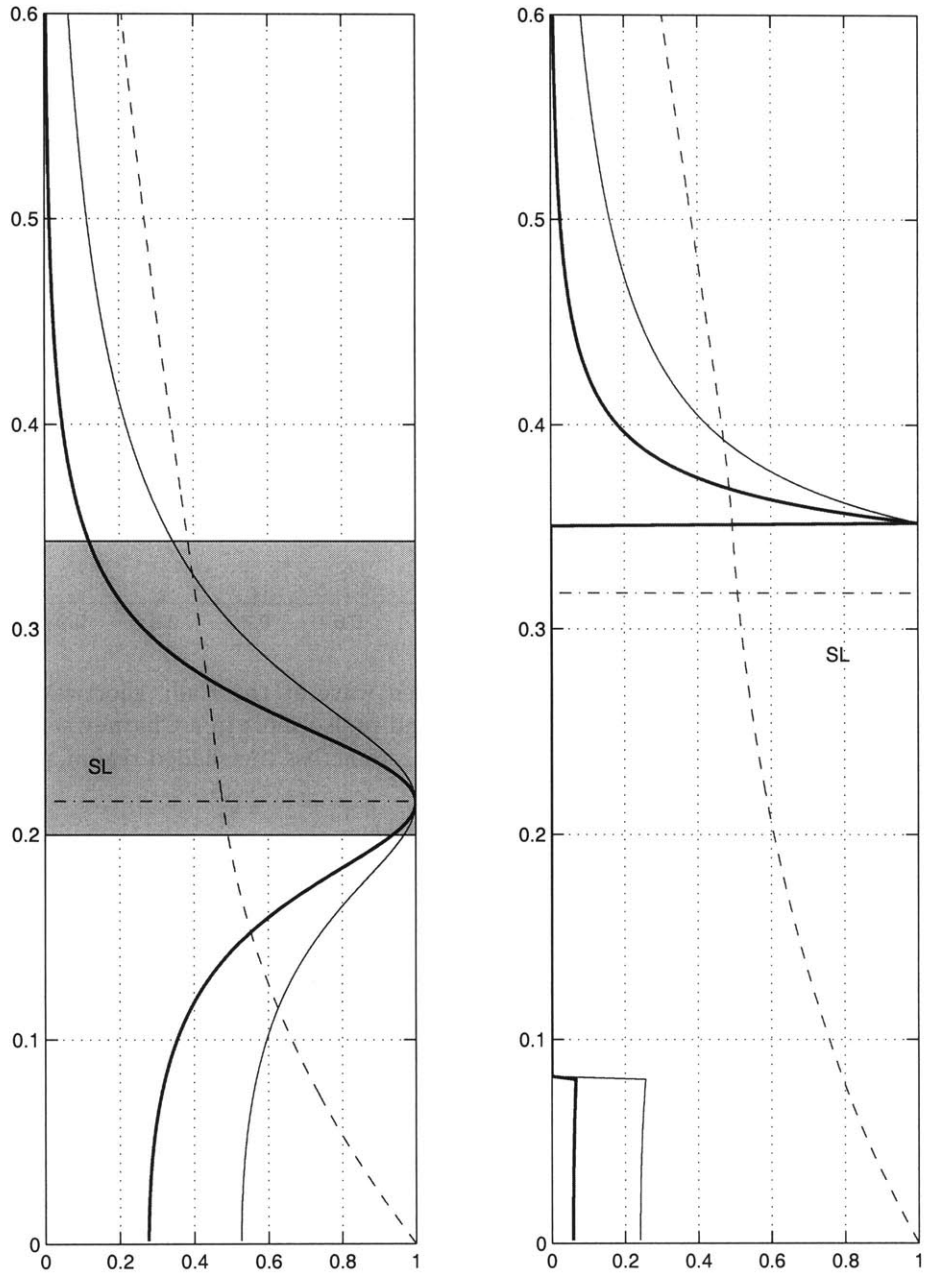


Figure 3-9: Vertical structure and steering level for Charney modes with $H/h = 1.6$. Left panel: mode with uniform interior PV gradient. Right panel: mode when the PV gradient is brought to zero across a broad region surrounding the original steering level. Note that the PV flux vanishes in the region of zero PV gradient, which includes the modified steering level, and yet the mode is still unstable. However, when the PV gradient is brought to zero across the region shaded in the left panel the mode becomes neutral. See text for details.

$H/h$ in the initial profile with uniform $\bar{q}_y$. As can be seen, even for the Charney problem most unstable mode it suffices to eliminate the PV gradients over a region of thickness $0.25H$. More generally, the simple argument leading to equation 3.11 tends to overestimate the homogenization depth significantly. This is due to the fact that the PV flux has a lot of structure around the steering level, particularly when $H/h$ is small (see figure 3-3). The half Rossby depth $H$ can be interpreted as the maximum depth over which the PV fluxes can extend; however, they only do so for the case of the most unstable wave. For shorter waves, the PV flux extends over a region shallower than $H$, typically of order $O(2c_i/\Lambda)$ (Lindzen et al., 1980).

On the other hand, the lower panel shows that the phase speed increases in all cases, as the positive interior PV gradient is reduced. The fact that the steering level is so sensitive to the reduction of the basic state interior PV gradient suggests that the equilibration process would require a fair amount of interior mixing as the steering level rises. However, the situation is more complicated because in reality the lower boundary temperature gradient, which was kept fixed in these linear simulations, should also be mixed, which would weaken eastward propagation relative to the unhomogenized case. In fact, when $H < h$ the modes are essentially edge waves in the sense that the PV inversion is dominated by the boundary perturbation. Hence, the dispersive properties of the modes should be more sensitive to the boundary temperature gradient than to the interior PV gradient. This can be seen in the asymptotic expansion of Branscome (1983) (equation 3.13), which shows that for $H/h = 1$ the edge wave component of the phase speed is 5 times larger than the $\beta$ contribution. This issue will be addressed in chapter 4 with fully nonlinear simulations.

### 3.5.3 Wave geometry interpretation

The analytical and numerical results presented above show that the elimination of the PV gradients at the steering level can be sufficient for neutrality. This admits a natural interpretation in terms of the wave geometry of the modified basic state.

The wave geometry has been proposed by Lindzen and collaborators (see Lindzen (1988) and references therein) as the underlying mechanism behind all forms of shear instability. In this framework, instability results when a wave over-reflected at the steering level is confined in some region, for instance by a rigid surface. The wave geometry essentially defines the basic setup for over-reflection to occur, depending on the sign of the refraction

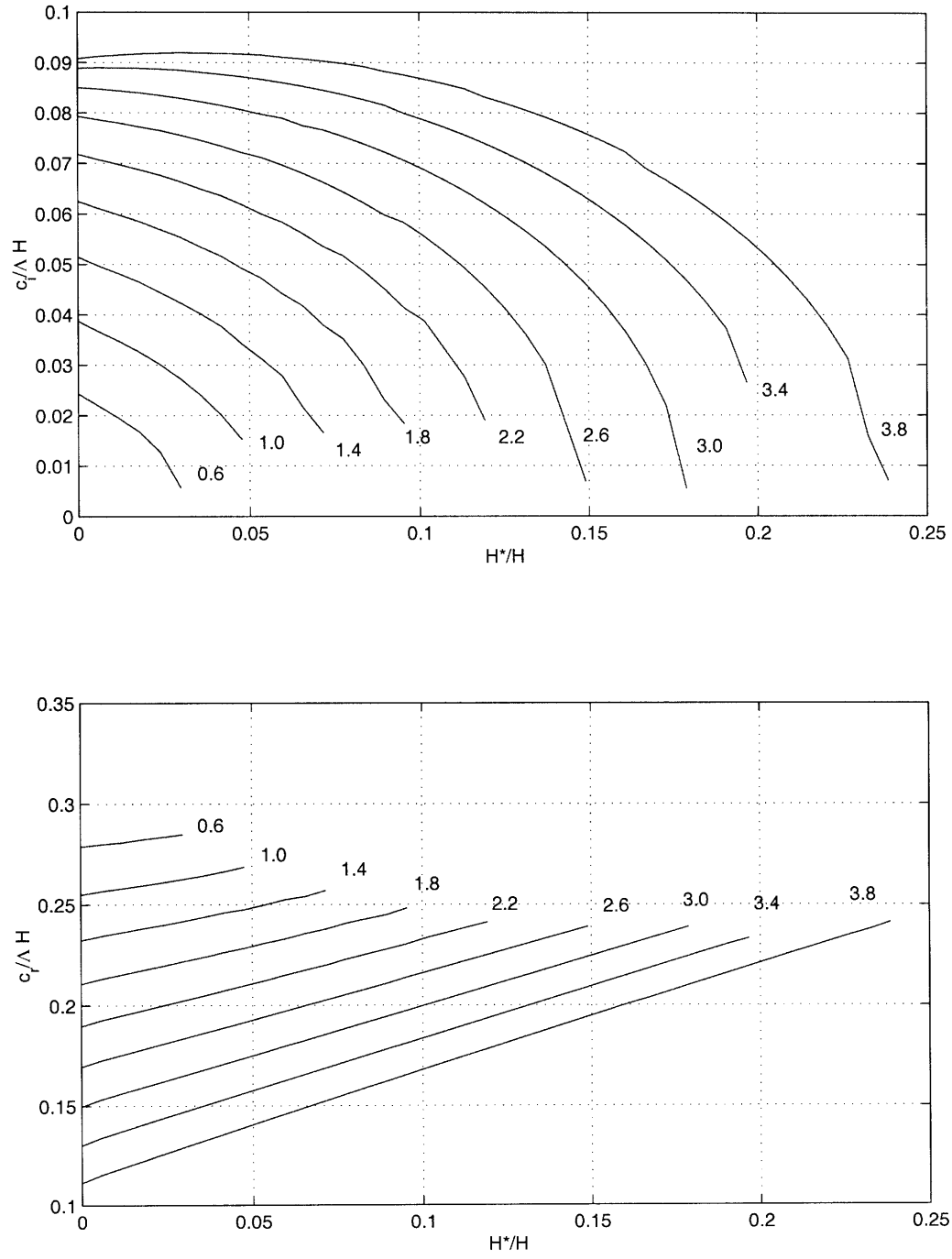


Figure 3-10: Growth rate (upper panel) and phase speed (lower panel), nondimensionalized with $\Lambda H$, as a function of the thickness of the region of homogenized PV gradient surrounding the steering level. The different curves correspond to different values of $H/h$ in the unhomogenized profile.

index $Q(z) = \frac{1}{\epsilon}\left[\frac{\bar{q}_y(z)}{U(z)-U_c} - k^2\right]$ ($U_c$ is the basic state zonal wind at the steering level). This setup consists of a primary wave propagation region, separated from the steering level by an evanescent region, and a wave sink (for instance, a second propagation region) at the other side of the steering level. In these conditions, waves propagating in the primary region are over-reflected at the steering level, which can give rise to growth provided that the over-reflected waves are prevented from radiating away. Without the evanescent region, the wave would be absorbed before reaching the steering level, where its group speed goes to zero. On the other hand, the purpose of the wave sink is to allow the wave to tunnel through the evanescent region, so that it can reach the steering level. As shown in figure 3-1, such a geometry exists in the Charney problem, provided that we regard the ground as an infinitesimal propagation region (Lindzen et al., 1980).

Now consider the case in which PV is homogenized across some region surrounding the steering level. In that case, there is still an infinitesimal region of wave propagation at the surface and an evanescent region below the steering level. The main difference from the previous case is that when $\bar{q}_y$ is zero at the steering level, the refraction index does not change sign at that level. Consider the analytical model first. In that case, $Q(z) = \frac{1}{\epsilon}\left[\alpha(\Lambda z - c) - k^2\right]$. This implies that there always exists a propagation region, from a height $k^2/(\alpha\Lambda)$ above the steering level and extending to infinity. However, for the short waves this propagation region is too far to be a wave sink, and the waves are unable to tunnel to the steering level. On the other hand, for the numerical model the modified basic state has zero PV gradient over a finite window, and constant elsewhere. The evanescent region extends up to a height $z_h$ above the steering level ($z_h$ is the top of the homogenized window), which could again be too far for the short waves to tunnel. Moreover, for the very short waves $z_h > z_t = \beta/(\Lambda k^2)$, where $z_t$ is the height of the turning point (calculated with constant $\beta$) above the steering level. In those cases the wave geometry lacks a wave sink.

In summary, from a wave geometry point of view, the mechanism through which instability is neutralized is by pushing away and/or eliminating the wave sink.

## 3.6 Summary

In this chapter we have analyzed the scaling of the Charney problem and introduced the concept of a short Charney wave. A short Charney wave is essentially a mode with limited

available positive PV gradient in the interior. This limitation can result from a geometric constraint that limits the penetration of the modes (Lindzen, 1993), or simply from a density depth constraint (Held, 1978). In either case, from the mixing depth arguments of section 2.4, when only short modes are allowed, the vertically integrated PV gradient (including the delta function at the surface) must be negative, and the temperature gradient at the surface cannot be eliminated.

We argued that the half Rossby depth $H$ gives a reasonable estimate of the maximum depth of the interior PV fluxes. Based on this, we defined a short Charney wave as a wave for which $H/h < 3.9$ (where $h$ is the Held scale), or shorter than the most unstable mode. We showed that short Charney modes are characterized by a PV flux peaking at the steering level, which is very shallow when $H/h$ is small.

We have also shown that neutrality can be achieved without full interior homogenization for waves with $H << h$, even in the inviscid case. The reason is that the linear diffusivity (basically the square of the Lagrangian displacement $\eta'$) away from the steering level is bounded. Hence, when the interior PV gradient is much smaller than the boundary contribution unstable normal modes can only be sustained in the presence of a non-zero PV gradient at that level, which drives a very large flux there. The homogenization of a narrow region around the steering level is thus sufficient for neutrality in those cases, despite the fact that the Charney-Stern condition for instability is satisfied. The neutrality of these partially homogenized states can also be explained in terms of the wave geometry. When the PV gradient is eliminated at the steering level, the wave sink region moves away from the steering level, or even disappears. In the absence of a wave sink, the waves in the propagation region may not be able to tunnel to the steering level.

We argued that for waves with $H \sim h$ there should still exist a well mixed region surrounding the steering level, whose dimension would depend on the ratio between the interior and boundary PV gradients. While linear runs suggest that basic states with partial homogenization could be neutral, mechanistically, an important objection against equilibration by localized mixing is the sensitivity of the steering level to the degree of homogenization. In the next chapter we will study in more detail how the equilibration proceeds in the fully nonlinear case.

# Chapter 4

# The equilibration of short Charney waves

In chapter 3, we introduced the concept of a short Charney wave. This is essentially a mode for which the available interior PV gradient is limited by its reduced vertical scale. Because of this limitation, short Charney modes do not grow as fast as the most unstable mode in the unbounded problem. Based on this observation, we define in practice a short Charney mode as any mode shorter than the most unstable one, which has $H/h = 3.9$. This value of $H/h > 1$ reflects the fact that, even for the most unstable wave, the modal diffusivity has some structure and weights the interior PV gradient.

We showed in chapter 3 through linear stability analysis that short Charney modes can be neutral when the interior PV gradient is brought to zero at the steering level alone, while longer modes require homogenization over a deeper region $H^*$. Because the linear PV flux of a short Charney mode peaks strongly at the steering level, it was also argued that short modes could equilibrate quasi-linearly, by smoothing out the PV gradient in a neighborhood of that level alone. However, there are some difficulties with this idea. Because the structure of the wave may change as it equilibrates, it is unclear that the modal PV flux is ultimately relevant for mixing. As the wave mixes PV and modifies the basic state its steering level might move, which would displace the focus of the PV mixing. It is not obvious a priori how robust the steering level remains during equilibration. In idealized numerical runs in which the PV gradient of the basic state was artificially set to zero across some interior region, the reduction of the net interior PV gradient resulted in weaker westward propagation and

higher steering levels. However, because in reality the surface shear should also be mixed, we argued in section 3.5.2 that the steering level should drop rather than rise, the reason being that the negative PV gradient at the surface dominates the positive PV gradient in the interior for a short Charney wave. But this is speculation at present.

In this chapter we attempt to provide an answer to these questions by studying the nonlinear equilibration of short Charney waves, using a simple numerical model. The chapter is divided into two main sections: section 4.1 is devoted to the equilibration of the barotropic point jet, while section 4.2 deals with the equilibration of the full 3D baroclinic problem. It is instructive to look at the 2D case first because the linear arguments of previous chapters were essentially two-dimensional. Also, by comparing both problems, we can get a better appreciation of what aspects of the 3D equilibration are dependent on the extra dimension. With this aim, the exposition of the 3D results was written mirroring the 2D discussion.

In the absence of forcing (or when the forcing is linear and homogeneous) the domain averaged zonal momentum is conserved in this problem. Our exposition will focus on understanding how the wave redistributes this zonal momentum, and what are the implications for the steering level. In the 2D case, the redistribution of momentum is due to the eddy PV flux alone, but in the 3D case there is an additional contribution by the mean meridional circulation. In the presence of dissipation, a net momentum flux from sources to sinks must be maintained, which has important implications. This will be discussed in section 4.1.3 for the 2D problem and section 4.2.5 for the 3D case. Finally, we close the chapter with a summary of our results in section 4.3.

## 4.1 The barotropic point jet

Before studying the full 3D problem, we examine in this section the equilibration of the barotropic point jet. In the linear regime, this problem is homomorphic with the Charney problem (Lindzen et al., 1983). However, this homomorphism does not carry to the nonlinear regime, during which stage meridional wave propagation becomes important (Simmons and Hoskins, 1978). As will be shown below, this essentially allows easterly momentum to be exported out of the jet, which has profound implications for equilibration.

The equilibration of the barotropic point jet has been studied before by Schoeberl and Lindzen (1984), Nielsen and Schoeberl (1984), and Schoeberl and Nielsen (1986). More

recently, Solomon and Lindzen (2000) has discussed the sensitivity of the numerical solutions to the model resolution. All these studies agree that in the absence of damping the barotropic point jet equilibrates by smoothing out the delta function negative PV gradient[1] at the vertex of the jet. This is true both for the wave-mean flow system and the fully nonlinear system, and would be equivalent to the equilibration mechanism proposed by Lindzen et al. (1980) for the baroclinic case, which requires the elimination of the surface temperature gradient.

However, the analysis presented in the previous chapters suggests that this may not always be the case, particularly when the scale of the waves or the interior PV gradient are small. Clearly, that was not an issue in the aforementioned studies, in which the unstable modes were not limited by the channel length[2]. To see whether the inviscid equilibration of the short waves also produces full potential vorticity homogenization, we have performed some numerical experiments in a truncated channel. By constraining the length of the channel, we prevent the most unstable mode of the unbounded problem from emerging.

In the barotropic problem the (meridional) penetration of the modes just scales as the zonal length, as opposed to the baroclinic problem, in which the (vertical) penetration scales as the shortest of the zonal and meridional scales. In the troposphere, the zonal length cannot limit the penetration of the waves because otherwise planetary wave 1 would dominate. The main argument for focusing on short Charney waves in this thesis is the fact that the meridional scale of the jet appears to constrain the penetration of the modes in the full 3D problem (Lindzen, 1993). However, there is nothing equivalent in the barotropic point jet problem. We must thus artificially truncate the channel length if we want to compare to the dynamics of the baroclinic problem in a parameter range in which such a constraint might exist.

As discussed in section 3.4, a short Charney wave is always more unstable than any of its harmonics. Hence, the most unstable mode in the truncated channel is always the longest wave fitting into the channel. This allows us to study how a wave of a certain scale equilibrates, as we can essentially choose the scale of the dominant wave by changing the channel length. Though this makes the dynamics of the equilibration quasilinear, in the

[1] In the barotropic problem the potential vorticity is just the absolute vorticity $q = f + \xi$. However, we shall still favor for simplicity throughout this section the term potential vorticity $q$, or PV in short.

[2] For instance, in Nielsen and Schoeberl (1984) the most unstable mode had zonal wavenumber 5.

sense that it is this wave that primarily modifies the basic state, the model is still fully nonlinear in that the harmonics of the primary wave are also included. A similar device was used by Cehelsky and Tung (1991) in the context of the two-layer model.

In practice, we keep a constant channel length (6000 $km$) and vary only the planetary vorticity gradient $\beta$. By changing $\beta$ we can change the Held scale $l = \Lambda/\beta$, and hence the dimensionless length of the mode $L/l$ (see section 3.2). Short Charney waves are associated to low values of $\beta$, or large Held scales. The meridional wind shear is also kept fixed: $\Lambda = 0.012\ ms^{-1}/km$, giving a maximum easterly velocity of 60 $m/s$ at the jet vertex.

We solve the barotropic vorticity equation on the beta plane using the spectral transform method and 3rd order explicit time-stepping. We include 26 waves in the zonal direction and 66 in the meridional (including the standard 2/3 truncation), which gives a resolution of about $110 \times 95\ km^2$. Though most of the runs presented below are fully inviscid, numerical diffusion is very efficient in removing the small scale enstrophy, particularly in the presence of the strong easterly flow. More details about the model are given in appendix B.

### 4.1.1 PV homogenization and steering level

Figure 4-1 shows the equilibration process for a case with $\beta = 5 \times 10^{-12}\ m^{-1}\ s^{-1}$, or $L/l = 1.25$, where $L = 3000\ km$ is half the channel length (see section 3.2). The upper left panel shows the absolute value of the zonal mean PV gradient, as a function of time and meridional distance. On the right, we show the equilibrium (solid) and initial (dashed) profile. The equilibrium profile is defined as the time-average for long times. The position of the steering level is highlighted by the horizontal marks, and values of the PV gradient smaller than the contour unit ($0.2\beta$) are non-shaded. The same is shown in the lower panel, but in this case for $|U - c|$.

It can be readily seen that the results are consistent with the linear predictions of chapter 3. For waves of this scale, there is not a full homogenization of the PV gradients. In particular, the positive PV gradient in the interior is brought to zero only at the steering level, where it changes sign. On the other hand, the maximum negative PV gradient appears to be largely reduced, since its peak value in the original profile (which depends on model resolution (Solomon and Lindzen, 2000)) was $-\Lambda/\Delta y + \beta \approx -\beta l/\Delta y >> \beta$. However, this is just a result of the stretching of the vorticity jump by the eddy motion (which smooths down the delta function over a finite length), rather than an indication of mixing. To be

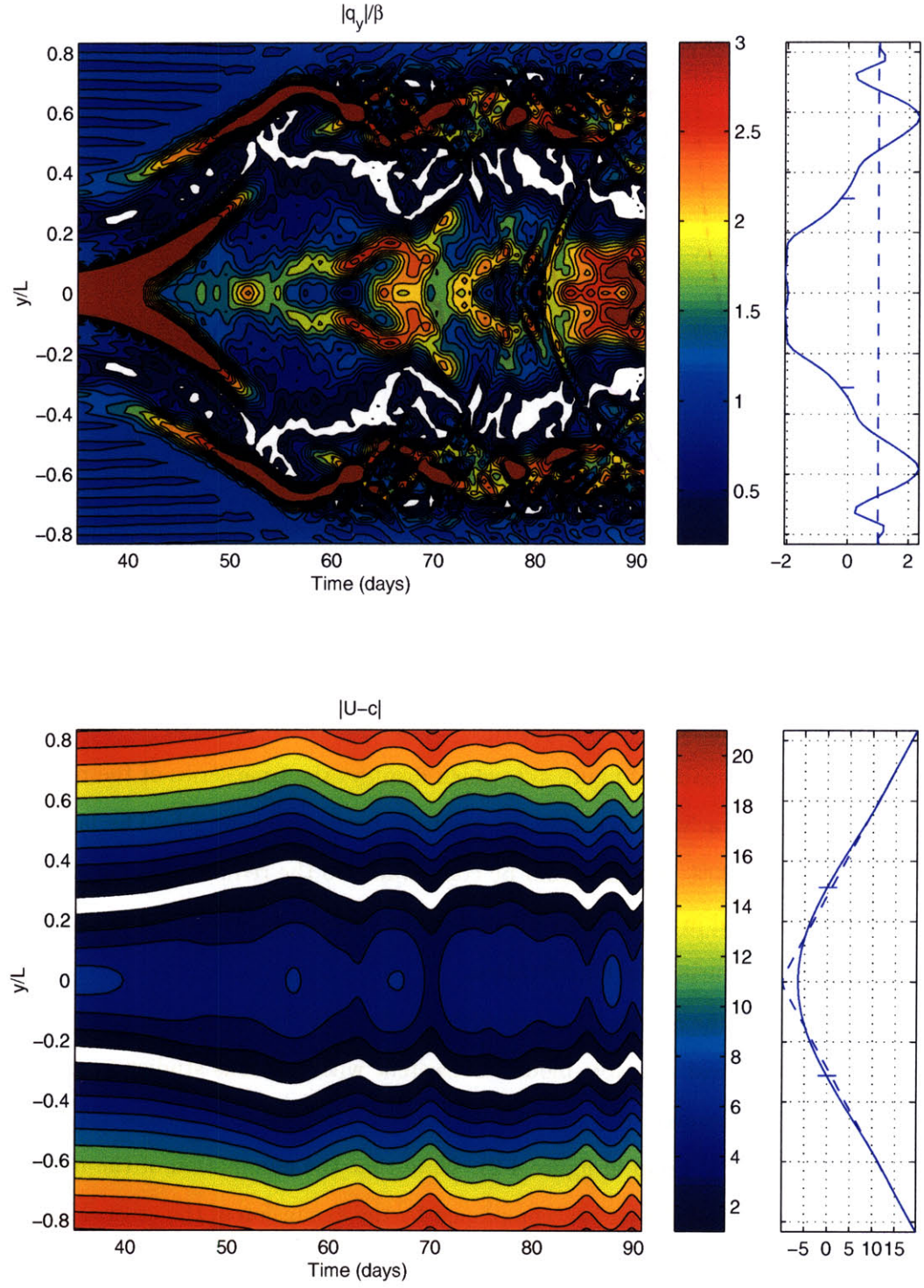


Figure 4-1: Time series of the zonal mean potential vorticity and zonal wind for the run with $\beta = 5 \times 10^{-12} m^{-1} s^{-1}$ (L/l=1.25). (top left) $|\overline{q}_y|/\beta$, contour unit $0.2\beta$, values smaller than the contour unit are non-shaded. (top right) zonal mean $|\overline{q}_y|/\beta$ (initial dashed; equilibration, solid). (bottom left) $|U-c|$, contour unit 2 $m/s$, values smaller than 1 $m/s$ are non-shaded. (bottom right) zonal mean $|U-c|$ (initial dashed; equilibration, solid). The horizontal marks show the position of the steering level.

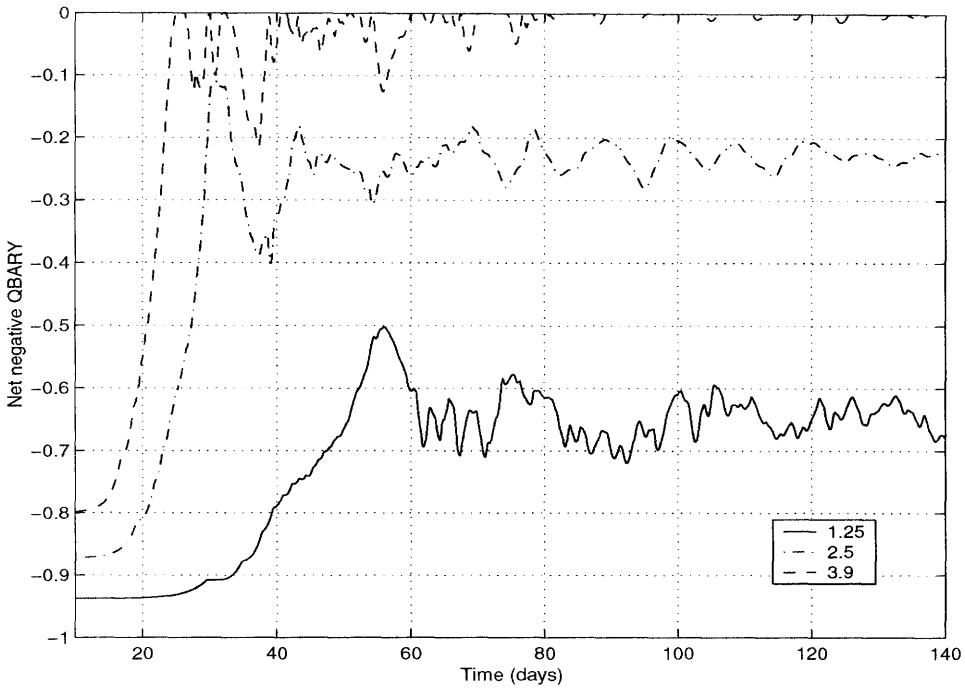


Figure 4-2: Time series of the net negative vorticity jump, normalized by $\Lambda$, for the runs with L/l=1.25 (solid), 2.5 (dash-dotted) and 3.9 (dashed).

precise, in an integral sense the negative PV gradient is not reduced as much. This is illustrated in the top panel of figure 4-2, which displays the time series of the net vorticity jump across the region with negative PV gradient (normalized by $\Lambda$). The latter is only reduced by about a 30%, which should be comparable to the reduction in the positive PV gradient. As discussed in more detail below, the net vorticity jump across the mixing length remains unchanged during the equilibration.

Figure 4-3 shows the results for a case with $\beta = 1.6 \times 10^{-11}\ m^{-1}s^{-1}$, or $L/l = 3.9$, which corresponds to the most unstable mode. Consistent with previous studies (Schoeberl and Lindzen, 1984), the negative PV gradient is completely eliminated (see also the time series of the net negative PV jump in figure 4-2). Note that the elimination of the negative PV gradient at the vertex of the jet is accompanied by the expansion of the critical layer to the center of the channel so that even in this case there is a good correspondence between the homogenized region and the position of the steering level.

These results, as well as those from other runs not shown, suggest that there is a very robust relation between the position of the steering level and the degree of PV homogenization for short Charney waves. It is therefore important to understand what controls the position of the steering level. In chapter 3, we examined numerically the dispersive prop-

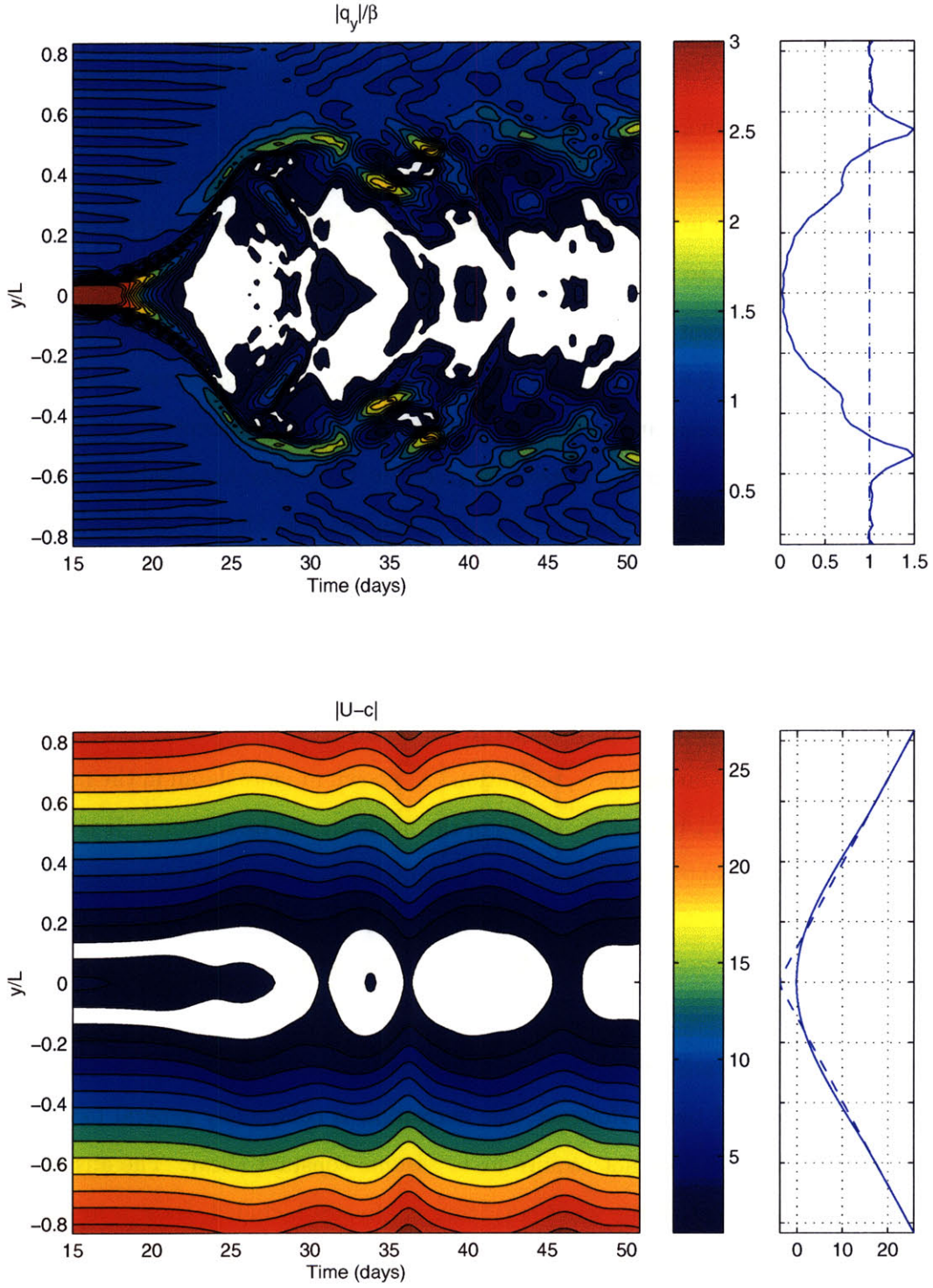


Figure 4-3: As figure 4-1, but for the case of the most unstable mode ($\beta = 1.6 \times 10^{-11} m^{-1} s^{-1}$, L/l=3.9).

erties of partially homogenized states. The linear stability analysis of section 3.5.2 showed that the phase speed of the modes increases as the interior PV gradient is mixed. However, the analysis of chapter 3 was too contrived in that only the interior PV gradient was mixed, while the surface delta function was kept unchanged. It was argued then that, because the phase speed of a short wave is more sensitive to the boundary than to the interior PV gradient (c.f., equation 3.13), the steering level should drop rather than rise. In fact, figures 4-1 and 4-3 show that, in a more realistic situation in which both are mixed, there appears to be a compensation, so that the steering level does not change that much.

This is also apparent in figure 4-4, which shows the time series of phase speed and minimum zonal wind (i.e., at the jet vertex) for the two cases considered. Note that, for the most part, the changes in the steering level result from adjustments to the zonal wind, rather than from changes in the phase speed. For instance, the broadening of the critical layer toward the center of the channel in figure 4-3 results from the deceleration of the zonal wind over the central region down to values on the order of the original phase speed, which changes relatively little in comparison.

In fact, the argument of whether the phase speed should be more sensitive to the interior or the boundary PV gradient is artificial in this context, because these gradients cannot change independently during the equilibration. As shown in more detail in the next section, the integrated PV gradient over the depth of the mode should be constant. It is illustrative in this regard to consider the integral constraint on the phase speed (see section 3.4):

$$c_r = \frac{\int \overline{U}\,|\nabla\eta|^2 dy}{\int |\nabla\eta|^2 dy} - \frac{1}{2}\frac{\int \beta\,|\eta|^2 dy}{\int |\nabla\eta|^2 dy}\,, \tag{4.1}$$

Note that only $\beta$, rather than the full PV gradient including the curvature contributions, appears in the second term. However, the derivation is completely general (see Pedlosky (1987) for details) and does not require us to assume constant shear. The answer to this puzzle is that any effect of the wind curvature is already included, though in an integral sense, in the first term. To be sure, the *local* Rossby propagation correction to the zonal wind is a function of the full PV gradient, including the local wind curvature. Indeed, in order to have an interior steering level the PV gradient must change sign, because otherwise the Rossby propagation component would have the same sign at all levels. However, the Rossby propagation component resulting from the curvature PV gradient disappears when

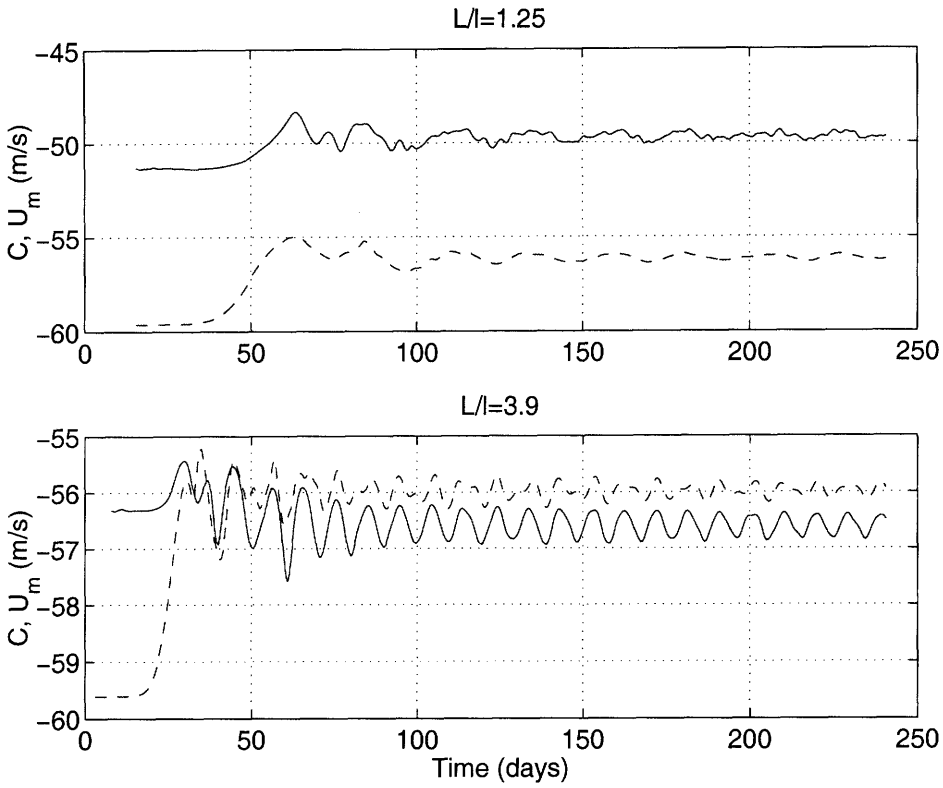


Figure 4-4: Time series of phase speed (solid) and minimum zonal mean wind (dashed) for the $L/l = 1.25$ (top) and $L/l = 3.9$ (bottom) runs.

integrated over the depth of the mode with these weighting functions, so that only the mean PV gradient $\beta$ remains in equation 4.1. Similarly, note that for damped/unstable modes that tilt, there is an additional phase speed correction at any given level resulting from the circulation induced by PV anomalies at other levels. However, this correction again disappears when integrated over the depth of the mode.

Hence, from equation 4.1, changes in the phase speed must arise through changes in the zonal momentum and/or the structure of the modes. Because the total momentum is conserved in this problem, we expect that the weighted integral of $\overline{U}$ (first term in 4.1) should also vary little. If the structure of the finite amplitude wave is robust during the adjustment, then the phase speed should be nearly constant, as observed. Note however that even when the phase speed is constant, the steering level can move due to the redistribution of the zonal wind $\overline{U}(y)$. In particular, the steering level will move inward (outward) from its original location $y_c$ when the net acceleration at $y_c$ is westerly (easterly).

Because the phase speed is so robust, the evolution of the critical surface in this problem is best understood in terms of the redistribution of zonal momentum. The primary effect

of the eddies is to transfer (easterly) momentum from the jet vertex to the interior, thereby reducing the westerly shear at equilibration. This is illustrated in panel A of figure 4-5, which shows the corrections to the zonal flow for 4 different cases ($L/l$ = 1.25, 2.5, 3.25, 3.9). The similarity of the mean flow correction for all four cases, despite their very different growth rate and vorticity distribution, is striking. Consistent with this, panel B shows that the time-integrated momentum flux is also very similar for all cases. The robustness of the momentum redistribution is particularly striking in view of the very different time variability observed in the momentum flux (see panels C-F).

The situation is summarized in figure 4-6. This figure shows the mean flow correction $\overline{U} - \overline{U_0}$ (thick, solid), as well as $\overline{U} - c$ at equilibration for different values of $L/l$ (the dash-dotted curves). To a good approximation, the solid line is universal for all values of $L/l$, whereas the dash-dotted lines are just shifted vertically depending on the value of $c(L/l)$. Also to a good approximation, the value of $c$ at equilibration is very close to that predicted by the dispersion relation because $c$ is found to vary little. Under these conditions, the intersections of the dash-dotted curves with the solid line (points A, B, C and D) give the original location of the steering level, whereas the intersections with the $x$ axis (points A', B', C' and D') give the equilibrium location. For the shorter waves (points A and B), there is a net easterly acceleration at the original steering level, which then moves outward from the vertex (points A' and B'). For point C ($L/l = 3.25$), there is no net acceleration at the initial steering level, which then stays fixed (C=C'). Finally, when the acceleration at the original steering level is westerly the steering level expands inward and, if this acceleration is sufficiently large, altogether disappears. Figure 4-6 shows that this is the case for the most unstable mode (point D, $L/l = 3.9$). Note that the disappearance of the steering level is intimately related to the elimination of the negative PV gradient.

Despite the robustness of the equilibrated flow, the zonal mean PV distribution varies widely from one case to another, as shown in figure 4-7. In fact, it will be argued below that most of this difference comes from $\beta$. From a potential vorticity viewpoint, the most noteworthy feature of the equilibrated flow is the well-mixedness of PV across localized regions on both sides of the jet, and collocated with the steering level. This is what would be expected from the quasilinear arguments of chapter 3 because the PV flux peaks at that level. However, it is not clear that the quasilinear picture is relevant because the PV flux is far from modal, and displays a strong variability, frequently reversing sign (not shown). For

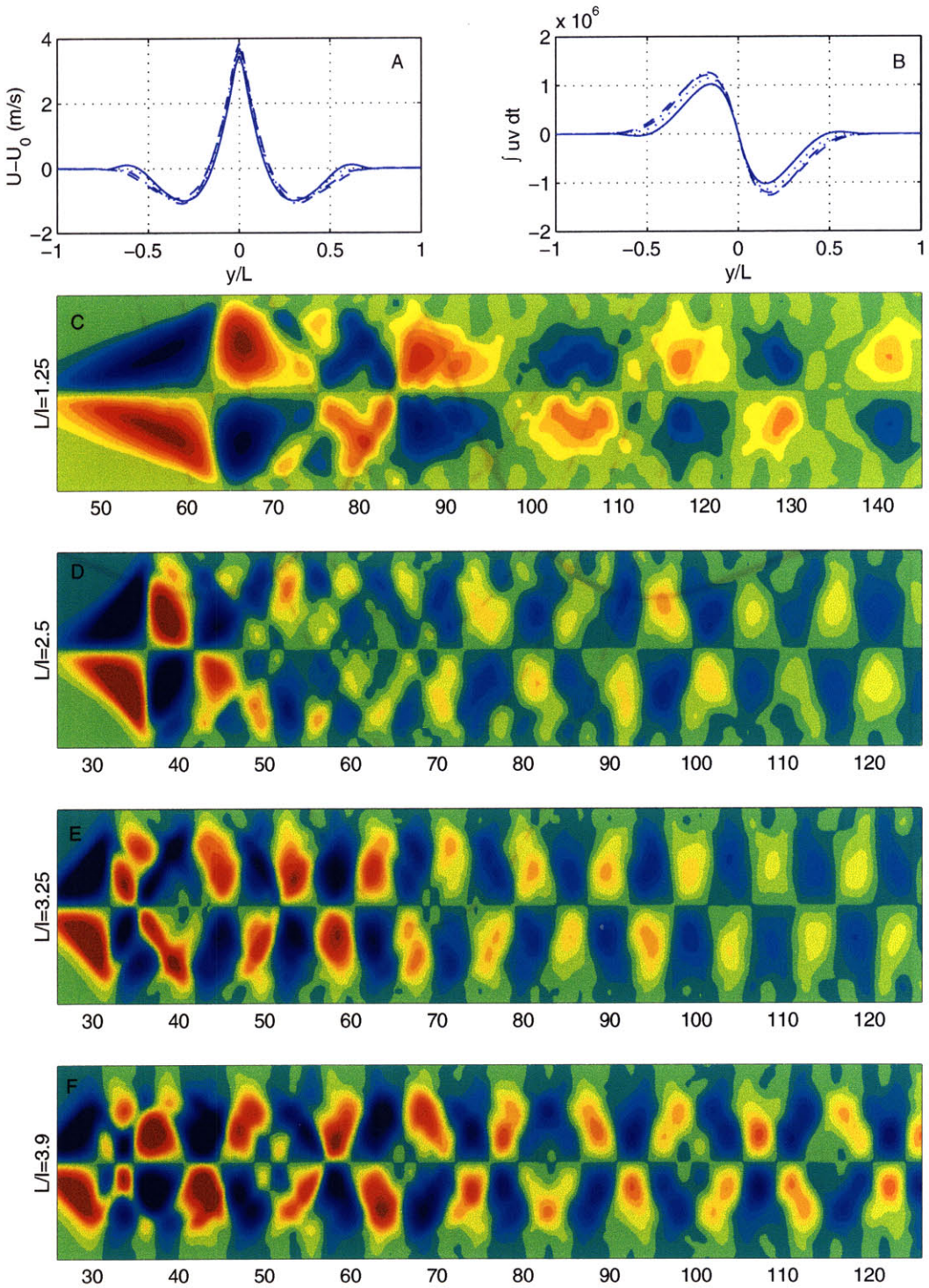


Figure 4-5: A) Time-mean correction to the zonal flow for $L/l = 1.25$ (solid), 2.5 (dashed), 3.25 (dash-dotted) and 3.9 (dotted). B) As A but for the time-integrated eddy momentum flux in $m^2/s^2 \times day$. C, D, E, F) Time series of the eddy momentum flux for the cases indicated.

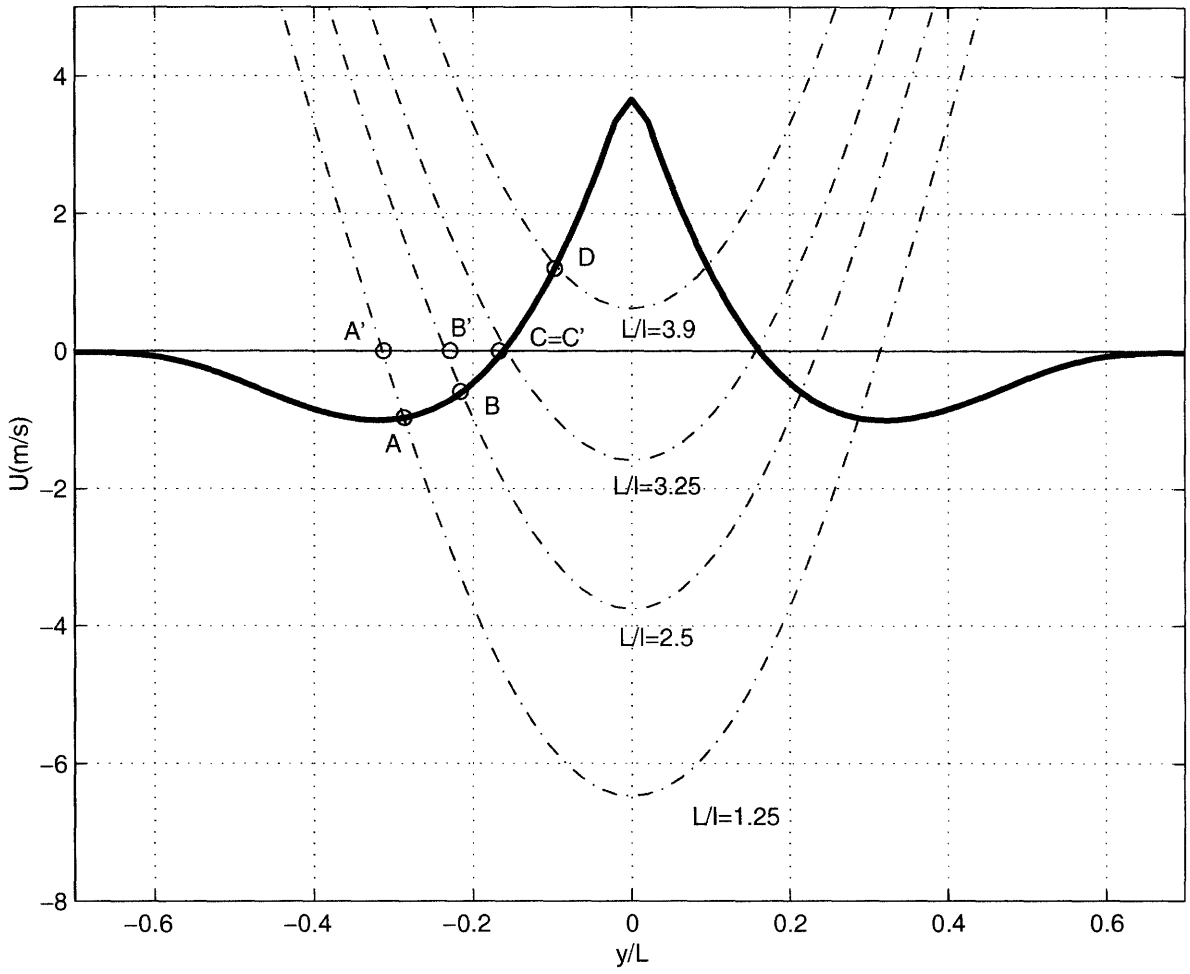


Figure 4-6: Mean flow correction $\overline{U} - \overline{U_0}$ (thick solid), and $\overline{U} - c$ (dash-dotted) for the cases indicated. Points A, B, C, and D show the position of the original steering level, whereas points A', B' and C' show its final position.

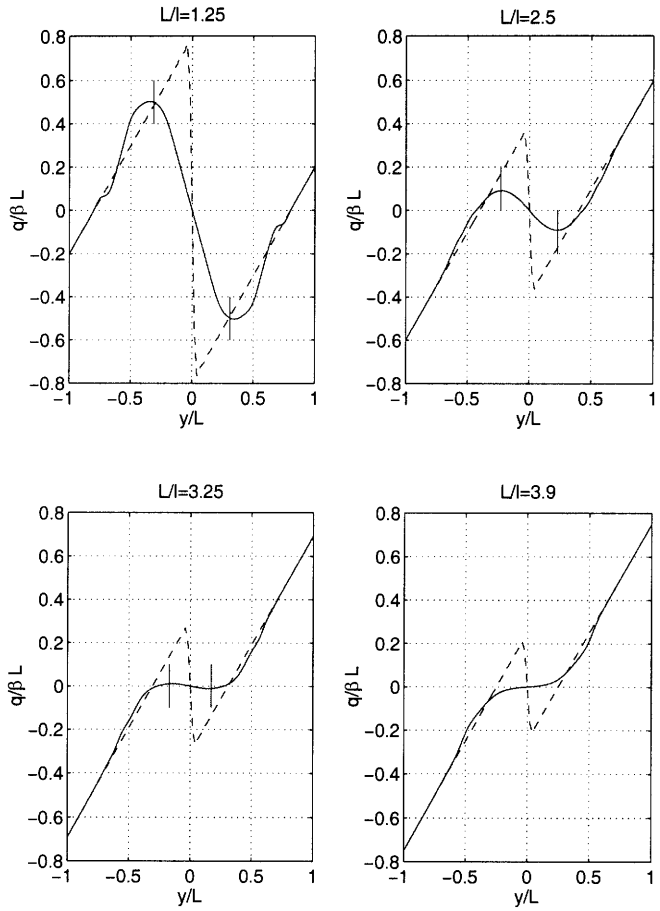


Figure 4-7: Zonal mean PV distribution, initial (dashed) and at equilibration (solid) for the cases indicated. The vertical marks indicate the position of the steering level.

instance, consider the case $L/l = 3.25$. As discussed above, there is no net acceleration at the steering level for this case, which implies that the time-integrated PV flux must vanish at that latitude. The efficient smoothing of the PV gradient there cannot then be attributed to the large magnitude of the PV flux!

To be sure, the notion of inhomogeneous PV mixing is not new, but has a long tradition in the stratospheric literature. In that context, the existence of well homogenized regions (or surf zones) at the zero wind line has long been recognized, and there exists a vast body of literature on inhomogeneous mixing and wave breaking. We will examine in chapter 6 the extent to which these concepts are relevant for the equilibration problem.

Finally, we note that another relevant feature of the equilibrated flow is the appearance of a model tropopause on the outer side of the mixed layer. The large PV gradients in these regions are not diabatically forced, but arise from the transition between the homogenized and unperturbed PV distributions.

### 4.1.2 The mixing length constraint

As shown above, in some cases the equilibration of the inviscid barotropic point jet is not successful in eliminating the negative PV jump. As discussed in section 2.4, this is just a consequence of the limited mixing length that the penetration scale $L$ imposes. Specifically, consider the integrated PV gradient over the mixing length $L_0$ (defined such that $\overline{\xi}(L_0) = -\Lambda$):

$$\int_0^{L_0} \overline{q}_y dy = \int_0^{L_0} (\overline{\xi}_y + \beta) dy = -\Lambda + \beta L_0$$

where it was taken into account that, by symmetry, $\overline{\xi}(0) = 0$. It is obvious from this expression that the integrated PV gradient between $y = 0$ and $y = L_0$ cannot be changed by the wave. In other words, all the wave can do is to redistribute the negative jump in relative vorticity over the mixing length. When this length is not enough for the given $\beta$, the net jump in potential vorticity must still be negative, while the opposite is true when $\beta$ is too large. This is illustrated in figure 4-8, which shows the relative vorticity profile at equilibration for the three cases discussed in this section. We also show for comparison the potential vorticity slope resulting from the $\beta$ contribution for all them. As can be seen, the zonal mean relative vorticity is very similar for all cases, consistent with the very similar profiles of zonal mean velocity apparent in figure 4-5. Hence, most of the difference in the PV profiles of figure 4-7 results from the $\beta$ contribution. The relative vorticity gradient for all cases is such that it roughly equals the $\beta$ slope of the most unstable mode.

The striking similarity of the relative vorticity profiles simply reflects the fact that the same vorticity jump is smoothed out over the same mixing length. However, the actual distributions of relative vorticity are very different for the three cases considered (not shown). In fact, even the simple stretching of a single contour can already produce a zonal-mean profile very similar to the one shown, as illustrated in figure 4-9. Hence, to first order the zonal mean profile is only sensitive to the mixing length, and not so much to the structure of the perturbation.

The inability of the short waves to eliminate the negative PV jump is just a direct result of their limited mixing length. In fact, the opposite is true when $\beta$ is too large, in which case there is a net positive vorticity gradient at equilibration. To illustrate this, figure 4-10 shows the profiles of zonal mean relative (left) and absolute (right) vorticity for the run

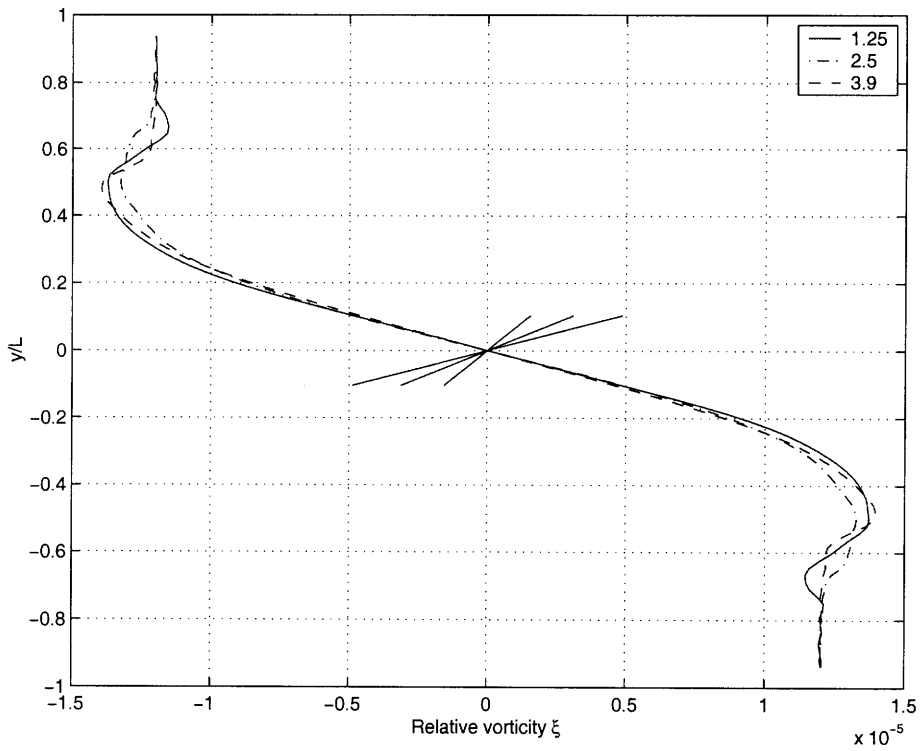


Figure 4-8: Zonal mean relative vorticity for the runs with L/l=1.25 (solid), 2.5 (dash-dotted) and 3.9 (dashed). Also shown is the $\beta$ slope for the same cases.

with $\beta = 2.1 \times 10^{-11}\ m^{-1}\ s^{-1}$. For that particular value of $\beta$, waves 1 and 2 have the same growth rate (see figure 3-4). The two lines shown in the figure correspond to runs initialized with either wave 1 (solid) or wave 2 (dashed) perturbations. As can be seen, the relative vorticity is smoothed out over a longer mixing length in the former case, which has $L/l = 5.1$. This results in a positive absolute vorticity gradient at the center of the channel. On the other hand, when wave 2 dominates (i.e., $L/l = 2.55$) the mixing length is too small and the negative vorticity gradient cannot be fully eliminated. Hence, the efficient PV homogenization observed by Schoeberl and Lindzen (1984) is a property of the most unstable mode alone, rather than an essential requirement for this problem. When the equilibration of the basic state is performed by shorter (longer) waves, the zonal mean PV gradient at the jet vertex is negative (positive).

This example also illustrates the fact that the equilibrium state is highly sensitive to the initial conditions, consistent with other barotropic equilibration studies. This was discussed for instance by Prieto and Schubert (2001) in a similar problem. The authors also constructed statistical theories to predict the equilibrium state of their barotropically unstable vortex. They found that both maximum and minimum entropy theories predicted

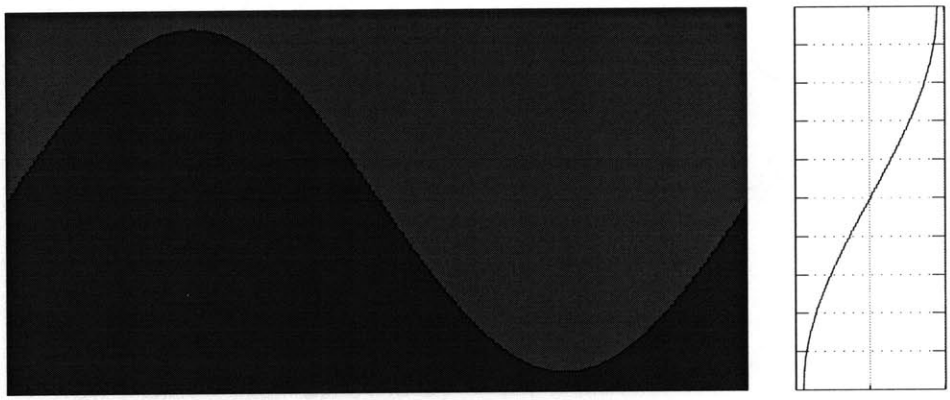

Figure 4-9: Sketch illustrating the smoothing effect on the zonal mean (right) resulting from the wavy distortion of a contour (left).

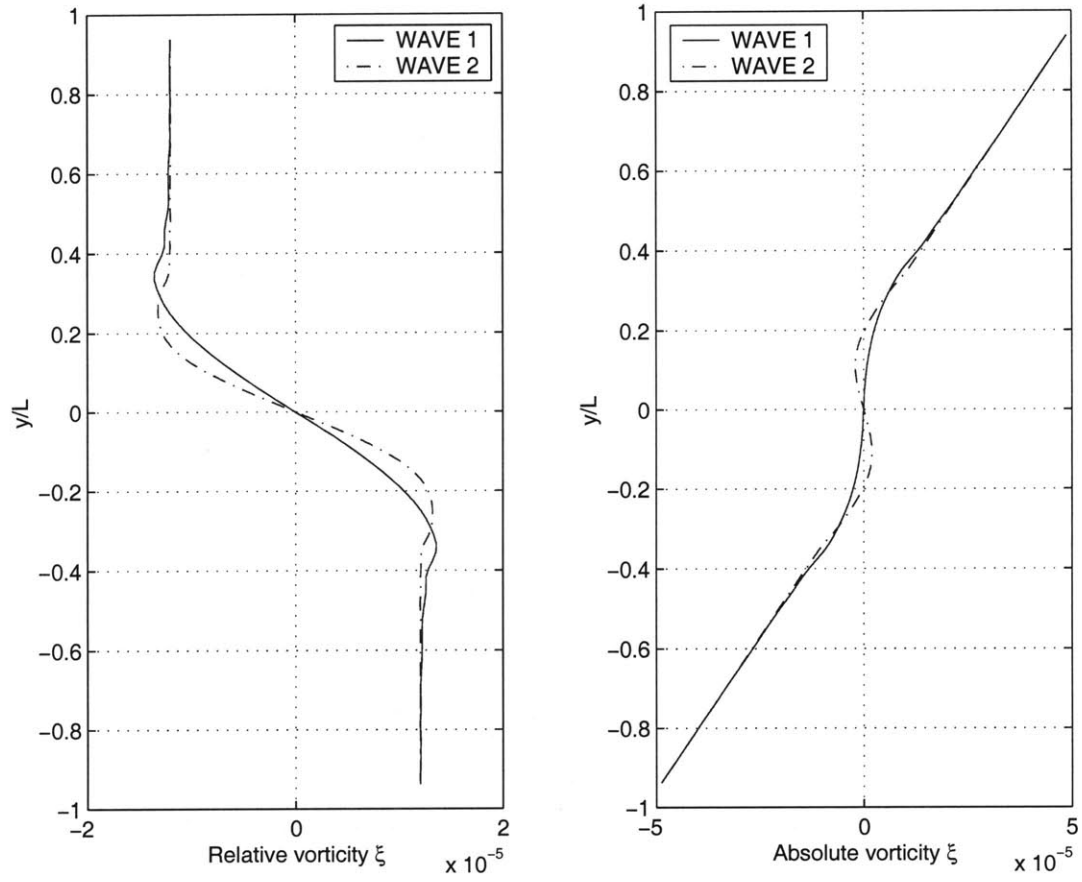


Figure 4-10: Zonal mean relative vorticity (left) and absolute vorticity (right) for the runs with $\beta = 2.1 \times 10^{-11}\ m^{-1}s^{-1}$. The solid and dashed lines correspond to runs initialized with perturbations of zonal wavenumbers 1 and 2, respectively.

an equilibrium state in good agreement with the observed one. The preceding discussion suggests that, in fact, a theory only needs to predict the right mixing length to be successful. The mixing length was an important parameter in their statistical model.

### 4.1.3 Forced-dissipative problem

To conclude this section, we briefly discuss the equilibration of the barotropic point jet in the forced-dissipative regime. We consider a flow that is linearly forced to some equilibrium vorticity distribution with time scale $\tau$, as described in appendix B. This is the same type of forcing that Schoeberl and Lindzen (1984) considered.

The evolution of the zonal mean potential vorticity $\overline{q}$, zonal mean flow $\overline{U}$ and zonal mean eddy enstrophy $\overline{q'^2}$ are described by the following equations:

$$\frac{\partial \overline{q}}{\partial t} + \frac{\partial}{\partial y}\left(\overline{v'q'}\right) = -\frac{\overline{q} - \overline{q}_0}{\tau} \tag{4.2}$$

$$\frac{\partial \overline{U}}{\partial t} - \overline{v'q'} = -\frac{\overline{U} - \overline{U}_0}{\tau} \tag{4.3}$$

$$\frac{\partial}{\partial t}\left(\frac{\overline{q'^2}}{2}\right) + \frac{\partial}{\partial y}\left(\frac{\overline{v'q'^2}}{2}\right) + \overline{v'q'}\,\overline{q}_y = -\frac{\overline{q'^2}}{\tau} \tag{4.4}$$

where $\overline{U}_0$, $\overline{q}_0$ are the initial zonal mean flow and potential vorticity. The eddy PV flux $\overline{v'q'}$ gives the eddy forcing of the zonal mean flow, so that:

$$\overline{U}(y,t) = \overline{U}_0(y) + \int_0^t \overline{v'q'}(y,t')e^{-\frac{t-t'}{\tau}}dt' \tag{4.5}$$

and in steady state (or long time average[3]):

$$\overline{v'q'} = \frac{\overline{U} - \overline{U}_0}{\tau} \tag{4.6}$$

A positive (negative) PV flux produces a westerly (easterly) drag on the mean flow, which must be balanced at equilibrium by a dissipative tendency of the opposite sign. Hence, for simple Rayleigh forcing there must be a net westerly (easterly) acceleration of the basic

[3]For simplicity, we will not use any special notation for time-averaging. Whether we refer to an instantaneous or time-average term should be clear from the context.

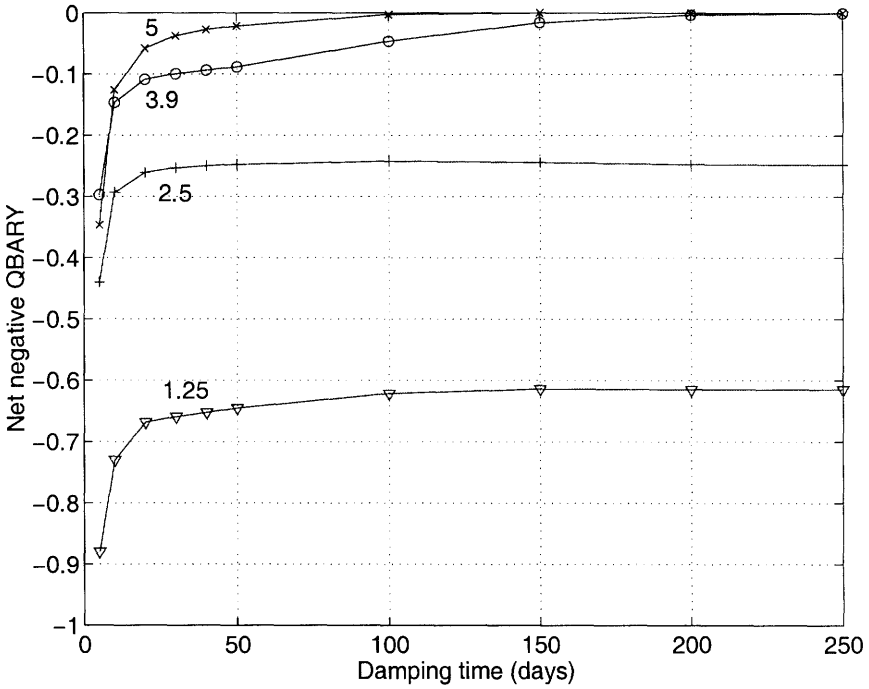


Figure 4-11: Net negative vorticity jump (normalized by $\Lambda$) at equilibration as a function of the forcing time scale $\tau$ for the values of $L/l$ indicated.

state at equilibrium over regions with positive (negative) PV flux. Note that $\overline{v'q'}$ integrates to zero, implying that the eddies can only redistribute the zonal mean momentum. In fact, as long as the forcing is linear, the net momentum is conserved in the forced-dissipative problem because equation 4.6 integrates to zero. However, while in the unforced problem the long-time average PV flux vanishes, in the forced case there must be a mean circulation from the momentum source to the momentum sink.

Figure 4-11 shows the net negative PV jump (i.e., as in figure 4-2) at equilibration as a function of the forcing time scale $\tau$ and for four different values of $L/l$. In agreement with previous studies, the equilibrated flow displays little sensitivity to $\tau$, except when $\tau$ is comparable to the inviscid growth rate. However, despite this little sensitivity, for weak or moderate forcing ($\tau \sim 20-50$ *days*) the equilibrated flow somewhat differs from that in the unforced regime. Most notably, there is a remnant negative PV gradient at equilibration at the jet vertex, even for the case of the most unstable mode and longer waves ($L/l = 5$). This result is also consistent with previous studies.

To understand these results, it is useful to look at the eddy enstrophy equation 4.4. Because eddy enstrophy dissipation is negative definite, there must be a generation of eddy enstrophy at the expense of the zonal mean PV gradient, or a downgradient eddy PV flux.

This can be made explicit by integrating the long-time average of equation 4.4:

$$\int \overline{v'q'}\,\overline{q}_y dy \leq 0 \tag{4.7}$$

For small wave amplitude, the eddy enstrophy advection term (second term in equation 4.4) is negligible. In that case, the PV flux is *everywhere* downgradient, and not just in an integral sense. Then, because $\overline{v'q'}$ changes sign, so must $\overline{q}_y$, consistent with the aforementioned results. This result can also be derived mathematically by dropping the first two terms in equation 4.4 and integrating in $y$:

$$\frac{1}{\tau}\int \frac{\overline{q'^2}}{\overline{q}_y} dy = 0 \tag{4.8}$$

However, the small amplitude assumption is not a priori justified because the equilibrated state consists of a finite amplitude wave. When the eddy enstrophy advection is non-negligible, the PV flux needs not be everywhere downgradient, and it is not possible to prove rigorously that $\overline{q}_y$ must change sign. Nevertheless, this appears to be a very robust result, even in the presence of large $\beta$ and very weak forcing. This is illustrated in figure 4-12, which shows some results for a long wave with $\beta = 2.0 \times 10^{-11}\ m^{-1}s^{-1}$ $(L/l = 5)$.

The top panel shows the equilibrium PV gradient (normalized by $\beta$) for the unforced problem (dashed) and for the forced problems with $\tau = 250\ days$ (solid) and $\tau = 30\ days$ (dash-dotted). In the unforced problem there is a positive PV gradient at the jet vertex, as would be expected from the mixing length arguments presented in section 4.1.2. However, in the forced cases the PV gradient at the vertex is negative, though only marginally for $\tau = 250\ days$. This is still consistent with the discussion in section 4.1.2, because the mixing length appears to be smaller for the forced cases. In particular, note that the region of modified PV gradients extends further away from the vertex for the unforced case (dash line in figure 4-12). We will discuss in chapter 6 the morphology of PV mixing. The distinction between the unforced problem and the forced problem with $\tau = 250\ days$ may seem surprising in view of the seemingly long forcing time scale. However, note that this negative PV gradient is only reestablished after long times; for the first part of the simulation the evolution is very similar in both cases (not shown).

The bottom panels of figure 4-12 show the different terms contributing to the eddy enstrophy balance for the $\tau = 250\ days$ (left) and $\tau = 30\ days$ (right) cases. The first

thing we note is that the wave-mean flow term is not everywhere positive, which implies that the PV fluxes are locally upgradient in some regions. As discussed, this is possible because the eddy advection term redistributes the eddy enstrophy, so that eddy enstrophy generation does not locally balance dissipation. From this figure, we can see that, though the eddy advection term is typically smaller than the other two, it is not completely negligible. Nevertheless, the upgradient PV fluxes are very small, and in particular they are much smaller than the eddy advection term. In fact, positive eddy advection tendencies are more often balanced by dissipation than they support upgradient wave-mean flow fluxes. Moreover, the regions of small upgradient PV fluxes are also regions in which the zonal mean PV gradient itself is not well defined. All this suggests that the downgradient character of the PV fluxes is a fairly a robust feature, even when the eddy advection term is not strictly negligible. In the presence of dissipation, this downgradient character of the PV flux requires that the basic state $\overline{q}_y$ changes sign, as observed. Note that $\overline{q}_y$ must be positive (negative) over regions in which the net mean flow acceleration $\overline{U}-\overline{U}_0$ is easterly (westerly).

We can estimate the net eddy enstrophy by plugging expression 4.6 into equation 4.4:

$$< \overline{q'^2} >= -\tau \int \overline{v'q'}\, \overline{q}_y dy = -\int (\overline{U} - \overline{U}_0)\, \overline{q}_y dy \tag{4.9}$$

Through integration by parts, this can be shown to be equivalent to the eddy enstrophy bound given by Schoeberl and Lindzen (1984):

$$< \overline{q'^2} >= -\tau \int \overline{v'q'}\, \overline{q}_y dy = \tau \int \overline{q} \frac{\partial}{\partial y} \left( \overline{v'q'} \right) dy = -\int \overline{q}(\overline{q} - \overline{q}_0) dy \tag{4.10}$$

As noted by Schoeberl and Lindzen (1984), this result is independent of the forcing time scale in the limit of linear, homogeneous forcing. Note that this last derivation also applies to the 3D quasigeostrophic problem at every pressure level, provided that dissipation is still linear in potential vorticity. This requires homogeneous linear Newtonian cooling and Rayleigh damping with the same time scale.

To conclude this section, we point out that another important difference with respect to the unforced case is that the flow always keeps an interior steering level, as would be expected from the fact that $\bar{q}_y$ changes sign. Though no longer a requirement in the presence of damping, we also found that the PV gradient is still very efficiently homogenized at the steering level (note the smallness of the wave-mean fluxes at that latitude in figure 4-12).

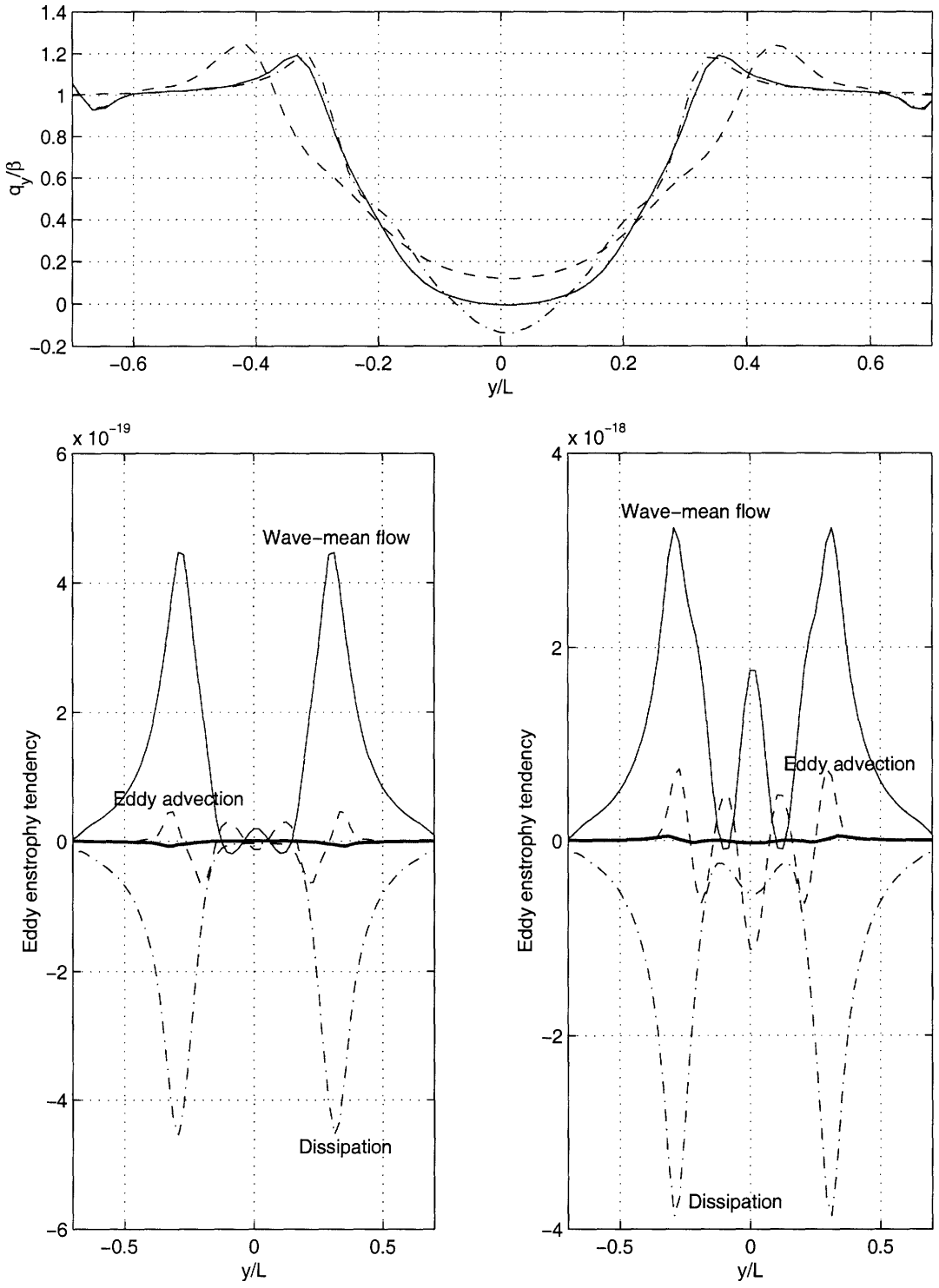


Figure 4-12: (Top) Mean PV gradient (normalized by $\beta$) at equilibration for the runs with $L/l = 5$ and forcing time $\tau = 250$ *days* (solid), $\tau = 30$ *days* (dash-dotted) and $\tau = \infty$ (dashed). (Bottom left) Eddy enstrophy balance for the run with $L/l = 5$ and $\tau = 250$ *days*: wave-mean flow interaction (thin solid), eddy advection (dashed), dissipation (dash-dotted) and residue (thick solid). (Bottom right) Same but for $\tau = 30$ *days*.

## 4.2 3D equilibration of the baroclinic problem

We discuss now the equilibration of the full 3D problem. As in the barotropic case, the setup of the numerical runs is such that geometric constraints prevent the most unstable mode from emerging, so that the equilibration of the basic state can be attributed to short Charney waves of predetermined scale. However, in the 3D case this scale selection is a result of the meridional confinement by the jet as well as of the truncated channel length. For the particular set of runs that we will discuss, we have considered a channel length $L = 4000\ km$ and a radiative equilibrium jet of the same width. In the 3D case the ratio between the zonal and meridional length scales introduces an additional dimensionless parameter, but we have not studied the sensitivity of our results to that parameter. With this choice of scales we get $k_x = \frac{2\pi}{4000}$, $k_y \approx \frac{\pi}{4000}$, $k \approx \frac{\sqrt{5}}{4000}\pi$, and a half Rossby depth $H \approx 17.9\ km$. This scale is kept fixed in all the runs to be shown but the ratio $H/h$ is still changed due to the varying interior PV gradient.

A rigid lid is used as the top boundary condition, but at enough distance (30 $km$) to prevent the interaction between both edge waves. The radiative equilibrium jet has constant vertical shear, such that it yields a velocity of 33 $m/s$ at a height of 10 $km$ (or 100 $m/s$ at the top). The fluid is Boussinesq and the inertial ratio is constant $\epsilon = 10^{-4}$. We use the spectral transform method, with horizontal resolution of $250x250\ km^2$ in grid space (for a 2/3 truncation). The 50 equally-spaced levels give a vertical resolution of 600 $m$. Many of the grid points are outside the domain of interest as the dimensions are made large to prevent interactions with the walls, both meridionally and at the top. This ensures that the boundaries to the mixing domain are internally set up by the eddies. The flow is relaxed to its radiative equilibrium profile with a time scale of 15 *days* and 6-th order hyperdiffusion is used to get rid of the small scale eddies. See appendix B for more details.

### 4.2.1 PV homogenization and steering level

Figure 4-13 shows the equilibrated PV gradients in a run with $\beta = 1.0 \times 10^{-11}\ m^{-1}s^{-1}$, which gives a ratio[4] of $H/h = 0.54$. The "equilibrated" states in this and subsequent figures were calculated by time-averaging between days 500 and 800 of the simulation (the model

[4]Note that this ratio is approximate because we only included $\beta$ in the definition of $h$, and not the curvature contributions to the interior PV gradient (which are height-dependent).

day is defined in terms of the advective time scale). By that time, the wave has completed most of the modifications of the basic state. Despite the small value of $H/h$, the interior PV homogenization seems to proceed efficiently everywhere below the steering level instead of just at that height, though not at the ground, where the temperature gradient fails to be homogenized. The extent of the homogenized region is somewhat surprising in view of the linear analysis of the previous section and the barotropic results, which showed that localized PV mixing could be enough for equilibration. Similar results were found for shorter waves (i.e., with smaller $\beta$), although in those cases the neglected curvature PV gradient is actually larger than $\beta$.

In fact, the snapshot in figure 4-14, taken as the wave starts to modify the basic state at time $t = 135$, shows that the interior PV gradient is initially homogenized only at the steering level. Figure 4-15 shows the time series of the zonal mean PV gradient and $|U - c|$ at the center of the channel. Comparing the top two panels, we can see that there is a good correlation between the region of homogenized PV and the steering level at all times. In fact, it appears that the main reason why the wave fails to equilibrate by localized PV mixing is that the steering level itself drops. This drop of the steering level is far more pronounced than in the barotropic case for the equivalent value of $L/l$. The lower panel of figure 4-15 shows the time series of the phase speed and surface wind at the center of the channel. The distance between these two curves is related to the height of the steering level. We can see that as the equilibration proceeds the phase speed increases, but only slightly. However, the steering level still drops because of the strong westerly acceleration of the zonal mean flow.

The situation is even more extreme as $H/h$ is increased. For instance, figures 4-16 and 4-17 show the 'equilibrated' states (in the sense defined above) and time series for the cases $\beta = 1.3 \times 10^{-11} m^{-1} s^{-1}$ ($H/h = 0.7$) and $\beta = 1.6 \times 10^{-11} m^{-1} s^{-1}$ ($H/h = 0.86$). In the former case, the steering level drops to the ground so that the surface shear is eliminated. In the latter, the steering level disappears as the zonal mean PV gradient becomes one-signed at the center of the channel. In fact, figures 4-16 and 4-17 show that none of these cases have fully equilibrated by day 700 of the integration. A westerly acceleration at the surface is still apparent at that time (the surface wind does not flatten down until about 1000 days). Moreover, unlike the previous case, the phase speed does change during the equilibration, closely following the zonal mean wind at the surface.

To understand the phase speed evolution, it is useful again to look at the integral constraint given by the semi-circle theorem (equation 3.12):

$$c_r = \frac{\int\int \overline{U}\,|\nabla\eta|^2 dydz}{\int\int |\nabla\eta|^2 dydz} - \frac{1}{2}\frac{\int\int \beta\,|\eta|^2 dydz}{\int\int |\nabla\eta|^2 dydz} \tag{4.11}$$

Note that two-dimensionality need not be assumed, so that this expression is valid for any $\overline{U}(y,z)$ (Pedlosky, 1987). We can then repeat the same arguments put forward in the barotropic case. In essence, the phase speed should be insensitive to the redistribution of the curvature PV gradients, both horizontal and vertical (unlike the *local* Rossby propagation corrections to the *local* wind, which do depend on the *local* PV gradients). If the structure of the mode does not change much, changes in the phase speed can only arise from changes in the weighted integral of the zonal momentum.

In the 2D case the net momentum of the column is conserved, so that the westerly acceleration at the jet vertex is compensated by easterly interior acceleration, consistent with the observed robustness of the phase speed. In the 3D problem, the global momentum is still conserved in the absence of friction, so that the observed westerly acceleration over the central part of the channel must also be accompanied by easterly acceleration on the margins of the jet. However, while the net momentum is exactly conserved, the weighted momentum is only approximately so, due to the fact that the mode has most of its structure concentrated at the center of the channel, where there is only westerly acceleration. (Indeed, because the sign of the refraction index allows meridional wave propagation in the region above the steering level, we expect the bulk of the easterly momentum to be deposited away from the main baroclinic zone). This is most likely the reason why the phase speed no longer remains constant, but undergoes a westerly acceleration.

We showed in section 4.1.1 that for the unforced barotropic problem, whether the steering level disappears or not ultimately depends on whether the acceleration at the original steering level is easterly or westerly. For short waves, this acceleration is easterly and the steering level moves away from the vertex; the flow also keeps its negative PV gradient. On the other hand, for long enough waves there is a westerly acceleration at the steering level, which then moves inward and disappears (provided this westerly acceleration is sufficiently large). As this happens, the negative PV gradient at the vertex is also eliminated. While in the barotropic problem the net momentum of the column is conserved, in the baroclinic

problem this is only true in a global sense. In fact, in the 3D case there is a westerly acceleration over the main baroclinic zone at all levels (see for example the bottom right panel of figure 4-13), due to the convergence of the eddy momentum flux. This is the reason why the steering level always drops, and it drops more than in the equivalent barotropic case with the same value of $L/l$.

Note that the results presented here share strong similarities with the more realistic adiabatic simulations of Simmons and Hoskins (1978), as described by James (1987). Like in their computations, the equilibration is characterized by the development of a strong barotropic jet, that appears to inhibit further growth despite the subsistence of PV gradients of opposite sign in the final state (see also Gutowski et al. (1989)). James (1987) argued that this stabilization could be due to the effect of the horizontal wind shear on the shaping of the critical surface, what he called the barotropic governor. Essentially the same results are obtained here. However, what seems to be more important is not so much the shear of the wind, as argued by James (1987), but the localized strong westerly acceleration over the central part of the channel, which makes the steering level disappear over that region. Note that the local disappearance of the steering level is also linked to the elimination of the negative PV gradients over those latitudes. [But regions of negative PV gradients associated to non-zero temperature gradients still persist at the surface on the margins of the jet as in Simmons and Hoskins (1978); see figure 4-17].

### 4.2.2 The role of surface friction

In the runs described above the model predicts too strong surface winds compared to observations, or even fails to equilibrate by the last day shown. This is due to the unbalanced momentum flux. As the wave develops finite amplitude, there is an eddy convergence of momentum at the center of the channel; without friction, this convergence is ultimately balanced (on very long time scales) by hyperdiffusion acting on the meridional curvature of the zonal mean wind. However, because hyperdiffusion is weak, this balance is only achieved after the jet has undergone a strong barotropic acceleration and developed a large curvature. Except for the shortwave case ($H/h = 0.54$, figure 4-13), which has weaker momentum fluxes, this acceleration is strong enough that the steering level disappears and the surface temperature gradient is eliminated. In fact, in less-diffusive runs (not shown) the westerly acceleration by the momentum flux is also unbalanced in this case, and the evolu-

tion resembles that shown in figure 4-17. This is of course very different from the observed momentum balance in the troposphere, in which surface friction plays a role in constraining the surface wind. We next examine how our results are affected by the inclusion of surface friction in the model.

Figure 4-18 shows the equilibrated state for the shortwave case $H/h = 0.54$, but now also including Rayleigh friction with a time scale of 5 days at the lowest resolved level. In the presence of surface friction, the eddy momentum fluxes can be balanced and the model reaches an equilibrium on much shorter time scales. As can be seen, the homogenization of the equilibrated state is more localized than in the inviscid case, although PV is still fairly well mixed below the steering level. The equilibrium state is very similar to the snapshot shown in figure 4-14 and the surface wind does not rise beyond 5 $m/s$. It is interesting to note that the phase speed remains nearly constant during the equilibration, as both the temperature mixing and buildup of the zonal wind are weaker than in the previous case (see figure 4-19). Based on our previous discussion, the robustness of the phase speed results from the reduced westerly acceleration at the center of the channel (but note that the global momentum is no longer conserved when there is friction only at one level). Most importantly, because of this reduced acceleration the steering level drops much less, consistent with the observed localization of the homogenized region. The key role of surface friction in containing the steering level is a robust result for other cases examined. This is illustrated in figure 4-20, which shows that even for the longer, more unstable waves ($\beta = 3.0 \times 10^{-11}\ m^{-1}s^{-1}$, $H/h = 1.61$), the equilibration of the zonal flow can occur without full homogenization, provided that surface friction is strong enough (1 day in this case).

These results are consistent with previous studies. For instance, Simmons and Hoskins (1978) already note that in the presence of friction, the baroclinic waves are not so efficient in eliminating the surface temperature gradient as in the inviscid case. The effect of the surface fluxes on the mean flow adjustment by an equilibrating baroclinic wave has been studied in detail by Gutowski et al. (1989), using a primitive equation model. These authors found that without surface friction, the mean flow adjustment is characterized by the development of a strong barotropic jet and the elimination of the surface temperature gradient, consistent with the results of Simmons and Hoskins (1978). However, in the presence of friction the barotropic acceleration of the jet is much more limited, and there is a remnant vertical shear at the surface at equilibration, in agreement with our results. The fact that friction

prevents the elimination of the surface temperature gradient is not a coincidence. It will be shown in section 4.2.5 that in the presence of friction, there must be a negative PV gradient over those latitudes with westerly surface wind.

All these examples point to the important role of surface friction for limiting the homogenization of the surface temperature gradient. However, while it is obvious that friction should prevent the development of a strong barotropic jet, it is not so clear a priori why this has such an impact on the mixing of surface temperature. Unlike with thermal damping (Swanson and Pierrehumbert, 1997), there is no obvious physical mechanism linking surface friction and temperature mixing (other of course than indirectly, through its impact on the growth rate, kinematic mixing efficiency, etc.). The results presented above suggest a possible mechanism, which is quite subtle. In simple words, by preventing the strong westerly acceleration of the jet, surface friction prevents the drop of the steering level, thus constraining the expansion of the well-homogenized region. However, we should be cautious about this interpretation. Though the disappearance of the steering level and the local elimination of the negative PV gradients are obviously linked, as well as dynamically self-consistent, it is somewhat misleading to talk about cause and effect in this context. More properly speaking, they are both just a result of the three-dimensional redistribution of zonal momentum by the baroclinic eddies. The relation between momentum and the surface temperature gradient will be made clear in chapter 5, in which we derive a momentum-based formulation of the baroclinic dynamics. This will help clarify the role of surface friction.

In summary, much like in the barotropic problem, the equilibration can be described in terms of the time evolution of the critical surface. Provided that there is some surface friction, the phase speed still remains fairly robust, so that the evolution of the critical surface is essentially associated to the redistribution of momentum. However, the geometry is much more complicated now. While in the barotropic case the steering level can only move up and down in one direction, in the 3D case there is also a net acceleration of the column at the expense of lateral easterly acceleration, which pushes the steering level to the sides and away from the baroclinic zone. As this happens, the negative PV gradient is eliminated over the primary baroclinic zone. The simple generalization of the one-dimensional mixing length arguments given in section 4.1.2 is not really appropriate, and the full three-dimensional structure has to be considered. This will be done in the section 4.2.4. Before, we look in

more detail at the characteristics of the equilibrated flow.

### 4.2.3 Mean circulation and fluxes

In this section we briefly discuss the structure of the equilibrated state for some of the runs presented. Since we are looking at simple Boussinesq-Charney waves, we do not expect the equilibrated state to closely resemble the observed troposphere, and will not perform a detailed comparison. However, it is still important to understand what aspects of the model circulation differ qualitatively from observations, and for what reasons.

#### PV structure

The PV structure of the equilibrated state has already been described extensively in figures 4-13 to 4-20. This structure is very similar for all cases, and also shares important similarities with the mean tropospheric state described in section 2.3. Generally speaking, the PV gradients are reduced over the mixing domain, though strict homogenization only occurs locally at the steering level. For large enough $H/h$, the negative PV gradients are eliminated over the central part of the channel in the inviscid runs, but not when there is surface friction.

In all cases examined the homogenization of potential vorticity in the interior is accompanied by the buildup of large PV gradients at the edges of the mixing domain. In the vertical, there is a concentration of the PV gradient at heights of order $0.5H = 9\ km$, roughly consistent with observed tropopause heights. This is not altogether surprising because the static stability is also close to the observed one; our results just prove the relevance of the 'dynamical constraint' for the tropopause height proposed by Held (1982). It is also interesting to note that these large PV gradients are a result of small changes in the vertical curvature of the wind, unlike the real tropopause, for which the changes in static stability are thought to be more important (note that the static stability is fixed in our model). This highlights the relevance of the underlying PV dynamics.

In the horizontal, there is also a concentration of the PV gradients at the margins of the jet. Such concentration seems unrealistic for the real atmosphere but our model does not incorporate any tropical dynamics. Moreover, in the atmosphere the adiabatic mixing of potential vorticity is not horizontal but along isentropic surfaces (Pierrehumbert and Yang, 1993), and the mean isentropic slope is such that all the extratropical isentropes intersect either the ground or the tropopause. Thus, in isentropic coordinates the moving Earth

surface represents an additional barrier to PV mixing.

Another characteristic feature of the observed PV distribution that our model fails to reproduce is the large positive PV gradients over the atmospheric boundary layer. The most likely reasons for this deficiency in our model are the fixed static stability and the lack of vertical mixing. In the real troposphere, the strong vertical homogenization of temperature over the boundary layer tends to produce steep isentropic slopes, and large meridional PV gradients.

### Maintenance of the equilibrated state

We next discuss the maintenance of the equilibrated state. The equations describing the evolution of the basic state in our model are:

$$\frac{\partial \overline{U}}{\partial t} + \frac{\partial}{\partial y}\overline{u'v'} - f_0 \overline{v}_a = -\alpha_M \overline{U} \quad \left(-\nu \partial_y^4 \, \overline{U}\right) \tag{4.12}$$

$$\frac{\partial \overline{\theta}}{\partial t} + \frac{\partial}{\partial y}\overline{v'\theta'} + \overline{w}_a \Theta_z = -\alpha_T(\overline{\theta} - \overline{\theta}_R) \tag{4.13}$$

$$\frac{\partial \overline{v}_a}{\partial y} + \frac{\partial \overline{w}_a}{\partial z} = 0 \tag{4.14}$$

$$\frac{\partial \overline{U}}{\partial z} = -\frac{g}{f_0 \Theta_0}\frac{\partial \overline{\theta}}{\partial y} \tag{4.15}$$

where $\alpha_M$, $\alpha_T$ are the linear damping coefficients for Rayleigh friction and Newtonian cooling, respectively, and $\theta_R$ is the radiative equilibrium profile to which temperature is relaxed. For the runs presented, $\alpha_T$ is constant, while $\alpha_M$ is non-zero only at the lowest resolved level (when there is friction). Because the hyperdiffusion term is typically negligible, it was written within brackets in the momentum equation 4.12.

We illustrate our discussion with the results for the run with $\beta = 3.0 \times 10^{-11}\ m^{-1}s^{-1}$ ($H/h = 1.6$) and surface damping 1 day (the results for other cases are qualitatively similar). The main results are shown in figure 4-21. Panels A and B show the zonal mean wind (solid) and potential temperature (dashed) for the radiative equilibrium profile and equilibrated flow, respectively. We can see that the isentropic slope and meridional temperature gradient are reduced for the equilibrated flow, particularly over the main baroclinic zone. On the other hand, the vertical shear of the zonal mean wind decreases, and the horizontal curvature increases as the jet narrows. There is a barotropic westerly acceleration of the jet, with

compensating surface easterlies appearing on the sides. The structure of the mean flow and the sign of the eddy tendencies are in rough agreement with the the observed extratropical circulation (Peixoto and Oort, 1992).

It is interesting to look at this problem in terms of the redistribution of momentum, so as to compare with the equilibration of the barotropic point jet. In this framework, the primary effect of the eddies is a reduction in the vertical wind shear, which is analogous to the barotropic case. However, the dynamical mechanism is very different because there is no (advective) vertical momentum flux in equation 4.12. In qg theory, the vertical momentum flux arises from the Coriolis force acting on the mean meridional circulation (MMC). For an indirect circulation (panel E), the Coriolis force induces a westerly (easterly) zonal wind tendency over its lower (upper) branch, which results in an upward flux of easterly momentum. In the quasigeostrophic framework, the MMC arises in response to the reduction of the meridional temperature gradient by the eddy heat flux (panel C), to keep thermal wind balance (equation 4.15). However, both the eddy heat flux and MMC should more appropriately be regarded as part of the same (non-geostrophic) mean Lagrangian circulation (Andrews and McIntyre, 1978).

The MMC only redistributes momentum vertically, while the horizontal redistribution of momentum is due to the eddy momentum flux. The eddy momentum flux is such that there is a convergence of westerly momentum at all levels at the center of the channel (panel D). This momentum convergence is responsible for the enhanced meridional curvature of the equilibrated flow described above. Because the eddy momentum flux has some vertical structure, it also forces the thermal wind, and an additional component of the meridional circulation must appear to transport heat and maintain the temperature field in thermal wind balance. For instance, in our runs the eddy momentum flux decreases with height and thus tends to weaken the vertical shear. In order to keep thermal wind balance, a thermally direct circulation must appear that reduces the temperature gradient accordingly, and its contribution should weaken the indirect MMC described above. However, as noted by other authors (Chang, 1996), the identification of what fraction of the MMC is forced by what term, either diabatic or dynamical, is ambiguous because the forcing terms themselves are not independent and affect each other through the modifications that they induce in the basic state (see also Kim and Lee (2001)).

The relative role of the eddy heat and momentum fluxes in forcing the zonal mean flow

can be appreciated in the EP diagram shown in panel F. The fact that the vectors are almost vertical and the dominant term in the Eliassen-Palm convergence is $\partial F_z/\partial z$ suggests that momentum is primarily redistributed vertically through the mechanism described above. This is in basic agreement with observations (Edmon et al., 1980). However, an important difference is that in our model the horizontal component of the EP flux is largest at the surface, whereas in the real troposphere the eddy momentum flux peaks strongly at upper levels (Peixoto and Oort, 1992). This qualitative difference is probably related to a well known deficiency of the Charney modes, which are too bottom-trapped compared to observations; the same problem is in fact found in most other measures of wave activity. For instance, the eddy enstrophy has a maximum at tropopause levels (not shown), but this maximum is still much smaller than at the surface. Though the equilibration of the model spontaneously generates large PV gradients at the upper edge of the mixing domain, the real tropopause is probably also forced diabatically, and plays a bigger role in the dynamics than our model would suggest.

Despite this important deficiency, we feel that our model is still useful in providing simple dynamical mechanisms that could also be at work in more complicated models, as well as in the real troposphere. Furthermore, because of the dominant role of the eddy heat flux in forcing the thermal wind, the vertical structure of the eddy momentum flux convergence should only have a small impact on the net rate of upward momentum transport. In fact, we believe that what is most important for the equilibration of the model is the vertically integrated momentum flux, rather than its specific vertical structure. It is this vertical integral that constrains the net westerly acceleration of the column, and with it the narrowing of the jet and the drop of the steering level. The question however remains of how sensitive these mean fluxes are to the unrealistic vertical structure of the modes predicted by our model.

### Linear stability of the equilibrated state

An interesting and often controversial question in equilibration studies is whether the final equilibrium state is supercritical. To answer this question in the context of our model, we have performed a linear stability analysis. The methodology followed was to evolve a linearized version of the model, with basic state the equilibrated flow of the nonlinear run.

In all cases we found that the final state was neutral, or quite nearly so. Because the

length of the integrations is ultimately limited by the available computational resources, this should be taken with caution, as it is often difficult to differentiate very small growth rates (both positive and negative) from zero. Hence, it is possible that the final state could still be weakly unstable to secondary development.

Note that this linear stability analysis is based on a linearized version of the model which already includes the linear forcing terms (i.e, Newtonian cooling and Rayleigh damping). Given that these terms typically produce a negative tendency in *eddy* enstrophy (see sections 4.1.3 and 4.2.5 below), we expect the basic state to be unstable when they are omitted. As described in section 4.1.3 for the 2D case, the local balance of eddy enstrophy reflects an equilibrium between eddy enstrophy generation at the expense of the mean flow (i.e., the downgradient PV fluxes) and in-situ diabatic dissipation, with the nonlinear advection term introducing a small correction. This is consistent with the fact that the final state is neutral (unstable) when the damping terms are included (omitted).

The fact that our model equilibrates in this manner is not really surprising because the setup of the runs favors a quasilinear type of equilibration, in which the primary wave modifying the basic state is the longest wave fitting into the channel. As a result, wave saturation is essentially equivalent to linear stability. This is consistent with the results of Cehelsky and Tung (1991) for the two-layer model. These authors found that their model equilibrated differently depending on which wave was the dominant transporter, but was always nearly neutral for that wave. With strong enough forcing, the most unstable wave saturates in favor of a longer wave, yielding a final state which is supercritical for the shorter mode. However, this only happens when the channel is long enough: wavenumber one cannot saturate and is always neutralized. Note that in our runs there is no distinction between the most unstable mode and the dominant heat transporter because the longest wave fitting into the channel is also the most unstable one.

Finally, we emphasize that the linear stability of the final state occurs in most cases in the presence of PV gradients of opposite sign, which is in violation of the Charney-Stern condition for instability. In fact, we proved in section 4.1.3 for the 2D problem that in the forced-dissipative case the equilibrium PV gradient *must* change sign (a similar derivation will be given in section 4.2.5 for the 3D problem). When a external constraint exists on the mixing length, the equilibrium PV gradient also changes sign in the fully inviscid case.

### 4.2.4 The mixing depth constraint

It was argued in section 2.4 that when the depth of the mixing domain is limited, there is a geometric constraint that prevents the elimination of the negative PV gradients. The argument goes as follows (also refer to figure 2-5). In order to eliminate the surface shear while still meeting some unperturbed shear $\Lambda$ at the mixing depth $H_0$, the zonal mean flow must develop some curvature. However, there is a limit to how much curvature the flow can develop, a limit that depends on $\beta$. The reason is that when the curvature is too large compared to $\beta$, the flow develops negative PV gradients in the interior. This constraint on the curvature translates in turn to a constraint on how much reduction in shear can be achieved over a given mixing depth $H_0$. In simple words, when the mixing domain is not deep enough, the wave 'lacks the room' to eliminate the surface shear.

This argument was found to work in the barotropic case, as discussed in section 4.1.2. It was shown in that section that modes shorter than the most unstable one lack enough depth to eliminate the negative PV gradient, and must equilibrate by smoothing out the PV gradient at the steering level. However, it is clear from the results of the previous section that the simple argument no longer works in the full 3D case. The problem with this argument is that it is one-dimensional. The elimination of the westerly shear at the ground requires the export of easterly momentum out of the surface. In the barotropic problem this momentum is deposited in the interior, but in the 3D case most of the easterly acceleration occurs outside the column, on the margins of the jet. It is thus necessary to consider the full redistribution of momentum, and the associated changes in the PV structure.

Consider the top right panel of figure 4-22. This figure shows the contributions to the zonal mean PV gradient resulting from the vertical curvature of the zonal wind (top), the horizontal curvature (middle), and the total PV gradient, also including $\beta$ (bottom), for the run with $H/h = 0.86$ and damping time scale 3 days. For the simple basic state considered, the radiative equilibrium PV gradient resulting from the vertical curvature term (shown dashed) is zero in the interior and a negative delta function at the surface. This negative delta function reflects the transition from the constant interior vertical shear of the Charney problem to zero shear right underneath the surface (Bretherton, 1966). As the wave equilibrates and redistributes momentum vertically, the negative PV jump across the surface delta function is reduced, and part of the adjustment in shear occurs across a finite

layer with negative vertical-curvature PV gradient. In order to prevent negative interior PV gradients, the one-dimensional mixing depth constraint would demand that this negative contribution be smaller than $\beta$. However, larger values, order $O(2\beta)$ are observed. This is possible because the horizontal curvature term, which is positive, increases, thus allowing larger vertical curvatures and further adjustments in shear while still keeping a non-negative interior PV gradient. Both the acceleration of the mean flow $\overline{U}$ and the reduction in the meridional scale of the jet $L$ contribute to this increase in the horizontal curvature term $\overline{U}_{yy}$ (not shown). The pronounced enhancement of the horizontal curvature PV gradient found here has also been noted in other modeling studies (e.g., Gutowski et al. (1989)).

This effect is even more prominent when surface friction is reduced or eliminated. For instance, figure 4-23 shows the same results but now with a slower damping time scale of $\tau = 10$ *days*. This weaker damping allows a more intense barotropic development, and a significant enhancement in the horizontal curvature of the jet. For the particular case shown here, this horizontal curvature allows the development of a vertical curvature large enough to yield the required adjustment in shear over the prescribed mixing depth. This is also shown in figure 4-24, which compares the zonal mean flow at equilibrium for the initial profile and the weak and strong damping cases[5]. It is illustrative to compare this figure with the sketch of figure 2-5.

From a momentum viewpoint, the eddy momentum fluxes allow a more efficient vertical transport of (easterly) momentum out of the surface baroclinic zone than in the equivalent 2D problem. Admittedly, this is partly due to the vertical structure of the momentum fluxes, which peak at the surface and thus tend to reduce the vertical shear. As commented above, this is an unrealistic feature of the Charney problem compared to observations, and this mechanism could never be at work in the real atmosphere. However, this is *not* the mechanism that we are emphasizing here. Even when the momentum fluxes increase with height, so that their direct effect would seem to be the strengthening of the vertical shear, the net westerly acceleration of the column can favor an overall reduction in shear through an enhanced vertical transport of momentum by the mean meridional circulation. The reasons for this are subtle, and will be best understood using the formulation of chapter 5.

The proper way to account for these effects in the 3D problem is to generalize the mixing

[5]Note that a barotropic component, different for each case, has been subtracted from the flow to make the profiles agree above the mixing depth.

depth constraint by also integrating in $y$. If we concentrate for simplicity on the Boussinesq limit, we can express the meridional PV gradient as:

$$\overline{q}_y = \beta - \tilde{\nabla}^2 \overline{U} = \beta - \frac{\partial^2 \overline{U}}{\partial y^2} - \frac{\partial^2 \overline{U}}{\partial \tilde{z}^2}, \tag{4.16}$$

where $\tilde{z} = z/\epsilon$ is the stretched vertical coordinate. Hence, integrating over the $y$-$\tilde{z}$ domain and applying the divergence theorem:

$$\frac{1}{\Delta y} \int \int_A \overline{q}_y = \beta H_0 - \frac{1}{\Delta y} \int_{\partial A} \tilde{\nabla} \overline{U} \cdot \hat{n} ds = \beta H_0 - \Lambda_m, \tag{4.17}$$

where $\Lambda_m$ is the vertical shear of the zonal wind at the height $H_0$, averaged in $y$ over the mixing domain $\Delta y$. Note that we assumed above no meridional shear $\frac{\partial \overline{U}}{\partial y} = 0$ at the lateral edges of the mixing domain, and formally included the negative PV gradient delta function at the surface in the integral by taking $\frac{\partial \overline{U}}{\partial \tilde{z}} = 0$ at $\tilde{z} = 0$.

As in the 2D case, the eddies can only redistribute the zonal mean potential vorticity but cannot change the net integrated PV gradient over the mixing domain. In particular, when $\beta$ and/or $H_0$ are too small for the given shear, the net integrated PV gradient must be negative. However, in the 3D case this does not preclude $\overline{q}_y$ from becoming everywhere positive at some latitudes, provided that the negative PV gradients are enhanced elsewhere. This is what was observed in the inviscid runs, and this is also what Simmons and Hoskins (1978) found. In their simulations, the surface temperature gradient was eliminated over the primary baroclinic zone, but regions of enhanced gradients appeared to the sides.

We argued in chapter 3 that because of the meridional confinement by the jet, tropospheric waves are short Charney modes. The implicit assumption is that the equilibration of the waves tends to narrow the jet (i.e. to reduce $H$), which should prevent longer modes from emerging. The results presented in this chapter do confirm this expectation, as one of the main effects of the eddy momentum flux is the self-focusing of the jet, in agreement with previous studies (Ioannou and Lindzen, 1986). However, a more careful analysis reveals that the *dimensionless* scale of the waves $H/h$ increases rather than decreases during the equilibration. The reason is that when the jet narrows, the Held scale $h$ also decreases because the positive PV gradient in the interior is reinforced by the enhanced curvature. This is in fact what ultimately allows modes that were initially short to get rid of the surface shear, by concentrating the positive PV gradient from the sides, as figures 4-22- 4-24

strikingly demonstrate.

Note that the proposed mechanism relies on the fact that the horizontal and vertical curvature of the zonal wind are of the same order, as is evident from inspection of figures 4-22 and 4-23. This was in fact anticipated by the scaling analysis of section 2.3.1, based on the premise that the width of the jet can be linked to the meridional scale of the eddies and thus scales as the Rossby radius. The data analysis of figure 2-4 suggests that this is also the case in the extratropical troposphere, in which the baroclinic and barotropic PV gradients appear to be comparable despite the frequent claim to the contrary (Fullmer (1982), Stone and Nemet (1996)).

In conclusion, surface friction is what ultimately constrains the scale of the modes in our runs, by preventing the self-focusing mechanism described above. Moreover, by constraining the development of the horizontal curvature, surface friction constrains the development of the vertical curvature, and thus the reduction in the surface temperature gradient. This simple argument thus explains why surface friction prevents the elimination of the surface temperature gradient, as found in previous studies, and is also consistent with our findings of section 4.2.1 that the flow keeps an interior steering level in such cases. The role of friction in preventing temperature homogenization at the surface will be demonstrated in the next section, where we show that in the presence of friction, there is always a negative PV gradient at equilibration over those latitudes with westerly surface wind.

### 4.2.5 Eddy enstrophy dissipation and the frictional forcing of momentum

We showed in section 4.1.3 for the barotropic problem that, when the PV fluxes are everywhere downgradient, the PV gradient must change sign in a forced-dissipative flow. We show below that a similar constraint in fact applies for the full 3D case.

To derive this constraint, we again require that the PV fluxes are everywhere downgradient for the time-mean flow. In the barotropic case, this is always the case when the eddy advection of eddy enstrophy is negligible. However, in the 3D case we must also demand that the diabatic dissipation of eddy enstrophy is negative definite. This is the case, for instance, when vorticity and temperature are damped linearly with the same time scale. In a more general situation however, a negative correlation between temperature and vorticity perturbations could in principle give rise to a local diabatic generation of eddy enstrophy.

If the PV fluxes are everywhere downgradient, the same argument of the 2D problem

applies: because $\overline{v'q'}$ integrates to zero, $\overline{q}_y$ must change sign over the domain. However, it is no longer possible to identify locally a positive (negative) PV gradient with a westerly (easterly) momentum forcing by the dissipative processes. The reason is that in the 3D problem $\overline{v'q'}$ is not the only dynamical forcing of momentum, but there is an additional tendency resulting from the Coriolis force acting on the Lagrangian mean circulation. To address this issue, we will define in chapter 5 a generalized momentum that is *locally* forced by the PV flux alone. In terms of the transformed Eulerian mean formulation:

$$\frac{\partial \overline{U}}{\partial t} - f_0 \overline{v}^* = \overline{v'q'} - \alpha_M \overline{U} \tag{4.18}$$

In this equation, the term $f_0\overline{v}^*$ gives the Coriolis acceleration associated to the residual circulation (an approximation to the Lagrangian circulation), and $\overline{v'q'}$ the eddy forcing of zonal momentum. The last term gives the non-conservative forcing, which we modeled as simple Rayleigh friction. We will also assume for the sake of argument that $\alpha_M$ is zero except at the surface, but the discussion presented below generalizes easily to other forms of mechanical dissipation.

In the traditional mean meridional circulation, $\overline{w}_a$ is zero at the surface. Hence, $\overline{v}_a$ integrates vertically to zero at all latitudes, which implies that the MMC only redistributes momentum vertically but applies no net torque on the column. However, the situation is different for the residual circulation because there is a non-zero $\overline{w}^*$ at the surface, associated with the non-zero surface heat flux. Nevertheless, it is still possible to define a closed circulation by modeling the heat flux at the surface as a delta function PV flux in the interior, in the usual manner (Bretherton, 1966). For the residual circulation, this would be equivalent to a delta-function return flow at the surface.

In that framework, the Coriolis forcing on the residual circulation disappears when integrating vertically, so that the residual circulation can also be thought to simply redistribute momentum vertically. Of course, this is just an artifact: from the point of view of the interior flow, the redistribution of momentum occurs at the expense of a momentum reservoir just underneath the surface, associated with the delta function.

If the PV gradient were everywhere positive at a given latitude then, by our assumption of downgradient PV fluxes, the vertically integrated PV flux at that latitude would be negative. From equation 4.18, this would imply a net, vertically-integrated easterly drag on

the column (including the artificial momentum reservoir). This dynamical forcing can only be balanced by friction when the surface wind is easterly. Hence, *in the presence of surface westerlies the time-mean PV gradient must be negative somewhere along the column*[6].

This can also be expressed mathematically as follows:

$$\int_0^\infty \overline{v'q'}dz = -\int_0^\infty \kappa(z)\overline{q}_y \, dz = -\int_0^\infty \frac{\partial}{\partial y}\left(\overline{u'v'}\right) dz = \alpha_M \delta \overline{U}_S \tag{4.19}$$

where $\kappa$ is an ad-hoc defined diffusivity, $\overline{U}_S$ is the surface wind and $\delta$ the depth of the mixed layer. Note that the vertical integral includes the surface delta-function PV flux, which is why the heat flux contribution to the PV flux vanishes and the net contribution comes from the momentum flux alone. While $\overline{v}^*$ vertically integrates to zero at every latitude, $\overline{v'q'}$ does not. Rather, there is a net positive (negative) eddy PV flux over those latitudes with westerly (easterly) surface wind. This cross-latitude eddy PV flux is entirely due to the eddy momentum flux, and must be balanced by surface friction. We can see from equation 4.19 that for positive definite $\kappa$, $\overline{q}_y$ must be negative somewhere along the column if $\overline{U}_S > 0$. This negative PV gradient is manifest in the actual atmosphere in the form of a nonzero surface temperature gradient.

The argument presented above is straightforward but subtle. In particular, it is the convergent character of the eddy momentum flux (and the associated westerly acceleration of the mean flow) that demands a nonzero temperature gradient. This may seem confusing at first, but for a balanced flow temperature and momentum are intimately related. This will be made clear in chapter 5, where we develop a momentum-based formulation of the circulation. In that formulation, the surface temperature gradient can be interpreted as a momentum source.

As demonstrated above, in the presence of surface westerlies the vertically integrated PV flux must be positive. However, this net positive flux arises through severe cancellation because in the interior the eddy PV flux is usually negative (due to the positive interior PV gradient). This negative PV flux thus exerts an easterly drag over the column of fluid, which is balanced by the Coriolis acceleration acting on the upper branch of the residual circulation. Note that the interior easterly drag must be due to the heat flux component of the PV flux, since the eddy momentum flux typically produces a westerly tendency.

[6]Of course, the reverse is also true, and surface easterlies require positive interior PV gradients, but this is not as powerful a result because this requirement is easily satisfied.

However, the eddy heat flux only redistributes momentum vertically and does not change the net momentum of the column: the easterly drag in the interior occurs at the expense of westerly drag on the aforementioned momentum reservoir. This is the reason why the net eddy forcing of the column -essentially the convergence of the eddy momentum flux- is still westerly.

On the other hand, the return flow of the residual circulation occurs as a delta function at the surface, and can be thought of as inducing an easterly tendency (via Coriolis force) over the fictitious reservoir of momentum. However, because this easterly tendency is exactly balanced by the westerly eddy forcing PV flux, no net tendency arises over that layer. Similarly, there is also a lot of cancellation in the interior because the dominant terms in the TEM momentum balance are the heat flux component of the eddy forcing $\overline{v'q'}$ and the Coriolis force acting on the residual circulation, itself dominated by the heat flux contribution, with the net forcing (the convergence of the eddy momentum flux) being much smaller than the other two. The severity of the cancellation in the transformed Eulerian mean momentum balance has also been noted by Pfeffer (1987).

## 4.3 Summary

In this chapter we have studied the equilibration of the barotropic point jet and the 3D baroclinic problem. The goal was to test the quasilinear arguments put forward in previous chapters, which suggested that short Charney waves might be able to equilibrate by localized PV mixing at the steering level. To test this idea, we have studied how a wave of predetermined scale equilibrates in both problems. The scale of the wave was constrained by the channel length and/or the meridional jet width (in the 3D problem), while its dimensionless scale (either $L/l$ or $H/h$) was changed by varying $\beta$. Since a fair amount of material has been presented in this chapter, we summarize the main findings below.

First we looked at the equilibration of the barotropic point jet, and found that the results of Schoeberl and Lindzen (1984) are not robust when the equilibration of the basic state is due to waves of different scale than the most unstable mode of the unbounded problem. For waves shorter than this mode, there is a remnant negative PV gradient at the jet vertex at equilibration, while the opposite is true for longer waves. We showed that this result can be easily explained in terms of the mixing length of the waves. In particular, the zonal

mean gradient of *relative* vorticity at equilibration was found to be very similar for all cases (which share the same mixing length but have a different $\beta$), and also similar to what one would get without any mixing just from the wavy distortion of the PV jump. Depending on the value of $L/l$, this relative vorticity gradient may be smaller, equal or larger than $\beta$, and the net integrated PV gradient positive or negative.

As predicted by linear instability theory, we found that the equilibrium PV gradient of the inviscid problem is zero at the steering level, where it changes sign. This is a very robust result, so that there is a one to one correspondence between the disappearance of the steering level and the elimination of the negative PV gradient. We also found that the phase speed of the wave remains fairly robust as it equilibrates, due to the fact that the net zonal momentum is conserved in this problem. The robustness of the phase speed implies that the displacement of the steering level is in the most part due to the redistribution of momentum. As the basic state shear is reduced, there is a transfer of (easterly) momentum from the jet vertex to the interior. For short waves, the steering level is initially in a region of easterly acceleration, so that it moves further away from the jet vertex as the wave equilibrates. However, when the waves are long enough there is a westerly acceleration at the original steering level, so that it moves inward toward the center, until it disappears.

The situation is a bit different for the forced-dissipative problem, in which case there is always a remnant negative PV gradient at equilibration (and hence an interior steering level). This was found to be the case even for waves longer than the most unstable mode and large diabatic time scales. The reason is that in the forced-dissipative problem there is a sustained eddy momentum transport from the source to the sink regions. The eddy forcing of zonal momentum is in the form of a PV flux $\overline{v'q'}$, and must integrate to zero. Because eddy enstrophy is purely dissipated by the diabatic processes, the wave-mean flow term must be downgradient everywhere (neglecting the eddy advection of eddy enstrophy). As a result, the PV gradient must also change sign, so that it is positive (negative) over regions where the dissipative forcing of momentum is westerly (easterly).

We have also studied the equilibration of the 3D baroclinic problem. The approach followed in this case was to force the basic state through Newtonian cooling. As in the barotropic point jet, we found a vertical transport of (easterly) momentum from the surface to the interior, though in this case the momentum transport relies on a mean meridional circulation. This mean meridional circulation should be regarded as part of the heat flux

response, its role being to redistribute momentum vertically so as to keep the zonal wind in thermal wind balance with the modified temperature field at all times. If there was no momentum flux, this problem would be equivalent to the barotropic point jet, with the eddy heat flux playing the role of the eddy momentum flux in the barotropic problem. However, the fact that there is also an eddy momentum flux in the 3D problem makes things more complicated. First of all, because the horizontal eddy convergence of momentum has some vertical structure it also forces the thermal wind; as a result, the mean meridional circulation can no longer be attributed to the eddy heat flux alone. Most importantly, in the presence of an eddy momentum flux the net momentum of the column is no longer conserved and there is a net westerly acceleration of the column at the expense of easterly lateral acceleration. This westerly acceleration has two important and related effects. On the one hand, it makes the steering level drop and eventually disappear (in the absence of friction), as was also the case in the barotropic point jet when the acceleration was westerly. On the other hand, the momentum convergence favors a narrower jet with enhanced horizontal curvature. This in turn allows a larger vertical curvature and further adjustment in the vertical shear, while still keeping a positive PV gradient in the interior. Hence, in the baroclinic problem the one-dimensional mixing length constraint no longer applies, and a 2D generalization should instead be considered. When the mixing depth is not large enough, there must still be remnant negative PV gradients, but these may occur at the sides of the jet and away from the initial baroclinic zone.

As in the barotropic case, in the presence of forcing there is a transfer of momentum from sources to sinks, and a non-zero time-mean PV flux. Again, this implies that the PV gradient must change sign for the equilibrated flow, provided that the diabatic generation of eddy enstrophy is negative definite and the eddy advection of enstrophy negligible. However, the eddy PV flux is no longer the only dynamical forcing in the zonal momentum equation, but there is an additional forcing associated to the residual circulation. As a result, it is not possible to identify locally a negative PV gradient with a westerly forcing of momentum by the dissipative processes, like we did in the barotropic case. Nevertheless, because the mean meridional circulation only redistributes momentum vertically, it cannot change the net momentum of the column and its contribution disappears when integrating vertically. Hence, the vertically integrated PV flux must be negative (i.e, easterly drag) over columns for which the net frictional forcing is westerly, and the reverse is also true. If the bulk of the

frictional forcing occurs over the boundary layer, this implies that there must be a negative PV gradient (typically in the form of a surface temperature gradient) over those latitudes with surface westerlies.

In the next chapter, we establish a more transparent analogy between the barotropic and baroclinic problems using a new, momentum-based formalism. By recasting the thermodynamic equation as a momentum equation, we define a generalized momentum, which also includes a 'potential' momentum contribution related to the thermal structure. When this total momentum is considered, the redistribution by the mean meridional circulation disappears, and the only dynamical forcing is the eddy PV flux. We then get a local balance between the dynamical and non-conservative momentum forcing as in the barotropic case.

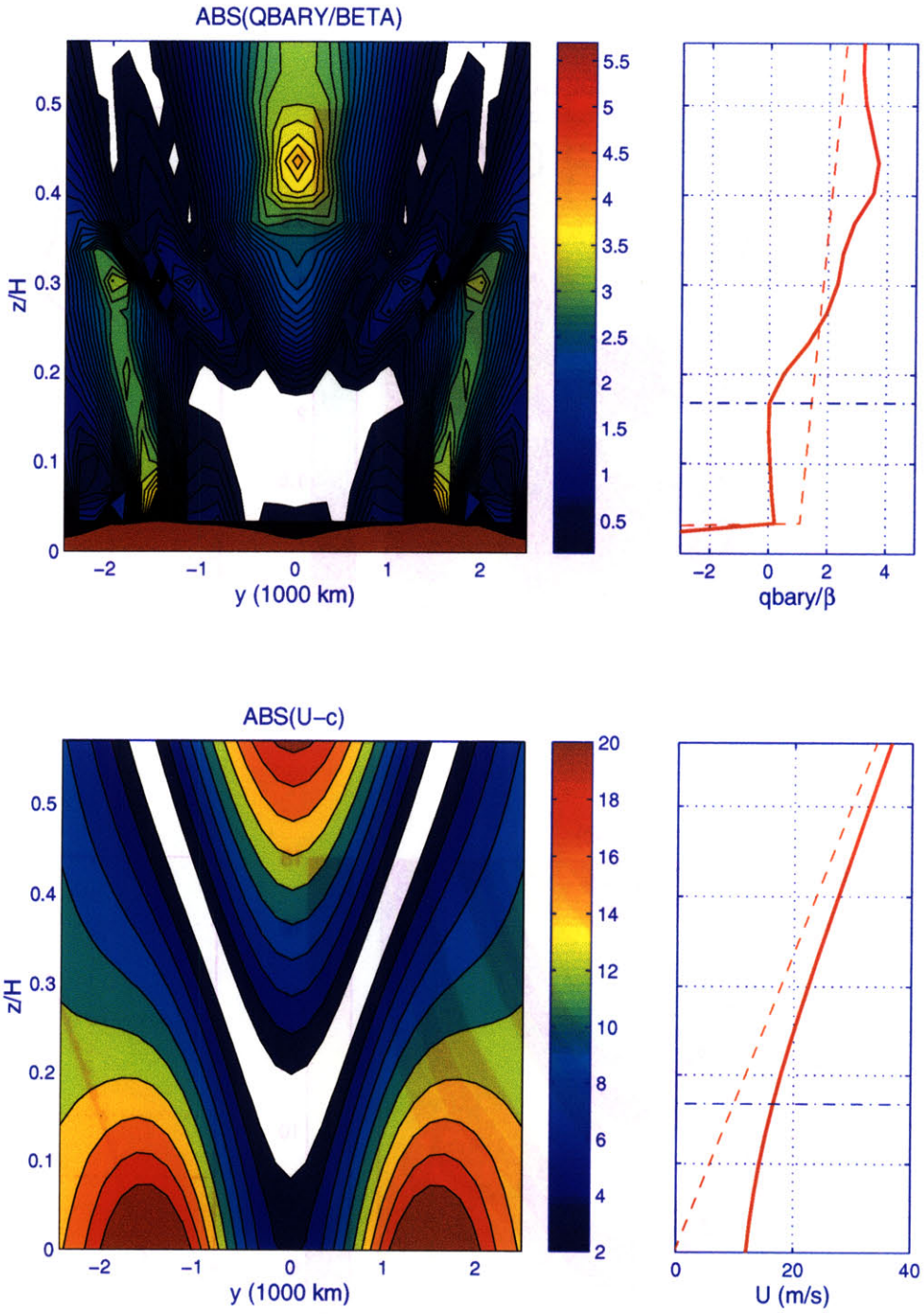


Figure 4-13: Time-mean equilibrium state for the run with $\beta = 1.0 \times 10^{-11}\ m^{-1}s^{-1}$ ($H/h = 0.54$). (Upper panel). Left: absolute value of the zonal mean potential vorticity gradient, normalized by $\beta$ (contour unit $0.15\beta$). Right: profile at the center of the channel at equilibration (solid) and radiative equilibrium (dashed). (Lower panel). Left: absolute value of $\overline{U} - c$ (contour unit $2\ m/s$). Right: zonal velocity $\overline{U}$ at the center of the channel at equilibration (solid) and radiative equilibrium (dashed). The horizontal line highlights the steering level. Regions with values of $|\bar{q}_y|$ and $|U - c|$ smaller than the corresponding contour unit are non-shaded in the contour plots. Vertical distances are nondimensionalized with the half Rossby depth $H$ and the lowest level PV gradient includes the delta function at the ground smoothed at model resolution.

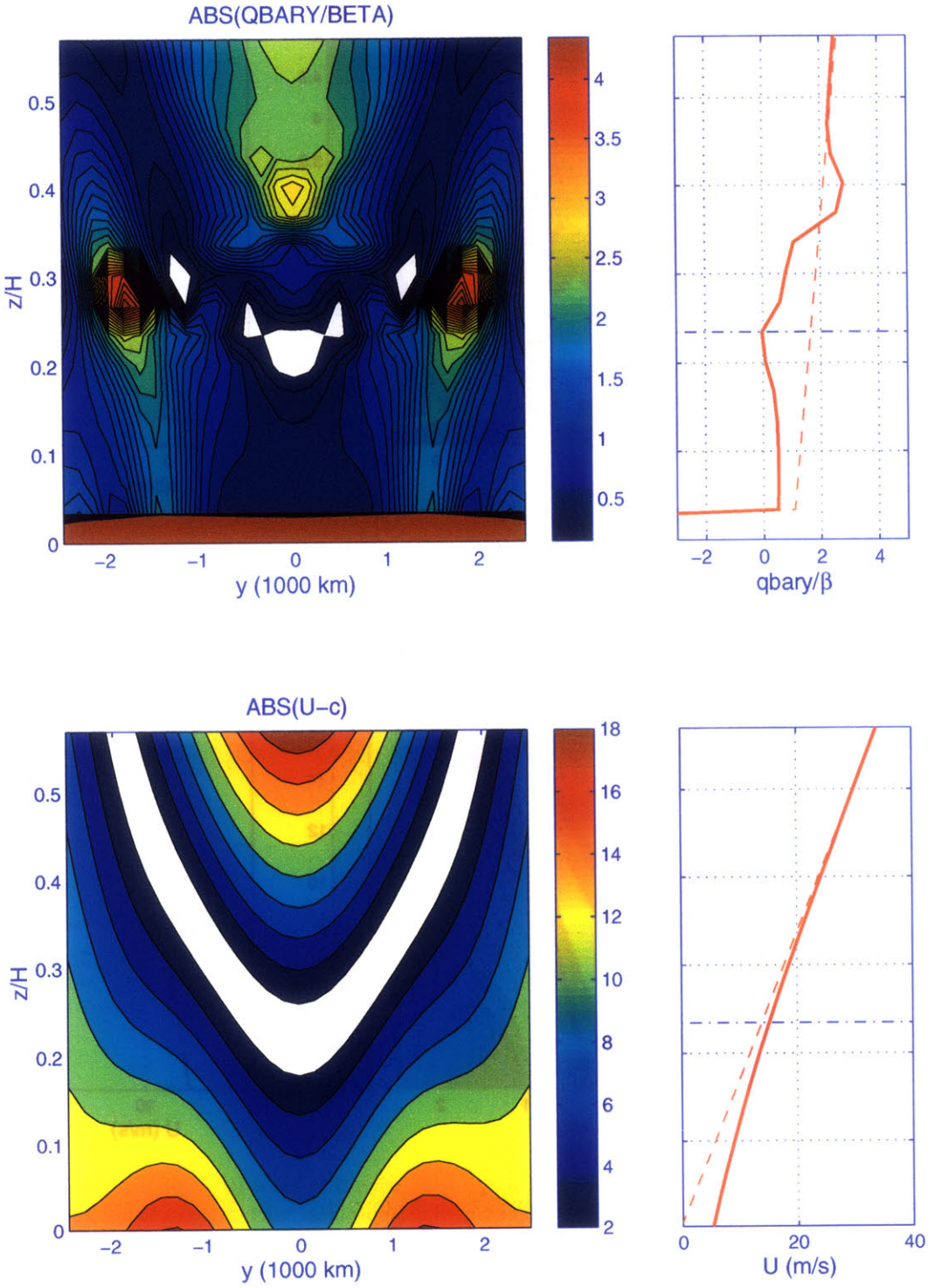


Figure 4-14: As in figure 4-13 but for a snapshot at time $t = 135$, when the wave is just starting to modify the basic state.

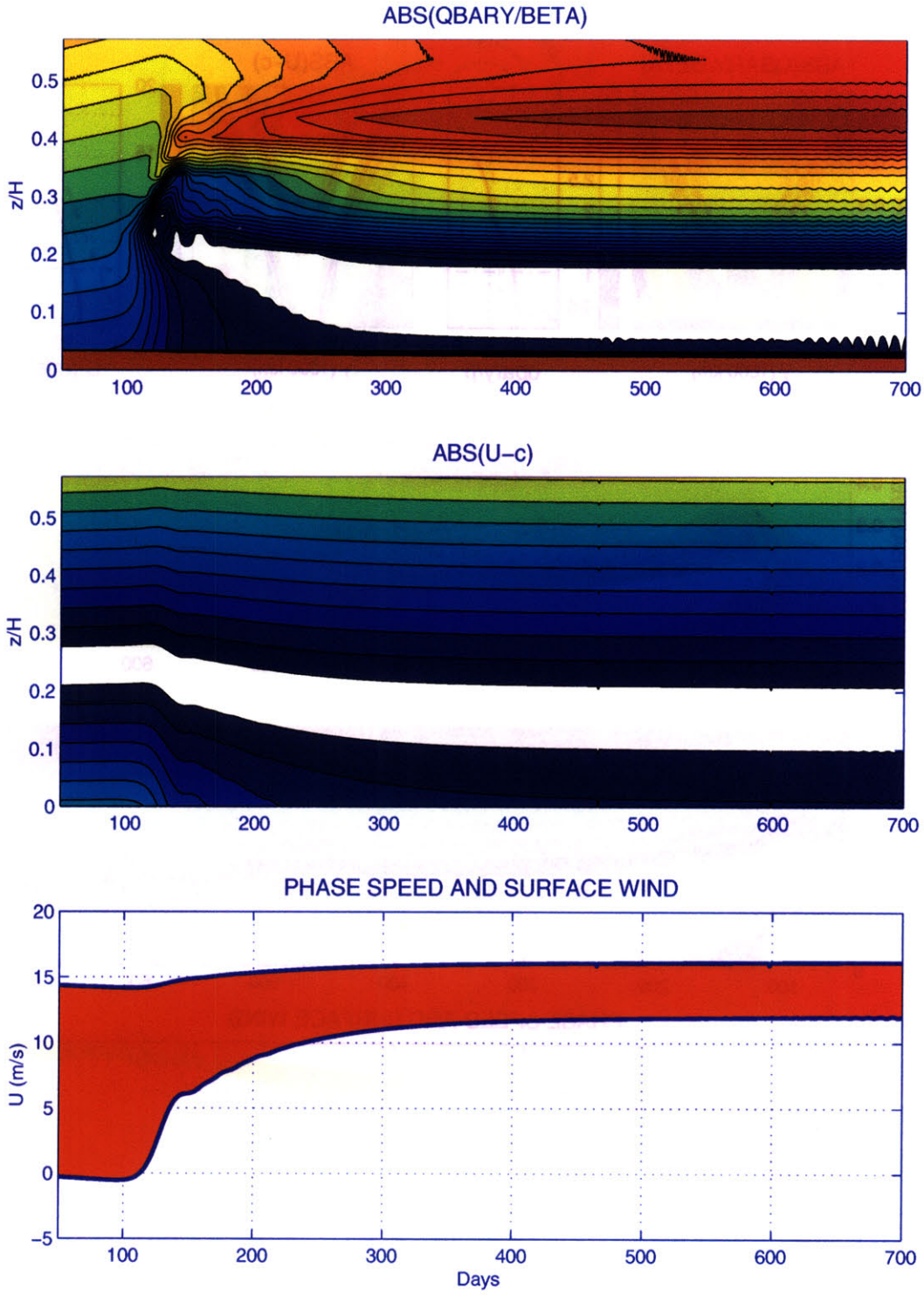


Figure 4-15: Time series at the center of the channel for the run with $\beta = 1.0 \times 10^{-11}\ m^{-1}s^{-1}$ ($H/h = 0.54$). Upper panel: $|\bar{q}_y|$ (contour unit $0.15\beta$). Medium panel: $|U - c|$ (contour unit $2\ m/s$). Lower panel: surface wind (lower curve) and phase speed of the wave (upper curve). The thickness of the shaded region is related to the height of the steering level.

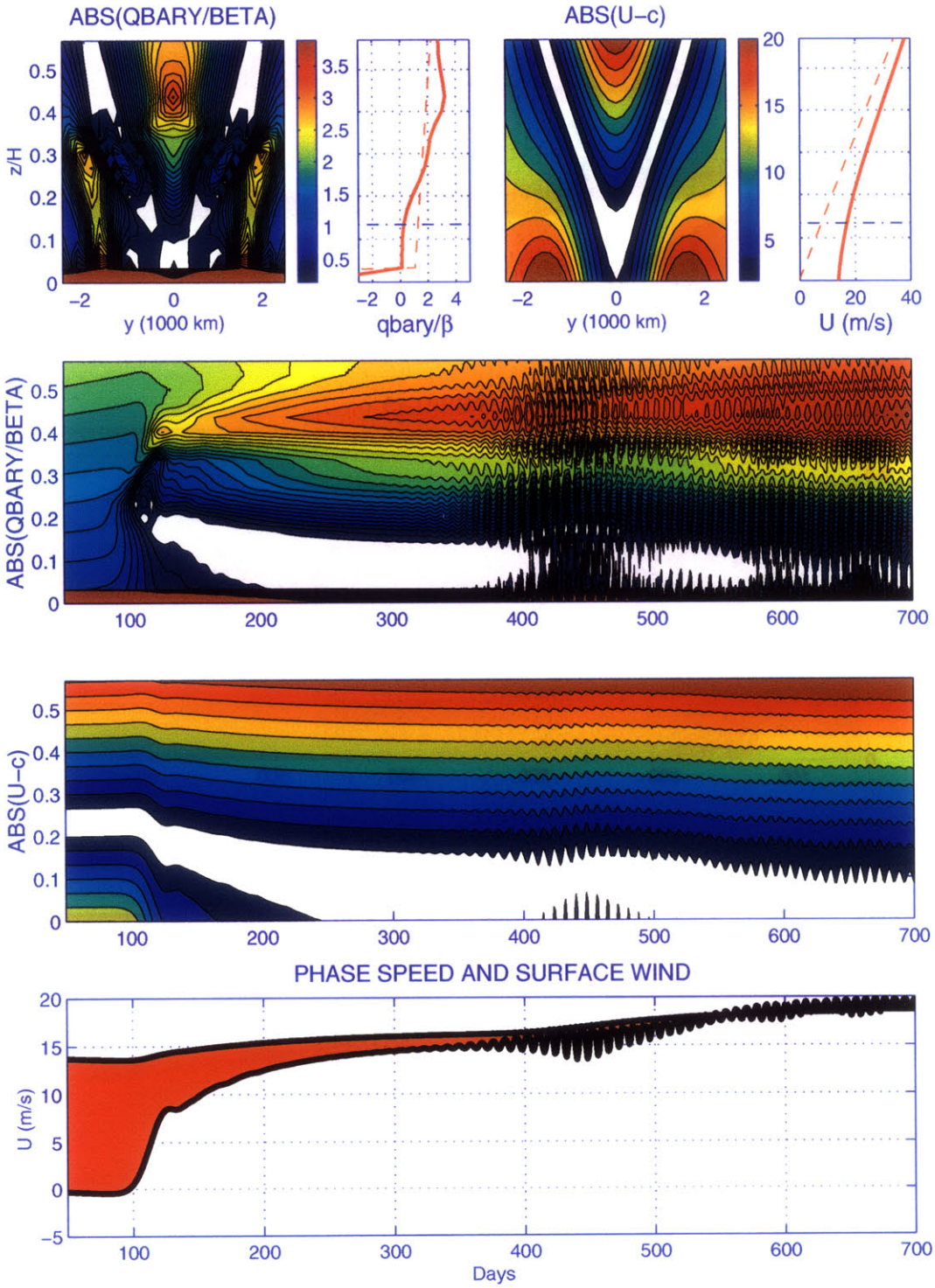


Figure 4-16: As in figures 4-13, 4-15 but for the run with $\beta = 1.3 \times 10^{-11}\ m^{-1}s^{-1}$ $(H/h = 0.7)$.

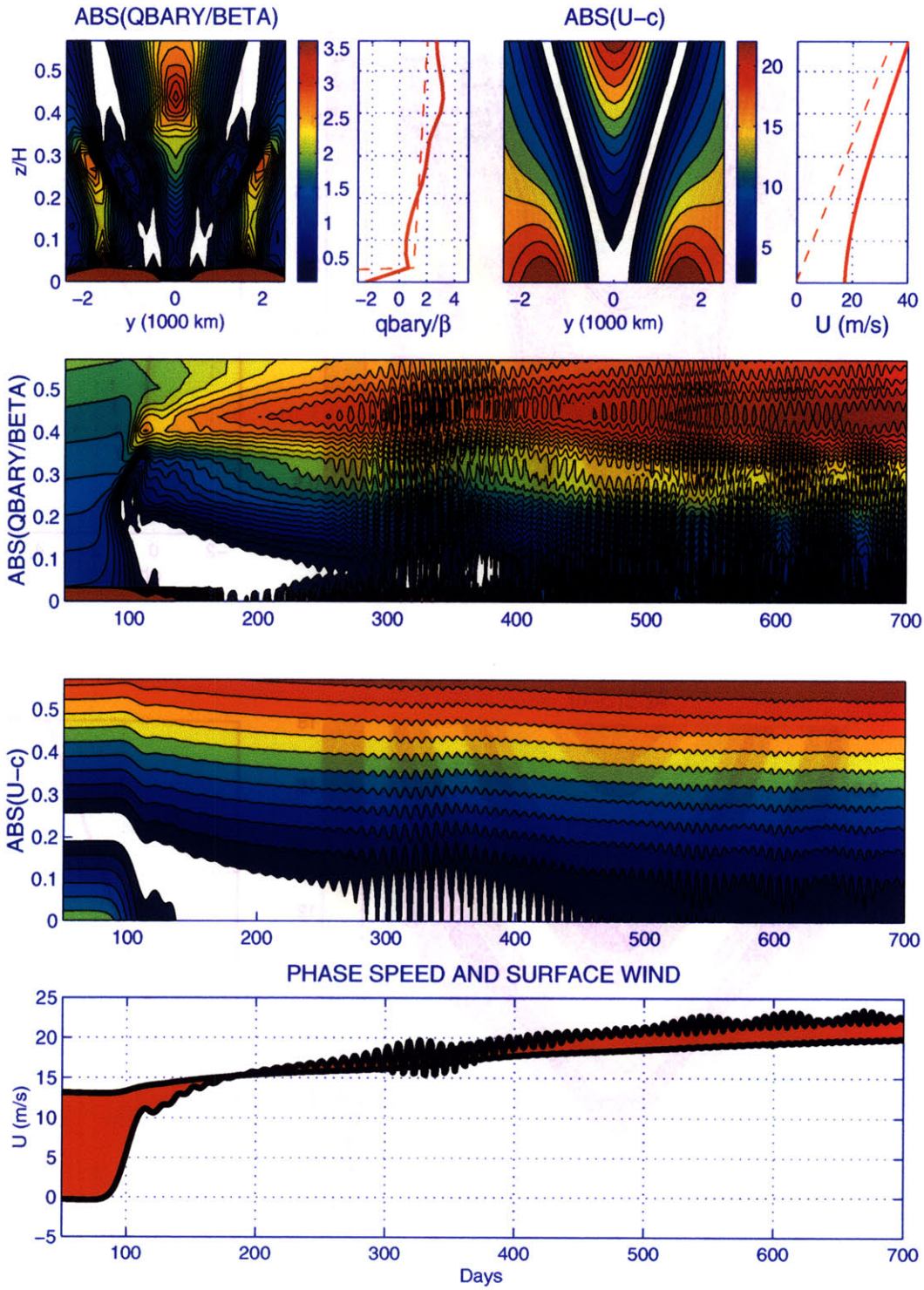


Figure 4-17: As in figures 4-13, 4-15 but for the run with $\beta = 1.6 \times 10^{-11}\ m^{-1}s^{-1}$ $(H/h = 0.86)$.

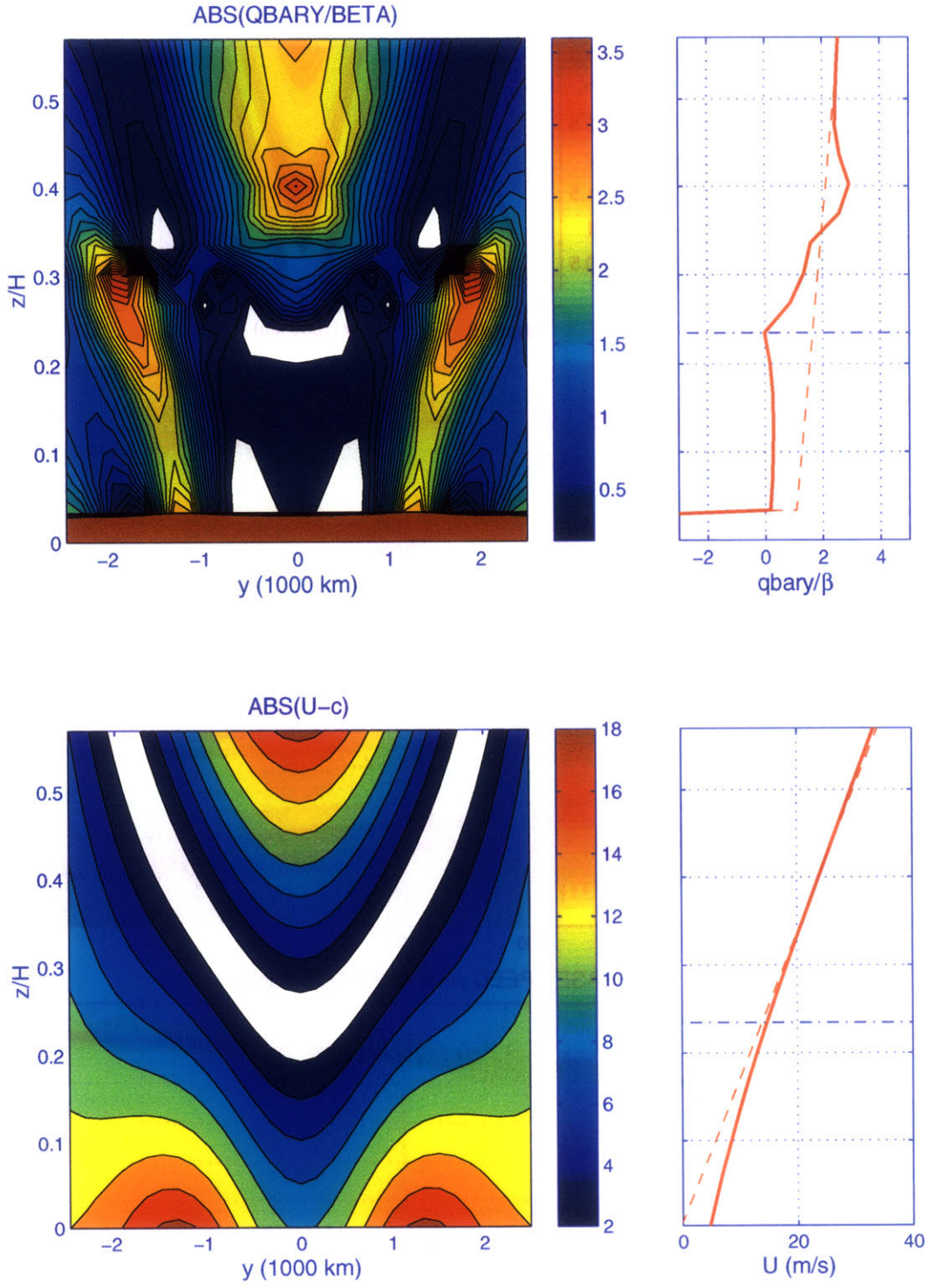


Figure 4-18: As in figure 4-13 but for the run with $\beta = 1.0 \times 10^{-11}\ m^{-1}s^{-1}$ $(H/h = 0.54)$ and surface damping time scale 5 days.

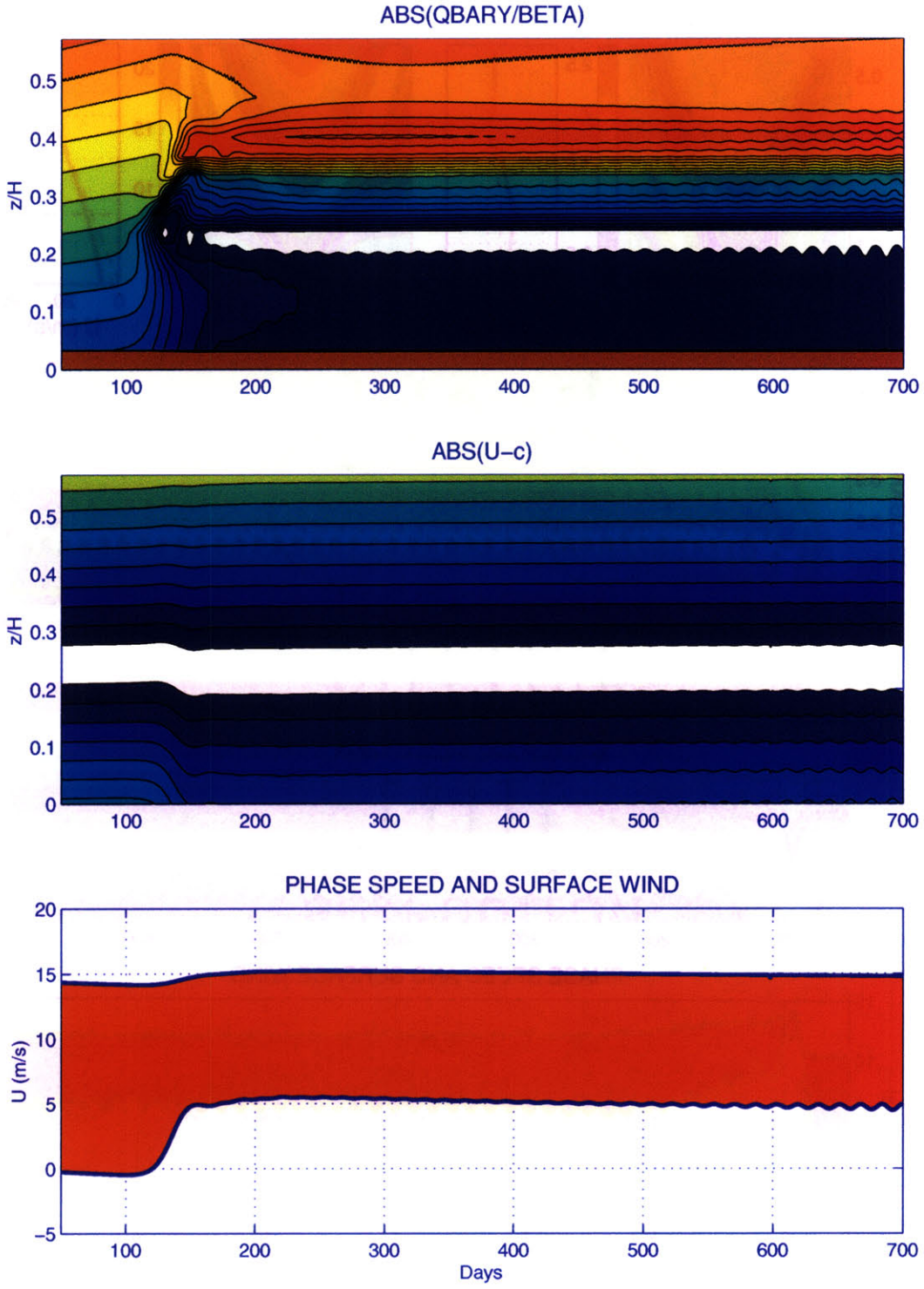


Figure 4-19: As in figure 4-15 but for the run with $\beta = 1.0 \times 10^{-11}\ m^{-1}s^{-1}$ $(H/h = 0.54)$ and surface damping time scale 5 days.

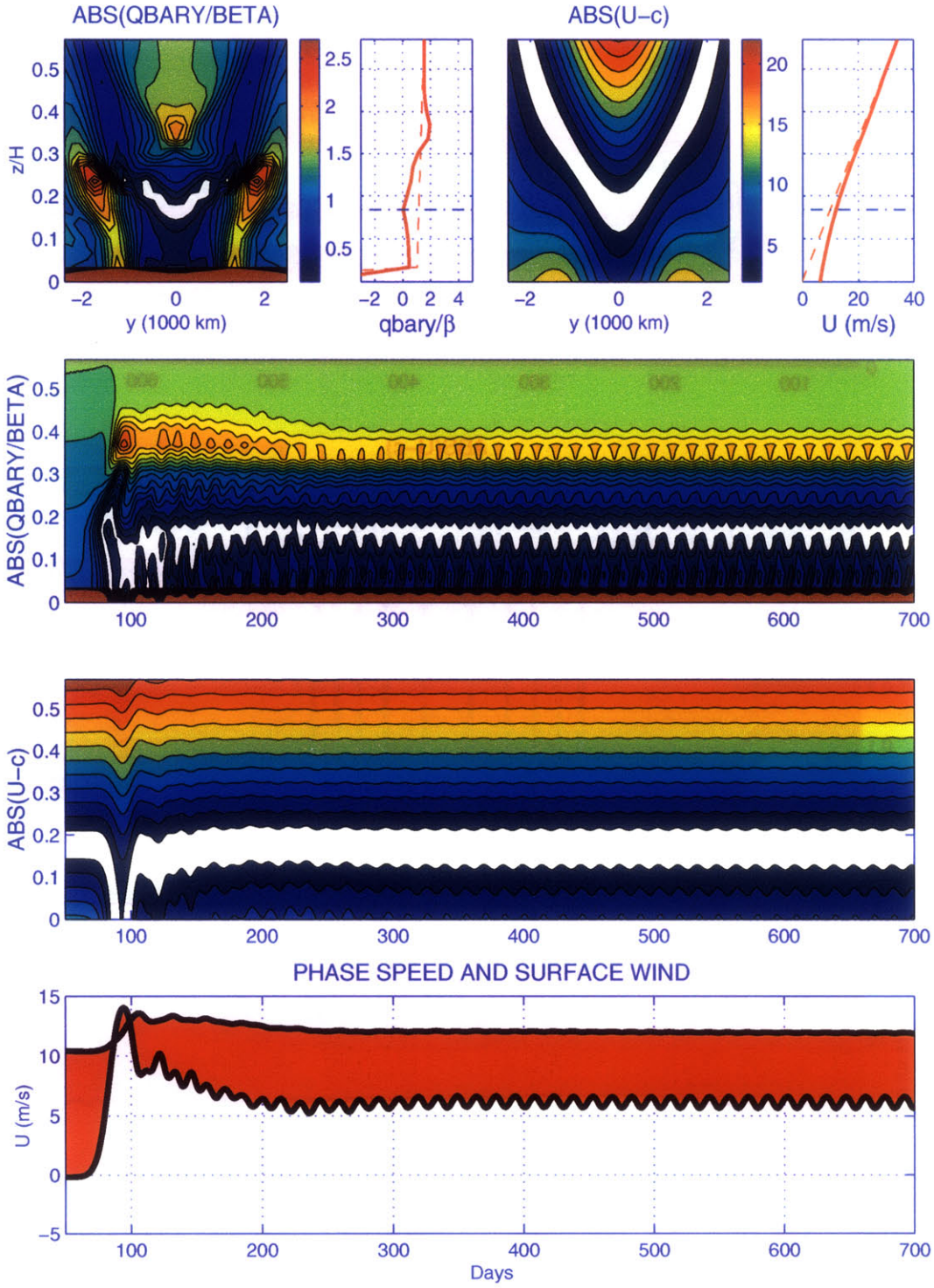


Figure 4-20: As in figures 4-13, 4-15 but for the run with $\beta = 3.0 \times 10^{-11}\ m^{-1}s^{-1}$ $(H/h = 1.6)$ and surface damping time scale 1 day.

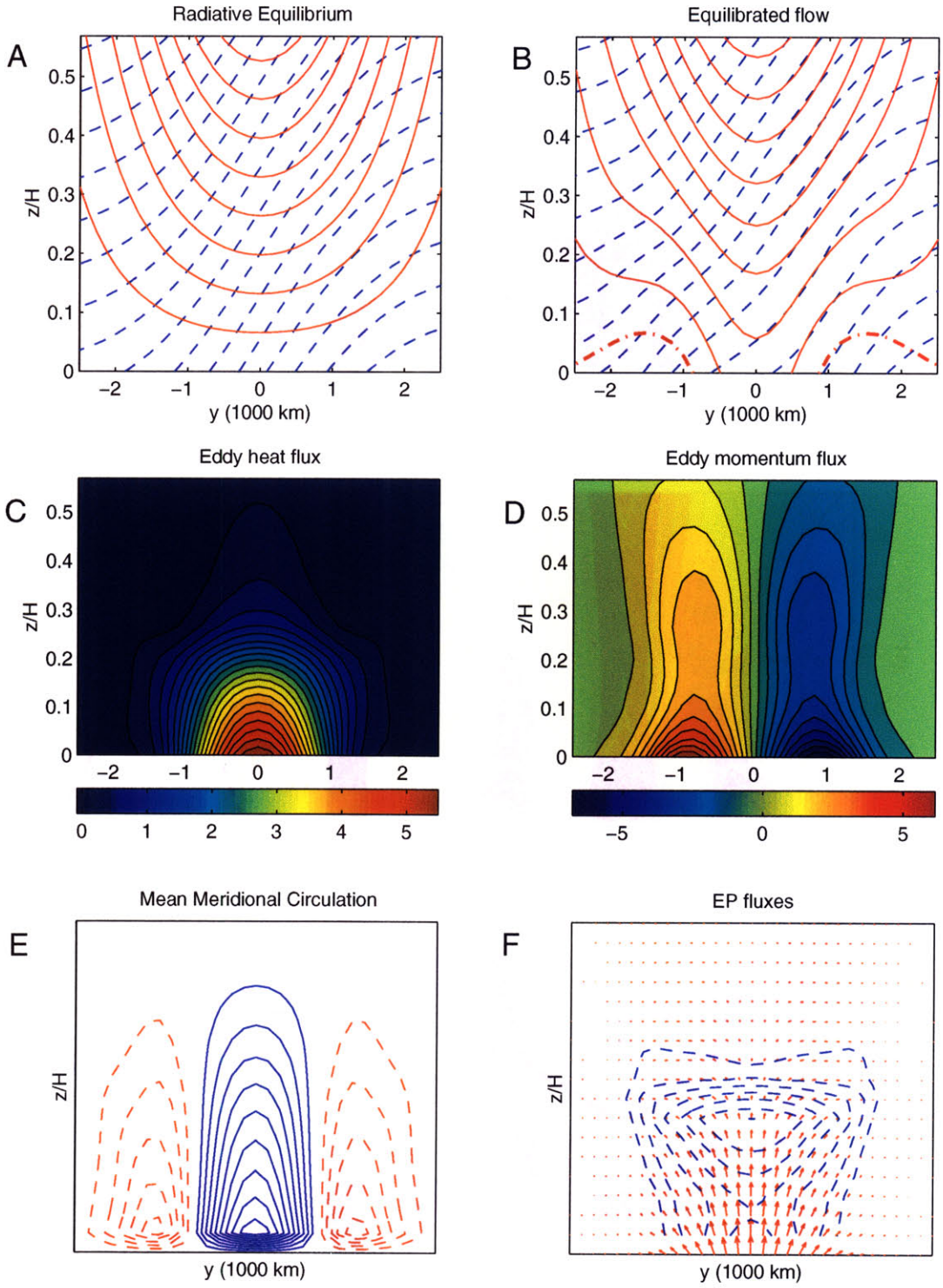


Figure 4-21: Maintenance of the equilibrated state for the simulation with $\beta = 3.0 \times 10^{-11}\ m^{-1}s^{-1}$ ($H/h = 1.6$) and 1 day surface damping. (A) Potential temperature (dashed) and zonal mean wind (solid) in radiative equilibrium. (B) Same but for the equilibrated flow. Contour unit: 4 K for temperature and 4 m/s for zonal wind, the zero wind line is dash-dotted. (C) Eddy heat flux in $Kms^{-1}$. (D) Eddy momentum flux in $m^2s^{-2}$. (E) Mean meridional circulation (solid is counterclockwise). (F) Eliassen-Palm fluxes (vectors) and convergence in $s^{-2}$ (dashed line)

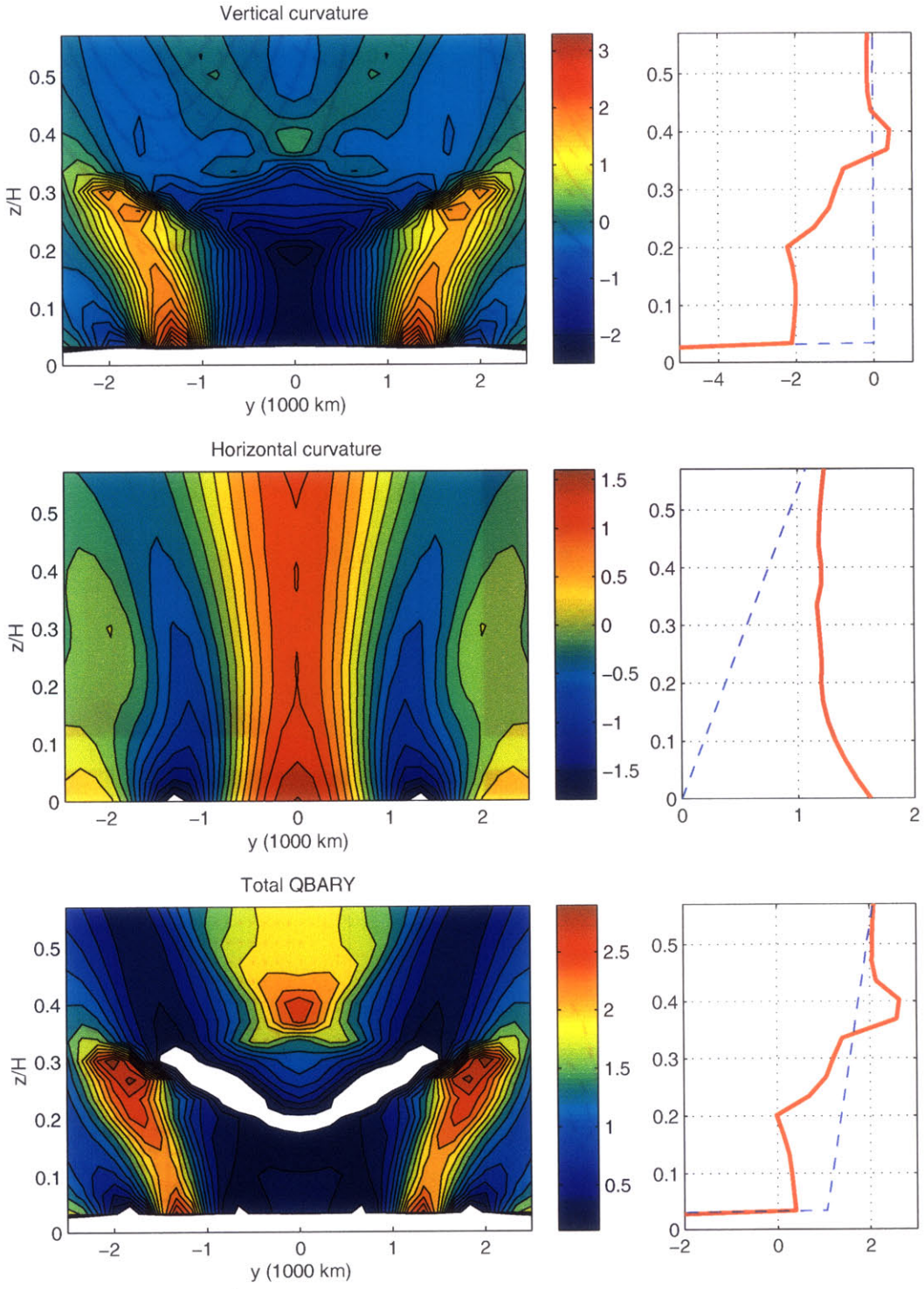


Figure 4-22: (Left) Contributions to the zonal mean PV gradient resulting from: (top) vertical curvature, (mid) horizontal curvature, and (bot) total PV gradient, normalized by $\beta$ for the run with $\beta = 1.6 \times 10^{-11}\ m^{-1}s^{-1}$ ($H/h = 0.86$), and surface damping time scale 3 days. (Right) Same but for the vertical profiles at the center of the channel, with radiative equilibrium distributions shown dashed.

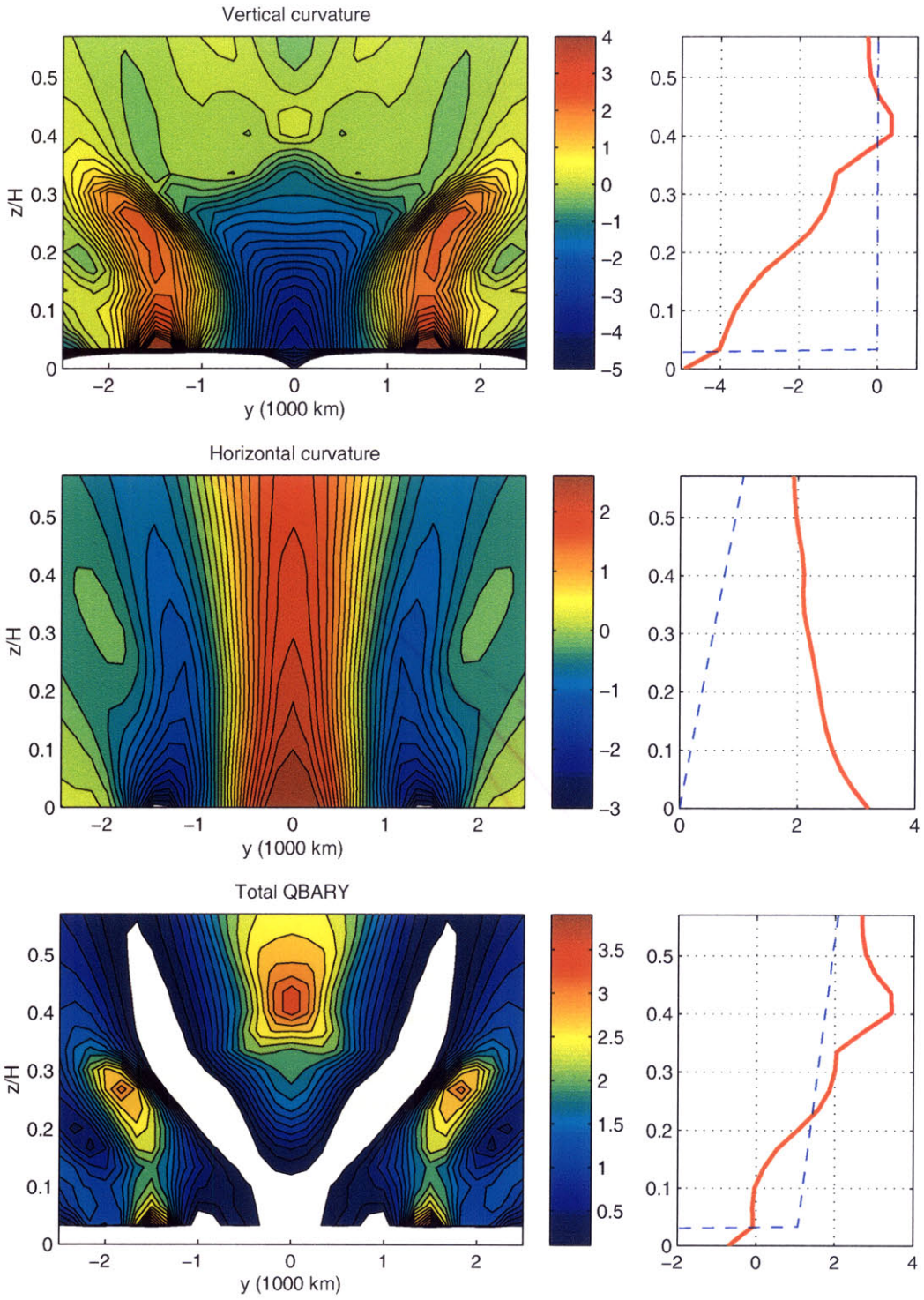


Figure 4-23: As figure 4-23 but with surface damping 10 days.

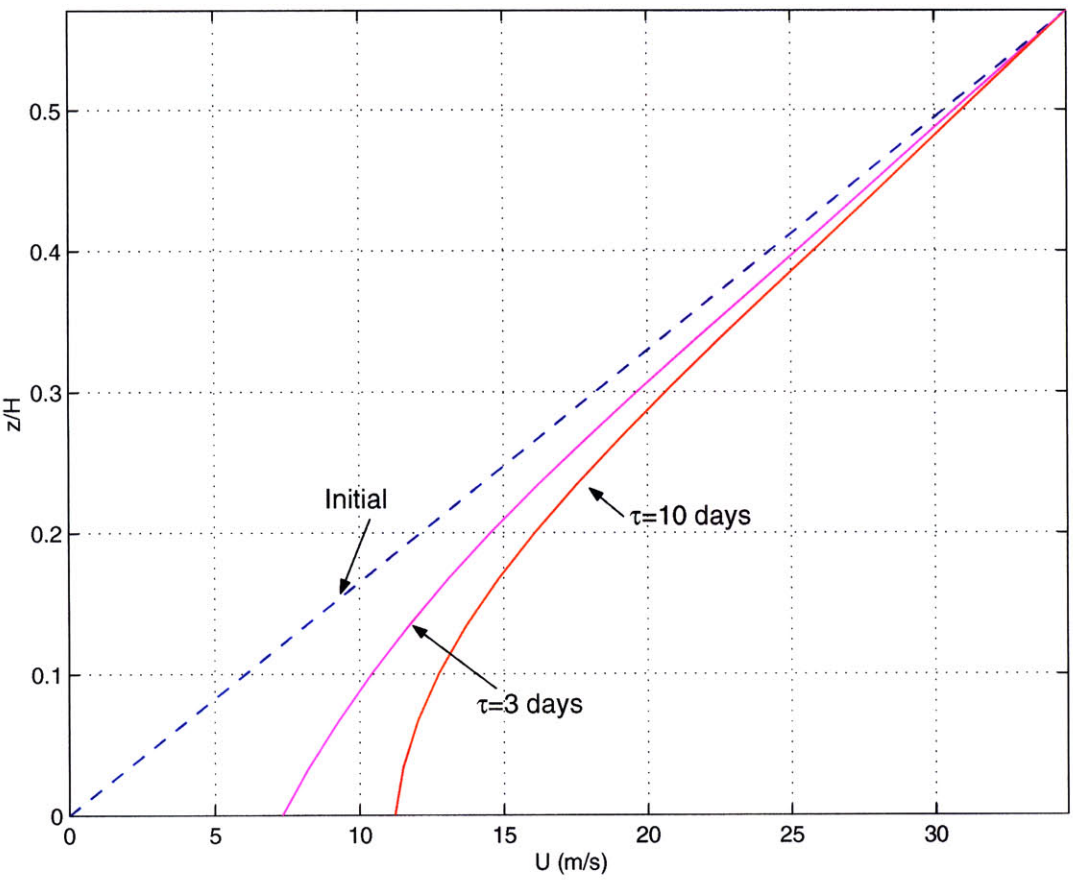


Figure 4-24: Comparison of the zonal mean flow for the initial profile (dashed), and the equilibrated states for the runs with $H/h = 0.86$ and the surface damping time scales indicated.

# Chapter 5

# A momentum-based formulation of the 3D extratropical circulation

## 5.1 Motivation: local vs non-local forcing of momentum

We studied in the previous chapter the equilibration of the barotropic point jet and 3D baroclinic Charney problem. It was argued in that chapter that a useful way to look at these problems is to think in terms of the redistribution of zonal momentum by the wave: this dynamical forcing must ultimately balance the non-conservative forcing of momentum.

In the barotropic problem, all the dynamical forcing of momentum occurs in the form of a PV flux, which implies that there is a local balance between the frictional forcing of momentum and this eddy momentum drag. This is a strong constraint, which allows us to infer some interesting results about the nature of the equilibrated flow. For instance, to the extent that the PV fluxes are downgradient, the PV gradient must change sign, so that it is positive (negative) over regions with westerly (easterly) frictional generation of momentum.

However, things are more complicated in the 3D problem. In that case, there is also a vertical redistribution of momentum by the mean meridional circulation (MMC), so that the non-conservative forcing of momentum and the eddy drag no longer balance locally, except when vertically integrated. An additional difficulty with the MMC is that it reflects non-local effects, as it can be forced by remote diabatic sources of heat and momentum.

To be sure, the same is true to some extent for the eddy forcing of momentum (i.e., the PV flux $\overline{v'q'}$). In particular, the very fact that $\overline{v'q'}$ must globally integrate to zero reminds

us that, at least conceptually, the PV flux at any given location cannot be fully determined without consideration of the rest of the fluid. This idea is at the root of Bretherton's theorem and the Charney-Stern condition for instability.

Yet on the other hand, for an *equilibrated* flow one has a balance of the form (in its simplest formulation, neglecting cubic terms in wave amplitude):

$$\overline{v'q'}\,\overline{q}_y = -\frac{1}{\tau}\overline{q'^2} \tag{5.1}$$

between the dissipation of eddy enstrophy and its generation at the expense of the mean flow (here $\tau$ is a dissipative time scale). Note that this is a fully local balance, and suggests that the PV flux at a given location can be fully determined as a function of the local PV gradient and eddy enstrophy dissipation rate.

The answer to this apparent contradiction lies in the word 'equilibrated'. Consider a wave that is remotely forced and propagates into some region. As the wave propagates into that region, there is an eddy drag $\overline{v'q'}$ on the mean flow. This eddy drag is clearly non-locally determined, because it depends on the wave having been forced elsewhere. The eddy drag induces a modification of the mean flow, which evolves accordingly. However, if a (statistically) steady state is reached, this equilibrium must be controlled locally (as indicated by equation 5.1), even though the forcing is properly speaking non-local. For instance, if the region is non-dissipative the only possible *steady* solution has $\overline{v'q'} = 0$, so that the wave can only propagate through that region to dissipate elsewhere and does not interact with the mean flow. Note that the maintenance of this equilibrium may require in the dissipative case a local restoring force, a forcing by the MMC, or both.

It is the fact that equation 5.1 is a local constraint that makes it so useful. For instance, equation 5.1 tells us right away that the dynamical momentum forcing is westerly (easterly) when the PV gradient is negative (positive). Unfortunately, the local nature of the dynamical momentum forcing is lost in the 3D problem, in which momentum is also redistributed by a remotely forced mean meridional circulation. From a mathematical point of view, the non-local character of the MMC results from the ellipticity of the Eliassen-Kuo equation.

In this chapter, we develop an alternative formulation of the extratropical circulation. By introducing a generalized momentum (which includes a *non-local* contribution called potential momentum), the time-evolution of the basic state can be cast in a form in which

the only dynamical forcing is the eddy PV flux $\overline{v'q'}$. Hence, in this formulation we recover the local nature of the 2D momentum balance. This allows us to infer some general results about the nature of the circulation, from considerations such as that brought up above for the 2D case. Moreover, the results of chapter 4 pointed to the relevance of the redistribution of momentum for the equilibration of baroclinic waves. By establishing a link between momentum and thermal structure, this formulation gives some insight into the nature of the equilibration and how friction may limit the homogenization of surface temperature.

The structure of this chapter is as follows. We introduce the concept of potential momentum and derive its evolution equation in section 5.2. We also discuss in this section in some extent how some well-known results of qg theory 'read' in this formulation. Section 5.3 is concerned with the maintenance of the potential momentum balance, and section 5.4 discusses some implications of this balance. Finally, the results of chapter 4 are reviewed in section 5.5 at the light of the new diagnostics.

## 5.2 The concept of potential momentum

We start with the quasigeostrophic Boussinesq zonal-mean equations on the $\beta$ plane:

$$\frac{\partial \overline{U}}{\partial t} + \frac{\partial}{\partial y}\overline{u'v'} - f_0 \overline{v}_a = -\alpha_M \overline{U} \tag{5.2}$$

$$\frac{\partial \overline{\theta}}{\partial t} + \frac{\partial}{\partial y}\overline{v'\theta'} + \overline{w}_a \Theta_z = -\alpha_T (\overline{\theta} - \overline{\theta}_R) \tag{5.3}$$

$$\frac{\partial \overline{v}_a}{\partial y} + \frac{\partial \overline{w}_a}{\partial z} = 0 \tag{5.4}$$

$$\frac{\partial \overline{U}}{\partial z} = -\frac{g}{f_0 \Theta_0}\frac{\partial \overline{\theta}}{\partial y} \tag{5.5}$$

where $\alpha_M$, $\alpha_T$ are the linear damping coefficients for Rayleigh friction and Newtonian cooling, respectively, and $\theta_R$ is the radiative equilibrium profile to which temperature is relaxed. We will assume $\alpha_T$ to be constant, while $\alpha_M$ is allowed to be height-dependent (for instance, when it is non-zero only in the boundary layer). Finally, $\Theta_z$ is the reference stratification of qg theory, which may also be height-dependent.

Consider a latitude $y_0 = 0$, such that $\overline{v}_a = v' = 0$ at $y_0$. Our goal is to rewrite the thermodynamic equation as a momentum equation. With that purpose, we multiply

equation 5.3 by $-f_0/\Theta_z$, integrate meridionally between $y_0$ and $y$ and differentiate with respect to $z$. Applying continuity, the thermodynamic equation can then be written:

$$\frac{\partial \overline{M}}{\partial t} - \frac{\partial}{\partial z}\left(\frac{f_0}{\Theta_z}\overline{v'\theta'}\right) + f_0\overline{v}_a = -\alpha_T(\overline{M} - \overline{M}_R) \tag{5.6}$$

where we define the *potential momentum* $M$ as:

$$M = -\int_0^y \frac{\partial}{\partial z}\left(\frac{f_0}{\Theta_z}\theta\right) dy' \tag{5.7}$$

The rationale of calling $M$ potential momentum will become clear below, when we show that the baroclinic conversions essentially convert this potential momentum into zonal momentum $U$. For the time being, note that M does have units of momentum and that equation 5.6 formally looks like a momentum equation. In particular, the second term in equation 5.6 is interpreted in the Eliassen-Palm formalism as a vertical eddy momentum flux (Edmon et al., 1980). This term can also be rewritten:

$$-\frac{\partial}{\partial z}\left(\frac{f_0}{\Theta_z}\overline{v'\theta'}\right) = -\overline{v'\frac{\partial}{\partial z}\left(\frac{f_0}{\Theta_z}\theta'\right)} = \overline{v'\frac{\partial m'}{\partial y}} \tag{5.8}$$

where $m'$ is the eddy component of the potential momentum $M$, and we took into account the thermal wind relation for $v'$ and the definition, $\frac{\partial M}{\partial y} = -\frac{\partial}{\partial z}\left(\frac{f_0}{\Theta_z}\theta\right)$. This gives the following alternative expression for the thermodynamic equation:

$$\frac{\partial \overline{M}}{\partial t} + \overline{v'\frac{\partial m'}{\partial y}} + f_0\overline{v}_a = -\alpha_T(\overline{M} - \overline{M}_R) \tag{5.9}$$

Comparing equations 5.2 and 5.9 we can see that the term $f_0\overline{v}_a$ simply converts potential momentum to physical momentum. We can eliminate this term by adding together equations 5.2 and either equations 5.6 or 5.9, to obtain the following expressions for the evolution of the total momentum:

$$\frac{\partial}{\partial t}\left(\overline{U} + \overline{M}\right) + \alpha_T\left(\overline{M} - \overline{M}_R\right) + \alpha_M\overline{U} = \overline{v'q'} = \frac{\partial}{\partial z}\left(\frac{f_0}{\Theta_z}\overline{v'\theta'}\right) - \frac{\partial}{\partial y}\overline{u'v'} = -\overline{v'\frac{\partial}{\partial y}(u' + m')} \tag{5.10}$$

As can be seen, in this formulation the forcing by the mean meridional circulation disappears, so that the only dynamical forcing is the eddy PV flux $\overline{v'q'}$. Hence, this equation

can be regarded as a generalization of the barotropic momentum equation (equation 4.3), and retains all the advantages emphasized above. Like the transformed Eulerian mean formulation, this equation makes explicit the role of the PV flux as an eddy forcing of momentum. However, in this case the eddy PV flux forces the total momentum, also including the potential momentum defined above, rather than just the traditional momentum.

It is important to note that $M$, as defined in 5.7, is *not* a local function of the basic state, but depends on the full isentropic structure equatorward of the given location. In a sense, the non-local character of the original equations has been hidden in the definition of the basic state. This has the conceptual advantage of placing the wave-mean flow interaction in a simpler, local framework.

Equation 5.10 is nothing more than the $y$-integral of the zonal mean PV equation. This is obvious when we realize the very simple relation between PV and total momentum:

$$\overline{q} = f_0 + \beta y - \frac{\partial}{\partial y}\left(\overline{U} + \overline{M}\right) \tag{5.11}$$

In fact, it would also be possible to include in the same manner the planetary vorticity contribution in the definition of the total momentum. However, there is not much point to it because this term trivially disappears in equation 5.10.

Differentiating equation 5.11, we also get the following simple expression for the basic state PV gradient:

$$\overline{q}_y = \beta - \frac{\partial^2}{\partial y^2}\left(\overline{U} + \overline{M}\right) \tag{5.12}$$

As mentioned above, the role of the ageostrophic circulation $f_0\overline{v}_a$ is to exchange potential and physical momentum. At any time, the partition of these two contributions to the total momentum must be such that thermal wind balance is satisfied:

$$\frac{\partial^2 \overline{M}}{\partial y^2} = \frac{\partial}{\partial z}\left(\frac{f_0^2}{N^2}\frac{\partial \overline{U}}{\partial z}\right) \tag{5.13}$$

This constraint allows us to obtain an Eliassen-Kuo equation for the mean meridional circulation $\overline{v}_a$ through the manipulation of equations 5.2, 5.9 in the usual manner. The ellipticity of the Eliassen-Kuo equation implies that the partition between physical and potential momentum is non-locally determined. However, for the *total* momentum, there

is a local balance between dynamical and non-conservative forcing (equation 5.10). Note that equation 5.13 also implies that $\overline{M}$ and $\overline{U}$ are of the same order when $\overline{M}$ changes in horizontal length scales of the order of the deformation radius.

It is also possible to rewrite equations 5.2, 5.6 in terms of the Transformed Eulerian Mean (TEM) formalism (Edmon et al., 1980):

$$\frac{\partial \overline{M}}{\partial t} + f_0 \overline{v}^* = -\alpha_T \left( \overline{M} - \overline{M}_R \right) \tag{5.14}$$

$$\frac{\partial \overline{U}}{\partial t} - f_0 \overline{v}^* = \overline{v'q'} - \alpha_M \overline{U} \tag{5.15}$$

where $\overline{v}^* = \overline{v}_a - \frac{\partial}{\partial z}\left(\frac{\overline{v'\theta'}}{\Theta_z}\right)$ is the residual meridional velocity.

In the TEM formulation, the residual circulation is the only dynamical forcing of potential momentum, and results in a conversion from potential to physical momentum. Physical momentum on the other hand is forced both by this conversion and by an eddy drag in the form of the eddy PV flux. Finally, the *total* momentum, is just forced by the eddy PV flux.

To conclude this section, we point out that the assumption of no meridional velocity at the latitude $y_0 = 0$ is not really necessary, and the formulation can be easily generalized to include non-zero mean or eddy fluxes at that latitude. Indeed, one of the appealing features of a momentum-based formulation is that it might provide a more transparent framework to look at tropical-extratropical interactions. However, because this thesis is only concerned with the equilibration of an isolated baroclinic jet, we will ignore any such boundary contribution and carry on with this assumption for the remaining of this chapter.

### 5.2.1 Physical interpretation

The concept of potential momentum is somewhat similar to that of available potential energy. While the concept of available potential energy exploits the sloping of the isentropes, the concept of potential momentum is based on the non-uniformity of the isentropic thickness. As implied by its name, $\overline{M}$ represents the zonal momentum that would be realized if the basic state stratification were brought to its reference value $\Theta_z$ while conserving the same potential vorticity distribution. This is evident from its definition:

$$\frac{\partial \overline{M}}{\partial y} = -\frac{\partial}{\partial z}\left(\frac{f_0}{\Theta_z}\overline{\theta}\right)$$

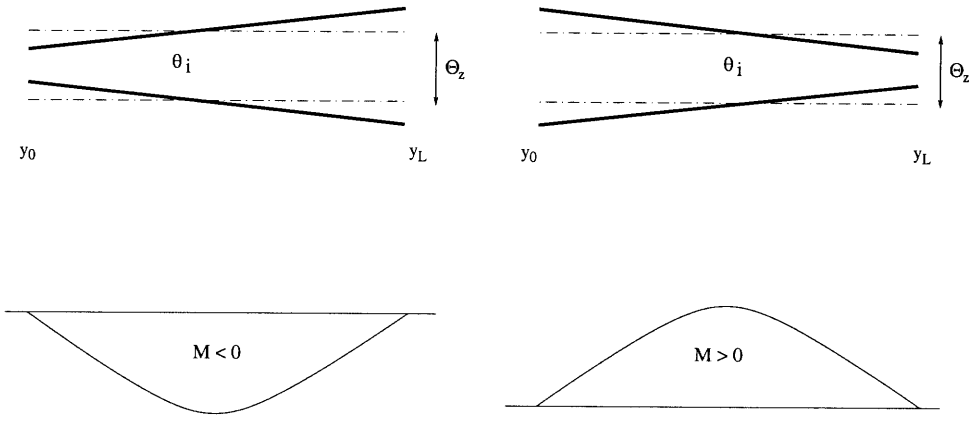


Figure 5-1: Sketch illustrating the potential momentum distribution associated to an isentropic layer whose thickness: (left) increases with latitude, (right) decreases with latitude.

For a stratified rotating fluid, an important component of the basic state potential vorticity is locked in the stretching term $\frac{\partial}{\partial z}\left(\frac{f_0}{\Theta_z}\overline{\theta}\right)$. If this term were entirely converted into relative vorticity, it would produce a meridional wind shear $\frac{\partial \overline{M}}{\partial y}$. Hence, $\overline{M}$ gives the net change in zonal momentum which would result from bringing the isentropic thickness down to its reference value (which may be height-dependent) at all latitudes poleward of $y_0$.

This is illustrated in figure 5-1, which shows two idealized distributions of the isentropic thickness for a generic isentropic layer $\theta_i$, together with the corresponding distribution of $\overline{M}$. Also shown is the reference thickness (dashed).

When the isentropic thickness is larger than in the reference state (i.e., $\frac{\partial \overline{\theta}}{\partial z} < 0$), $\overline{M}$ must increase with latitude. In other words, if the thickness were brought down to its reference value, the flow would generate an enhanced meridional westerly shear so as to decrease its absolute vorticity and keep constant potential vorticity. The reverse is also true, so that $\overline{M}$ decreases with latitude when the isentropic thickness is smaller than in the reference state.

For the sketch shown in the left panel, the thickness increases with latitude monotonically. If the mean stratification agrees with the reference stratification, this implies that the thickness must be smaller than the reference thickness for the first half of the profile, and larger for the second. Consequently, $\overline{M}$ initially decreases with latitude, and increases near the end. Taking into account that $\overline{M}(y_0) = 0$, this produces an $\overline{M}$ profile as shown. If the mean stratification agrees with the reference stratification, then $\frac{\partial \overline{\theta}}{\partial z}$ has zero mean and hence $\overline{M}(y_L) = 0$ as well at the right endpoint $y_L$ (c.f., equation 5.7).

The reverse is true for the case shown in the right panel, for which the thickness decreases monotonically with latitude. Hence, we can see that an easterly (westerly) potential

momentum $\overline{M}$ is associated with isentropic layers that open up (close down) with latitude, as represented schematically in figure 5-1. When the dependence of $\frac{\partial\overline{\theta}}{\partial z}$ on latitude is linear, $\overline{M}$ is quadratic in $y$.

Because of the boundary conditions $\overline{M}(y_0) = \overline{M}(y_L) = 0$, negative (positive) midlatitude values of $\overline{M}$ are typically associated with positive (negative) values of $\overline{M}_{yy}$. From equation 5.12, this implies that the $\overline{M}$ contribution to the PV gradient is negative (positive) when $\overline{M}$ is easterly (westerly). In the troposphere, the slope of the isentropes increases with height (Stone and Nemet, 1996), which implies that the isentropic layers open up with latitude, as is also apparent in figure 2-2. This is what would be expected based on a simple planetary vorticity approximation: for positive $\beta$, the isentropes must open up with latitude if PV is to be homogenized. From a potential momentum viewpoint, this isentropic pattern produces easterly $\overline{M}$, and hence a negative contribution to the zonal mean PV gradient. Note that this is in agreement with the observations discussed in section 2.3, where it was shown that the only negative contribution to the zonal mean PV gradient results from the tendency of the isentropes to have increasing slopes with height. However, it was argued in that section that the isentropes do not open enough, so that there is still a net positive PV gradient in the interior.

As usual in qg theory, it is useful to regard the lower boundary as an isothermal surface (Bretherton, 1966), which requires the inclusion of a delta-function interior PV gradient right above it. This delta-function PV gradient results from the $\overline{M}$ contribution to the total PV gradient, and can be easily derived by generalization of equation 5.7:

$$\overline{M}(y,z) = -\frac{f_0}{\Theta_z}\int_0^y \left(\overline{\theta} - \Theta_0\right)\delta(z)dy' \qquad at\ z = 0 \tag{5.16}$$

where $\Theta_0$ is the uniform temperature of the isothermal surface. It is convenient to define this reference temperature as the mean surface temperature between $y_0$ and $y_L$. By doing that, we can make $\overline{M}$ go to zero at both endpoints at the surface.

Note that when the surface temperature decreases with latitude as observed, equation 5.16 also produces an easterly potential momentum and a negative delta-function contribution to the total PV gradient. Physically, this can be interpreted again in terms of the isentropes opening up with latitude. Specifically, the disappearance of the isentrope $\theta_i$ equatorward of the latitude $y_i$ can be conceptualized as a jump in thickness between 0 and

its interior value at that latitude.

Finally, we point out that in the previous discussion and in figure 5-1 it was implicitly assumed that the isentropic layers were quasi-horizontal. This makes the interpretation easier because we can identify integrating at constant height with moving along an isentrope. However, this assumption is not strictly valid for planetary dynamics because the isentropic slope is not small: in reality, the integral in equation 5.7 is taken along different isentropic layers. While this complicates the interpretation, the basic concepts should still be valid.

## 5.3 Potential momentum balance

The picture described above makes clear the connection between the concept of potential momentum and the non-uniformity of the isentropic thickness. In this section, we use this simple idea to discuss the potential momentum balance.

First, it should be noted that when the surface delta function is included, there is a constraint on the vertically integrated potential momentum. From equations 5.7, 5.16:

$$\int_0^\infty \overline{M} dz = -\frac{f_0}{\Theta_z} \int_0^y \left( \overline{\theta}_\infty - \Theta_0 \right) dy = \int_0^\infty \overline{M}_R dz \tag{5.17}$$

In a seminfinite domain $\overline{\theta}_\infty$ would be the temperature at infinity, which cannot be changed by the dynamics (assuming a finite mixing depth). Alternatively, in the presence of an upper rigid lid, $\overline{\theta}_\infty$ would be the constant temperature of the top boundary when the boundary temperature gradient is included as an interior delta-function PV gradient. In both cases, equation 5.17 implies that the vertically integrated potential momentum is constant. When the horizontal wind curvature is neglected, this directly translates into a constraint on the vertically integrated PV gradient, as discussed in previous chapters.

Physically, the reason for this constraint is that the sum of the isentropic thicknesses of all layers must add up to a constant because we assumed that potential temperature was fixed at two reference heights. As a result, the eddies and diabatic processes can only redistribute the mass between the different isentropic layers. For instance, as the surface temperature gradient is reduced an isentropic layer that is initially absent at a given latitude may acquire a finite thickness at the expense of the interior layers.

The potential momentum balance is best understood in terms of the TEM formulation. We repeat for convenience equations 5.14, 5.15 below:

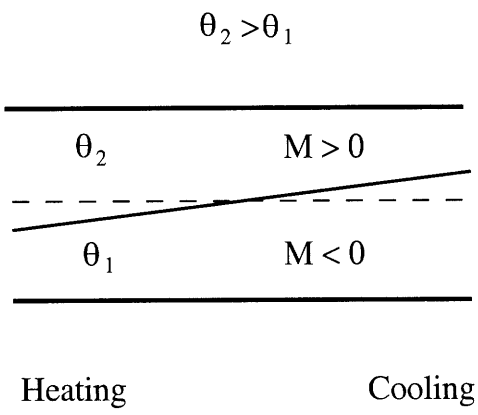


Figure 5-2: Sketch illustrating how low latitude heating and high latitude cooling results in a downward transfer of easterly potential momentum.

$$\frac{\partial \overline{M}}{\partial t} + f_0 \overline{v}^* = -\alpha_T \left( \overline{M} - \overline{M}_R \right) \tag{5.18}$$

$$\frac{\partial \overline{U}}{\partial t} - f_0 \overline{v}^* = \overline{v'q'} - \alpha_M \overline{U} \tag{5.19}$$

According to the TEM formulation, potential momentum can be created or destroyed diabatically, or it can be transformed into physical momentum through the residual circulation. However, because each of the terms in equation 5.18 integrates independently to zero in the vertical, the generation and conversion terms only redistribute potential momentum vertically, but conserve the net potential momentum of the column.

Diabatic processes transfer mass between the different isentropic layers, thus changing the distribution of isentropic thicknesses at a given latitude. This results in a vertical redistribution of potential momentum, with no net creation or destruction along the column. In particular, heating at low latitudes and cooling at high latitudes is equivalent to an upward transfer of westerly potential momentum for a stably stratified fluid. This is illustrated in figure 5-2, which shows two adjacent isentropic layers $\theta_1$ and $\theta_2$, with $\theta_2 > \theta_1$. Low latitude heating results in a transfer of mass from $\theta_1$ to $\theta_2$, while the reverse is true for high latitude cooling. Based on the ideas of the previous section, we can see that this tends to generate easterly potential momentum along the lower isentrope, and compensating westerly potential momentum aloft.

Additionally, there is a conversion between potential and physical momentum through the residual circulation. When this circulation is poleward, potential momentum is con-

verted into physical momentum, while the reverse is true when the circulation is equatorward. This can be easily understood because, as McIntosh and McDougall (1996) have shown, the residual circulation is an approximation to the isentropic mass circulation. Hence, a poleward residual circulation transfers mass from low to high latitudes along the isentropes, thus generating easterly potential momentum in the interior. Because of potential vorticity conservation, this adiabatic generation of easterly potential momentum must be accompanied by an equal generation of westerly physical momentum, so that the total momentum $\overline{M} + \overline{U}$ is conserved. Mechanistically, the generation of physical momentum can be associated to the Coriolis force acting on the residual circulation. Hence, in this framework the westerly acceleration characteristic of the equilibration of baroclinic instability comes up naturally because an equilibrating wave tends to generate easterly potential momentum in the interior. According to equation 5.19, this westerly acceleration in the interior is balanced by the easterly eddy drag $\overline{v'q'}$ and mechanical friction.

On the other hand, the generation of easterly potential momentum in the interior must also be accompanied by westerly potential momentum generation elsewhere because the vertically integrated $\overline{M}$ is conserved. This westerly potential momentum acceleration occurs at the surface, where the residual circulation closes with a delta-function return flow. Note that from equation 5.16, the westerly potential momentum acceleration at the surface is equivalent to a reduction in the surface temperature gradient. Finally, for completeness the surface westerly potential momentum acceleration must also be accompanied by an equal easterly acceleration in physical momentum. However, this only affects a massless layer of fluid right underneath the surface, what we called the momentum reservoir in section 4.2.5. Note that the momentum reservoir is just an artifact introduced for conceptual consistency, but plays no real dynamical role; what really matters dynamically is that the surface temperature gradient can be interpreted as a source of easterly momentum. To be precise, in this framework potential momentum can only be generated dynamically through conversions to/from physical momentum. Hence, if we use Bretherton's 1966 formulation to model surface temperature as delta-function potential momentum (equation 5.16), dynamical modifications in surface temperature must be associated with delta-function momentum tendencies. However, note that the momentum reservoir is not subject to any net tendency in practice because the easterly acceleration resulting from this conversion is exactly balanced by the westerly delta-function eddy drag at the surface $\overline{v'q'}$.

The previous description also illustrates why a poleward eddy heat flux or, more generally, a poleward isentropic circulation, can be interpreted as an upward flux of physical momentum, as implied by the vector convention in the Eliassen-Palm formulation (Edmon et al., 1980). The crucial point in this regard is the conservation of the column-integrated potential momentum. Because the conversion of potential momentum into physical momentum in the interior must be accompanied by the opposite conversion at the surface, the net result is an upward flux of easterly momentum.

The momentum balance can then be summarized as follows. In radiative equilibrium, there is easterly potential momentum at the surface, which is equivalent to a negative delta-function PV gradient and supports baroclinic instability. The equilibration of the baroclinic waves produces a poleward residual circulation, which redistributes potential momentum vertically. In the interior, this circulation converts (westerly) potential momentum into physical momentum; as a result of this easterly potential momentum acceleration the isentropic layers open up with latitude. The opposite is true at the surface, where the westerly potential momentum acceleration results in a reduced temperature gradient. The interior momentum acceleration is balanced by the eddy drag $\overline{v'q'}$ and surface friction, both of which are easterly. Finally, the vertical flux of momentum is maintained by the diabatic processes, which tend to produce easterly potential momentum in the lower troposphere and compensating westerly potential momentum aloft.

## 5.4 Implications

The description provided above is consistent with other existing descriptions of the equilibrated circulation in a forced-dissipative baroclinic system. However, the formalism derived here has two distinct advantages over others. On the one hand, it allows us to formulate a local balance between the nonconservative and dynamical forcing of momentum. Additionally, it brings temperature and momentum to a common framework, in which they can be directly compared. This allows us to gain a better understanding of the role played by the barotropic governor and surface friction in the baroclinic equilibration. In this section, we use these simplifications to discuss some important results for a baroclinic system.

### 5.4.1 The 3D mixing depth constraint

In chapter 4 we described the baroclinic equilibration in terms of the redistribution of the zonal momentum by the eddies. We found that the westerly acceleration of the jet had important dynamical consequences, and this is the reason why surface friction plays such an important role. This result is most transparent in a momentum-based formalism, in which the baroclinic equilibration is described in terms of the eddies redistributing vertically the potential momentum initially locked at the surface. In the limit, the surface temperature is fully homogenized over the meridional domain of interest when all the surface potential momentum is transferred to the interior.

If momentum is only redistributed vertically, there is a geometrical constraint that prevents the homogenization of surface temperature when the scale of the waves is not deep enough. In simple words, there is a limit to how much interior easterly potential momentum the flow can develop. The reason is that the easterly potential momentum gives a negative contribution to the zonal mean PV gradient, which should not exceed the positive PV gradient resulting from other contributions. We can state this condition as a requirement that the total momentum (including the beta contribution, which can also be regarded as a generalized momentum as discussed in page 129) be westerly in the interior. Because the elimination of the surface temperature gradient requires a transfer of easterly momentum from the surface into the interior, this restriction sets up a limit to the maximum reduction in the surface potential momentum and surface temperature gradient.

However, as pointed out in section 4.2.4, the mixing depth constraint does not really work in the 3D case because of the compensating generation of positive PV gradient through the enhanced meridional curvature of the zonal flow. This is most transparent in a potential momentum framework, in which we can write $\overline{q}_y = \beta - \frac{\partial^2}{\partial y^2}(\overline{M} + \overline{U})$. Because the dynamical generation of easterly potential momentum $\overline{M}$ occurs through conversion to physical momentum $\overline{U}$ (c.f., equations 5.14, 5.15), the total momentum $\overline{U} + \overline{M}$ and the net interior PV gradient remain relatively unchanged. The reduction of the interior PV gradient thus requires that the conversion from potential to physical momentum is also accompanied by actual momentum drag, either in the form of the eddy PV flux $\overline{v'q'}$, or friction.

Moreover, note that from the definition of the residual circulation:

$$\int_{0+}^{\infty} \left( f_0 \overline{v}^* + \overline{v'q'} \right) dz = - \int_0^{\infty} \frac{\partial}{\partial y} \overline{u'v'} dz > 0, \tag{5.20}$$

which implies that the easterly eddy drag is not strong enough to balance the net conversion of potential to physical momentum in the interior. This is consistent with the results of chapter 4, which showed that, without friction, there is a sustained westerly acceleration of the jet. We also found in the frictionless runs that the westerly interior acceleration is accompanied by the reduction of the surface temperature gradient as the steering level drops. This admits a natural interpretation in a potential momentum framework, in which the westerly acceleration of the jet can be linked to the easterly generation of interior potential momentum, and thus to the depletion of the surface potential momentum. Indeed, in the frictionless runs of chapter 4 the transfer of potential momentum to the interior only ceases when the steering level drops to the ground and the surface temperature gradient is eliminated over the central part of the channel, i.e. when the easterly potential momentum at the surface is exhausted over the relevant meridional scale.

However, this is no longer the case when friction is included. Then, a statistical equilibrium is eventually reached, in which the conversion of potential to physical momentum is balanced by the combined effect of friction and the eddy PV flux. Indeed, it was shown in section 4.2.5 that in the presence of surface friction, there must be a negative PV gradient (typically at the surface) over those latitudes with surface westerlies. The relation between friction and surface temperature is most transparent in a potential momentum framework, in which the temperature gradient is equivalent to potential momentum. Note that the arguments presented here are completely general, and not restricted to short Charney modes.

The previous discussion brings up the important question, what determines the rate of conversion from potential to physical momentum, and thus the partition between both forms of momentum?. The answer is the thermal wind constraint, equation 5.13. As discussed in section 5.2, this constraint implies that, when potential momentum varies in horizontal scales of the order of the deformation radius, the potential and physical momentum should be of the same order. Note that this also implies that their negative and positive (respectively) contributions to the interior PV gradient should nearly cancel, thus yielding a net interior PV gradient of order $\beta$ (plus the Boussinesq correction). This is in qualitative agreement with the observations discussed in chapter 2.

### 5.4.2 Local momentum balance in a forced-dissipative system

In section 5.3 we described the general circulation of a forced baroclinic system in terms of momentum. Diabatic heating generates easterly potential momentum at the surface, which is then redistributed in the interior by the residual circulation. This process also generates westerly physical momentum, which is ultimately damped by the combined effect of the eddy drag and surface friction. An equilibrium is reached when all three terms: diabatic generation, conversion and drag are equal. This can be seen dropping the time derivatives in equations 5.18, 5.19, which yields for an equilibrated system:

$$-f_0\overline{v}^* = \alpha_T\left(\overline{M} - \overline{M}_R\right) = \overline{v'q'} - \alpha_M\overline{U} \tag{5.21}$$

where the left hand side gives the rate of conversion from potential to physical momentum, the middle term the diabatic momentum generation, and the right hand side the net momentum drag. In equilibrium, all three terms must be equal.

As discussed in the introduction, it is conceptually useful to think of $\overline{v'q'}$ as locally forced, since for an equilibrated system the wave-mean flow interaction must balance the local dissipation of eddy enstrophy (neglecting eddy enstrophy advection). Mathematically:

$$\overline{v'q'} \approx -\frac{\mathcal{D}}{\overline{q}_y} \tag{5.22}$$

where $\mathcal{D}$ is the nonconservative dissipation of eddy enstrophy. On the other hand, $\overline{v}^*$ satisfies the Eliassen-Kuo equation and is forced non-locally. When the total momentum $\overline{U} + \overline{M}$ is considered, this conversion term disappears so that we get:

$$\alpha_T\left(\overline{M} - \overline{M}_R\right) + \alpha_M\overline{U} = \overline{v'q'} \tag{5.23}$$

which represents a balance between the net dynamical forcing of *total* momentum, the eddy PV flux $\overline{v'q'}$, and the non-conservative forcing of *total* momentum. This non-conservative forcing consists of two parts: a diabatic forcing of potential momentum $\alpha_T(\overline{M} - \overline{M}_R)$, and a frictional damping of physical momentum $\alpha_M\overline{U}$. Equation 5.23 is the 3D analog to the barotropic momentum balance 4.6 and, like that equation, also represents a local balance (except from the fact that $\overline{M}$ is a non-local property of the mean flow).

Hence, when the PV fluxes are everywhere downgradient, this implies that the PV

gradient must be negative (positive) over the regions where the non-conservative forcing of momentum is easterly (westerly). Neglecting the frictional dissipation above the boundary layer, this implies that the PV gradient must be positive in regions of interior easterly (relative to radiative equilibrium) potential momentum. In those regions, the isentropes open up with latitude, but not enough to eliminate the positive PV gradient.

We argued in section 4.2.5 that when the PV fluxes are downgradient, the maintenance of surface westerlies requires that the PV gradient be negative somewhere along the column. The same result can be obtained integrating equation 5.23 vertically. Then, the forcing of potential momentum disappears so that there is a balance between the vertically integrated eddy PV flux (the net dynamical forcing of momentum along the column) and the frictional damping. However, the positive PV fluxes and associated negative PV gradient are in general much larger than indicated by this integral because the positive and negative PV fluxes cancel out for the most part when integrating vertically. Physically, the bulk of the interior westerly acceleration resulting from the potential momentum conversion in equation 5.21 is balanced by the eddy drag, rather than by friction.

Moreover, if friction is negligible everywhere except at the boundary layer, then equation 5.23 essentially reflects a balance between the diabatic generation of momentum and the eddy drag in the free atmosphere. On the other hand, the eddy drag $\overline{v'q'}$ can be related through equation 5.22 to the diabatic dissipation of eddy enstrophy, which should also be primarily thermal. This implies that the eddy drag is also linear in $\alpha_T$ (i.e. $\mathcal{D} = -\alpha_T \, \overline{q'm'_y}$), so that the thermal damping coefficient drops out of the balance:

$$\alpha_T \left( \overline{M} - \overline{M}_R \right) \overline{q}_y \approx -\alpha_T \, \overline{q'm'_y} \tag{5.24}$$

This is analogous to the forced-dissipative barotropic problem, in which the single forcing time scale trivially disappears (equation 4.10). As shown in section 4.1.3, the equilibrium flow in that problem is relatively insensitive to the damping time scale (c.f. figure 4-11). This may also explain why the baroclinic problem itself exhibits such weak sensitivity to the diabatic time scale, as found by numerous studies (e.g., Stone and Branscome (1992)).

Nevertheless, the fact that neither $\alpha_T$ nor $\alpha_M$ appears in equation 5.24 does not necessarily imply that the final state is insensitive to dissipation. The reason is that equation 5.24 represents an equilibrium situation, in which the terms have been brought to balance;

however, the time-evolution, and hence the final state, may still depend on damping. Indeed, it was argued above that it is friction that essentially constrains the homogenization of surface temperature. Though the net frictional damping may be much smaller than the eddy drag, friction is still essential because the latter alone can never balance the net momentum conversion.

To conclude this section, we emphasize the connection between surface temperature $\overline{\theta}_S$ and momentum by relating the former to the net interior drag. Making use of equations 5.16, 5.17, 5.21, and assuming that friction is non-zero only over a mixed layer of depth $\delta$:

$$\frac{f_0}{\Theta_z}\int_0^y \left(\overline{\theta}_S - \overline{\theta}_{RS}\right) dy' = -\int_0^{0^+} \left(\overline{M} - \overline{M}_R\right) dz = \int_{0^+}^{\infty} \left(\overline{M} - \overline{M}_R\right) dz = \\ = \frac{1}{\alpha_T}\left[-\alpha_M \delta \overline{U}_S + \int_{0^+}^{\infty} \overline{v'q'} dz\right] = -\frac{f_0}{\alpha_T}\int_{0^+}^{\infty} \overline{v}^* dz \qquad (5.25)$$

where $\overline{U}_S$ is the surface wind.

The rationale of equation 5.25 is as follows. Because of the integral potential momentum constraint, the reduction in (easterly) potential momentum at the surface from radiative equilibrium must be compensated by an interior easterly acceleration in potential momentum. This imbalance from radiative equilibrium supports a diabatic generation of westerly potential momentum in the interior, which is converted to physical momentum through the residual circulation and ultimately balanced by the combined easterly drag of the eddy PV flux and Rayleigh friction. The nearly-vertical orientation of the EP fluxes (see chapter 4) suggests that the latter dominates. Note that this balance also gives the intensity of the residual circulation $\overline{v}^*$, as potential momentum must be converted into physical momentum at the same rate that the former is generated and the latter is dissipated.

In summary, in this framework the diabatic heating can also be regarded as a momentum source, which allows to relate the surface thermal imbalance to the net momentum drag. However, it should be noted that equation 5.25 represents an equilibrium situation, in which terms have evolved to balance. Hence, it would be misleading to infer any causality from it. For instance, the same balance is valid for the equilibration of a baroclinic wave and the stratospheric circulation. However, while in the former case the circulation is ultimately driven by the diabatic forcing, in the latter the circulation is thought to be mechanically driven by the eddy PV flux, with the thermal dissipation being secondary to this circulation.

## 5.5 Potential momentum diagnostics of the idealized runs

To conclude this chapter, we illustrate the concept of potential momentum and the maintenance of the momentum balance using the idealized runs described in chapter 4. This is also useful for summarizing the main ideas introduced in this chapter.

Figure 5-3 shows some results for the run with $\beta = 3.0 \times 10^{-11}\ m^{-1}s^{-1}$ ($H/h = 1.6$) and surface friction of time scale 1 day. Panels A, B and C show the (interior) potential momentum, zonal mean flow and total momentum (i.e., the sum of the former two) respectively, for the equilibrium state. We also show superimposed the isentropic distribution.

For our choice of basic state, the interior potential momentum is zero in radiative equilibrium $\overline{M}_R = 0$. However, as the flow equilibrates, an easterly jet of potential momentum develops over the mixing domain. As expected, the potential momentum goes to zero at the lateral sides, where the stratification remains essentially unchanged. Also note that as required by the thermal wind constraint (equation 5.13), the physical and potential momentum of the final state are of the same order. This also implies that they should have a comparable (but opposite) contribution to the interior PV gradient. For the example shown the potential momentum jet is nearly barotropic, but this is not always the case.

As explained in previous sections, the concept of potential momentum is based on the non-uniformity of the isentropic thickness: the potential momentum of the basic state is easterly when the isentropic layers open up with latitude. Some hints of this can be seen by comparing the potential momentum distribution with the superimposed isentropic contours. However, because the stratification is dominated by the reference stratification, this is not so easily appreciated by inspection. Panel D shows the distribution of the isentropic thickness, normalized by this reference value. Consistent with the sign of the potential momentum, the thickness is smaller than average at low latitudes, and larger at high latitudes.

Note that the isentropic slope is not small. Rather, when the horizontal and vertical scales are nondimensionalized with the dimensions of the mixing domain, the isentropic slope is $O(1)$. To emphasize this, we have plotted with thicker line a reference isentrope: this isentrope has the property that it spans the mixing domain both meridionally and vertically. The same is true for the real atmosphere, in which the isentrope leaving the subtropical boundary layer reaches the tropopause at polar latitudes (Hoskins (1991), Schneider and Held (1999)). Note that because of this large isentropic slope, the changes in thickness

moving at constant height are different from the changes in thickness following an isentrope. From figure 5-3 the former are significantly larger, which is partly the reason why, visually, the isentropic layers do not appear to open up that much. Another way to look at the changes in thickness is by plotting the vertical profile of the Held scale $h$ (which is proportional to the isentropic slope) at selected latitudes. As shown in panel G, $h$ increases linearly with height. Note the similarity between this figure and figure 2-1, taken from Stone and Nemet (1996). The main difference is that in our runs the isentropic slope does not go to zero above the tropopause, due to the choice of forcing.

Panel E shows the contribution of the potential momentum curvature to the zonal mean PV gradient, normalized by $\beta$. As expected, this contribution is negative over the mixing domain, which results in a reduction in the interior positive PV gradient. However, the generation of interior easterly potential momentum is still insufficient to bring the interior PV gradient to zero, except at the steering level (see panel F and figure 4-20). This is as expected for a forced-dissipative system.

As discussed in section 5.3, the vertically integrated potential momentum is constant when the surface delta function is included. Hence, the development of the interior easterly jet of figure 5-3A must occur at the expense of the depletion of the surface potential momentum. This is illustrated in panel H, which shows the vertically integrated potential momentum in the interior (dashed) and at the surface (solid). Also shown with dash-dotted line is the radiative equilibrium surface potential momentum, which equals the sum of the other two. Note that two different sets of surface values are plotted. The reason is that the definition of the surface potential momentum (equation 5.16) is not unique, but depends on the somewhat arbitrary specification of the endpoints $y_0$, $y_L$: the two sets shown correspond to two alternative choices. This ambiguity in the definition of the surface potential momentum has physical grounds because the amount of potential momentum that can be generated in the interior does depend on the meridional scale of the eddies. Note that the reading of this figure is also somewhat different depending on our choice. With the narrow choice (black lines), the integrated potential momentum at the surface and in the interior are of the same order. However, when a broader domain is considered (red lines) the eddies are seemingly not very efficient in depleting the surface potential momentum.

We next describe the maintenance of the momentum balance. As explained in section 5.3, above the boundary layer there is a balance between the diabatic generation of potential

momentum (panel 5-3I) and the dynamical drag of physical momentum by the eddy PV flux (panel 5-3J). In this framework, the residual circulation simply provides the conversion between both forms of momentum. Comparing panels I and J, we can see that there is indeed an excellent agreement between both forcing terms. This comparison also illustrates the fact that, unlike with the traditional description, in the present formulation there is a *local* balance between the dynamical and non-conservative forcing of momentum. This has important implications because it allows us to unambiguously relate at every position the eddy forcing to the mean flow imbalance[1]. For instance, there must be negative eddy PV fluxes over regions of easterly potential momentum, and viceversa. Moreover, the existence of such a local balance provides some conceptual support to developing diffusive theories of the general circulation (Held, 1999), which relate the local fluxes and gradients.

Nevertheless, it should be borne in mind that, as pointed out in the introduction, the existence of this local equilibrium is dependent upon the flow reaching a statistical steady state. Then, a three-way balance exists between the wave-mean flow interaction, the forcing of the basic state momentum and the rate of dissipation of eddy enstrophy. However, this is no longer the case when either the wave amplitude or the basic flow is unsteady. Moreover, the equilibrium values of wave amplitude, mean flow imbalance, etc. do depend on the adjustment and are therefore non-local in nature. Consider for instance the momentum balance above the boundary layer, as described by panels I, J. Though surface friction does not enter explicitly this balance, the equilibrium PV fluxes do depend on friction.

This is illustrated in panels K, L, which show the time series of the three momentum forcing terms (diabatic, eddy drag and friction), vertically integrated in the interior (including the boundary layer but *not* delta-function contributions at the surface). Panel K corresponds to the run under discussion, while panel L was calculated for a run with weaker surface friction (5 days). We can see that in both cases the diabatic forcing of potential momentum is balanced in the long term by friction and eddy drag, in agreement with equation 5.23. The frictional term is smaller than the other two, but not completely negligible.

Note that the diabatic forcing of potential momentum is larger for the weakly damped case, which implies that the equilibrium potential momentum jet is stronger, and the surface temperature gradient weaker. It may seem surprising at first that the diabatic generation of momentum is larger for this case, since the frictional drag is weaker. The explanation is that

[1]However, note that potential momentum is a non-local definition of the mean flow.

the eddy drag is also larger, and large enough to compensate for the reduced frictional drag. This enhanced eddy drag is in turn associated to an enhanced conversion from potential to physical momentum by the residual circulation. In fact, in the absence of mechanical dissipation the flow fails to equilibrate because the eddy drag is always insufficient to balance the net conversion of potential to physical momentum.

In summary, in the present formalism the baroclinic equilibration can be described in terms of the vertical redistribution of potential momentum. Due to the thermal wind constraint, the interior physical and potential momentum are of the same order. As a result, it is the characteristic values of the zonal wind, rather than the availability of interior PV gradient, that ultimately constrains the interior potential momentum. This is why surface friction is so important. The relation between surface friction and surface temperature gradient is demonstrated in figure 5-4. The left panels of this figure show the partition between the surface and interior potential momentum at equilibration for a number of runs, which have the same interior PV gradient $\beta = 1.6\times10^{-11}\ m^{-1}s^{-1}$ ($H/h = 0.86$) but different frictional time scale. As friction is increased, the transfer of potential momentum into the interior is inhibited and the eddies are less efficient in reducing the surface temperature gradient. This is consistent with the fact (see right panels of the same figure) that the interior jets of physical and potential momentum have comparable magnitude, both being stronger with weaker friction. On the other hand, the diabatic time scale was found to have a much weaker influence over a broad range of the parameter space (not shown).

The formalism derived in this chapter suggests that moderate meridional variations in static stability may have important dynamical implications. This raises many interesting questions about the possible relevance of other forcings and/or feedbacks in more realistic models, as well as in the real atmosphere. For instance, the qg model considered here does not include vertical heat fluxes. While the role of these fluxes for the mean static stability has long been recognized (Gutowski, 1985), it is plausible that their meridional modulation could also be important. Similarly, in our simple model the 'radiative equilibrium' profile to which the flow is relaxed has constant (with $y$) static stability. However, in the real atmosphere diabatic processes are also likely to force the static stability at a local level. In particular, moist convection forces moist adiabatic lapse rates in the subtropics, while the strong radiative cooling at the polar surface favors enhanced stability in those regions. Consistent with this, a more appropriate radiative equilibrium profile should perhaps have

westerly potential momentum in the interior. In this regard, it is intriguing that observations do not seem to show strong contrasts in static stability (Peixoto and Oort, 1992); however, it is fair to say that this specific feature of the thermal structure has received little attention in the past, and local corrections to the mean stratification are both small and noisy. Finally, another feedback that could be potentially important for the baroclinic equilibration in the extratropical troposphere is the momentum forcing by the Hadley cell. By interpreting the baroclinic equilibration in terms of the redistribution of momentum, we have shown in this thesis that the disposal of the westerly momentum by friction is a key ingredient of the equilibration process. This suggests that other forms of momentum forcing, such as the Hadley circulation, could also be important, and the formalism introduced in this chapter provides a suitable framework to look at this issue.

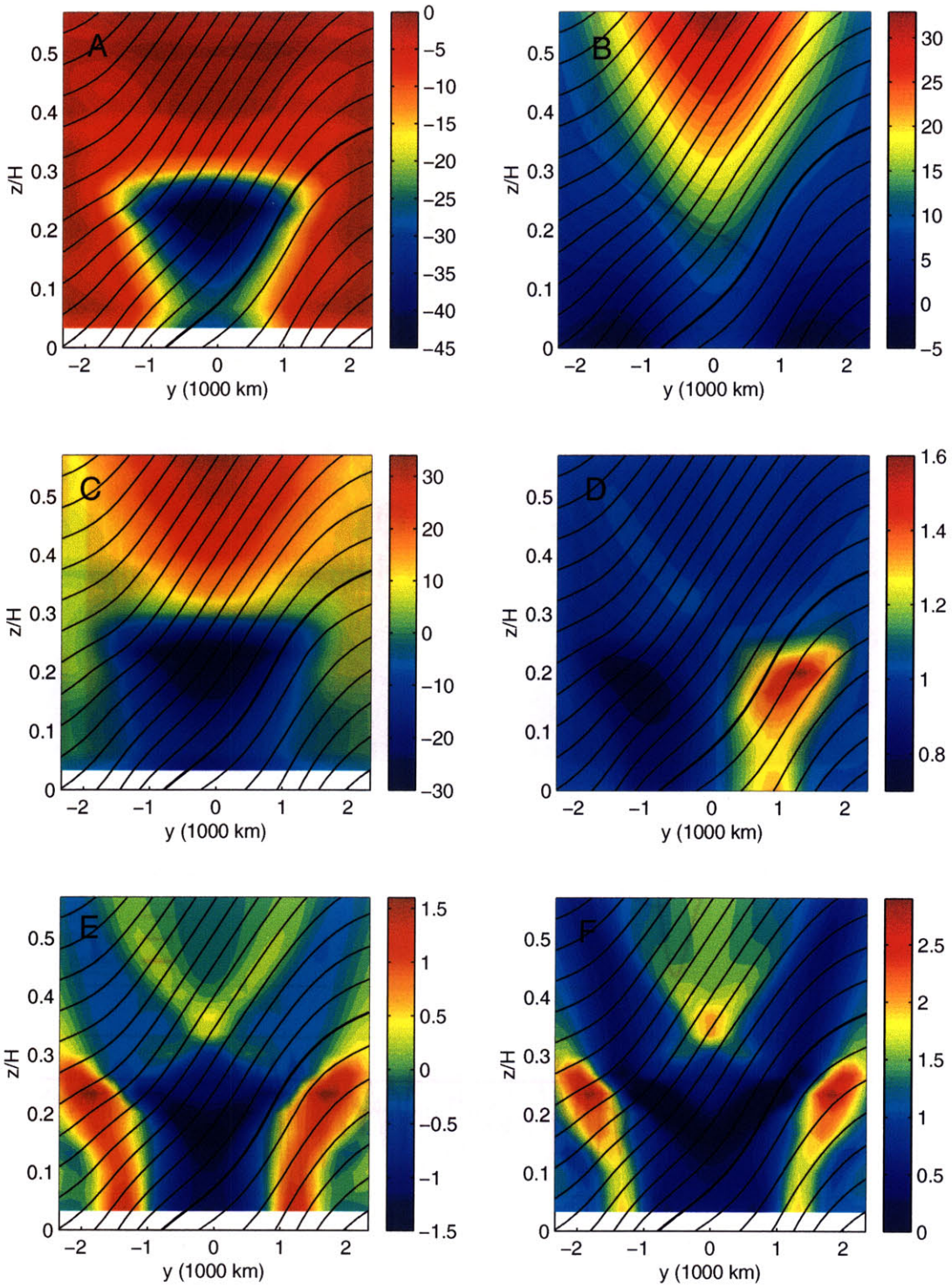


Figure 5-3: Potential momentum diagnostics for the run with $\beta = 3.0 \times 10^{-11}\ m^{-1}s^{-1}$ ($H/h = 1.6$) and friction time scale 1 day. (A) Interior potential momentum (in m/s). (B) Zonal mean flow. (C) Total momentum. (D) Isentropic thickness, normalized by the reference thickness. (E) Potential momentum contribution to the zonal mean PV gradient, normalized by $\beta$. (F) Zonal mean PV gradient, normalized by $\beta$.

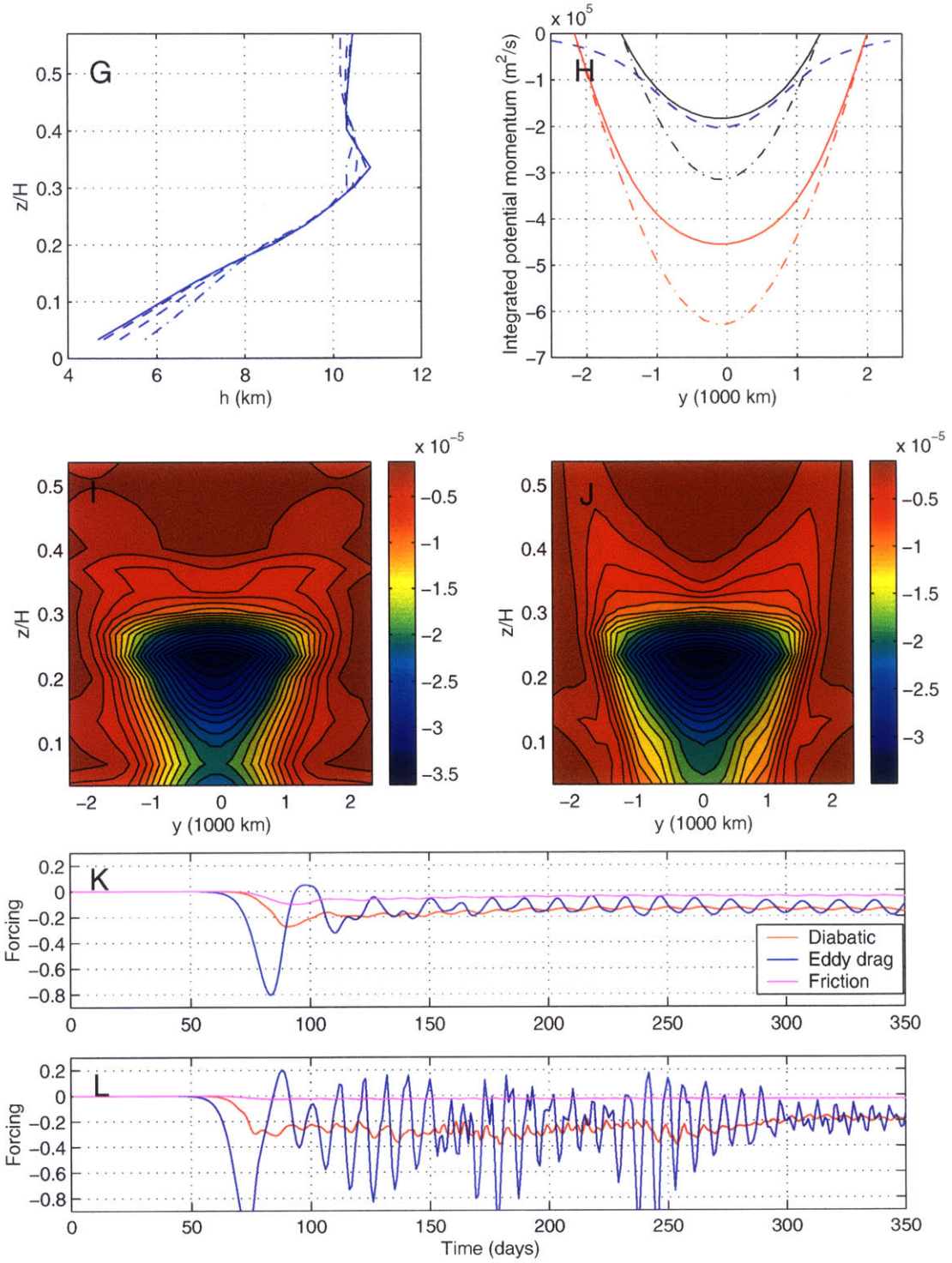


Figure 5-3: (continued) (G) Vertical profile of the Held scale $h$ at selected latitudes. (H) Vertically integrated potential momentum at the surface (solid), in the interior (dashed), and at the surface in radiative equilibrium (dash-dotted). For the surface profiles, two alternative distributions corresponding to different choices of $y_0$, $y_L$ are shown (see text for details). (I) Diabatic forcing of potential momentum in the interior, in $m/s^2$. (J) Interior eddy drag $\overline{v'q'}$ in $m/s^2$. (K) Time series of the different contributions to the interior forcing of total momentum, vertically integrated at the center of the channel: diabatic (red), eddy drag (blue) and frictional (magenta). (L) As K, but for a run with weaker surface friction, of time scale 5 days.

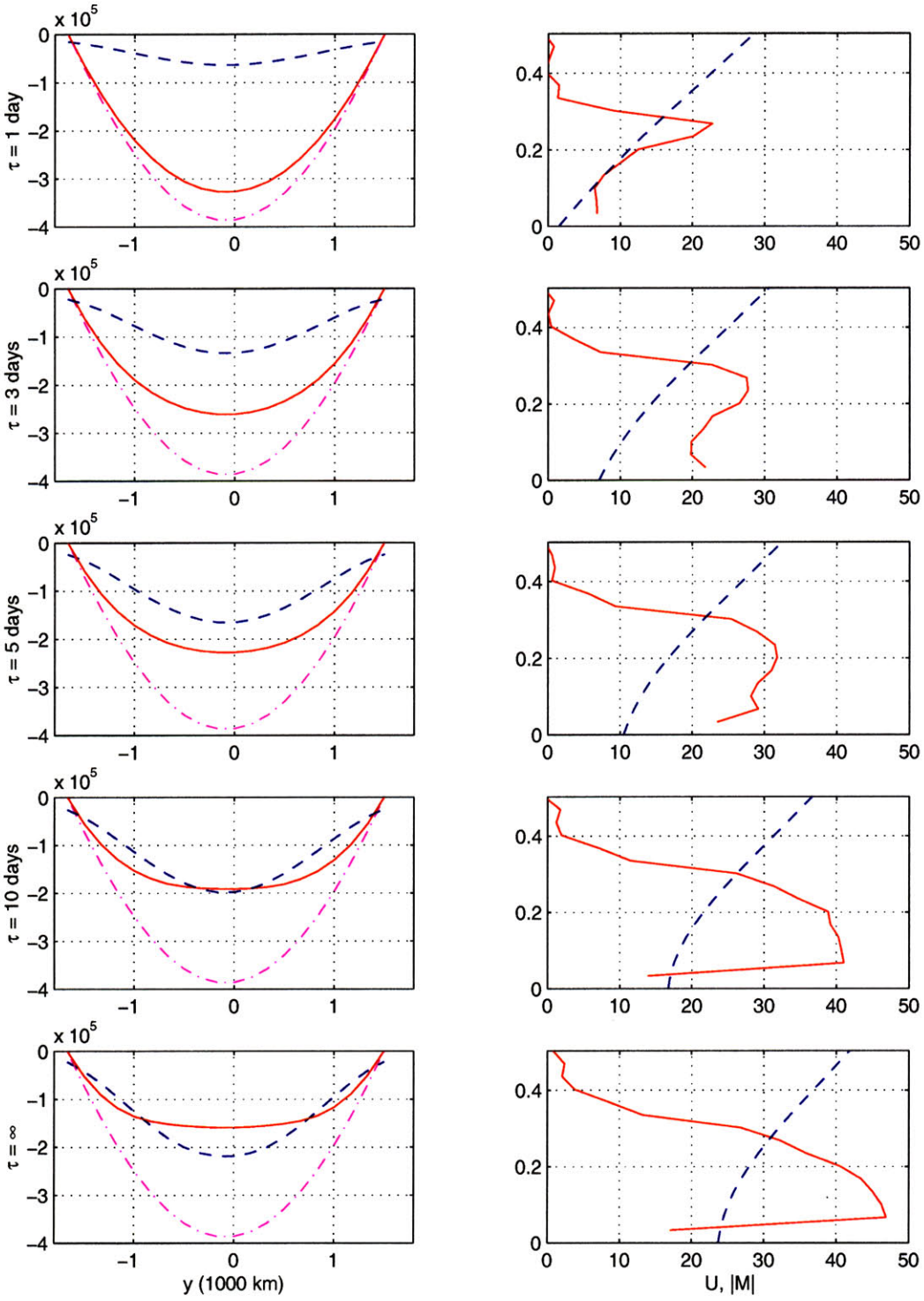


Figure 5-4: For the runs with $\beta = 1.6 \times 10^{-11}\ m^{-1}s^{-1}$ ($H/h = 0.86$) and the frictional time scales indicated: (Left) Integrated potential momentum in the interior (dashed), at the surface (solid), and in radiative equilibrium (dash-dotted). (Right) Vertical profiles of zonal mean flow (dashed) and (easterly) potential momentum (solid) at the center of the channel.

# Chapter 6

# Kinematic aspects

We described in chapters 4 and 5 the equilibration of the barotropic point jet and 3D baroclinic problem, using a momentum framework. The main difference between both problems is the fact that in the baroclinic case momentum can also be imported from the margins of the jet, which affects both the PV gradient distribution and the evolution of the steering level. However, despite this difference we found that a very robust result in both problems is the efficient mixing of the PV gradients at the steering level. In comparison, the elimination of the negative PV gradient is not as robust a result, and only occurs when the region with negative PV gradients is overtaken by the expanding critical layer.

This robust agreement between the well-homogenized region and the critical layer is one of the main results of this thesis, and has been justified in previous chapters using a number of arguments. For instance, the elimination of the PV gradients at the critical level is a necessary condition for the linear neutrality of the final state (Bretherton, 1966). Moreover, because the modal PV flux peaks at the steering level, in a quasilinear equilibration the PV gradients should be smoothed out preferentially at that level. Ultimately, both the evolution of the critical layer and the change in the PV structure are a result of the redistribution of zonal momentum by the waves.

However, while all these are dynamical arguments, the preferential mixing observed at the steering level would also be expected just on kinematic grounds. For instance, it has long been recognized in the stratospheric literature that the spatial distribution of PV and tracers is quite inhomogeneous (see Shepherd (2000) for a review). There are strong gradients at the edge of the polar vortex, and a well-mixed region in the midlatitudes, called

the surf zone. The surf-zone is conceptually associated with the zero-wind line, where the quasi-stationary planetary waves dominant in the stratosphere have their steering level. The well-mixedness of PV and chemical tracers in that region can be explained in terms of the basic kinematic structure of the flow. First, the fact that the streamlines are closed in that region favors a more efficient mixing, and makes it easier for the fluid particles to cross the streamlines. Moreover, because of the intense deformation field, the large scale waves preferentially break in that region (i.e., the enhanced generation of small PV structure in that region favors the diabatic dissipation of enstrophy, see McIntyre and Palmer (1984)).

Given that the equilibration of a baroclinic wave can be described in terms of potential vorticity mixing, it is interesting to examine how applicable the kinematic models used in the stratospheric literature are for this problem. This question is thoroughly investigated below, though we shall concentrate for simplicity on the barotropic point jet. The structure of this chapter is as follows. In section 6.1 we give a literature review on mixing for nondivergent 2D flow, with an emphasis on critical layer dynamics. In section 6.2 we describe the degree of homogenization found in the equilibrated state of the barotropic point jet, using a number of techniques. Section 6.3 gives a Lagrangian view of the dynamical evolution that leads to this PV rearrangement. Finally, section 6.4 provides a conceptual model to understand the evolution of the potential vorticity distribution on the streamlines.

## 6.1 Motivation and literature review

In this section we give a brief review about simple models of mixing in geophysical fluid dynamics. We emphasize the inhomogeneity of mixing, and the mechanisms that might lead to enhanced mixing at the steering level for steady and non-steady flow.

Consider first the case of steady flow, for which we can define streamlines $\Psi(x, y)$. In the non-dissipative limit, the net amount of tracer between two streamlines is conserved exactly. However, in the presence of dissipation there is also a non-conservative tracer flux, both along and across the streamlines, which cannot be balanced by advection. It is important to note that even in the steady case, diffusive processes are not completely independent of advection. In fact, when diffusion is weak, advection can greatly enhance the diffusive fluxes by shearing the tracer along the streamlines, thus augmenting the cross-stream tracer gradients. Rhines and Young (1983) argue that in this limit, the cross-stream

flux is controlled after a short adjustment time by the mean tracer concentration along the streamlines, rather than by its local values. In that sense, the flow can be thought to homogenize the tracer along the streamlines in the short adjustment time, though the actual along-stream homogenization may occur on the longer diffusive time scale[1]. The tracer field is homogenized along the streamlines $J(\Psi, q) = 0$ in the eventual steady state.

In this context, the tracer field is most efficiently homogenized in regions with closed streamlines, which are isolated from the boundaries. This can be essentially understood as a two-stage process, in which the tracer field is initially homogenized along the closed streamlines, and then slowly diffused inward. These simple ideas have been used successfully to explain PV homogenization in the interior (unventilated) ocean (Pedlosky, 1996). The same is true at the critical layer, where the streamlines are closed in a reference frame moving with the wave phase speed. In this context, PV homogenization has important dynamical implications because it makes the critical layer reflective (see Killworth and McIntyre (1985) for a review of critical layer theory). However, the application of these ideas to the stratospheric surf zone is problematic because for steady flow, homogenization only occurs on very long time scales. In reality though, transient effects associated to the planetary wave forcing are thought to greatly enhance the mixing.

As with shear augmented diffusion, transient effects enhance the mixing through the development of small scale structure and large tracer gradients. However, this is much more efficient now than in the steady case, at least because of two reasons. First of all, for steady flow the principal axe of deformation are constant (i.e., the tracer is sheared along a fixed direction). Hence, over the time scales of interest the tracer is just stirred or homogenized along the streamlines, rather than fully mixed. In comparison, the creation of small scale is much more isotropic in the non-steady case, allowing true spatial homogenization. Moreover, particle trajectories diverge exponentially with time for non-steady flow, while the basic state shear only gives linear dispersion in the steady case. Hence, the generation of small scale structure proceeds much faster in the non-steady case, as measured by the Lyapunov exponents (note that the Lyapunov exponent is zero for steady flow).

A useful tool to look at the effect of time-dependence on mixing is chaotic advection (Ottino, 1990). The basic idea is that regular Eulerian kinematic fields can still give rise

[1]In practice, numerical models tend to be artificially diffusive in the along-stream direction (see appendix B), which also contributes to the along-stream homogenization

to chaotic Lagrangian trajectories, and hence to mixing, provided that the flow is time dependent. In the non-dissipative limit, the passive advection of a tracer is a Hamiltonian system, with $\mathcal{H} = \Psi$. This allows us to borrow useful ideas from the theory of dynamical systems. For instance, in the steady limit the system cannot support chaos because it only has two degrees of freedom. In that limit, all orbits are integrable under the appropriate coordinate transformation and the solution is regular; the tracer is then simply stirred along the streamlines. The same is true when the time-dependence is trivial, as for a steadily propagating wave: in the corrotating frame this flow is still steady. However, in the presence of non-trivial time-dependence, the Hamiltonian system has 3 degrees of freedom, and is found to produce chaotic trajectories even for the simplest flows. The theory of chaotic advection is based on this paradigm, that regular but time-dependent Eulerian motion can produce chaotic Lagrangian behavior and hence small scale homogenization.

There are many idealized chaotic advection studies in the literature, which examine the mixing achieved by simple velocity fields with prescribed time-dependence. In this regard, it is often illuminating to study the transition to chaos when perturbing some reference steady system, which is deemed representative of the large scale flow. In the geophysical context, such a system is provided by the steadily propagating wave. A classical way to perturb this system is by means of the two-wave model (Pierrehumbert, 1991), in which a second wave with different phase speed is added. We can then study the transition to chaos by examining how the structure of the phase space, as seen for instance in a Poincare diagram, changes with the amplitude of the second wave. Depending on this amplitude, chaotic and regular regions of different sizes appear; trajectories diverge exponentially in the former but only linearly in the latter, and the resulting mixing is inhomogeneous. This can be understood in terms of the unperturbed phase space structure. In particular, chaos first appears around the unstable manifold of the unperturbed problem, i.e., the Kelvin's cat eye associated to the steering level of the primary wave, and extends further in phase space as the amplitude of the second wave is increased. However, for moderate amplitudes the behavior on the trajectories surrounding the heteroclinic orbit (i.e., the open streamlines) is still regular, so that this region acts as a mixing barrier. The destruction of this mixing barrier requires global chaos, which in the two-wave model occurs when the amplitude of the second wave is large enough that its own cat's eye overlaps with that of the primary wave (see for instance Del Castillo Negrete and Morrison (1993)). Similar results are found with

other idealized forms of time-dependence, for instance when adding a stochastic component to the advecting field (Ngan and Shepherd, 1999) or the phase speed of the wave (Bowman, 1995). If the system is weakly perturbed, the phase space structure of the unperturbed problem is still relevant for the inhomogeneous mixing. This provides a useful paradigm in which to understand the enhanced mixing at the steering level.

The chaotic advection models described above are kinematic models, in the sense that the idealized velocity field is simply prescribed. While these models are useful for understanding how certain flows can mix passive tracers, things are more complicated when the mixing of potential vorticity is considered. The problem is that the kinematic models are not dynamically consistent because the velocity fields that do the PV mixing should depend on the PV distribution itself. These models can still be useful, however, provided that we are only concerned with the mixing of the fine-grained potential vorticity. The scale selectivity of the Laplacian operator implies that the advecting velocity field is primarily associated to the large scale PV, and should therefore be unaffected by the mixing of the small scale potential vorticity. A well-known example in which this uncoupling is made explicit is classical critical layer theory (Killworth and McIntyre, 1985). To first order, the advecting velocity field is externally imposed, and is independent of the PV structure inside the critical layer (Ngan and Shepherd, 1997).

Alternatively, actual dynamical models can be considered. For instance, Pierrehumbert (1991) integrated the initial-value two-wave problem, and interpreted his results in terms of the phase space structure. A more relevant geophysical example is the equilibration of a barotropically unstable vortex, which may have applications for the 4-day wave sometimes observed in the wintertime middle atmosphere (Lait and Stanford, 1988). A series of papers have modeled in recent years the instability and equilibration of an idealized vortex representative of the polar night jet (e.g., Ishioka and Yoden (1994), Bowman and Chen (1994), Orsolini and Simon (1995), and others). Ishioka and Yoden (1995) produced a regime diagram for an idealized jet, for which vacillating and irregular solutions can be found depending on the values of the parameters. Mizuta and Yoden (2001) compared the mixing properties of these solutions using finite time Lyapunov exponents, and found that the structure of the phase space provides a good description of the inhomogeneous mixing.

The results of these dynamical models thus suggest that the phase space structure of the final equilibrium state provides a consistent description of the inhomogeneous mixing

in that state. However, from an equilibration point of view, a more relevant problem is what determines that phase space structure, which is a result of the transient dynamical evolution. In particular, the structure of the final state depends on the mixing of potential vorticity as the wave equilibrates. Note that this problem is not very amenable to chaotic advection theories: because the basic structure of the flow changes as the wave equilibrates, there exists no robust phase space. Recently, Malhotra and Wiggins (1998) have developed a generalization of the phase space that also includes time.

A more physical framework in which to understand the dynamical evolution of the large scale PV field is provided by contour models. In these models, the continuous PV distribution is discretized in a reduced number of contours. The dynamical evolution can then be described in terms of the evolution of these contours, as they are advected by the Lagrangian flow that they induce. The simplest such model is the one-contour model; this minimal model can still provide insight into the nature of the large scale rearrangement of PV. For instance, Polvani and Plumb (1992) used a one-contour shallow water model to study the evolution of a perturbed vortex. For small amplitude, the wave does not break and there is no transport to or from the perturbed vortex, even though the wave dynamics may be nonlinear if the amplitude is large enough. However, the behavior is qualitatively different when the amplitude is sufficiently large that the perturbed vortex reaches the external critical line. In that case, a stagnation point forms and there is extrusion of vortex air through filamentation and wave breaking. Similar results were found in the study of Swanson et al. (1997). These authors used a one-contour model to study the barotropic modulation of a wavepacket as it propagates along a zonally varying flow characteristic of the Northern winter upper troposphere. What they found is that for small initial amplitude, wave action is conserved as the wavepacket propagates, and any modulation is reversible. However, for large enough amplitude the waves break as they enter the region of weakest zonal flow, where the critical level is closest. Swanson et al. (1997) were able to predict the threshold amplitude based on when the contour reaches a stagnation point, and suggested that wave breaking should effectively limit the amplitude to this value.

This idea has been recently used by Held (2001) to provide a closure for his diffusive stormtrack model, by arguing that the wave amplitude (and hence the lower level diffusivity) is constrained by the position of the zero wind line at upper levels. Part of the motivation for the study described in this chapter was to test this hypothesis, and to see whether the

position of the steering level does indeed have any bearing to the maximum wave amplitude at equilibration. This issue will be investigated in section 6.3, but we shall concentrate for simplicity in the barotropic point jet problem. Before that, we discuss in section 6.2 the degree of homogenization found in the equilibrated state of the model.

## 6.2 PV homogenization in the barotropic problem

In this section we describe the structure of the mixing for the barotropic point jet, using kinematic ideas. We refer the reader to section 4.1 for specific details about the setup of the runs, dynamical evolution and equilibrated states. As described there, this problem equilibrates by mixing PV at the steering level. This involves the elimination of the negative PV gradient at the jet vertex in the case of the most unstable mode ($L/l = 3.9$), but not for the shorter waves (see figure 4-7).

It is tempting to argue that the efficient elimination of the negative PV gradient by the most unstable mode is due to its larger growth rate, which should favor a more efficient mixing. However, while the mixing efficiency should be connected at some level to the growth rate, the zonal mean PV gradient does not really provide a good indication of mixing in the full two-dimensional sense. As discussed in section 4.1.2, the zonal mean PV gradient at equilibration depends on the scale of the wave, rather than on its growth rate. Waves that are longer than the most unstable mode and more weakly growing are also successful in eliminating the negative PV gradient (c.f., figure 4-10).

We can get a qualitative idea of the thoroughness of the mixing by looking at the full two-dimensional PV structure of the final state. This structure is shown in figure 6-1 for the cases with $L/l = 1.25$, 2.5, 3.9, 5.1. Consistent with other barotropic equilibration studies (Kwon and Mak, 1988), in all four cases the final state consists of a finite amplitude, quasi-steady wave (plus its harmonics). Note that though the PV gradients at the center of the channel are smallest for the most unstable mode ($L/l = 3.9$), even in that case homogenization only occurs along localized regions. These well-homogenized regions are on the sides of the perturbed jet, which still appears to act as a weak mixing barrier. In fact, figure 6-1 suggests that the reduced zonal mean PV gradients at the jet vertex for this case are a consequence of the meridional tilt of the PV contours, rather than an indication of spatial homogenization (what we mean by that is small PV gradients *in all directions*).

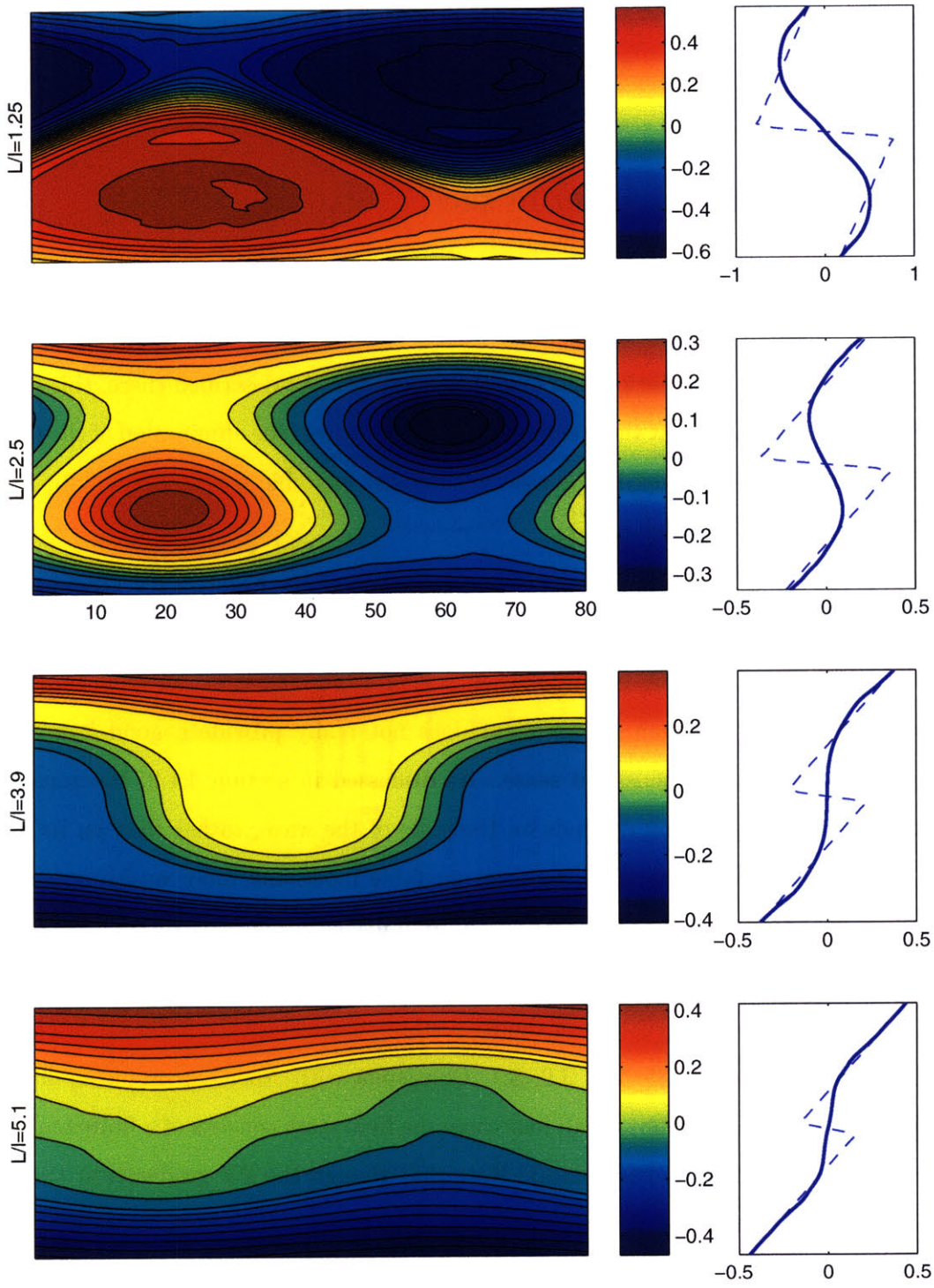


Figure 6-1: Snapshots of the long-time potential vorticity field for the runs indicated (contour unit $0.1\beta L$). Also shown on the right panels are the zonal-mean profiles of $\overline{q}/\beta L$ for the equilibrated state (solid) and radiative equilibrium (dashed).

The same is true for the small zonal-mean PV gradients observed at the steering level in the top two panels. Figure 6-1 shows that these small PV gradients do not necessarily imply the spatial homogenization of the PV field at the critical latitudes. In particular, full spatial homogenization would also require that eddy potential enstrophy vanish at these latitudes, which is not observed. This is emphasized in figure 6-2, which compares the zonal mean PV gradient and eddy enstrophy profiles. As can be seen, the eddy enstrophy does not vanish in general at the latitudes of zero PV gradient; indeed, for the $L/l = 2.5$ case there is an eddy enstrophy maximum at that latitude.

Note that global spatial homogenization would demand that eddy enstrophy vanish over the central part of the channel. This would be the case if either eddy enstrophy was pushed away to the boundaries of the mixing domain, or it cascaded to scales sensitive to diffusion or unresolved by the model. However, it is apparent from figure 6-2 that neither is the case for the short Charney modes (i.e., $L/l \leq 3.9$), all of which have a mid-channel eddy enstrophy maximum. Also note that though the model does lose some enstrophy, a large fraction of the enstrophy lost by the zonal mean still remains in the large scale eddy field. It is noteworthy in this regard that the domain-integrated eddy enstrophy is very similar for all short Charney modes. This is not surprising because, as discussed in section 4.1.2, the reduction in zonal mean enstrophy is also very similar for all cases (c.f., figure 4-8). These results are also consistent with the findings of Schoeberl and Lindzen (1984) that the eddy enstrophy saturation limit is independent of the wavenumber. Finally note that for the longwave run ($L/l = 5.1$), there is a better homogenization at midchannel: the model appears to lose more enstrophy to unresolved scales, and the maxima of the large scale eddy enstrophy field are found on the sides, at the model tropopause.

The persistence of mixing barriers in these simulations may be related to the quasi-steadiness of the velocity field. As explained in section 6.1, for stationary flow passive tracers are essentially homogenized along the streamlines. Weak time dependence induces some cross-stream mixing or local chaos, but not enough to destroy the mixing barriers, which can only be eliminated in the presence of intense time-dependence and widespread chaos. As mentioned above, the final state in our simulations consists of a quasi-steady wave. Though there is some non-trivial time-dependence (for instance, the phase speed of the waves is unsteady, see figure 6-8), it appears to be too weak to induce significant cross-stream dispersion. This is ultimately the reason why the mixing barriers still persist,

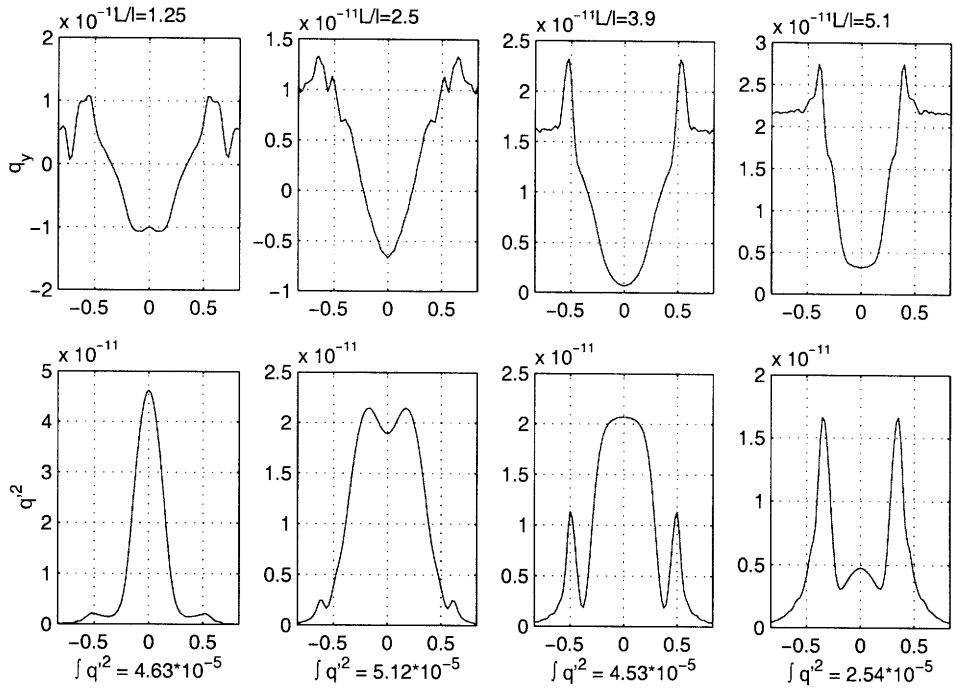


Figure 6-2: Comparison of the zonal mean PV gradient (top) and eddy enstrophy (bottom) profiles for the cases indicated. We also provide for reference the domain-integrated eddy enstrophy.

as will be confirmed below looking at some Lagrangian trajectories.

Even in the absence of spatial homogenization, the flow is still very efficient at locally eliminating the zonal-mean PV gradients at the steering level. This can be explained using simple kinematic arguments, without invoking wave breaking or chaotic advection. Essentially, the flow reaches a quasi-steady solution, in which the PV field is homogenized along the streamlines in a reference frame moving with the wave phase speed: $J(\Psi, q) = 0$ (where $\Psi$ is the streamfunction in the corrotating frame). This is illustrated in figure 6-3 for the case with $L/l = 3.9$. Panels A and B show the $\Psi$ streamlines and PV field at time $t = 45$ *days*, shortly after the wave reaches its maximum amplitude, while panels C and D show the same fields for the steady state that eventually sets in ($t = 191$ *days*). Despite the very different PV fields, the streamlines are remarkably similar at both times, illustrating the well-known fact that the kinematics of the flow are essentially a function of the coarse-grained potential vorticity. Once the kinematic structure of the top left panel is reached, the coarse-grained PV remains invariant, and the fine structure is for the most part simply homogenized along the streamlines, with some minor cross-stream dispersion. The efficient homogenization of PV along the streamlines is manifest in panels E and F, which show a scatter plot of these two fields at the aforementioned times. The same is true for the shortwave case $L/l = 1.25$

(panels G, H), but in this case the $q - \Psi$ relation is multi-valued.

By definition, $U - c = 0$ at the steering level, so that the flow is purely meridional in a reference system moving with the wave. As a result, when PV is homogenized along the streamlines, it can only be a function of $x$ in those regions. This explains why the zonal-mean meridional PV gradients at the steering level are small, even though the PV field is not strictly homogenized. This is apparent in the quasi-meridional tilt of the PV contours at the jet vertex for the case of the most unstable mode, and at the steering level for the top two panels of figure 6-1. Note that because the growth of the perturbation occurs primarily at the expense of the zonal mean, from a linear stability point of view it is irrelevant whether potential vorticity is truly homogenized or just meridionally stretched. In this regard, note that the wave-mean flow and fully nonlinear models of Schoeberl and Lindzen (1984) and Nielsen and Schoeberl (1984) equilibrate in the same manner.

In the experiments presented above, the channel length is truncated so that most of the mixing is accomplished by a single mode. Hence, it is not surprising that the solution consists of a single finite amplitude wave. Seeking more complicated time-dependence, which could perhaps favor more efficient mixing, we have performed additional experiments with a longer channel, in which the most unstable mode has wavenumber 4. The final state in that case was found to depend on the initial conditions. In general, the solution no longer consists of a single finite amplitude wave, but there are several peaks in the frequency domain. Figure 6-4 compares snapshots of the PV field for this case and for the standard run. We can see that for the long channel, longer waves than the most unstable mode seem to dominate. The mixing barrier is significantly weaker than for the short Charney modes, but still not fully destroyed. In that sense, the final state of this run shows some resemblance to the longwave ($L/l = 5.1$) simulation of figure 6-1.

### 6.2.1 Statistical diagnostics

As shown above, short Charney modes are unable to destroy the mixing barrier at the perturbed jet. Though this barrier typically traverses the critical latitude, the zonal-mean PV gradient there is still small because the barrier is meridionally oriented across that latitude. In principle, it is plausible that the equilibration could just involve the stretching and reorientation of the contours in this manner. After all, the zonal-mean PV gradient is all that really matters for the linear stability of the large scale, and this is just a function

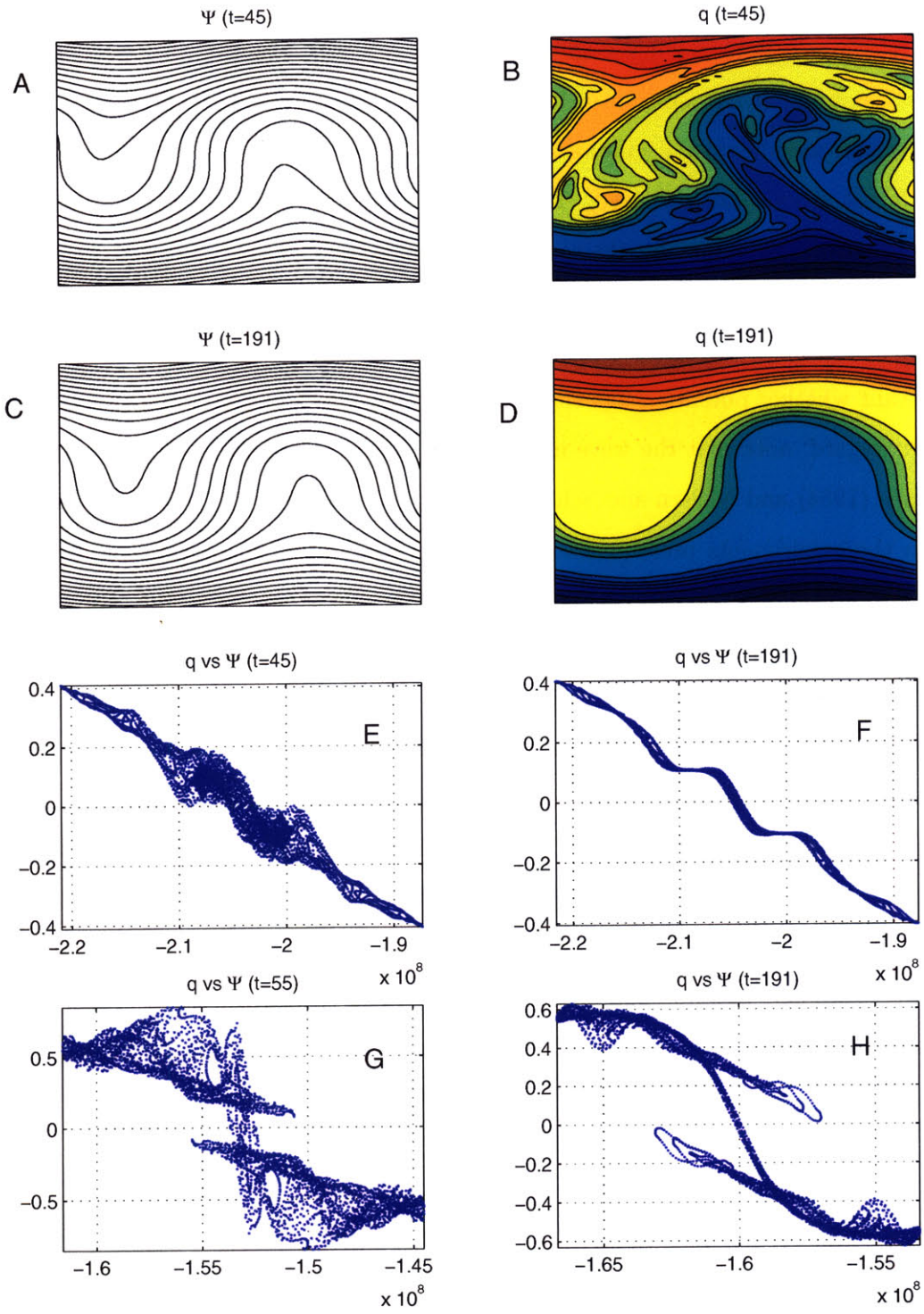


Figure 6-3: For the run with $L/l = 3.9$: A) Streamlines in the corrotating frame at $t = 45$ *days*, B) Potential vorticity field at the same time. C) and D) As A and B but for $t = 191$ *days*. E) Scatter plot of $q$ (normalized by $\beta L$) vs $\Psi$ at $t = 45$ *days*. F) As E but at $t = 191$ *days*. G) and H) As E and F but for the run with $L/l = 1.25$.

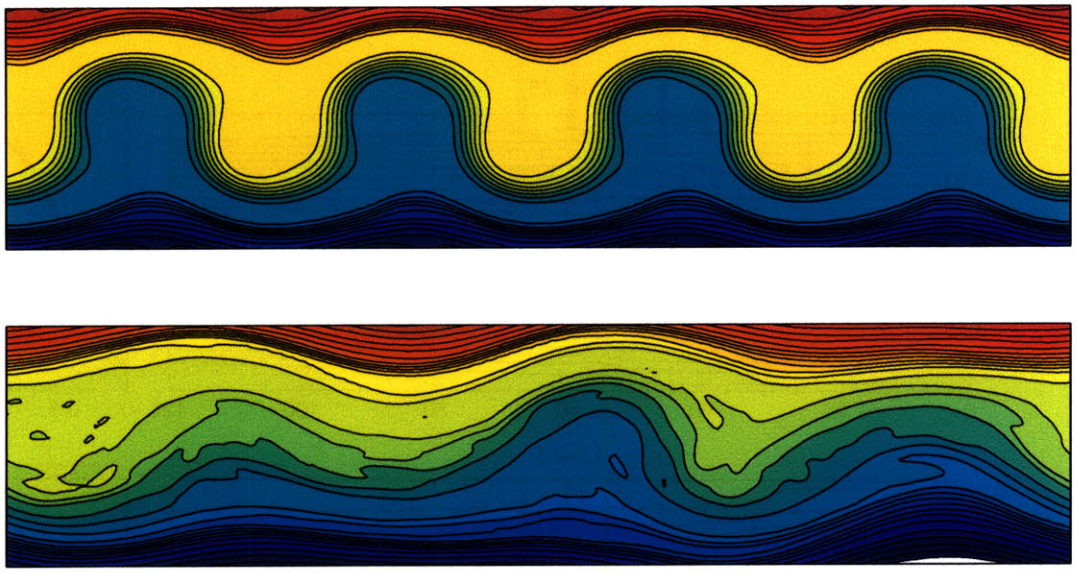

Figure 6-4: Snapshots of the PV field (repeated 4 times) for the standard channel length with $L/l = 3.9$ (left), and for a channel 4 times longer (right).

of the mixing length, regardless of the degree of homogenization. Even when the PV jump across the jet changes sign at equilibration (as is the case for the most unstable mode), this can be achieved just by adiabatic rearrangement of PV.

However, it is also apparent from inspection of figure 6-1 that well-homogenized regions do exist, even if they do not appear to stretch all the way along the critical latitudes. One way to estimate this mixing is by looking at the PDF of the potential vorticity field (Sparling, 2000), and how it evolves with time. In particular, well-mixed regions are characterized by peaks in the distribution, and mixing barriers by local minima (see also Neu (2001)). These PDFs can be easily estimated in our model, by simply binning the two-dimensional gridded output. Note that if potential vorticity were simply rearranged adiabatically, this PDF would remain unchanged. Though our model does not incorporate any explicit dissipation, there is an implicit numerical dissipation associated with the truncation of the unresolved scales (see appendix B for details).

Figure 6-5 shows the time series of the cumulative PDF of the PV field for the same four cases of figure 6-1. We also compare on the right panels the initial (dashed) and final (solid) cumulative distributions. Note that well-mixed regions can be identified in these plots by a clustering of the density contours (i.e., the cumulative PDF grows steeply), whereas well spaced contours indicate poorly populated values, and thus identify mixing barriers.

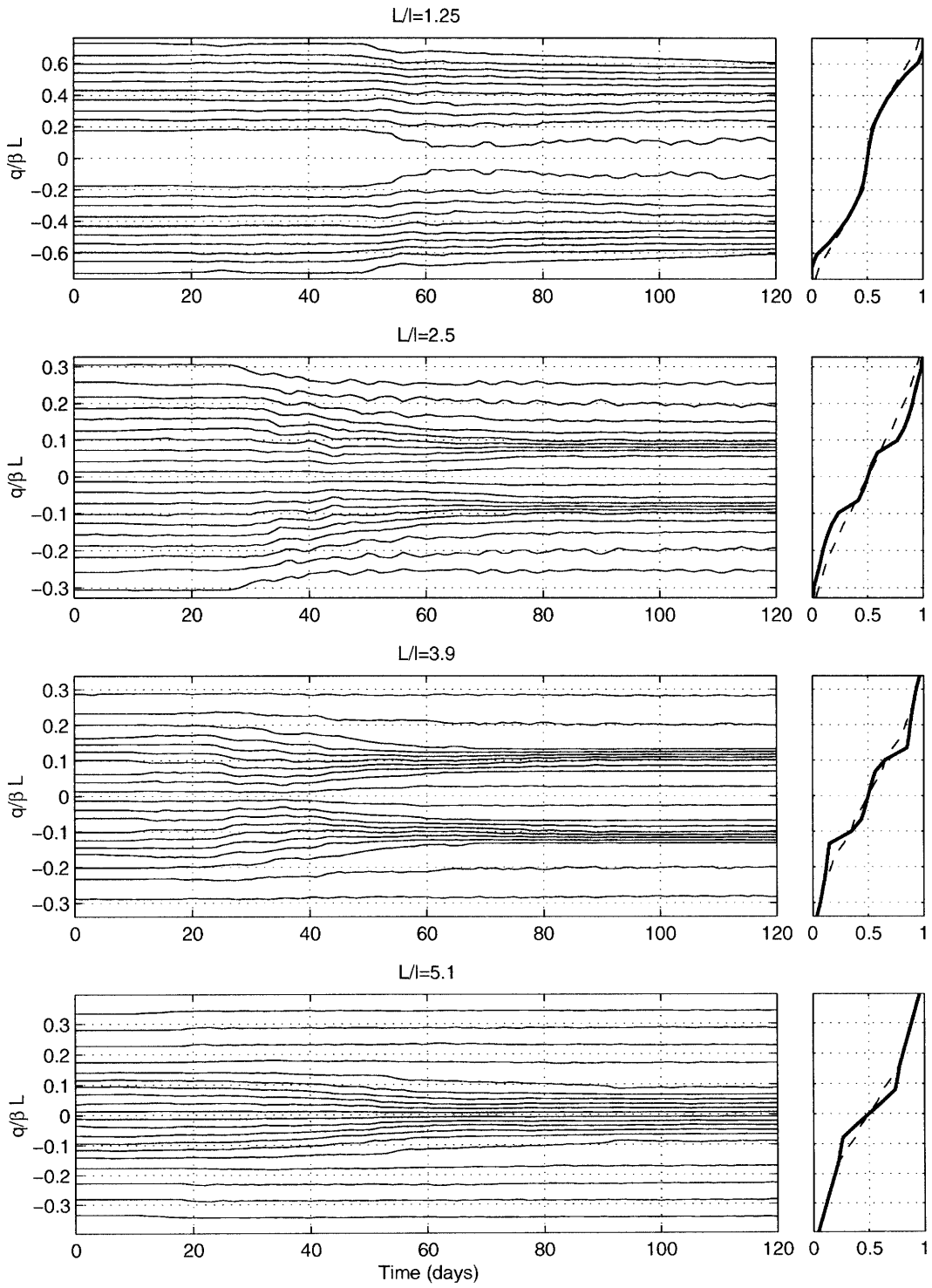


Figure 6-5: Time series of the potential vorticity cumulative distribution for the runs indicated; a 5% of the total distribution lies between any two adjacent contours. Also shown on the right are the initial (dashed) and final (solid) cumulative distributions.

In the initial state, the contours appear to be for the most part evenly spaced, suggesting that the associated PV distribution is uniform (indeed the interior PV gradient is constant: $\overline{q}_y = \beta$). However, because there is also a negative jump at the jet vertex, the PV field is multi-valued. This implies that moderate values of $q$ are populated by grid points from both halves of the domain, while extreme values reflect contributions from just one half[2]. As the flow equilibrates, the contours tend to cluster together in some regions, and to separate in others. The clustering of the contours is indicative of PV homogenization. Remarkably, the highest degree of homogenization is observed for the most unstable mode ($L/l = 3.9$), even though the longer wave ($L/l = 5.1$) seems to be more successful in destroying the central mixing barrier. This is not in contradiction because the well homogenized regions are found on the margins of the jet for the former, and at the center of the channel for the latter.

### 6.2.2 Discussion

The equilibrium solutions of the barotropic point jet that we have found are quasi-steady, which ultimately prevents chaotic advection from fully eliminating the mixing barriers. Though there are regions of well-mixed PV, the flow fails to achieve PV homogenization in a global sense. In the next section, we examine in more detail the dynamical evolution in this problem, and argue that this mixing pattern arises from a combination of along-stream homogenization and weak cross-stream dispersion. This weak mixing can be explained using the theory of chaotic advection, based on the kinematic fields associated to the quasi-steady large scale vorticity structure described here.

However, a more relevant question from an equilibration point of view is, what defines this vorticity structure? One possibility would be that the PV contours are just stretched across some finite distance. In fact, this is what the simple one-contour models discussed in section 6.1 envision. In those models, the maximum displacement of the PV contour, and thus the amplitude of the PV perturbation, is ultimately constrained by the position of the steering level. However, this is not what is going here, at least not for the $L/l = 3.9$ case. To be sure, the sign of the PV jump across the jet is reversed in this run, which requires an exchange of material between both sides of the contour. As a result, the amplitude of the

[2]To see this, think of the initial PV distribution (dashed profiles in figure 6-1). In this regard, note that the PDF for the shortest wave ($L/l = 1.25$) is zero for $|q| < 0.2\beta L$. The reason is that the negative PV jump dominates the integrated $\beta$ over the mixing length, thus creating two disjoint populations in the PDF

PV perturbation is a function not just of the contour displacement, but also of the mean PV jump across the perturbed contour. Regardless of whether PV is also homogenized as it is rearranged, it is this rearrangement that is dynamically significant, and what ultimately constrains the kinematic fields that are responsible for any subsequent chaotic mixing.

It is plausible that in more realistic flows with complicated time dependence, like in the study of Mizuta and Yoden (2001), chaotic advection could contribute to the destruction of the resonant islands, favoring a better homogenized surf zone at the steering level than seen here. However, whether this occurs or not is in some sense dynamically irrelevant, as long as chaotic advection only homogenizes the small scale structure at the critical latitudes without changing the basic structure of the flow. In this regard, there is a conceptual subtlety (already noted by Pierrehumbert (1991)) that suggests that chaotic advection models could never be relevant for large scale mixing. For one thing, chaotic advection models assume that a time-dependent but regular Eulerian velocity field is responsible for the chaotic Lagrangian motion. However, if the Lagrangian chaos was indeed global in scale, it would act to destroy the mixing barriers, and hence the large scale vorticity structure and the very velocity fields supporting the Lagrangian chaos. For this reason, a kinematic model displaying global chaos could never be dynamically consistent, and chaotic advection models based on regular Eulerian kinematic fields should only be applicable for small scale mixing. The maintenance of *global* Lagrangian chaos would then seem to require a truly turbulent field, in which the Eulerian velocity is itself chaotic. In this regard, it is interesting that the recent paper of Finn and Del-Castillo-Negrete (2001) suggests that such a connection does exist between the appearance of Eulerian chaos and the global extension of the Lagrangian chaos for an idealized problem.

## 6.3 Dynamical evolution

We argued in the previous section that the dynamically relevant rearrangement of PV in this problem occurs in a single episode following the growth and breaking of the wave. In this section, we examine in more detail the time sequence of events leading to this rearrangement. Note that because there is not a robust phase space, the standard tools of dynamical systems used in the context of chaotic advection are not necessarily applicable. As the wave grows, the phase space evolves, and hyperbolic points form. Whether the

associated unstable manifold is relevant for mixing or not depends on the growth rate. If the wave is slowly growing or nearly saturated by the time the hyperbolic points form, the resulting phase space is relatively robust, and can be used to diagnose the subsequent mixing. Otherwise, the hyperbolic points carry no real significance, as the phase space will continue to evolve. In fact, when the flow is strongly unsteady intense mixing can occur even in the absence of a heteroclinic structure in the instantaneous phase space. Recently, Malhotra and Wiggins (1998) have developed a generalization of the phase space for non-periodic flows. In that case, it is still possible to define hyperbolic trajectories in the extended phase-time space, and the corresponding stable and unstable manifolds. However, the calculation of the extended phase space is complicated and may not bring new light to the problem.

Thus, to investigate mixing in this problem we have rather chosen to use a more physical approach and look at how a material contour initially at the jet vertex deforms. In the initial flow, this contour separates regions of high PV to its south and low PV to its north. As the wave grows and breaks, there is an exchange of material between both sides of the perturbed contour, which in the case of the most unstable mode is vigorous enough to reverse the initial negative PV gradient. Note that because we are using a gridpoint dynamical model (as opposed to a contour model), the potential vorticity distribution at later times is continuous and no vorticity jump actually occurs at the perturbed contour. Nevertheless, because of the symmetry properties of the flow, this contour can still be thought to mark the edge of the perturbed vortex at all times.

The methodology followed is essentially that described by Waugh and Plumb (1994). We advect a large number of material particles using velocity fields interpolated from the numerical grid. When the distance between two adjacent particles exceeds some predetermined threshold, additional particles are added in between. Redundant particles which get too close to each other are also eliminated for computational efficiency. At the expense of large computation times, we have chosen not to apply surgery. This allows us to study how much area the deformed contour fills, much like in a Poincare map, but puts a severe constrain on the length of the time integration which is computationally feasible. Other technical details about the contour advection algorithm, such as the parameters used for this study, are given in appendix B. We next discuss the dynamical evolution for a shortwave and for the most unstable mode.

### 6.3.1 Evolution of the weakly growing wave ($L/l = 1.25$)

Figure 6-6 shows the results for the case with $L/l = 1.25$; we recall that the scale of this wave is too small to eliminate the negative PV gradient. The left panels show the perturbed contour (thick, solid) superimposed to the streamlines in the corrotating reference frame (or instantaneous phase space). Closed streamlines are plotted broken and can be conceptually identified with the nonlinear critical layer. Finally, the shaded area emphasizes regions where $|U - c| < 1\ m/s$. On the other hand, the right panels show the PV field at the same times. Our discussion will also make reference to figure 6-8, which shows the time series of growth rate and phase speed.

At time $t = 26\ days$, an area of closed streamlines appears centered at the steering level. At that time, the deformation of the material contour at the jet vertex is still hardly observable. As the wave grows, the critical layer (defined as the region with closed streamlines) broadens, and a hyperbolic point becomes prominent at the steering level. Some PV stirring can already be seen in the region of closed streamlines at time $t = 42\ days$. However, the material contour, where most of the gradient is concentrated, still displays a wavelike behavior. Figure 4-1 shows that the PV gradient at the critical level is homogenized about this time; note that the zonal mean negative PV jump is also smoothed, simply because of the stretching of the contour. However, the elimination of the PV gradient at the steering level seems to be insufficient to stabilize the wave, partly because the steering level moves slightly outward as PV is mixed (see figure 6-8).

After $t = 53\ days$ the material contour reaches the steering level for the first time, and the critical layer occupies the whole domain. Because the growth rate is largely reduced by that time, the contour reaches the steering level in the close neighborhood of the stagnation point. As a result, a thin filament is ejected (by symmetry from both sides), and is seen to wrap around the steering level at subsequent times. Note that this filament is very thin, so that the exchange of material between both sides of the jet is minimal, and the PV jump remains well defined for subsequent times. This would be comparable to the microfilamentation examples of Polvani and Plumb (1992). By the end of our integration ($t = 98\ days$) the deformed contour has filled an area surrounding the heteroclinic orbit, but not the whole phase space. This behavior is alike the stochastic bands sometimes seen on a Poincare map for periodic flow, and in the same manner indicates local rather than

widespread chaos.

As mentioned in section 6.1, chaotic advection requires some time variability in the Eulerian kinematic field. Otherwise, the fluid would just be stirred and homogenized along the streamlines, but not fully mixed. A nice illustration of this is provided by the well-mixedness along the region of closed streamlines, as demonstrated in the top panel of figure 6-1. If the flow were steady, the fluid parcels would just describe closed orbits in that region. In practice, however, they are found to spiral in through the closed orbits (see for instance the panel at $t = 53$ *days*), thus facilitating a more thorough homogenization. This spiraling is due to the fact that the growth rate adds an additional component to the velocity field (see below), which essentially allows the fluid parcels to cross the closed orbits.

Similarly, the stochastic band described above requires some time variability in the Eulerian kinematic field. This might be provided by the phase speed oscillations and/or the growth/decay episodes apparent in figure 6-8. Both induce small perturbations in the instantaneous phase space, which results in manifold stretching and localized chaotic mixing. Note that, reversibly, this time variability is also a result of the mixing of the fine-grained vorticity which it induces, since our model is dynamically consistent. For instance, it might be possible to relate the period of these oscillations to some physical time scale, such as the Lagrangian circulation time around the resonant islands. However, we have not explored this fully. In any case, because the large scale vorticity has already reached a steady pattern by that time, this time variability only introduces a small perturbation to the phase space, which remains robust for subsequent times. This is why in the final state there is only local chaos, and the concepts used in the context of chaotic advection still apply.

Finally note that this example also supports the hypothesis put forward in section 6.1 that the position of the steering level might constrain the maximum wave amplitude, as suggested by the studies of Polvani and Plumb (1992) and Swanson et al. (1997). In essence, wave breaking prevents any perturbation to the vortex to overshoot the steering level. However, this is not always the case, particularly when the growth rate is large.

### 6.3.2 Evolution of the most unstable mode ($L/l = 3.9$)

We analyze now the temporal evolution of the most unstable mode ($\beta = 1.6 \times 10^{-11}\ m^{-1}s^{-1}$, $L/l = 3.9$), which is described in figure 6-7. Note that in this case the interior PV gradient, integrated over the meridional scale of interest, is of the same order as the vorticity jump

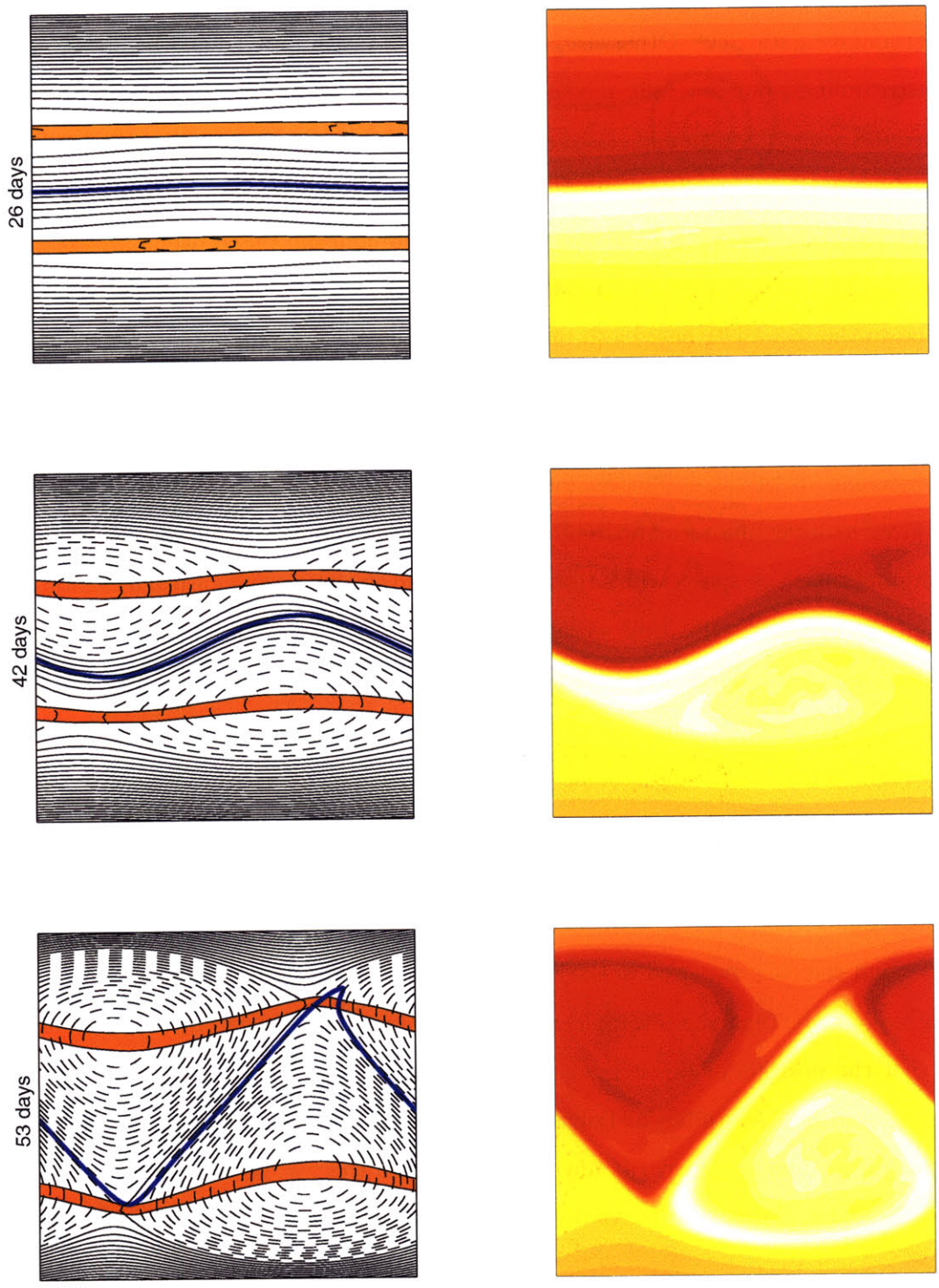


Figure 6-6: For the run with $\beta = 5 \times 10^{-12}\ m^{-1}s^{-1}$ ($L/l = 1.25$) and $t = 26$, 42, 53, 57, 68 and 98 *days*. Left: streamlines in the corrotating frame (dashed when closed), and material contour initially at the jet vertex (thick, solid line); areas with $U - c < 1\ m/s$ are also shaded. Right: PV fields for the same times.

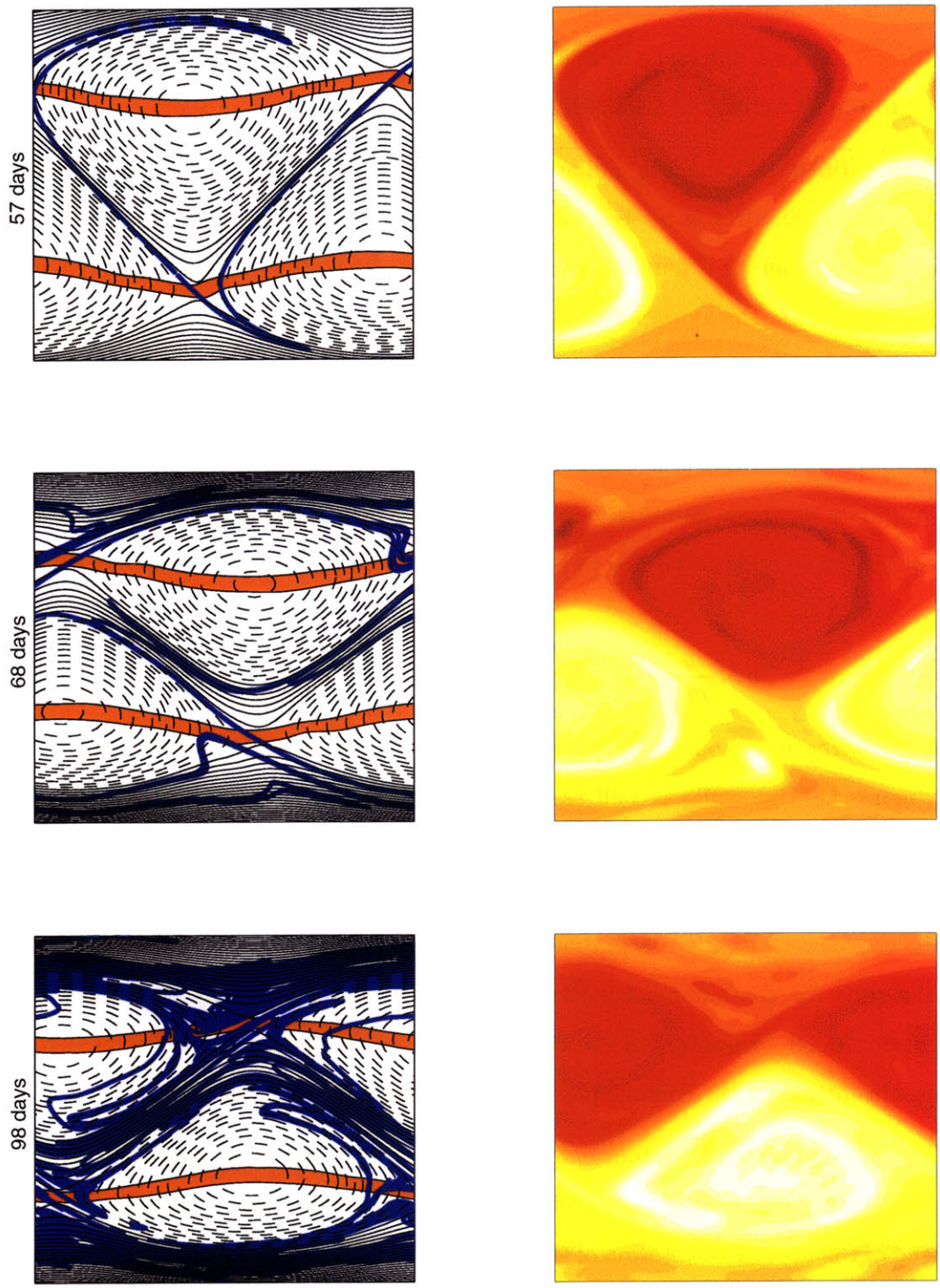


Figure 6-6: (continued)

at the vertex. As a result, there are comparable values of vorticity on both halves of the domain, which makes it harder than in the previous case to visually distinguish both air masses in the vorticity plots (the line of large PV gradients still provides a good indication). Another important difference from the previous case is that the steering level is also much closer to the jet vertex, as discussed in chapter 3.

The initial development is similar to the previous case, though significantly faster. Thin critical layers can already be seen in the streamline field of figure 6-7 by $t = 15$ *days*, while the perturbed contour is found to reach the steering level after 23 *days*. However, unlike in the previous case, this does not occur in the vicinity of a stagnation point. Though there are still hyperbolic points in the shaded region, they appear to be out of phase with the contour by approximately 90 degrees and are found to have little impact on the dynamics because the phase space is still evolving at this stage. On the other hand, the contour does not approach any fixed point because the meridional flow is strong at the longitude at which it reaches the steering level. We can rationalize this by writing the meridional velocity as

$$v = \frac{d\eta}{dt} = \frac{\partial \eta}{\partial t} + u\frac{\partial \eta}{\partial x} + v\frac{\partial \eta}{\partial y} \approx \sigma\eta + (u - c)\frac{\partial \eta}{\partial x} + v\frac{\partial \eta}{\partial y} \tag{6.1}$$

where $\eta$ is the meridional Lagrangian displacement and $\sigma$ is the growth rate. At the $\eta$ maximum (i.e. $\eta_x = 0$), as well as at the steering level, we can then approximate $v \approx \eta\sigma/(1 - \eta_y)$. This shows that the perturbed contour can never reach the steering level at exactly the stagnation point, which should be a fixed point of the flow ($\eta = 0$). Nevertheless, in the shortwave case discussed above the growth rate has already weakened significantly by the time the contour reaches the steering level, and this is why it happens near the stagnation point. However, in the case of the most unstable mode the growth rate only drops abruptly once the contour passes the steering level (see figure 6-8).

Because the material contour enters the critical layer at a large distance from the stagnation point, of the order of the wavelength itself, large scale blobs of vorticity are produced instead of the microfilamentation of the previous case. This is similar to the large amplitude cases of Polvani and Plumb (1992). As a result, there is an intense exchange of material between both sides of the vortex, which leads to the much reduced (and reversed!) PV jump. Note that this *large scale* vorticity mixing changes the basic structure of the phase space. The modified phase space has no hyperbolic point or heteroclinic structure, due to

the fact that the steering level of the wave collapses at the center of the channel.

The panel at time $t = 85$ shows that over the course of the integration the particles initially at the jet vertex undergo a strong dispersion. In a Poincare diagram, this is often an indication of widespread chaos. However, large scale chaos would appear incompatible with the subsistence of a region with large PV gradients at the edge of the perturbed vortex, as seen in figure 6-1. Additionally, it is not clear, in terms of the phase space structure and the time-dependence of the kinematic fields, what could make chaotic mixing more efficient in this case than in the previous one. For instance, the phase speed and growth rate appear to display comparable time variability as in the shortwave run (figure 6-8). Moreover, unlike in that case, the phase space lacks a heteroclinic structure.

We believe that the more efficient filling of the domain by the fluid particles in this case is due to a different mechanism than global chaos. The key point to note is that, while for the most unstable mode the perturbed contour is nearly transversal to the streamlines by the time the wave saturates, in the short wave run the perturbed contour and the streamlines are nearly aligned (compare figures 6-6 and 6-7). As a result, if the flow simply homogenizes PV along the streamlines at subsequent times, the perturbed contour will presumably fill a much larger area in the former case than in the latter, as it is sheared down along the quasi-steady streamlines. As shown in figure 6-3, these streamlines remain fairly robust after saturation so that they already define at this time the edge of the equilibrated vortex.

Hence, in this framework the large scale dispersion of the contour actually occurs in two stages. There is cross-stream dispersion during the linear growth phase, followed by along-stream shearing after saturation. From a mixing perspective, the flow creates PV variance along the streamlines during the first stage, and homogenizes that variance during the second. Chaotic advection only enters to second order in this picture: it provides some additional cross-stream dispersion, but not more than in the previous case, and certainly not enough to destroy the newly formed mixing barrier. We provide some evidence to support this argument in section 6.4 below.

In summary, it is not always true that the position of the steering level limits the maximum displacement of the perturbed contour. Only in quasi-steady situations, in which the contour reaches the steering level in the vicinity of a stagnation point, does this constraint apply. In those cases, the wave would be clipped in the manner described by Swanson et al. (1997) to this maximum amplitude, and there would be little exchange of material

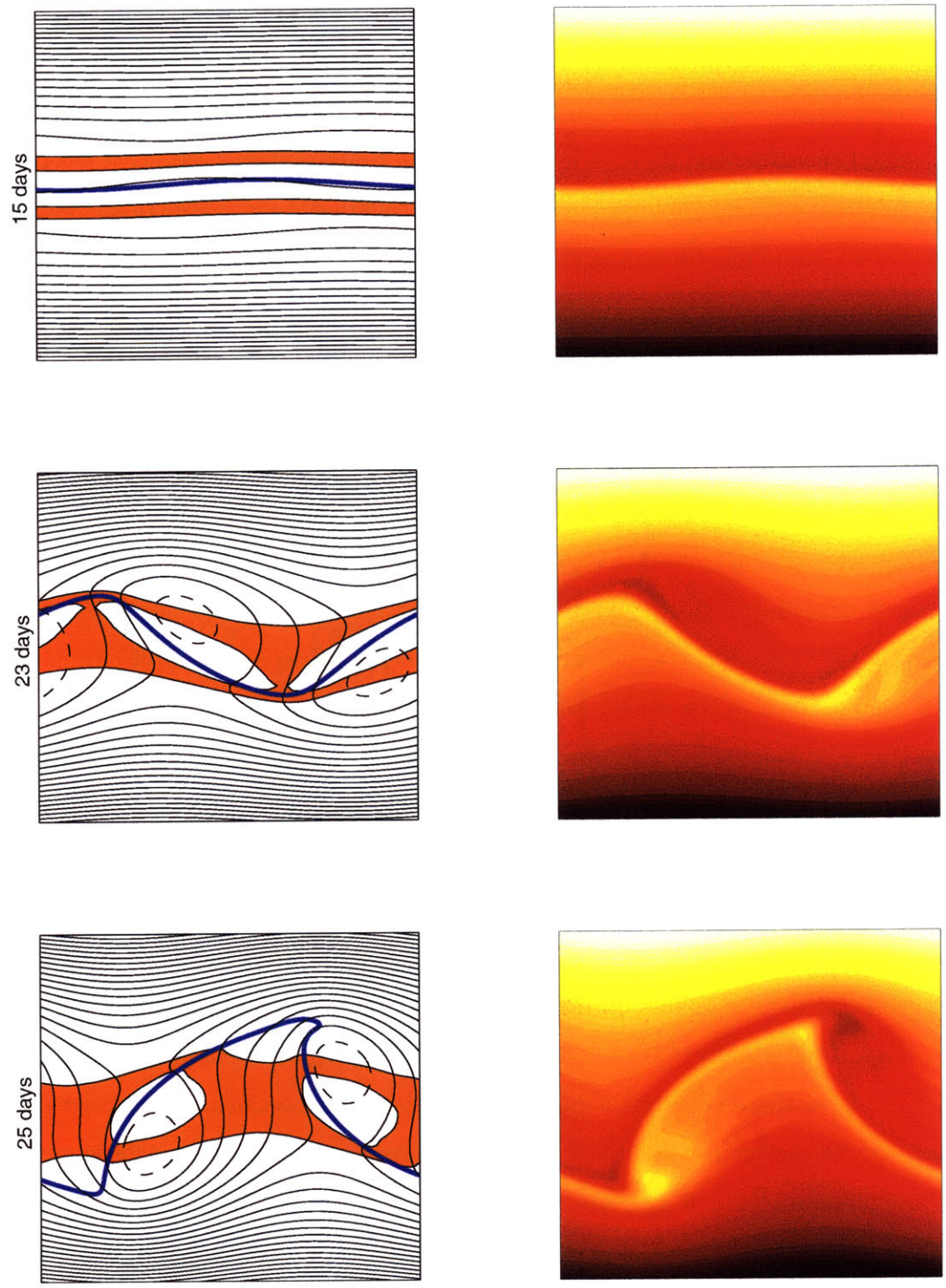


Figure 6-7: As figure 6-6 but for the run with $\beta = 1.6 \times 10^{-11}\ m^{-1}s^{-1}$ $(L/l = 3.9)$ and the times indicated.

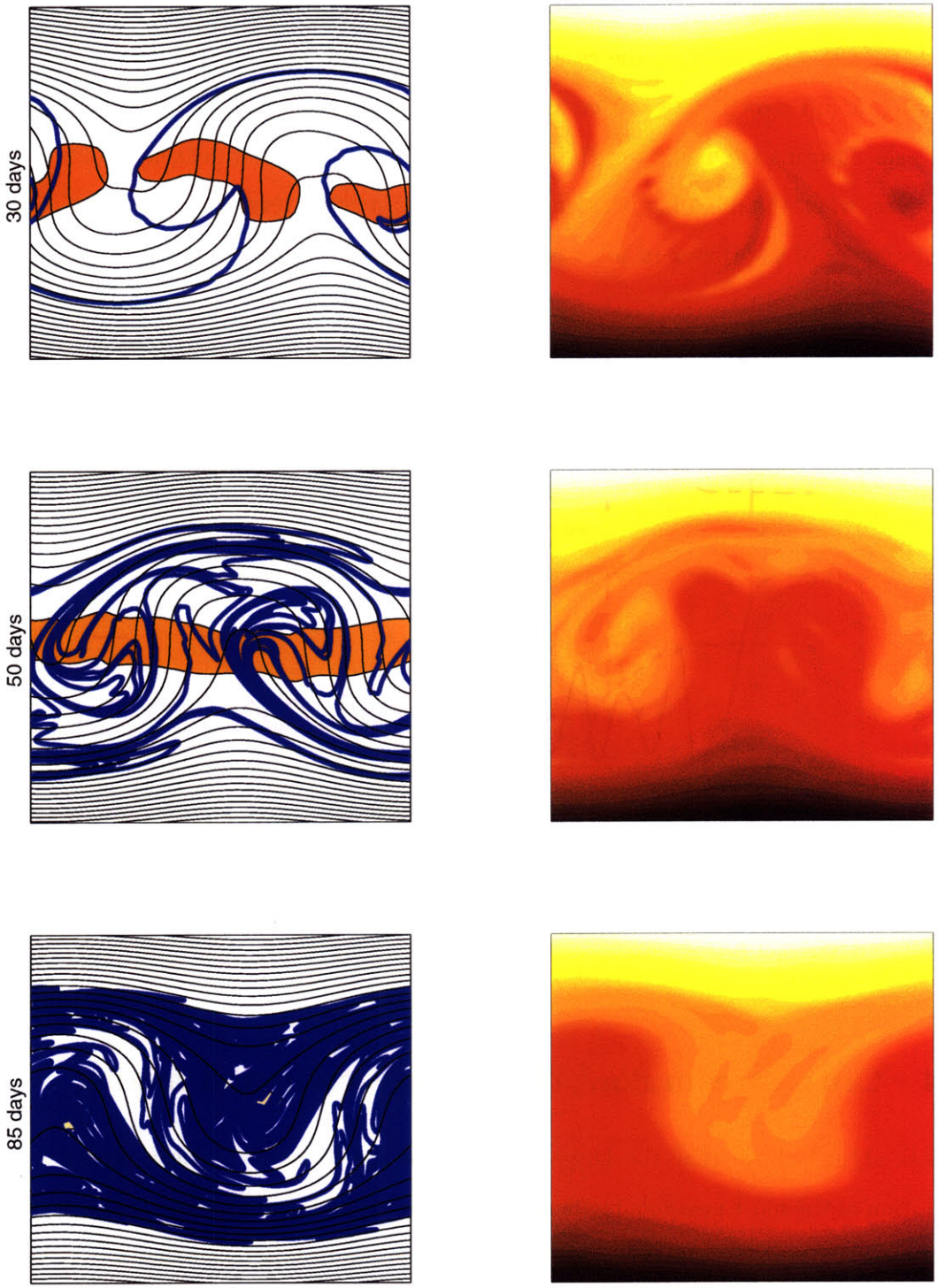


Figure 6-7: (continued)

between both sides of the contour. This is what happens for instance in the shortwave case $L/l = 1.25$, in which the growth rate has significantly slowed down by the time the contour reaches the steering level, presumably as a result of the preliminary mixing at the steering level. On the other hand, in the case of the most unstable mode $L/l = 3.9$ the wave is still growing at full growth rate at that time, and the perturbed contour overshoots the steering level, favoring the mixing of the large scale vorticity and the weakening of the vortex. However, when the damping is strong enough, the steering level also limits the maximum displacement of the vortex in this case (not shown).

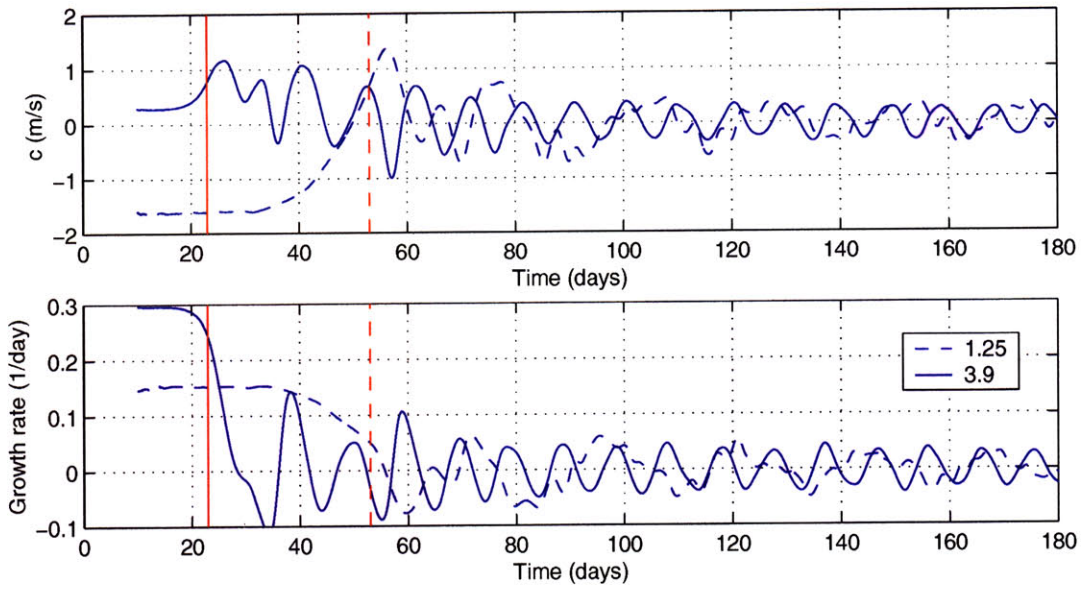


Figure 6-8: (Top) Time series of phase speed for the short wave run (dashed) and the most unstable mode (solid), with the long-time mean subtracted. (Bottom) Same but for the instantaneous growth rate. In both panels, the vertical axis line shows the time at which the perturbed material contour described in the text first reaches the steering level.

## 6.4 Cross-stream flow, chaotic advection and mixing

It was argued above that the large dispersion of the material particles seen during the evolution of the most unstable mode is not an indication of global chaos. In this section, we analyze in more detail the physical mechanism leading to this rearrangement of the large scale potential vorticity field.

As discussed in section 6.1, an essential ingredient for mixing is the unsteadiness of the flow. For steady two-dimensional flow, streamlines can be defined such that the net amount of tracer between two adjacent streamlines is conserved. In that sense, the streamlines can

be regarded as mixing barriers in the steady case. However, when the flow is not perfectly steady the fluid particles are allowed to cross the instantaneous streamlines, thus permitting a more thorough mixing. Alternatively, we can think of the streamlines as material entities that by moving around engulf material from adjacent regions, which would not be available for mixing if the flow were steady. This suggests that the velocity at which the streamlines move (which is equal and opposite to the velocity at which the material particles cross the streamlines at a given time) might provide a useful diagnosis for mixing. We can estimate the velocity at which a streamline $\Psi(x, y)$ moves as follows:

$$U_n = -\frac{\nabla\Psi}{|\nabla\Psi|^2}\frac{\partial\Psi}{\partial t} \tag{6.2}$$

To illustrate this concept, figure 6-9 shows the velocity field on the mean streamline for a few selected times in the evolution of the $L/l = 3.9$ run. Note that though the distribution of velocities along the streamline displays a primarily large scale pattern, the actual Lagrangian motion (which would also include an along-stream component) is still chaotic. As emphasized by chaotic advection models, this is a result of the time-dependence, which makes adjacent material particles decorrelate in very short times. However, when the emphasis is on mixing, it is not necessary to distinguish between individual particles, and all that really matters is the net flux of tracer across the streamlines.

This suggests that the cross-stream tracer flux could be used as a diagnostic tool. However, there is an inherent ambiguity in this concept which limits its applicability. The main difficulty is that the streamlines do not keep their identity because they are not material lines. Hence, it is not clear that it is physically meaningful to compare the tracer flux across a given streamline for different cases, or even at different times. Because of the symmetry of this problem, the mean streamline ($\Psi = 0$) marks the edge of the vortex for all times; however, other streamlines also undergo a mean drift as the flow equilibrates. For instance, consider a streamline $\Psi_1$. By definition, the net zonal transport in the corrotating frame between this streamline and the mean streamline is constant at all times. If the mean shear between them is reduced as the wave equilibrates (in the corrotating frame, this also depends on the relative position of the steering level), the $\Psi_1$ streamline must drift away.

Figure 6-10 shows some diagnostics for the $L/l = 3.9$ run. Panel A shows the time-integrated PV flux across the $\Psi = 0$ streamline, while panel B shows the time series of the

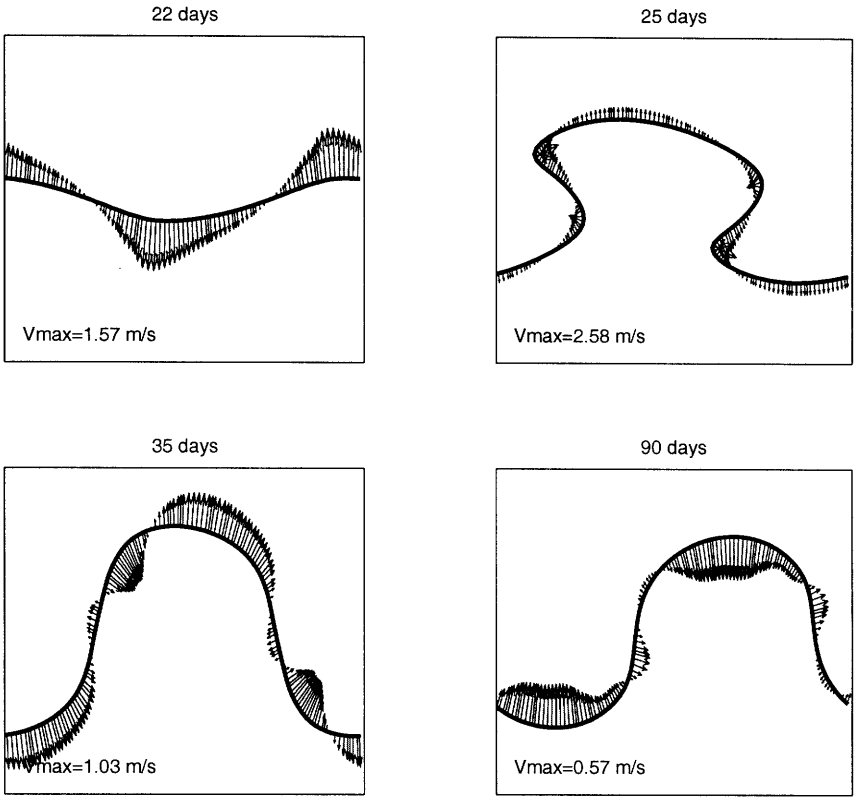


Figure 6-9: Distribution of the cross-stream velocity on the mean streamline at selected times.

RMS velocity on the same contour. As can be seen, the bulk of the flux occurs during the linear-growth phase, suggesting that after saturation the flow essentially homogenizes PV along the streamlines, consistent with the two-stage mechanism proposed above. Because the cross-stream velocity is not entirely negligible during the later part of the evolution, chaotic advection should also play a role in this mixing. However, the robustness of the large scale flow implies that the amount of chaos is insufficient to destroy the large scale structure. Finally, panel C of figure 6-10 shows the spatial distribution of the time-mean (RMS) cross-stream velocity between days 100 and 150 of the simulation[3]. We also show for comparison the potential vorticity contours, averaged during the same times in the steady reference frame. As can be seen, there is an excellent agreement between the magnitude of the cross-stream velocity and the degree of PV homogenization.

Finally, figure 6-11 illustrates how the distribution of potential vorticity along the streamlines changes with time. Panels A-C show three snapshots of this distribution for the

[3]Note that this is an Eulerian mean value, and thus reflects an average over all the streamlines that pass through any given gridpoint at different times.

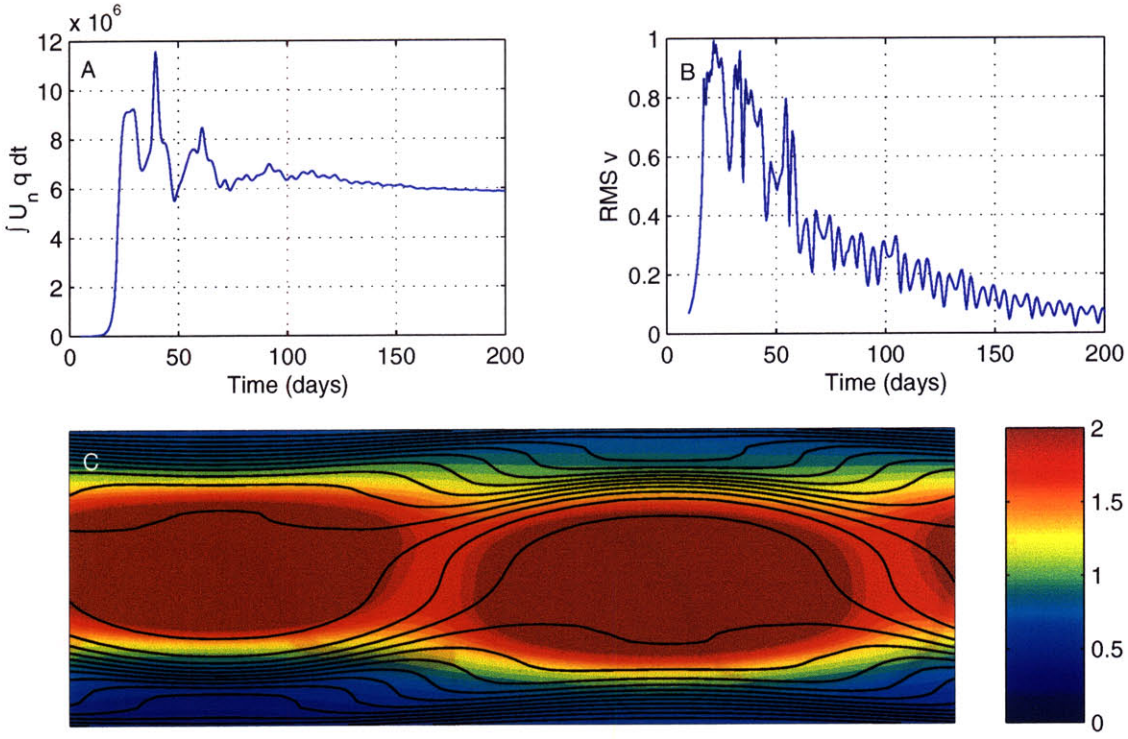


Figure 6-10: For the $L/l = 3.9$ run: A) Time-integrated flux of PV across the $\Psi = 0$ streamline. B) Time series of the RMS of the cross-stream velocity on that contour. C) Spatial distribution of the time-mean RMS cross-stream velocity (days 100-150), and contours of mean potential vorticity.

layer defined by the streamlines $\Psi = 1 - 2 \times 10^6\ m^2 s^{-1}$, using the same color contouring for all them. In the initial state (panel A), the flow is zonally symmetric and hence potential vorticity is constant along the streamlines. As the wave grows to finite amplitude (panel B), there is a significant development of PV variance over the layer. Figure 6-7 shows that this is simply due to the out-of-phase relation between streamlines and PV contours. Finally, as time goes on, PV is slowly homogenized along the streamlines (panel C). The same can be seen in panels E-G, which show the time-series of the mean, variance, and full PDF of this distribution. The most striking feature of this evolution is the abrupt increase in variance before saturation, followed by slow subsequent homogenization. This can be compared with figure 6-12, corresponding to the shortwave case. Though in this case the distribution is not unimodal, the variance along the individual patches does not seem to change that much.

In summary, the results presented here suggest that most of the cross-stream flux of PV arises during the linear-growth phase, while after saturation the flow essentially homogenizes the PV along the streamlines. Hence, the global chaos paradigm is not appropriate for this problem, despite the large dispersion in the Lagrangian trajectories of figure 6-7.

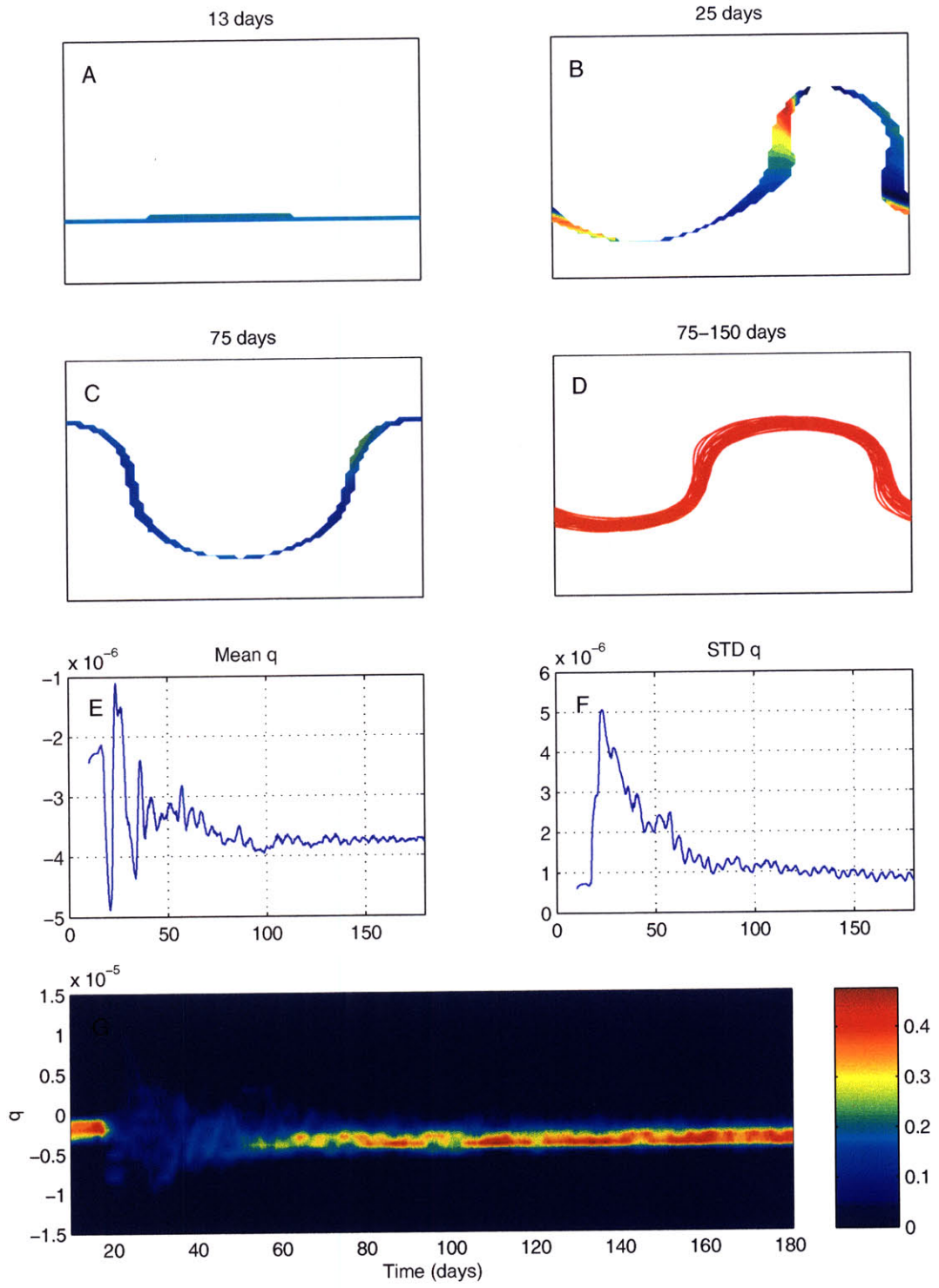


Figure 6-11: Distribution of PV on the layer defined by the streamlines $\Psi = 1 - 2 \times 10^6\ m^2 s^{-1}$ for the $L/l = 3.9$ run. A-C) Snapshots of the distribution at selected times. D) Range of positions occupied by the mean streamline. E) Time-series of the mean PV on the layer. F) Time-series of the PV variance on the layer. G) Time-series of the full PDF.

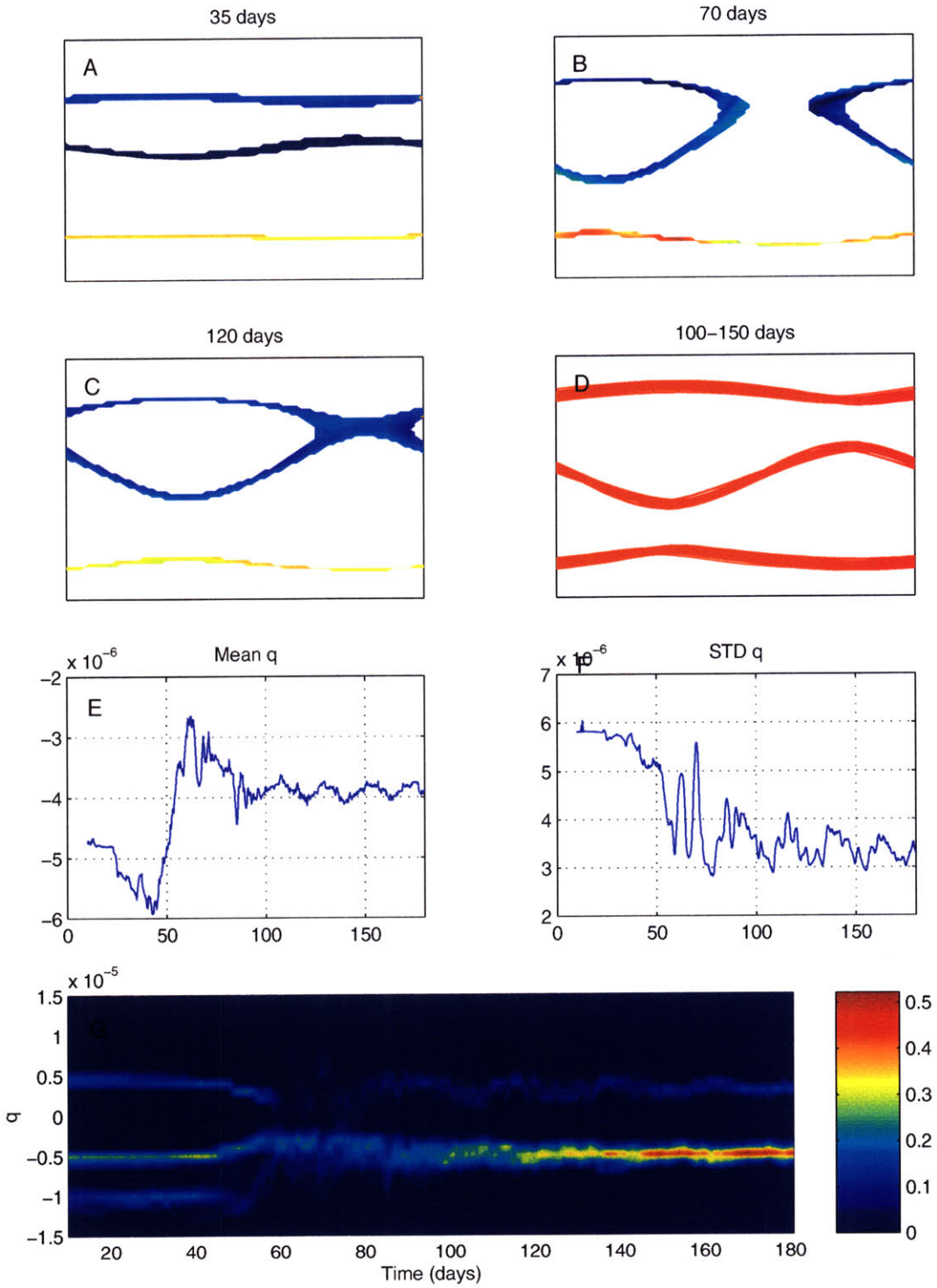


Figure 6-12: As figure 6-11 but for the $L/l = 1.25$ run.

# Chapter 7

# Conclusion

## 7.1 Summary of the main results

We summarize below the main arguments and results of this thesis. For easier reference, this summary respects the original chapter structure in which the results were presented. Since this summary is quite exhaustive, an abbreviated version of the conclusions follows.

### Chapter 2

In this chapter we reviewed the theory of baroclinic adjustment, and discussed the degree of homogenization observed in the extratropical troposphere.

The mean interior PV gradient in the extratropical troposphere is not zero, but order $\beta$ or larger. This implies that in an integral sense, the PV gradient is as poorly homogenized in the interior as at the surface. Observations suggest that potential vorticity is only well homogenized across a shallow region at about 700 mb. This is roughly the level at which baroclinic eddies have their steering level. Hence, while the observed tropospheric state violates the Charney-Stern condition for instability, it still satisfies Bretherton's theorem.

Moreover, the contribution from the horizontal curvature to this PV gradient does not appear to be negligible either (though it may be severely smoothed on the zonal average due to the meandering of the jet). This is what would be expected if the meridional scale of the jet confined the vertical penetration of the modes. Then, the width of the jet scales as the Rossby radius, and the jet has horizontal and vertical curvatures of the same order.

The net integrated PV gradient across the mixing domain cannot be changed by the eddies. In the 2D problem, this implies that the column-integrated PV gradient is constant. If

the dimensions of the mixing domain are constrained externally, the positive PV gradient in the interior may be insufficient to balance the negative delta-function. When this happens, the net integrated PV gradient is negative. In that case, the eddies can only eliminate the delta-function PV gradient by developing negative interior PV gradients, which would also be unstable. When applied to the baroclinic case this implies that short waves are unable to eliminate the surface temperature gradient. However, as discussed below, this is not really appropriate because the baroclinic problem is not two-dimensional. This argument was called the mixing depth constraint in the text.

### Chapter 3

In this chapter we introduced the concept of a short Charney wave, and studied the implications of this concept for the stability of partially homogenized states.

We defined short Charney waves as waves for which the positive PV gradient in the interior (appropriately weighted) is smaller than the integrated delta function at the surface. For this purpose, we used the half Rossby depth $H$ as a scale for the interior PV fluxes, and the Held scale $h$ as a scale for the interior PV gradient. Short Charney waves were defined as waves with $H/h < 3.9$, or shorter than the most unstable mode.

The PV flux of a short Charney wave peaks at the steering level, and is very shallow when $H/h$ is small. One way to understand this result is to note that the positive and negative PV fluxes have to integrate to zero. When the PV gradient is much smaller in the interior than at the surface, this condition can only be satisfied through a large PV flux at the steering level, where the PV diffusivity is essentially unbounded. This argument suggests that short Charney modes should be neutral when the PV gradient vanishes in a neighborhood of the steering level alone. We confirmed this hypothesis by means of numerical simulations and a simplified analytical model.

We speculated that short Charney modes could equilibrate by mixing PV at the steering level alone, and that all modes could equilibrate in this manner by also narrowing the jet through the convergent momentum fluxes. We further argued that the observed eddies are short Charney modes, due to the meridional confinement by the jet. However, as pointed out below, this is not so clear when the curvature PV gradient is also taken into account.

## Chapter 4

In this chapter we studied how waves of prescribed scales equilibrate, both for the barotropic point jet and 3D Charney problem.

*Barotropic point jet*

In this problem the mixing length constraint applies. As a result, the net integrated PV gradient is just a function of the scale of the waves. When the waves are short, there is a remnant negative PV gradient at the jet vertex, though it is smoothed out due to the stretching of the PV contours across the mixing length. On the other hand, for waves longer than the most unstable mode the PV gradient at the jet vertex is positive.

In all cases, the PV gradient is very robustly smoothed out at the steering level. As the scale of the waves increases, the steering level moves closer to the jet vertex, and so does the well-homogenized region. In fact, the elimination of the negative PV gradient at the jet vertex can be linked to the expansion of the critical layer to the center of the channel.

The phase speed of the wave remains fairly robust as it equilibrates. We argued that this is due to the fact that the eddies only redistribute the zonal momentum, without changing its mean value. The momentum redistribution is such that there is westerly acceleration at the jet vertex and interior easterly acceleration, which reduces the westerly shear.

Despite the robust phase speed the steering level still moves, due to the redistribution of momentum. For short waves, the original steering level is far from the vertex, in the region of easterly acceleration; as a result, it moves outward as the wave equilibrates. For longer waves on the other hand, the initial steering level is in a region of westerly acceleration, so that it moves inward, toward the center of the channel, until it disappears.

In the forced-dissipative case, there is always a remnant negative PV gradient at equilibration, even for the longer waves and for weak dissipation. This can be justified as follows. Because the diabatic generation of eddy enstrophy is negative definite, the equilibrium PV fluxes must be on average downgradient. Neglecting the eddy advection of eddy enstrophy, the PV fluxes are also everywhere downgradient. This implies that $\overline{q}_y$ must change sign for the equilibrated flow, simply because $\overline{v'q'}$ integrates to zero.

There is a local equilibrium between the eddy forcing of momentum (the eddy PV flux) and the non-conservative momentum forcing. For downgradient PV fluxes, this requires a positive (negative) PV gradient at equilibrium in regions of easterly (westerly) acceleration.

*3D Charney problem*

As potential vorticity is mixed, the flow naturally develops large PV gradients at the boundaries of the mixing domain. This is true both for the 2D and 3D problem. Hence, the model is able to internally generate a tropopause without any diabatic forcing, simply through the redistribution of the PV gradients.

As in the 2D case, there is a robust agreement between the homogenized region and the position of the steering level, so that the flow only eliminates the surface temperature gradient when the steering level drops to the ground. In the presence of friction the phase speed still remains relatively robust, but not otherwise. This may be due to the net westerly acceleration of the column (only the domain-averaged momentum is conserved).

This problem can also be interpreted in terms of the redistribution of momentum. Like in the 2D case, the reduction in shear requires a westerly acceleration at lower levels and an easterly acceleration aloft. This vertical transfer of momentum is associated with the heat flux (or rather, to the mean meridional circulation induced to keep thermal wind balance). However, there is now an additional westerly acceleration of the column due to the eddy momentum flux, which has no equivalent in the 2D case. This has important implications.

First of all, because of this westerly acceleration the steering level always drops, and it drops much more than in the equivalent barotropic problem with the same parameters. In fact, without mechanical friction the steering level was found to always disappear. Consistent with this, the well-homogenized region also drops, and the surface temperature gradient is eliminated in the absence of friction.

The elimination of the surface temperature gradient for short Charney waves violates the mixing depth constraint. The reason why this constraint no longer applies in the 3D problem is because its derivation assumes that momentum is just redistributed vertically, while in the 3D problem there is a net import of westerly momentum at the expense of lateral easterly acceleration. The generalization of this constraint thus requires that a full 2D integral of the PV gradient be considered. For short waves the area-integrated PV gradient must still be negative, but the negative PV gradients may occur on the sides.

In the 3D problem, the flow can develop enough vertical curvature to accommodate the required difference in shear without developing negative PV gradients in the interior. This is possible because there is a compensating generation of positive interior PV gradient, as the horizontal curvature is enhanced by the eddy momentum convergence. Hence, to the extent

that friction limits the westerly acceleration of the column, it also limits the reduction in the vertical shear and surface temperature gradient.

These results cast some doubt on the equilibration scenario proposed in chapter 3. It was argued in that chapter that short modes could equilibrate by mixing PV at the steering level alone, and all modes could become short by narrowing the jet. However, because the narrowing of the jet also increases the positive PV gradient, it is not clear that this makes the modes shorter in a dimensionless sense. The fact that the steering level drops and the surface shear is eliminated (in the absence of friction) suggests that it does not.

As in the 2D case, the PV gradient must change sign in the forced-dissipative problem, provided that the PV fluxes are downgradient. However, this does not constrain the surface temperature gradient because the negative PV gradients may occur on the sides of the jet.

In the 3D problem, the eddy PV flux no longer balances locally the frictional forcing of momentum because there is an additional momentum redistribution by the residual circulation. However, because this circulation only redistributes momentum vertically, it does not apply any net torque on the column and the vertically-integrated PV flux is still balanced by friction. For downgradient PV fluxes, the momentum balance then requires that there is a negative PV gradient somewhere along the column at any latitude with surface westerly wind. This implies that in the presence of friction, the surface temperature gradient cannot be eliminated at those latitudes.

### Chapter 5

In this chapter we derived a momentum-based formulation of the zonally-averaged extratropical circulation. By rewriting the thermodynamic equation as a momentum equation, we eliminated the forcing by the mean meridional circulation in the zonal momentum equation. This introduces a new variable, which is related to the thermal structure but has momentum units. We called this variable potential momentum.

Physically, potential momentum can be interpreted as the momentum that the flow would develop if the isentropic thickness were brought to its (height-dependent) reference value everywhere poleward of a reference latitude, while conserving the zonal-mean potential vorticity. It can be shown that this implies that potential momentum is easterly (westerly) when the isentropes open up (close down) with latitude. At the surface, the negative temperature gradient is equivalent to a delta function in easterly potential momentum.

The equation describing the conservation of total (i.e., potential plus physical) momentum is simply the $y$-integral of the quasigeostrophic potential vorticity equation. When the total momentum is considered, the eddy PV flux is the only dynamical forcing of momentum and is locally balanced in equilibrium by the non-conservative forcing (which now also includes a diabatic potential momentum forcing). This is analogous to the barotropic case.

The residual circulation simply transforms potential to physical momentum (for a poleward circulation). At any time, the partition between both forms of momentum must be such that thermal wind balance is satisfied. When potential momentum varies in distances of the order of the deformation radius, thermal wind balance requires that potential and physical momentum have the same order of magnitude. As a result, there is a compensation between the negative and positive PV gradients associated to their respective curvatures.

When a finite mixing domain can be defined, the vertically-integrated potential momentum is constant. Moreover, because all the forcing terms integrate independently to zero, they just redistribute potential momentum vertically. In particular, the conversion of potential to physical momentum at one level must be accompanied by the opposite conversion at some other level, so that the net result is a vertical flux of physical momentum.

In the potential momentum framework the circulation can be described as follows.

1. Diabatic processes generate easterly potential momentum at lower levels, and compensating westerly potential momentum aloft. In particular, they force the surface temperature gradient, which can be interpreted as a reservoir of easterly potential momentum at the ground. Because the surface easterly potential momentum is equivalent to a negative delta-function PV gradient, this supports baroclinic instability.

2. The equilibration of the baroclinic waves produces a poleward residual circulation, which transforms westerly potential to physical momentum in the interior. Because this conversion must be accompanied by the opposite conversion at the surface, the interior westerly acceleration also involves a depletion of the easterly potential momentum locked at the surface, or a reduction in the surface temperature gradient.

3. The interior westerly acceleration resulting from the potential momentum conversion is balanced by the combined easterly drag of the eddy PV flux and surface friction. The system reaches an equilibrium when the diabatic generation of westerly potential

momentum in the interior is balanced by the total easterly drag, and both are equal to the rate of conversion by the residual circulation.

Though friction may only account for a small percentage of the easterly eddy drag, it plays an essential role because the eddy PV flux alone is insufficient to balance the westerly generation of momentum by the residual circulation. In that sense, it is friction that prevents the depletion of the easterly potential momentum at the surface, and hence the elimination of the surface temperature gradient. This can also be reasoned as follows. To the extent that friction limits the westerly acceleration of the jet, it also limits the easterly acceleration of the potential momentum jet, and hence the depletion of the easterly potential momentum at the surface. The thermal wind constraint requires that both jets are of the same order, which is ultimately forced through the momentum conversion by the residual circulation.

The potential momentum formulation derived in this chapter makes explicit the connection between temperature and momentum, a result that is in fact implicit in the Eliassen-Palm formulation of Edmon et al. (1980).

### Chapter 6

In this chapter we looked at PV homogenization in our problem from a kinematic viewpoint.

The robust elimination of the zonal-mean PV gradients at the steering level found in chapter 4 is not indicative of full spatial homogenization, but is due to the meridional tilt of the PV contours at those latitudes. This tilt is related to the homogenization of PV along the streamlines: in the corrotating frame, the flow is purely meridional at the steering level.

Even for the case of the most unstable mode a mixing barrier persists in the form of the perturbed jet, and full spatial homogenization is only observed across localized regions. The persistence of the mixing barrier suggests that the final state only support local chaos. We argued that large scale homogenization is inconsistent with the concept of chaotic advection, and should require Eulerian turbulence rather than quasi-regular kinematic fields.

We also investigated the mixing of large scale PV as the wave equilibrates, and in particular whether the position of the steering level constrains the maximum meridional excursions of the vortex. We found that this is only the case when the growth rate is already largely reduced by the time the perturbed contour reaches the steering level. On the other hand, when the growth rate is large there is a strong meridional flow at the

perturbed contour as it reaches the steering level, and the stagnation point forms far away from the contour. As a result, large blobs of potential vorticity form, rather than filaments.

For the case of the most unstable mode, the material particles initially at the edge of the vortex undergo a large dispersion, consistent with the efficient PV mixing observed in this case. We interpreted this as a two-stage process. As the wave grows, it develops potential vorticity variance along the streamlines, and the perturbed contour is oriented transversally to them. However, once the wave saturates the dominant process is just along-stream PV homogenization, with some weak cross-stream dispersion, but there is not global chaos. It is only the first stage that distinguishes the evolution of this case and that of the shorter waves, and makes the mixing most efficient for the most unstable mode.

### 7.1.1 Conclusions

In this thesis we have shown that the observed PV gradients in the extratropical troposphere are not small, but are comparable to the surface PV gradients. PV is only well homogenized around 700 mb, at the steering level of the waves. Because the atmosphere is not an unbounded fluid, it is not clear that the most unstable mode of the unbounded problem is the most relevant for equilibration. Short Charney modes, which see too little interior PV gradient, can be neutralized through partial PV homogenization at the steering level.

However, in the 3D problem the availability of interior PV gradient is not such a constraint because the waves can enhance the positive PV gradient in the interior by narrowing the jet. This is a consequence of the convergent momentum fluxes which, in the absence of friction, favor a strong barotropic jet with reduced vertical shear. Because qg scaling implies that the horizontal and vertical curvatures of the jet are comparable, friction not only constrains the barotropic acceleration of the jet, but also the vertical redistribution of momentum that leads to the elimination of the surface shear. These results are most transparent in the formalism of chapter 5, in which temperature and momentum can be directly compared. In this framework, the surface temperature gradient can be interpreted as a reservoir of momentum, which is depleted by the same residual circulation that accelerates the jet. In our idealized model, both processes are ultimately limited by friction.

Finally, the double role played by the eddy PV flux in forcing the zonal momentum and modulating the wave-mean flow interaction allows us to infer some important results for an equilibrated system. Because the diabatic generation of eddy enstrophy is typically negative

definite, the eddy PV fluxes are downgradient (neglecting cubic terms in wave amplitude). In the presence of surface westerlies, the net frictional forcing of momentum along the column is easterly, and must be balanced by westerly eddy drag, or positive PV fluxes. The downgradient character of these fluxes then implies that there must be a negative PV gradient (i.e., a nonzero temperature gradient) over those latitudes with surface westerlies.

## 7.2 Limitations of this work and possible extensions

The main limitations of this work are due to the simplicity of the model used, which discourages any serious attempt to compare the model equilibrium and the observed tropospheric state. Perhaps the most severe deficiency in this regard is the absence of a (diabatically-forced) tropopause. Though the model generates large PV gradients at the boundaries of the mixing domain, this internally-generated tropopause is by definition passive, and does not play much role in the dynamics. As a result, the eddies are unrealistically bottom-trapped (most strikingly, the eddy momentum flux peaks at the surface). It would be possible to get a more active tropopause through diabatic forcing. It is also conceivable that by lowering the tropopause, a stratospheric circulation could increase the coupling with the surface. However, because the main interest of our study is theoretical and we do not aspire to reproduce the observed climate, we chose not follow any of these two approaches.

The inclusion or not of a model tropopause has also important conceptual implications for the definition of short Charney modes, which are characterized by weak interior PV gradients. If the tropopause is included in this definition, these PV gradients can never be weak. Indeed, because the isentropic slopes are small in the stratosphere, the baroclinic contribution to the interior PV gradient must vertically integrate to zero when the tropopause is also included. However, because these large PV gradients are found at the boundary of the mixing domain, it is not obvious whether they should be included or not in the definition of $h$. We chose for simplicity not to include them, but this is debatable.

On the other hand, the use of the simple model made it easier to understand the dynamical mechanisms connecting zonal momentum and surface temperature gradient. These dynamical mechanisms could also be at work in the real atmosphere, though the specific details of the mechanical and thermal balances are probably different. Because the horizontal and vertical curvatures of the midlatitude jet are comparable (see section 2.3.1), it

is plausible that friction also constrains the homogenization of surface temperature in the troposphere.

Another unrealistic aspect of our model is the fact that the channel truncation artificially favors the dominance of a single mode. While this simplifies the study, in the real atmosphere there is a full spectrum of waves. This opens the possibility that wave-wave interactions could also play a role. Moreover, the modifications of the basic state by one wave are likely to affect the others. For instance, our results suggest that the condition of PV homogenization at the steering level is a very robust one. In the model, the evolution of the steering level essentially depends on the vertical redistribution of zonal momentum by the fluxes of the equilibrating wave. In the presence of many waves, the momentum redistribution should be a function of the total fluxes, but this would not invalidate the basic result that it is friction that ultimately constrains this vertical redistribution. Note that the depth of the well-homogenized region in the extratropical troposphere is not inconsistent with the observed range of phase speeds.

We have not performed a sensitivity analysis of the results. In our runs, the halfwidth of the radiative equilibrium jet was kept fixed, so it would be interesting to see how robust are the results in other cases. We suspect that for broader meridional forcing several jets would form, each of them having comparable horizontal and vertical curvatures.

The potential momentum framework derived in this thesis is a novel diagnostic, which opens new avenues of research. An important advantage of this formalism is that it makes more transparent the role of the momentum forcing in the baroclinic equilibration. A problem for which this could be useful is tropical-extratropical interactions.

# Appendix A

# Vertical scales

| Symbol | Name | Explanation | Reference |
|---|---|---|---|
| $H_S$ | Density height scale | | Page 29 |
| $H_0$ | Mixing depth | Depth of the eddy fluxes | Page 40 |
| $H$ | Half Rossby depth | Estimate of the mixing depth | Page 48 |
| $h$ | Held scale | Ratio of interior to boundary PV gradients | Eqn. 3.8 |
| $h_0$ | | Value of the Held scale at the surface | Page 41 |
| $H^*$ | Homogenized depth | Homogenization depth required for neutrality | Page 53 |
| $z_c$ | | Height of the steering level | Page 47 |
| $z_t$ | | Height of the turning point | Page 59 |
| $L$ | Half wavelength | Mixing length for the barotropic problem | Eqn. 3.9 |
| $l$ | | Held scale for the barotropic problem | Eqn. 3.9 |

Table A.1: Summary of length scales used in the text. See also figure A-1

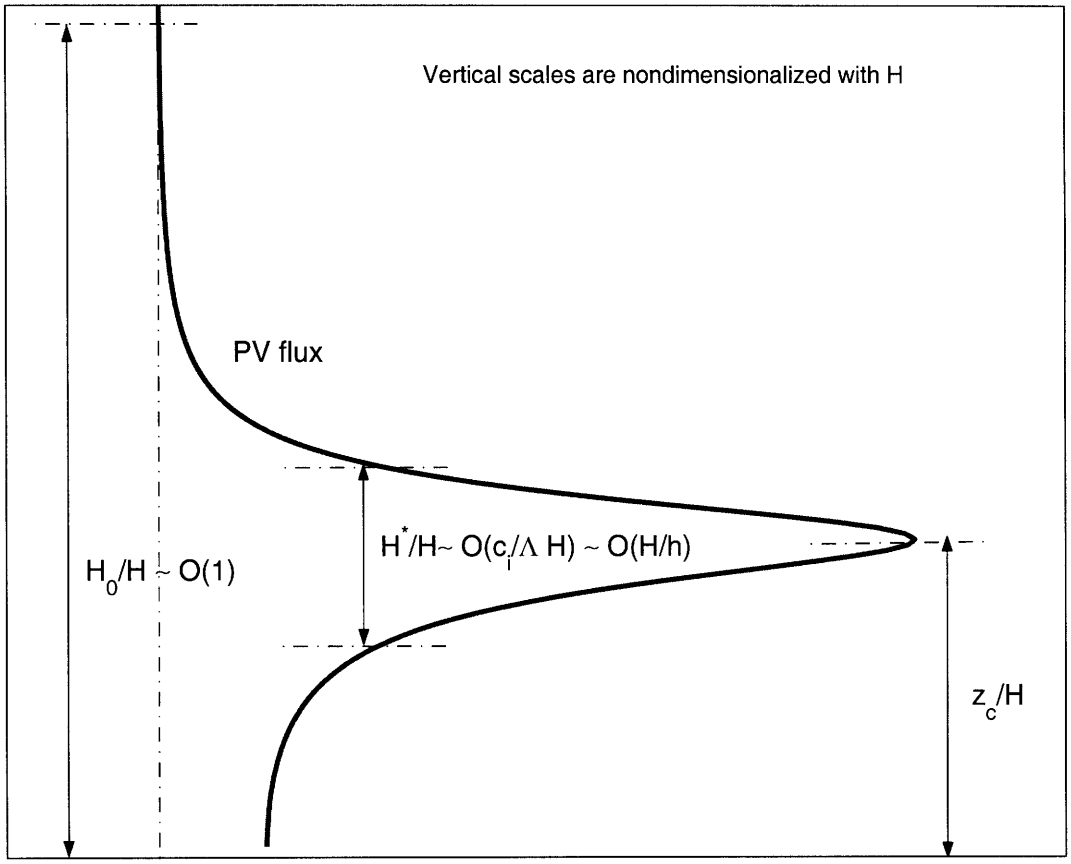


Figure A-1: Sketch illustrating the meaning of the different vertical scales for a short Charney mode. The maximum depth of the PV fluxes scales as $H$, but they are usually shallower, $O(H/h)$. Neutrality requires homogenization over a depth $H^*$ of that order.

# Appendix B

# Model description

We describe in this appendix the numerical models used for the runs presented in this thesis. Two different models were written: a barotropic model for the point jet experiments and a multilevel quasigeostrophic model for the 3D runs. The formulation is standard. In both cases, the basic equation is the quasi-conservation of potential vorticity on the beta plane:

$$\frac{\partial q}{\partial t} = -J(\psi, q) + F \tag{B.1}$$

where $q$ is the potential vorticity, $J(\psi, q) = \psi_x q_y - \psi_y q_x$ is the nonlinear jacobian, and $\psi$ is the streamfunction for the nondivergent 2D flow. $F$ is the nonconservative forcing, and the potential vorticity $q$ is defined as:

$$\begin{aligned} q_2 &= q(x,y) = f_0 + \beta y + \nabla^2 \psi(x,y) && \text{for the barotropic model, and} \\ q_3 &= q(x,y,z) = f_0 + \beta y + \left(\nabla^2 + \epsilon \frac{\partial^2}{\partial z^2}\right) \psi(x,y,z) && \text{for the quasigeostrophic model} \end{aligned}$$

Here, $\nabla$ is the two-dimensional gradient operator and $\epsilon = \frac{f_0^2}{N^2}$ the inertial ratio. We assume in the 3D case that the fluid is Boussinesq and the stratification $\Theta_z$ is constant. Note that we use a subscript to differentiate between the barotropic and qg formulations.

**Geometry and boundary conditions**

The model domain is periodic in $x$ and meridionally confined by rigid walls. These walls are located at enough distance that they do not affect the dynamics, and the channel is truncated zonally so that wavenumber one dominates. Specifically, we choose $LX = 6000\ km$, $LY = 12500\ km$ for the barotropic model and $LX = 4000\ km$, $LY = 15000\ km$

for the qg model. At the meridional boundaries the perturbation meridional velocity vanishes, so that $\psi = constant$. The value of this constant is calculated from the condition that the ageostrophic velocity also vanishes $\overline{v}_a = 0$, which implies that $\overline{U} \neq f(t)$ at the walls.

For the qg model, we also use a rigid lid in the vertical at $z = 0,\ z_T$, where $z_T = 30\ km$. Again, this height is chosen much larger than any dynamical mixing depth (and well above the turning point), so that the eddies are insensitive to the artificial lid. This condition is implemented by enforcing $w(0,\ z_T) = 0$ in the vertical discretization of the stretching term.

**Forcing**

We force the barotropic model by linear relaxation to some specified vorticity profile $q_0$ (an easterly triangular jet with constant shear $\Lambda = 0.012\ ms^{-1}/km$, as shown in B-1A):

$$F_2 = -\frac{q - q_0}{\tau} + F_\nu$$

In the 3D case, we use Rayleigh damping with time scale $\alpha_M^{-1}$ in the momentum equations, and Newtonian cooling with time scale $\alpha_T^{-1}$ in the thermodynamic equation. This yields for the potential vorticity equation:

$$F_3 = -\alpha_M \nabla^2 \psi - \alpha_T \frac{f_0}{\Theta_z} \frac{\partial}{\partial z} (\theta - \theta_R) + F_\nu$$

where $\theta_R$ is a 'radiative equilibrium' profile towards which temperature is relaxed. The diabatic time scale is $\alpha_T^{-1} = 15\ days$ for all cases and mechanical friction is only applied at the lowest resolved level. The radiative equilibrium profile (figure B-1B) is such that the associated thermal wind $U_R$ has constant vertical shear $\Lambda = 3.3\ ms^{-1}/km$, and is meridionally modulated by a Gaussian envelope of halfwidth $\sigma = 2000\ km$:

$$U_R = (\Lambda z)\ e^{-(y/\sigma)^2}$$

Finally, we also include in some cases 6-th order hyperdiffusion $F_\nu = -\nu \nabla^6 \psi$ (with $\nu = 10^{16}\ m^4/s$) to dissipate the small scale enstrophy. Note that though most of the barotropic runs are non-diffusive, we found that in practice the strong zonal flow ($O(60\ m/s)$, see figure B-1A) over the turbulent region introduces strong numerical diffusion. This is illustrated in figure B-2, which shows snapshots of the PV field from 3 different runs: (A) a non-diffusive run with the standard basic state; (B) a non-diffusive run in a modified basic state in which

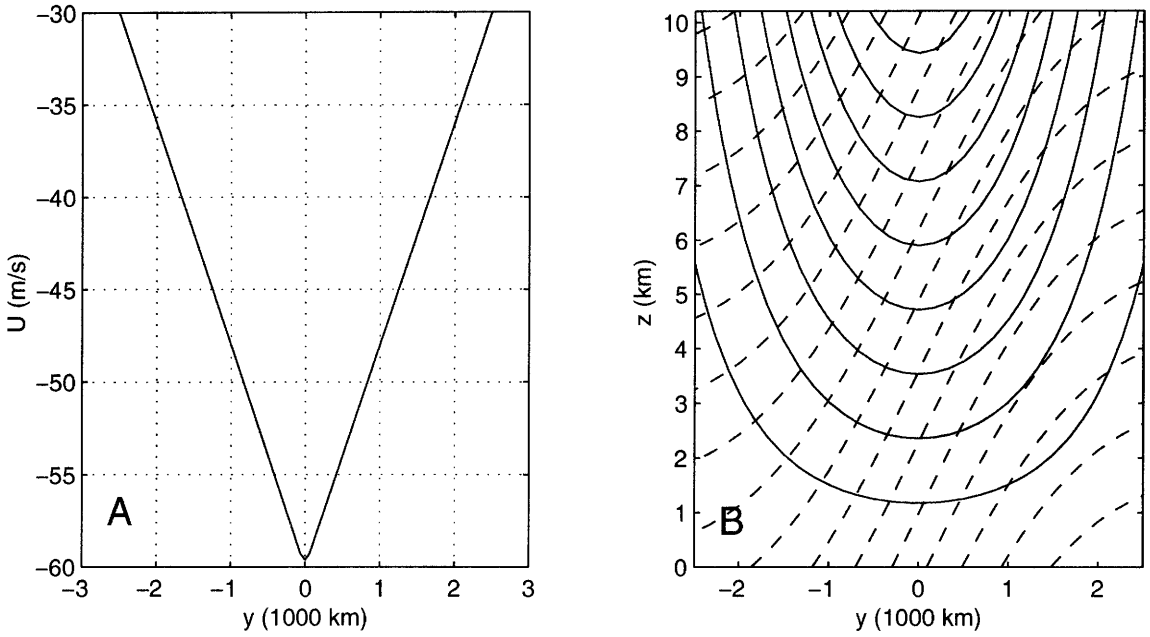


Figure B-1: Model basic state. (A) Zonal velocity for the barotropic model. (B) Contours of zonal velocity (solid) and potential temperature (dashed) for the qg model. Contour unit: $4\ m/s$ and $4K$.

a uniform zonal flow is added to make the primary wave stationary; and (C) a diffusive run in the modified basic state. The large scale PV is similar for all cases, but there is a lot more small scale enstrophy in panel B.

**Numerics**

The model is discretized using a spectral expansion in $x$ and $y$, and centered differences in the vertical. Because of the meridional boundary conditions, all the zonal harmonics of $\psi$ but the zonal mean vanish at the wall. Hence, when the zonal mean is subtracted, $\psi$ can be expanded in $y$ using sines alone. Thus we write:

$$\psi(x,y,z,t) = \overline{\psi}(y,z,t) + \sum_{j,k} \left[A_{jk}(z,t)\sin(j\pi x)\sin(k\pi y) + B_{jk}(z,t)\cos(j\pi x)\sin(k\pi y)\right]$$

The Fourier coefficients $A_{jk}$, $B_{jk}$ are evolved in time using equation B.1, with the right hand side discretized explicitly by means of a 3rd order Adams-Bashford scheme (Durran, 1991). The zonal mean component $\overline{\psi}$ is independently diagnosed enforcing the boundary condition $\overline{U} = 0$ at the lateral walls.

We use a spectral transform method to calculate the nonlinear term in grid space, with a 2/3 truncation to prevent aliasing and nonlinear instability. The conversion between spectral and grid space is performed using the 'Fastest Fourier Transform of the West'

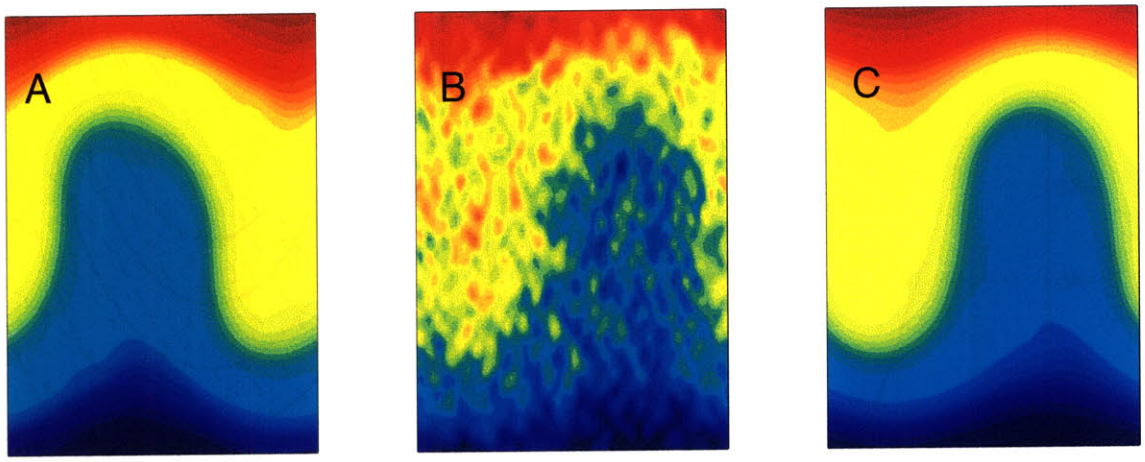


Figure B-2: Snapshots of the potential vorticity field for 3 different runs. (A) Non-diffusive with standard basic state. (B) Non-diffusive with a modified basic state in which the primary wave is stationary. (C) Diffusive in the stationary basic state.

(FFTW) subroutines developed by Frigo and Johnson (1998). These subroutines work very efficiently by reducing the space dimension $M$ to its prime components (not just powers of two), for which optimal algorithms are developed. This is illustrated in figure B-3, which shows the required computing time for performing 5000 direct and inverse double transforms of various dimensions. This performance is compared to the number of operations required by the regular Fourier transform ($O(M^2)$, upper curve) and by the standard Fast Fourier Transform for dimensions powers of two ($O(M \log(M)$, lower curve). As can be seen, except for nearly prime dimensions, FFTW has comparable efficiency to the standard FFT, without requiring a dimension power of 2. This gives us more flexibility in choosing the resolution than is standard in most spectral models.

For each harmonic, the $q - \psi$ inversion is trivial in the barotropic model and a simple ODE in the qg model. Using second order centered differencing in $z$ for the latter, this produces a tridiagonal matrix, which can be easily inverted using a TDMA algorithm.

There are $80 \times 200$ gridpoints in the barotropic model and $24 \times 90$ in the qg model. With the 2/3 truncation, this gives $26 \times 66$ waves and a horizontal resolutions of $110 \times 95$ $km^2$ for the former, and $8 \times 30$ waves and a horizontal resolution of $250 \times 250$ $km^2$ for the latter. Finally, there are 50 vertical levels in the qg model, which gives a grid spacing of $\Delta z = 600$ $m$. The results did not show much sensitivity to improved resolution.

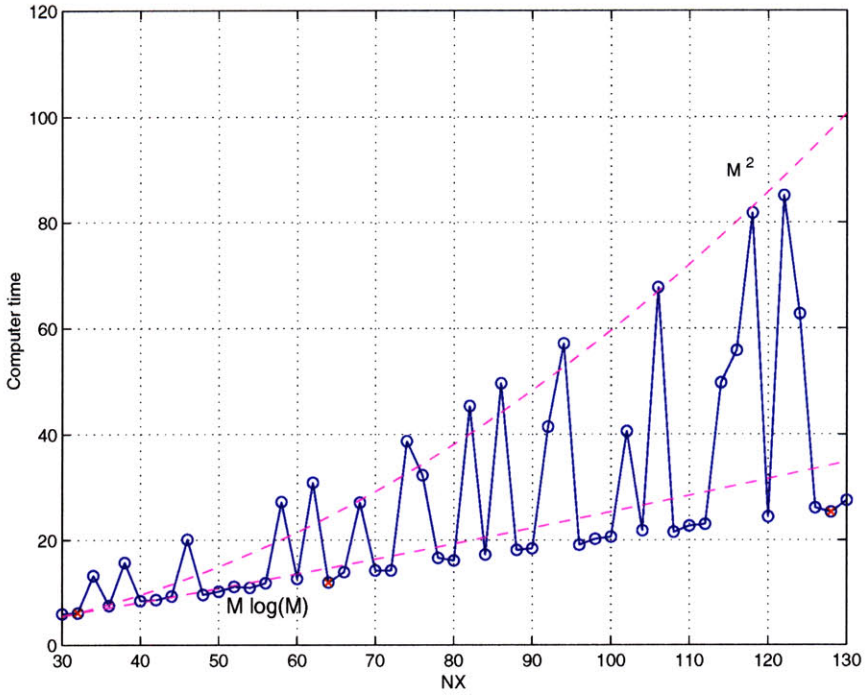


Figure B-3: Computer time required to perform 5000 direct and inverse Fast Fourier Transforms, with varying $NX$ and fixed $NY = 64$. This is compared to $O(M^2)$ (upper curve) and $O(M \log(M))$ (lower curve). Dimensions that are power of 2 are emphasized in red.

## B.1 Contour advection model

In chapter 6 a contour advection model is used to interpret the dynamical evolution of the barotropic point jet. The contour advection model used is an adaptation of that described by Waugh and Plumb (1994), except for the fact that we do not use surgery. The algorythm essentially advects all contour nodes, using a velocity field interpolated from the numerical grid. This is done on the same time step on which the dynamical model is evolved.

We start with 1000 zonally-alligned nodes, which gives an initial spacing between nodes of 6 $km$. However, because of the deformation of the flow, at any given time some nodes converge and others diverge, following the instantaneous manifolds. When the separation between 2 nodes exceeds 20 $km$, nodes are added in between until this spacing is reduced to 10 $km$. On the other hand, when the nodes get too close (closer than 3 $km$), a redundant node is eliminated for computational efficiency. These cutoff numbers were found to give a reasonable compromise between computational efficiency and resolution for the length of the integrations involved, and were not optimized further.

# Bibliography


Abramowitz, M. and I. A. Stegun: 1965, *Handbook of Mathematical Functions*. Dover.

Andrews, D. G. and M. E. McIntyre: 1978, An exact theory of nonlinear waves on a Lagrangian-mean flow. *J.Fluid.Mech*, **89**, 609–646.

Barry, L., G. C. Craig, and J. Thuburn: 2000, A GCM investigation into the nature of baroclinic adjustment. *J.Atmos.Sci*, **57**, 1141–1155.

Bowman, K. P.: 1995, Diffusive transport by breaking waves. *J.Atmos.Sci.*, **52**, 2416–2427.

Bowman, K. P. and P. Chen: 1994, Mixing by barotropic instability in a nonlinear model. *J.Atmos.Sci.*, **51**, 3692–3705.

Branscome, L. E.: 1983, The Charney baroclinic stability problem: approximate solutions and modal structures. *J.Atmos.Sci.*, **40**, 1393–1409.

Bretherton, F. P.: 1966, Critical layer instability in baroclinic flows. *Q.J.Meteor.R.Soc.*, **92**, 325–334.

Burger, A. P.: 1962, On the non-existence of critical wavelengths in a continuous baroclinic instability problem. *J.Atmos.Sci*, **19**, 31–38.

Cehelsky, P. and K. Tung: 1991, Nonlinear baroclinic adjustment. *J.Atmos.Sci*, **48**, 1930–1947.

Chang, E. K. M.: 1996, Mean meridional circulation driven by eddy forcing of different timescales. *J.Atmos.Sci*, **53**, 113–125.

Charney, J. G.: 1947, The dynamics of long waves in a baroclinic westerly current. *J.Meteor*, **4**, 135–162.

Charney, J. G. and M. E. Stern: 1962, On the stability of internal baroclinic jets in a rotating atmosphere. *J.Atmos.Sci.*, **19**, 159–172.

Del Castillo Negrete, D. and P. J. Morrison: 1993, Chaotic transport by Rossby waves in shear flow. *Phys. Fluids A*, **5**, 948–965.

Durran, D. R.: 1991, The third order Adams-Bashford method: An attractive alternative to leapfrog time differencing. *Mon.Wea.Rev.*, **119**, 702–720.

Eady, E. T.: 1949, Long waves and cyclone waves. *Tellus*, **1**, 33–52.

Edmon, H. J., B. J. Hoskins, and M. E. McIntyre: 1980, Eliassen-Palm cross-sections for the troposphere. *J.Atmos.Sci*, **37**, 2600–2616.

Finn, J. M. and D. Del-Castillo-Negrete: 2001, Lagrangian chaos and Eulerian chaos in shear flow dynamics. *Chaos*, **11**, 816–832.

Frigo, M. and S. G. Johnson: 1998, Fftw: An adaptive software architecture for the fft. *International Conference on Accoustics, Speech and Signal Processing*, IEEE, volume 3, 1381–1384.

Fullmer, J. W. A.: 1982, Calculations of the quasigeostrophic potential vorticity gradient from climatological data. *J.Atmos.Sci*, **39**, 1873–1877.

Green, J. S. A.: 1960, A problem in baroclinic stability. *Q.J.Meteor.R.Soc.*, **86**, 237–251.

Gutowski, W. J.: 1985, A simple model for the interaction between vertical eddy heat fluxes and static stability. *J.Atmos.Sci*, **42**, 1735–1745.

Gutowski, W. J., L. E. Branscome, and D. A. Stewart: 1989, Mean flow adjustment during lifecycles of baroclinic waves. *J.Atmos.Sci*, **46**, 1724–1737.

Harnik, H.: 2000, *The vertical structure of stratospheric planetary waves and its variability: Theory and observations*. Ph.D. thesis, Massachusetts Institute of Technology.

Held, I. M.: 1978, The vertical scale of an unstable baroclinic wave and its importance for eddy heat flux parameterizations. *J.Atmos.Sci*, **35**, 572–576.

— 1982, On the height of the tropopause and the static stability of the troposphere. *J.Atmos.Sci*, **39**, 412–417.

— 1999, The macroturbulence of the troposphere. *Tellus*, **51AB**, 59–70.

— 2001, A qualitative model of storm tracks. *13th Conference on Atmospheric and Oceanic Fluid Dynamics*, American Meteorological Society.

Held, I. M. and T. Schneider: 1999, The surface branch of the zonally averaged mass transport circulation in the troposphere. *J.Atmos.Sci.*, **56**, 1688–1697.

Hoskins, B. J.: 1991, Towards a PV-$\theta$ view of the general circulation. *Tellus*, **43AB**, 27–35.

Ioannou, P. and R. S. Lindzen: 1986, Baroclinic instability in the presence of barotropic jets. *J.Atmos.Sci.*, **43**, 2999–3014.

Ishioka, K. and S. Yoden: 1994, Non-linear evolution of a barotropically unstable circumpolar vortex. *J.Meteor.Soc.Japan*, **72**, 63–79.

— 1995, Non-linear aspects of a barotropically unstable polar vortex in a forced-dissipative system: flow regimes and tracer transport. *J.Meteor.Soc.Japan*, **73**, 201–212.

James, I. N.: 1987, Suppression of baroclinic instability in horizontally sheared flows. *J.Atmos.Sci*, **44**, 3710–3720.

Kalnay, E., M. Kanamitsu, M. Kistler, W. Collins, D. Deaven, L. Gandin, M. Iredell, S. Saha, G. White, M. Chelliah, W. Ebisuzaki, W. Higgins, J. Janowiak, K. C. Mo, C. Popolewski, J. Wang, R. Jenne, and D. Joseph: 1996, The NCEP/NCAR 40-Year Reanalysis Project. *B.Am.Meteorol.Soc.*, **75**, 437–470.

Killworth, P. D. and M. E. McIntyre: 1985, Do Rossby-wave critical layers absorb, reflect, or over-reflect? *J.Fluid Mech.*, **161**, 449–492.

Kim, H. and S. Lee: 2001, Hadley cell dynamics in a primitive equation model. Part II: Nonaxisymmetric flow. *J.Atmos.Sci*, **58**, 2859–2871.

Kirk-Davidoff, D. B.: 1998, *The implications of potential vorticity homogenization for climate and climate sensitivity*. Ph.D. thesis, Massachusetts Institute of Technology.

Kirk-Davidoff, D. B. and R. S. Lindzen: 2000, An energy balance model based on potential vorticity homogenization. *J.Climate*, **13**, 431–448.

Kwon, H. J. and M. Mak: 1988, On the equilibration in nonlinear barotropic instability. *J.Atmos.Sci*, **45**, 294–308.

Lait, L. R. and J. L. Stanford: 1988, Fast, long-lived features in the polar stratosphere. *J.Atmos.Sci.*, **45**, 3800–3809.

Lindzen, R. S.: 1988, Instability of plane parallel shear flow (toward a mechanistic picture of how it works). *PAGEOPH*, **126**, 103–121.

— 1990, *Dynamics in Atmospheric Physics*. Cambridge University Press.

— 1993, Baroclinic neutrality and the tropopause. *J.Atmos.Sci*, **50**, 1148–1151.

Lindzen, R. S., B. F. Farrell, and K. K. Tung: 1980, The concept of wave overreflection and its application to baroclinic instability. *J.Atmos.Sci*, **37**, 44–63.

Lindzen, R. S., A. J. Rosenthal, and B. Farrell: 1983, Charney's problem for baroclinic instability applied to barotropic instability. *J.Atmos.Sci*, **40**, 1029–1034.

Malhotra, N. and S. Wiggins: 1998, Geometric structures, lobe dynamics and Lagrangian transport in flows with aperiodic time-dependence, with applications to Rossby wave flow. *J.Nonlinear.Sci.*, **8**, 401–456.

McIntosh, P. C. and T. J. McDougall: 1996, Isopycnal averaging and the residual mean circulation. *J.Phys.Oceanogr.*, **26**, 1655–1660.

McIntyre, M. E. and T. N. Palmer: 1984, The "surf zone" in the stratosphere. *J.Atmos.Terr.Phys*, **46**, 825–849.

Mizuta, R. and S. Yoden: 2001, Chaotic mixing and transport barriers in an idealized polar vortex. *J.Atmos.Sci*, **58**, 2616–2629.

Morgan, M. C.: 1994, *Observationally and dynamically determined basic state for the study of synoptic scale waves*. Ph.D. thesis, Massachusetts Institute of Technology.

Neu, J. L.: 2001, *Tropical transport and the seasonal variability of the subtropical 'edges' in the stratosphere*. Ph.D. thesis, Massachusetts Institute of Technology.

Newell, R. E., E. V. Browell, D. D. Davis, and S. C. Liu: 1997, Western Pacific tropospheric ozone and potential vorticity: Implications for Asian pollution. *Geoph.Res.Letters*, **24**, 2733–2736.

Ngan, K. and T. G. Shepherd: 1997, Chaotic mixing and transport in Rossby-wave critical layers. *J.Fluid.Mech*, **334**, 315–351.

— 1999, A closer look at chaotic advection in the stratosphere. Part I: Geometric structure. *J.Atmos.Sci.*, **56**, 4134–4152.

Nielsen, J. E. and M. R. Schoeberl: 1984, A numerical simulation of barotropic instability. Part II: Wave-wave interaction. *J.Atmos.Sci*, **41**, 2869–2881.

Orsolini, Y. and P. Simon: 1995, Idealized life cycles of planetary-scale waves in the middle atmosphere. *J.Atmos.Sci*, **52**, 3817–3835.

Ottino, J. M.: 1990, Mixing and chaotic advection. *Annu.Rev.Fluid Mech.*, **22**, 207–253.

Pedlosky, J.: 1987, *Geophysical Fluid Dynamics*. Springer-Verlag, second edition.

— 1996, *Ocean Circulation Theory*. Springer-Verlag.

Peixoto, J. P. and A. H. Oort: 1992, *Physics of Climate*. AIP Press.

Pfeffer, R. L.: 1987, Comparison of conventional and transformed Eulerian mean diagnostics in the troposphere. *Q.J.Meteor.R.Soc.*, **113**, 237–254.

Pierrehumbert, R. and H. Yang: 1993, Global chaotic mixing on isentropic surfaces. *J.Atmos.Sci*, **50**, 2462–2480.

Pierrehumbert, R. T.: 1991, Chaotic mixing of tracer and vorticity by modulated travelling waves. *Geophys. Astrophys. Fluid Dyn.*, **41**, 2141–2162.

Polvani, L. and R. A. Plumb: 1992, Rossby wave breaking, microbreaking, filamentation and secondary vortex formation: The dynamics of a perturbed vortex. *J.Atmos.Sci*, **49**, 462–476.

Prieto, R. and W. H. Schubert: 2001, Analytical predictions for zonally symmetric equilibrium states of the stratospheric polar vortex. *J.Atmos.Sci*, **58**, 2709–2728.

Rhines, P. B. and W. R. Young: 1983, How rapidly is a passive scalar mixed within closed streamlines? *J.Fluid.Mech*, **133**, 133–145.

Rivest, C., C. A. Davis, and B. F. Farrell: 1992, Upper-tropospheric synoptic-scale waves. Part I: maintenance as Eady normal modes. *J.Atmos.Sci.*, **49**, 2108–2119.

Salmon, R. S.: 1980, Baroclinic instability and geostrophic turbulence. *Geophys. Astrophys. Fluid Dyn.*, **15**, 167–211.

Schneider, T. and I. Held: 1999, The slope of the isentropes in the extratropical troposphere. *12th Conference on Atmospheric and Oceanic Fluid Dynamics*, American Meteorological Society.

Schoeberl, M. R. and R. S. Lindzen: 1984, A numerical simulation of barotropic instability: 1. Wave-mean flow interaction. *J.Atmos.Sci*, **41**, 1368–1379.

Schoeberl, M. R. and J. E. Nielsen: 1986, A numerical simulation of barotropic instability. Part III: Wave-wave interaction in the presence of dissipation. *J.Atmos.Sci*, **43**, 1045–1050.

Shepherd, T. G.: 2000, The middle atmosphere. *J.Atmos.Solar.-Terr.Phys*, **62**, 1587–1601.

Simmons, A. J. and B. J. Hoskins: 1978, The lifecycles of some nonlinear baroclinic waves. *J.Atmos.Sci*, **35**, 414–432.

Solomon, A. B. and R. S. Lindzen: 2000, The impact of resolution on a numerical simulation of barotropic instability. *J.Atmos.Sci*, **57**, 3799–3816.

Solomon, A. B. and P. H. Stone: 2001, Equilibration in an eddy resolving model with simplified physics. *J.Atmos.Sci.*, **58**, 561–574.

Sparling, L. C.: 2000, Statistical perspectives on stratospheric transport. *Rev.Geophys.*, **38**, 417–436.

Stone, P. H.: 1978, Baroclinic adjustment. *J.Atmos.Sci*, **35**, 561–571.

— 1982, *Feedbacks between dynamical heat fluxes and temperature structure in the atmosphere*. Climate Processes and Climate Sensitivity. AGU Monograph 29.

Stone, P. H. and L. Branscome: 1992, Diabatically forced, nearly inviscid eddy regimes. *J.Atmos.Sci*, **49**, 355–367.

Stone, P. H. and B. Nemet: 1996, Baroclinic adjustment: a comparison between theory, observations, and models. *J.Atmos.Sci.*, **53**, 1663–1674.

Sun, D. Z. and R. S. Lindzen: 1994, A PV view of the zonal mean distribution of temperature and wind in the extratropical troposphere. *J.Atmos.Sci.*, **51**, 757–772.

Swanson, K. and R. T. Pierrehumbert: 1997, Lower-tropospheric heat transport in the Pacific storm track. *J.Atmos.Sci*, **54**, 1533–1543.

Swanson, K. L., P. J. Kushner, and I. M. Held: 1997, Dynamics of barotropic storm tracks. *J.Atmos.Sci*, **54**, 791–810.

Thorncroft, C. D., B. J. Hoskins, and M. E. McIntyre: 1993, Two paradigms of baroclinic-wave life-cycle behavior. *Q.J.Meteor.R.Soc.*, **119**, 17–55.

Thuburn, J. and G. C. Craig: 1997, GCM tests of theories for the height of the tropopause. *J.Atmos.Sci*, **54**, 869–882.

— 2000, Stratospheric influence on tropospheric height: the radiative constraint. *J.Atmos.Sci*, **57**, 17–28.

Waugh, D. W. and R. A. Plumb: 1994, Contour advection with surgery -a technique for investigating finescale structure in tracer transport. *J.Atmos.Sci*, **51**, 530–540.

Welch, W. and K. Tung: 1998, Nonlinear baroclinic adjustment and wave selection in a simple case. *J.Atmos.Sci*, **55**, 1285–1302.

Zurita, P. and R. S. Lindzen: 2001, The equilibration of short Charney waves: implications for PV homogenization in the extratropical troposphere. *J.Atmos.Sci*, **58**, 3443–3462.